Dissertation
submitted to the
Combined Faculties for the Natural Sciences and for Mathematics
of the Ruperto Carola University of Heidelberg, Germany
for the degree of
Doctor of Natural Sciences

presented by
Diplom-Physicist: Christina Peters
born in: Würselen

Oral examination: 06.07.2005

Studies of Reactive Halogen Species (RHS) in the Marine and mid-Latitudinal Boundary Layer by Active Longpath Differential Optical Absorption Spectroscopy

Referees: Prof. Dr. Ulrich Platt
Prof. Dr. Frank Arnold

Untersuchungen von Reaktiven Halogenverbindungen (RHS) in der Maritimen Grenzschicht und in Mittleren Breiten mit der Aktiven Langpfad DOAS Methode

Die Relevanz reaktiver Halogenverbindungen in der Troposphäre ist einerseits belegt durch den gravierenden Einfluss auf Ozon, welcher zum ersten Mal während des polaren Sonnenaufgangs in der vollständigen Zerstörung bodennahem Ozons durch reaktive Bromverbindungen beobachtet wurde. Weiterhin werden reaktive Iodverbindungen in Zusammenhang mit aktuell beobachteter Partikelbildung in Küstengebieten gebracht. Da Partikel in der Atmosphäre die mikrophysikalischen Eigenschaften von Stratocumulus Wolken beeinflussen, kann in diesen Beobachtungen eine große Bedeutung für das Klima liegen. Im Rahmen der vorliegenden Arbeit wurden drei Feldmesskampagnen unter Verwendung der aktiven Langpfad DOAS Messmethode durchgeführt, um das Vorkommen von reaktiven Halogenverbindungen, speziell BrO, IO, OIO und I_2 in verschiedenen mittlereren Breiten zu untersuchen. Während bodengebunder Messungen in der arktisch beeinflussten Region der Hudson Bay, Kanada wurden bis zu 35 ppt des BrO Radikals detektiert zeitgleich zur fast vollständigen Zerstörung des bodennahen Ozons. Bei zwei weiteren Feldmesskampagnen zur Untersuchung der RHS in maritim beeinflussten Gebieten an der deutschen Nordseeküste und der französischen Atlantikküste wurde IO als einziges Halogenoxid in beiden Umgebungen gefunden mit maximalen Konzentrationen von 7.7±0.5 ppt. In dieser maritimen Umgebung konnte BrO nicht oberhalb der Nachweisgrenze von 1.5 ppt nachgewiesen werden, ebenso verblieben OIO und auch I_2 unterhalb der Nachweisgrenze. Eine Reanalyse von DOAS Spektren, die während einer vorangegangenen Kampagne 1998 in Mace Head, Irland gewonnen wurden, ergaben 61±12 ppt I_2 während der Nacht und besonders tiefem Wasserstand während Springtide. Diese Beobachtungen werden erklärt unter der Annahme, dass Laminaria Algen, die den unteren Intertidenbereich bewohnen, während dieser Zeit in Kontakt mit der Atmosphäre molekulares Iod emittieren.

Studies of Reactive Halogen Species (RHS) in the Marine and mid-Latitudinal Boundary Layer by Active Longpath Differential Optical Absorption Spectroscopy

The importance of reactive halogen species in the troposphere is on the one hand due to their strong effect on tropospheric ozone levels, which has been discovered for the first time during ozone depletion events in the polar boundary layer during polar sunrise. On the other hand recent field and laboratory studies are indicating a great relevance of reactive iodine in new particle formation processes. Since particles in the marine atmosphere affect the microphysical properties of stratocumulus clouds, they have a potential impact on climate. Within the framework of this thesis three field campaigns using active longpath DOAS technique for studies of the reactive

halogen species BrO, IO, OIO and I_2 were conducted in different mid-latitudinal regions. Ground based measurements in the lower Arctic at the Hudson Bay yielded high levels of the BrO radical up to 35 ppt in the boundary layer, coinciding with nearly complete surface near ozone depletion. Two field campaigns investigated the appearance of RHS in the coastal environments of the German North Sea and the French Atlantic Coast, IO was the only halogen oxide found in both locations with concentrations reaching 7.7±0.5 ppt. BrO in the marine boundary layer was estimated to remain below 1.5 ppt, neither OIO nor I_2 could be identified in the spectra. Within a re-analysis of spectra taken during a former campaign in 1998 in Mace Head, Ireland 61±12 ppt I_2 were detected at night during extraordinary low water level most likely emitted by laminaria algae inhabiting parts of the lower intertidal zone.

Contents

Chapter 1

Introduction

It is well established that reactive halogen species (RHS) significantly influence a variety of atmospheric processes. This is impressively demonstrated during polar spring, when boundary layer ozone is depleted within days or even hours by catalytic cycles involving bromine, the so-called 'bromine explosion' events, e.g. [*Platt and Lehrer* 1996].
The presence of haologen oxides outside polar regions could influence the ozone budget and the oxidation capacity of the troposphere by affecting the NO/NO_2 and OH/HO_2 partitioning, e.g. [*Platt and Hönninger* 2003].
On local scales the presence of BrO in mid-latitudinal regions could be observed so far in a variety of different environments, e.g. salt lakes [*Hebestreit et al.* 1999], [*Stutz et al.* 2002], [*Hönninger et al.* 2004], [*Zingler and Platt* 2005] and volcanic plumes [*Bobrowski et al.* 2003] as well as in the marine boundary layer ([*Leser et al.* 2003], [*Saiz-Lopez et al.* 2004]), whereas significant appearance of reactive iodine species (IO, OIO, I_2) is presently reported mainly from coastal sites. IO could contribute to ozone destruction in a way comparable to BrO, even in low concentrations.
Additionally, recent field and laboratory studies are indicating a great relevance of reactive iodine in new particle formation processes [*Hoffmann et al.* 2001], [*O'Dowd et al.* 2002], [*Jimenez et al.* 2003], [*Burkholder et al.* 2004]. Events of particle formation with concentrations of up to 10^6 particles/cm^3 have been observed in marine environments, e.g. [*Mäkelä et al.* 2002], [*O'Dowd et al.* 2002]. As particles in the marine atmosphere affect the microphysical properties of stratocumulus clouds, they have a potential impact on climate. Therefore, the investigation of sources, appearance and distribution of reactive iodine species on a global scale is of high interest in present research activities, and is addressed within this thesis, by three field

campaigns, conducted in different mid-latitudinal regions.

The current understanding of the particle formation process is quite limited. *O'Dowd et al.* [2002] proposed that particle formation in coastal environments is dominated by polymerization of the OIO radical. However, field observations of OIO in the marine environment are rare [*Allan et al.* 2000], even though great effort was made for its detection. This, as well as observations which will be presented in this thesis from two different coastal sites, seem to indicate that OIO is maybe present in the marine environment, but in concentrations clearly below 10 ppt. These concentrations are insufficient to explain particle formation processes, according to *Burkholder et al.* [2004], thus they suggested an inhomogeneous source distribution in so-called 'hot spots' to explain this apparent discrepancy. However, inhomogeneous distribution of RHS along the lightpath cannot be resolved by longpath DOAS measurements, which were conducted for this work.
The most likely source of reactive iodine is the emission of organohalogens by macroalgae, which would excellently fit into the picture of inhomogeneous release due to the patchy distribution of algae in coastal regions. Diiodomethane is biogenically emitted by a variety of macroalgae as reported by e.g. [*Schall and Heumann* 1993], [*Carpenter et al.* 1999]. Due to the short photolytic lifetime of CH_2I_2, iodine atoms are released within minutes into the atmosphere, where they quickly react with ozone to form IO.

Recently, the detection of molecular iodine at Mace Head was reported by *Saiz-Lopez and Plane* [2004], who found highly elevated levels of I_2 closely correlated to minima in tidal height indicating again macroalgae to be the source. These findings could be confirmed by a re-analysis of DOAS spectra, which was done in the framework of this thesis. However, it is unclear if the appearance of I_2 is a common phenomenon in the marine boundary layer since the results have not been confirmed at further coastal sites so far.

Outline of the thesis
In the second chapter an overview on the impact of reactive halogen species on atmospheric chemistry is given. Reactive bromine and iodine chemistry are described both in detail, including a brief summary of the current knowledge of homogeneous nucleation of iodine oxides leading to observed particle burst events.
In the third chapter the measurement technique is introduced, starting with a general description of the DOAS method and the principles of the DOAS analysis procedure. In the following the application and the technical de-

scription and characterization of the main components of the active longpath DOAS telescope, which was used as the central measurement method for this thesis is given in full detail. Furthermore in this chapter an overview on the spectra analysis and evaluation procedure will be discussed, and the retrieval of concentrations for the species BrO, IO, OIO and I_2 will be explained in detail.
In the fourth and fifth chapter the description and the results of the 2002 North Sea campaign and the 2003 Brittany campaign will be given. Both campaigns were conducted in coastal environments and the discussion of the results will be given in chapter 5, including a comparison of both measurement sites, which differed significantly in their bioactivity. A detailed description of the DOAS spectra for the detection of OIO and I_2 will be given as well. Furthermore a comparison of the observations of the 2003 Brittany data was done with the marine boundary layer model MISTRA and the results of this model studies will be addressed at the end of chapter 5.
In the sixth chapter the re-analysis of the 1998 PARRFORCE campaign will be introduced, where molecular iodine in the DOAS spectra could be detected and the differences to the likewise bioactive coastal site of Brittany will be discussed.
In the seveth chapter the description of the 2004 Hudson Bay campaign and a discussion of two observed BrO events will be given.
A short summary and outlook for future tasks in the halogen research is given in the last chapter.

Chapter 2

The Chemistry of Reactive Halogen Species in the Atmosphere

In this chapter an overview on atmospheric chemistry involving **R**eactive **H**alogen **S**pecies (**RHS**) will be given. Sources, main reactions, and distribution of RHS will be discussed in the first section regarding the general aspects and in the following more special regarding bromine and iodine species.
The impact of RHS in the atmosphere is widespread. Especially the importance of halogen oxides on the ozone budget in the atmosphere (stratosphere as well as troposphere) is of high relevance in atmospheric chemistry, due to the highly destructive potential in autocatalytic processes (Ozone holes). By affecting the ozone budget, the oxidation capacity is as well influenced by halogen chemistry, since the loss of ozone by the catalytic reaction affects the NO/NO_2 and OH/HO_2 partitioning (e.g [*Platt and Hönninger* 2003]).
Moreover, studies in the last years show a potential impact of iodine on new particle production in coastal regions. Since particles in the MBL can affect the microphysical properties of stratocumulus clouds, the observed particle nucleation events may be relevant for the global climate. These findings are of current research interest and not well understood so far. An overview on the state-of-the-art knowledge on iodine chemistry on particle formation in coastal regions will be presented at the end of this chapter in Section 2.4.2.

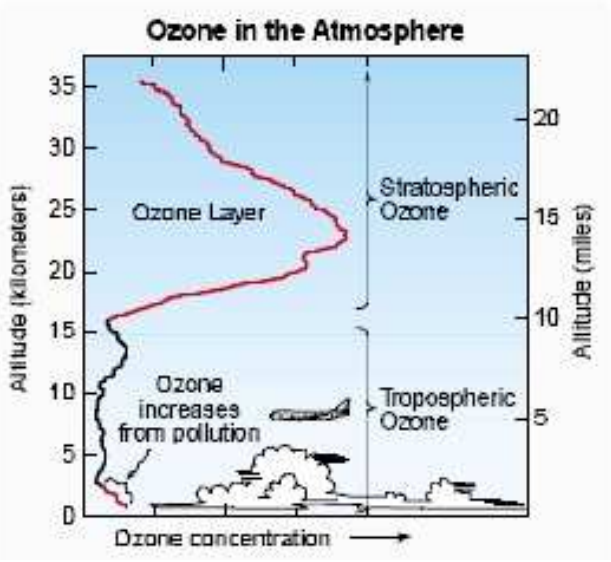

Figure 2.1: *Distribution of ozone in the atmosphere. More than 90% of the ozone is located within the stratosphere, acting as a protection shield against harmful UV-B radiation coming from the sun.*

2.1 Definition of RHS

The term Reactive halogen species (RHS) includes the halogen atoms itself (X,Y = F, Cl, Br, I, At), the halogen molecules (X_2), the interhalogen compounds (XY), the halogen monoxides (XO) and the higher oxides X_nO_m as well as the hypohalous acids (HOX). The reactivity of RHS is relatively high in comparison to hydrogen halides (HX) or halogen-NO_x compounds (XNO_x).

2.2 Ozone in the Atmosphere

In 1985 the discovery of the ozone hole by *Farman et al.* [1985] led to great interest in atmospheric chemistry involving halogens. Already in the 1970ies it was postulated by *Molina and Rowland* [1974] that the release of industrially produced halocarbons, in particular the chlorofluorocarbons (CFCs) $CFCl_3$ and CF_2Cl_2 could cause severe depletion of stratospheric ozone, by reactions involving the photolytical products from CFC radicals

Spec.	**Location**	**Max. Conc. [ppt]**	**Error $\pm(2\sigma)$ [ppt]**	**Reference**
IO	Mace Head, Ireland (1997)	6.7	0.5	*Alicke et al.* [1999]
IO	Mace Head (1998)	7.2	0.3	*Hebestreit* [2001]
IO	Mace Head (2002)	7	0.5	*Saiz-Lopez and Plane* [2004]
IO	Tasmania (1999)	2.2	0.4	*Allan et al.* [2000]
IO	Tenerife, Can. Islands (1997)	3.5	0.4	*Allan et al.* [2000]
IO	Kerguelen, Ind. Ocean (2002)	≤D.L. (1.4)	1.4	*Sebastián* [2004]
IO	North Sea, Germany (2002)	2.1	0.5	this work
IO	Atlantic Coast, France (2003)	7.7	0.5	this work
IO	Crete, Greece (2003)	≤D.L. (0.8)	0.8	*Hönninger* [2002]
IO	Dead Sea, Israel (2000)	10	2.4	*Zingler and Platt* [2005]
IO	Antarctic and Arctic	10	-	*Frieß et al.* [2001], *Wittrock et al.* [2000]
IO	Alert, Arctic (2000)	0.73	0.23	*Hönninger* [2002]
OIO	Cape Grim, Tasmania (1999)	3.0	0.5	*Allan et al.* [2001]
OIO	Mace Head, Ireland (1998)	6.7	0.5	*Hebestreit* [2001]
OIO	Mace Head, Ireland (2002)	3.0	0.5	*Saiz-Lopez and Plane* [2004]
I_2	Mace Head, Ireland (2002)	93	3	*Saiz-Lopez and Plane* [2004]
I_2	Mace Head, Ireland (1998)	61.3	12	this work
BrO	Mid.Lat. MBL	6.0	-	*Leser et al.* 2003, *Saiz-Lopez et al.* [2004]
BrO	Salt lakes (Dead Sea, Salt Lake City, Caspian Sea, Salar de Uyuni)	176	-	*Hebestreit et al.* [1999], *Matveev et al.* [2001], *Wagner et al.* [2001], *Stutz et al.* [2002], *Hönninger et al.* [2004]
BrO	Antarctic, Arctic	30	-	*Hausmann and Platt* [1994], *Tuckermann et al.* [1997], *Hegels et al.* [1998], *Martinez et al.* [1999], *Hönninger et al.* [2004], *Frieß* [2001]
BrO	Volcanoes	∼ 1000	-	*Bobrowski et al.* [2003]

Table 2.1: *Observation of RHS in the troposphere by active and passive DOAS technique.*

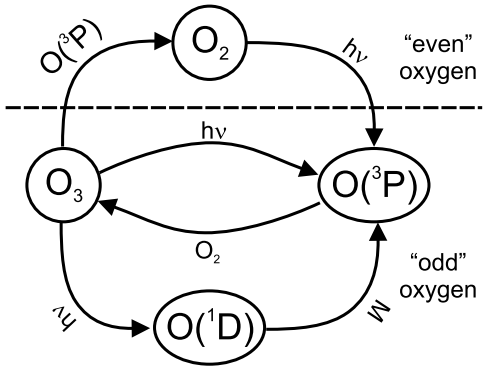

Figure 2.2: *The Chapman cycle*

Cl and ClO as catalysts.

2.2.1 Stratosphere

More than 90% of the total atmospheric ozone is located in the stratosphere. The maximum concentration is in 15-30 km altitude in the so-called ozone layer (see Fig. 2.1). Stratospheric ozone is considered as strongly important for humans and other life forms because it absorbs ultraviolet (UV)-B radiation coming from the sun, which can severely affect the health of humans, animals and plants.

In 1930 the first theory on the photochemical formation of ozone in the stratosphere predicting a maximum around 20 km was proposed by *Chapman* [1930].
Formation and destruction of ozone in the stratosphere is described by the so-called odd-oxygen chemistry, where the production of ozone is initiated by the photolysis of molecular oxygen [*Chapman* 1930].

$$O_2 + h\nu \longrightarrow 2O(^3P) \qquad \lambda \leq 242\ nm \tag{2.1a}$$

$$O(^3P) + O_2 + M \longrightarrow O_3 + M \tag{2.1b}$$

Ozone is formed via the reaction (2.1b) of O + O_2 with a collision partner M. The following reactions lead to destruction of ozone:

$$O_3 + h\nu \longrightarrow O_2 + O(^1D) \qquad \lambda \leq 320\ nm \qquad (2.2a)$$

$$O(^1D) + M \longrightarrow O(^3P) + M \qquad (2.2b)$$

$$O_3 + h\nu \longrightarrow O_2 + O(^3P) \qquad \lambda \leq 1180\ nm \qquad (2.2c)$$

$$2O(^3P) + M \longrightarrow O_2 + M \qquad (2.2d)$$

$$O(^3P) + O_3 \longrightarrow 2O_2 \qquad (2.2e)$$

Photolysis of ozone (2.2a and 2.2b) besides the reaction 2.1b interconverts O and O_3, which are the rationales of the concept of odd oxygen, whereas O_2 represents the even oxygen. Reaction 2.2e is the main loss process for odd oxygen in the chapman cycle, as reaction 2.2d is known to be too slow to be important for stratospheric chemistry. A sketch of the chapman cycle is shown in Figure 2.2. By observations it turned out, that the chapman cycle alone cannot explain the real ozone profiles. As the calculated stratospheric ozone abundance comprising only oxygen chemistry is overestimated by a factor 2, more ozone destroying mechanisms have to be considered. The observed lower ozone levels were subsequently explained in the following years by stratospheric chemistry cycles involving species such as hydrogen and nitrogen as well as halogen compounds ([*Bates and Nicolet* 1950; *Crutzen* 1970; *Johnston* 1971; *Crutzen* 1973]), see Figure 2.3.

2.2.2 Troposphere

UV light below 240 nm is necessary to photolyze O_2 via the reaction 2.1a, thus the production mechanism of ozone in the troposphere must be principally different from that in the stratosphere. It was commonly assumed until the late 1970s that tropospheric ozone has its origin in the stratosphere (e.g. *Junge* [1963]). It was believed that stratospheric ozone was mixed through the tropopause region exhibiting a gradient towards the earth's surface, which was thought to be the dominant sink. It was found by *Fishman and Crutzen* [1978] that only 50% of the tropospheric ozone could have its origin in the stratosphere, as the additional source they proposed the production of ozone in the troposphere by NO_x chemistry and reactions involving methane and other reactive hydrocarbons. A key sequence for the formation and destruction of tropospheric ozone are reactions involving NO_x:

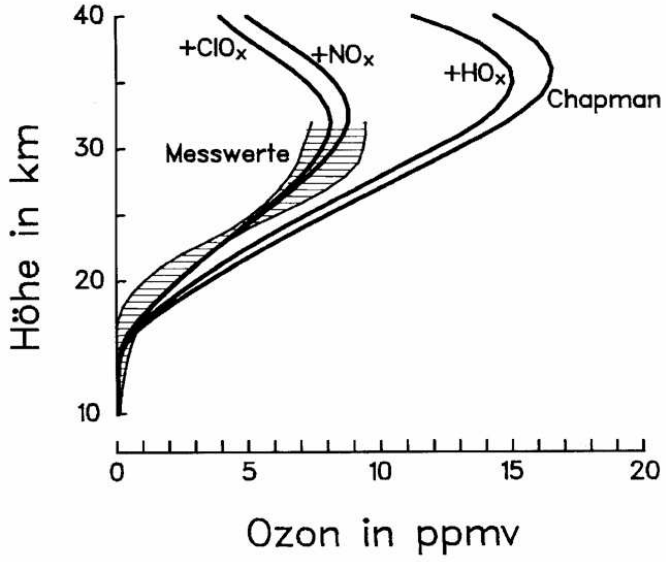

Figure 2.3: *Comparison between observed and modelled stratospheric ozone mixing ratios, if only the Chapman cycle is taken into account and by taking HO_x, NO_x and ClO_x chemistry into account (adapted from Röth [1994]).*

$$NO_2 + h\nu \longrightarrow NO + O(^3P) \qquad \lambda \leq 420\ nm \tag{2.3a}$$

$$O(^3P) + O_2 + M \longrightarrow NO + O_3 + M \qquad k_1 = 1.5 \cdot 10^{-14} \tag{2.3b}$$

$$NO + O_3 \longrightarrow NO_2 + O_2 \qquad k_2 = 1.8 \cdot 10^{-12} \tag{2.3c}$$

with the rate constants given in units of $cm^3 molec^{-1} s^{-1}$. The ozone concentration is then determined by the photo-stationary steady state of reaction cycles Eq. (2.3), which can be expressed as the so-called *Leighton-ratio* L:

$$L \equiv \frac{[NO]}{[NO_2]} = \frac{J(NO_2)}{[O_3] \cdot k_2} \tag{2.4}$$

In contrast to anthropogenic influenced areas, remote regions are characterized by NO_x mixing ratios below 5-10 ppt.
Under conditions of more elevated levels of NO_x, nitrogen and hydrogen oxides are able to produce ozone by the degradation of methane or higher

hydrocarbons in the following reaction sequence:

$$CH_4 + OH \longrightarrow CH_3 + H_2O \tag{2.5a}$$
$$CH_3 + O_2 + M \longrightarrow CH_3O_2 + M \tag{2.5b}$$
$$CH_3O_2 + NO \longrightarrow CH_3O + NO_2 \tag{2.5c}$$
$$CH_3O + O_2 \longrightarrow CH_2O + HO_2 \tag{2.5d}$$
$$CH_2O + h\nu \xrightarrow{50\%} HCO + H \tag{2.5e}$$
$$CH_2O + h\nu \xrightarrow{50\%} H_2 + CO \tag{2.5f}$$
$$HCO + O_2 + M \longrightarrow CO + HO_2 + M \tag{2.5g}$$
$$H + O_2 + M \longrightarrow HO_2 + M \tag{2.5h}$$
$$HO_2 + NO \longrightarrow OH + NO_2 \tag{2.5i}$$
$$NO_2 + h\nu \longrightarrow NO + O \tag{2.5j}$$
$$O + O_2 + M \longrightarrow O_3 + M \tag{2.5k}$$

net: $CH_4 + x \cdot O_2 \longrightarrow CO + 2H_2O + y \cdot O_3$

The number of ozone molecules produced by the degradation of one methane molecule is ∼2.5. Similar reaction schemes to that described above (Eq. 2.5) can also involve higher hydrocarbons. Besides the production of ozone, this reaction mechanism is an important source of CO in the troposphere. Furthermore, CO can produce additional ozone according to *Fishman and Crutzen* [1978]:

$$CO + OH \longrightarrow CO_2 + H \tag{2.6a}$$
$$H + O2 + M \longrightarrow HO_2 + M \tag{2.6b}$$
$$HO_2 + NO \longrightarrow OH + NO_2 \tag{2.6c}$$
$$NO_2 + h\nu \longrightarrow NO + O \tag{2.6d}$$
$$O_2 + O + M \longrightarrow O_3 + M \tag{2.6e}$$

net: $CO + 2O_2 \longrightarrow CO_2 + O_3$

This reaction mechanism requires sufficient presence of NO_x, above the threshold of typically 10 ppt, which represent conditions of remote areas. Instead, CO and hydrocarbons lead to destruction of ozone under low NO_x conditions:

$$CO + OH \longrightarrow CO_2 + H \tag{2.7a}$$
$$H + O_2 + M \longrightarrow HO_2 + M \tag{2.7b}$$
$$HO_2 + O_3 \longrightarrow OH + 2O_2 \tag{2.7c}$$
$$\text{net:} \quad CO + O_3 \longrightarrow CO_2 + O_2$$

Typical ozone concentrations found in the unpolluted marine boundary layer range from ∼13 ppb during summer to ∼30 ppb during winter [*Gros et al.* 1998]. This pronounced seasonal variation of ozone is partly due to the seasonal variation of O_3 input from the stratosphere and by long range transport of ozone producing pollutants from biomass burning. Ozone minima during summer can be explained by photochemical O_3 depletion , which is controlled by the availability of OH radicals. The concentration of OH depends on the solar flux since OH is generated by the photolysis of O_3 to $O(^1D)$, followed by its reaction with water vapor:

$$O_3 + h\nu \longrightarrow O_2 + O(^1D) \qquad \lambda \leq 320\ nm \tag{2.8a}$$
$$O(^1D) + H_2O \longrightarrow 2OH \tag{2.8b}$$

Removal of OH occurs for example via reaction with CO (2.6a and 2.7a), with CH_4 (2.5a) or reactions with other hydrocarbons.

The dramatic impact of halogen chemistry on the ozone budget is demonstrated during polar sunrise. Catalytic destruction of ozone leads to sometimes complete depletion of surface-near ozone, a tropospheric ozone hole. This phenomenon is strongly correlated to bromine chemistry in the troposphere and will be explained in detail in the next sections since the further investigation of this was one topic of this thesis (see Chapter 7). Moreover there are a variety of field studies at mid-latitudes showing a behavior of ozone mixing ratios, which could not be explained by the standard OH and NO_x chemistry. For example measurements by *Nagao et al.* [1999] and *Dickerson et al.* [1999] indicate already that halogen chemistry may play a significant role in the remote marine boundary layer at mid-latitudes as well as low-latitudes.

2.3 RHS in the Atmosphere

Within the last years significant amounts of halogen oxides, mainly BrO and IO were found in a variety of different environments in the troposphere, mainly reported in the marine boundary layer (MBL), besides a more localized appearance at salt lakes and volcanoes.
The most drastic effect of bromine chemistry is observed in polar regions, where the increase of BrO mixing ratios coincides with sudden ozone depletion events. These events are reported for both, the Arctic (e.g. [*Hausmann and Platt* 1994], [*McElroy et al.* 1999], [*Hönninger et al.* 2004]) and the Antarctic (e.g. [*Kreher et al.* 1997], [*Frieß* 2001]) boundary layer during polar sunrise. BrO clouds covering extended areas of several million square kilometers at both hemispheres are regularly observed during polar spring by satellite observations [*Wagner and Platt* 1998; *Richter et al.* 1998; *Hegels et al.* 1998]. Moreover, these areas are found to increase in longtime observations by GOME (Global Ozone Monitoring Experiment) during 1996 to 2001 by 10% as reported by [*Hollwedel* 2005].
Enhanced BrO in the boundary layer with coinciding ozone destruction was also detected at salt lakes e.g. [*Hönninger et al.* 2004], [*Stutz et al.* 2002], at the Dead Sea [*Hebestreit et al.* 1999] and the Caspian Sea [*Wagner et al.* 2001]. Studies by *van Roozendael et al.* [2000] suggest a free tropospheric background of 1-3 ppt BrO, according to multi-platform observations.
Recently, high amounts of BrO were found in volcanic plumes [*Bobrowski et al.* 2003]. Further observations of RHS in volcanic plumes give also good indications that ClO may be present as well [*Bobrowski* 2005]. Besides that, the only detection of ClO is reported by *Stutz et al.* [2002] during field measurements at the Great Salt Lake, Utah.
The first observation of IO was reported by *Alicke et al.* [1999]. They found IO up to 6 ppt in Mace Head, Ireland. Since then, IO was reported from various coastal regions such as Tenerife, Canary Islands and Cape Grim, Tasmania [*Allan et al.* 2000]. The detection of IO is also reported from the Arctic [*Wittrock et al.* 2000] and the Antarctic [*Frieß et al.* 2001] and from the Dead Sea [*Zingler and Platt* 2005]. In Table 2.1 an overview on detected RHS at various location and the respective detected concentration is given.
The main reaction schemes of the halogens Cl, Br and I in the troposphere appear to be similar. The differences regarding the rate constants and quantum yields concerning their photochemical reaction channels will be discussed later in this chapter.
Since the reactions for the different halogens involved are very similar X and Y will be used instead of the chemical symbols Cl, Br and I. In Table

2.2 and 2.3 the state-of-the-art rate constants and photolysis frequencies of RHS which are important regarding the two different ozone destruction cycles, are given.

2.3.1 Impact of RHS on Ozone

Halogen oxides (X,Y) and their monoxides (XO, YO) are the key species in the catalytic ozone destruction cycles [*Hausmann and Platt* 1994], [*LeBras and Platt* 1995], [*Platt and Janssen* 1995]. The halogen oxide itself is formed by the reaction with ozone (see Eq. 2.9a).
Cycle I:

$$X + O_3 \longrightarrow XO + O_2 \tag{2.9a}$$
$$Y + O_3 \longrightarrow YO + O_2 \tag{2.9b}$$
$$XO + YO \longrightarrow X + Y + O_2 \tag{2.9c}$$
$$\longrightarrow XY + O_2 \tag{2.9d}$$
$$\longrightarrow OXO + Y \tag{2.9e}$$

net: $2O_3 \longrightarrow 3O_2$

The halogen atom (X,Y) reacts very fast with the ozone, what leads to short lifetimes of the halogen atom in the troposphere ($\tau(Cl) = 0.13s, \tau(Br) = 1.3s, \tau(I) = 1.3s$, assuming a concentration of 50 ppb ozone).
The reaction products and the current branching ratios for the halogen oxide self- and cross reactions is given in Table 2.4.
Halogen or interhalogen compounds (XX, XY) are formed via reaction 2.9d, but photolyze quickly during daytime:

$$XY + h\nu \longrightarrow X + Y \tag{2.10}$$

The reaction 2.10 does not lead to a net destruction of ozone, since the photolysis of OXO leads to the formation of oxygen atoms, which recombine with O_2 to form O_3:

$$OXO + h\nu \longrightarrow XO + O \tag{2.11a}$$
$$O + O_2 + M \longrightarrow O_3 + M \tag{2.11b}$$

For X=I, the photo-dissociation of OIO may yield I and O_2, thus a net ozone destruction [*Allan et al.* 2001], [*Hebestreit* 2001]. This will be more detailed discussed in Section 2.4.2. The reaction XO with YO is the rate limiting step of the reaction cycle 2.9. Halogen oxide self reactions are usually slower

Reaction			k [$\frac{cm^3}{molec \cdot s}$]	Reference
ClO + ClO	$\longrightarrow$	Products[a]	k=$1.63 \cdot 10^{-14}$	[*Atkinson et al.*]
BrO + ClO	$\longrightarrow$	Products	k=$1.4 \cdot 10^{-11}$	[*Atkinson et al.*]
IO + ClO	$\longrightarrow$	Products	k=$1.2 \cdot 10^{-11}$	[*Atkinson et al.*]
BrO + BrO	$\longrightarrow$	Products	k=$3.2 \cdot 10^{-12}$	[*Atkinson et al.*]
BrO + IO	$\longrightarrow$	Products	k=$8.5 \cdot 10^{-11}$	[*Atkinson et al.*]
IO + IO	$\longrightarrow$	Products	k=$9.1 \cdot 10^{-11}$	[*Atkinson et al.*]
Cl + O_3	$\longrightarrow$	ClO + O_2	k=$1.2 \cdot 10^{-11}$	[*Atkinson et al.*]
Br + O_3	$\longrightarrow$	BrO + O_2	k=$1.2 \cdot 10^{-12}$	[*Atkinson et al.*]
I + O_3	$\longrightarrow$	IO + O_2	k=$1.2 \cdot 10^{-12}$	[*Atkinson et al.*]
ClO + HO_2	$\longrightarrow$	HOCl + O_2	k=$6.9 \cdot 10^{-12}$	[*Atkinson et al.*]
BrO + HO_2	$\longrightarrow$	HOBr + O_2	k=$2.4 \cdot 10^{-11}$	[*Atkinson et al.*]
IO + HO_2	$\longrightarrow$	HOI + O_2	k=$8.4 \cdot 10^{-11}$	[*Atkinson et al.*]
ClO + NO_2 + M	$\longrightarrow$	$ClONO_2$ + M	k=$1.9 \cdot 10^{-12}$	[*Atkinson et al.*]
BrO + NO_2 + M	$\longrightarrow$	$BrONO_2$ + M	k=$2.7 \cdot 10^{-12}$	[*Atkinson et al.*]
IO + NO_2 + M	$\longrightarrow$	$IONO_2$ + M	k=$3.5 \cdot 10^{-12}$	[*Atkinson et al.*]

[a] See reactions 2.9c, 2.9d and 2.9e for the possible products.

Table 2.2: *List of rate constants taken from IUPAC: Summary of Evaluated Kinetic and Photochemical Data for Atmospheric Chemistry, July 2004.*

than the cross reactions and especially cross reactions involving iodine (X = I, Y = Cl, Br) are very efficient in ozone destruction.

Reaction			photolysis frequency j $[\frac{1}{s}]$
$Cl_2 + h\nu$	$\longrightarrow$	2Cl	j = 0.0023
$Br_2 + h\nu$	$\longrightarrow$	2Br	j = 0.032
$I_2 + h\nu$	$\longrightarrow$	2I	j = 0.152
BrCl+$h\nu$	$\longrightarrow$	Br+Cl	j = 0.0104
IBr+$h\nu$	$\longrightarrow$	I+Br	j = 0.069
ICl+$h\nu$	$\longrightarrow$	I+Cl	j = 0.023
ClO+$h\nu$	$\longrightarrow$	Cl+O	j = 0
BrO+$h\nu$	$\longrightarrow$	Br+O	j = 0.035
IO+$h\nu$	$\longrightarrow$	I+O	j = 0.435
HOCl+$h\nu$	$\longrightarrow$	Cl + OH	$j = 2.35 \cdot 10^{-4}$
HOBr+$h\nu$	$\longrightarrow$	Br + OH	$j = 2.2 \cdot 10^{-3}$
HOI+$h\nu$	$\longrightarrow$	I + OH	$j = 5.9 \cdot 10^{-3}$
$ClONO_2$+$h\nu$	$\longrightarrow$	products	$j = 4.6 \cdot 10^{-5}$
$BrONO_2$+$h\nu$	$\longrightarrow$	products	j = 0.0126
$IONO_2$+$h\nu$	$\longrightarrow$	products	j = 0.0037

Table 2.3: *Photolysis frequencies at noon, calculated for 48° N clear sky conditions in the marine atmosphere for SZA 22° [von Glasow et al. 2002a], [Landgraf and Crutzen 1998].*

Cycle II involves HO_x radical:

$$X + O_3 \longrightarrow XO + O_2 \tag{2.12a}$$
$$OH + O_3 \longrightarrow HO_2 + O_2 \tag{2.12b}$$
$$XO + HO_2 \longrightarrow HOX + O_2 \tag{2.12c}$$
$$HOX + h\nu \longrightarrow OH + X \tag{2.12d}$$

net: $2O_3 + h\nu \longrightarrow 3O_2$

	ClO	k_{XO+YO} $[10^{-12}\frac{cm^3}{molec\cdot s}]$	BrO	k_{XO+YO} $[10^{-12}\frac{cm^3}{molec\cdot s}]$	IO	k_{XO+YO} $[10^{-12}\frac{cm^3}{molec\cdot s}]$
ClO	$\longrightarrow$ $Cl_2O_2^a$ $\xrightarrow{29\%}$ Cl_2+O_2 $\xrightarrow{50\%}$ $Cl+ClOO$ $\xrightarrow{21\%}$ $Cl+OClO$	1.6×10^{-2}[b]	$\xrightarrow{44\%}$ $Br+Cl+O_2$ $\xrightarrow{7\%}$ $BrCl+O_2$ $\xrightarrow{49\%}$ $OClO+Br$	13.9[b]	$\xrightarrow{55\%}$ $I+OClO$ $\xrightarrow{25\%}$ $I+Cl+O_2$ $\xrightarrow{20\%}$ $ICl+O_2$	6.1[c]
BrO	———		$\xrightarrow{85\%}$ $Br+Br+O_2$ $\xrightarrow{15\%}$ Br_2+O_2	3.2[b]	$\xrightarrow{\leq30\%}$ $I+Br+O_2$ $\xrightarrow{\leq5\%}$ $IBr+O_2$ $\xrightarrow{65-93\%}$ $OIO+Br$ $\xrightarrow{\leq15\%}$ $OBrO+I$ $\xrightarrow{\sim0\%}$ $IBrO_2+M$	85[d]
IO	———		———		$\longrightarrow$ $2I+O_2$ $\longrightarrow$ I_2+O_2 $\xrightarrow{\sim40\%}$ $OIO+I$ $\xrightarrow{\sim60\%}$ I_2O_2+M	82[e]
$\frac{k_{XO+YO}}{k_{BrO+BrO}}$	$\frac{k_{ClO+ClO}}{k_{BrO+BrO}}=5\times10^{-3}$		$\frac{k_{ClO+BrO}}{k_{BrO+BrO}}=4.3$ $\frac{k_{BrO+BrO}}{k_{BrO+BrO}}=1$		$\frac{k_{ClO+IO}}{k_{BrO+BrO}}=1.9$ $\frac{k_{BrO+IO}}{k_{BrO+BrO}}=27$ $\frac{k_{IO+IO}}{k_{BrO+BrO}}=26$	

[a] not stable in the troposphere due to thermal decomposition
[b] rate constant and branching ratios taken from [*DeMore et al.* 1997]
[c] [*Bedjanian et al.* 1997]
[d] [*Rowley et al.* 2001]
[e] [*Crowley* 2004]

Table 2.4: *Rate constants and branching ratios of halogen oxide self- and cross-reactions*

Reactive bromine is the most important species for catalytic ozone destruction in the troposphere. At 15 ppt BrO the net effect of the HO_x cycle (Cycle II) is comparable to that of Cycle I (at a typical level of 1 ppt HO_2). Note that the efficiency of Cycle II is linearly dependent on the XO concentration, whereas the XO dependence of Cycle I is quadratic. Thus at high XO levels Cycle I will dominate, at low XO Cycle II. At 30 ppt BrO, which are observed during ozone depletion in the Arctic boundary layer, 66% of the ozone destruction takes place via Cycle I. In addition, the efficiency of Cycles I and II can be enhanced by the presence of other halogen oxide species (i.e. IO, ClO) due to cross reactions (e.g. reaction 2.9c for BrO + IO) when reaction 2.9b occurs with IO or ClO instead of BrO.
An important loss channel for the halogen oxide formed in reaction (2.9a) is its photolysis and the reaction with NO:

$$XO + h\nu \longrightarrow X + O \tag{2.13a}$$
$$XO + NO \longrightarrow X + NO_2 \tag{2.13b}$$

The photolysis of halogen oxides of Eq. 2.13a leads to a null cycle with respect to ozone destruction since the oxygen atom formed, quickly recombines with O_2 to yield ozone (reaction 2.11b).

Stutz et al. [1999] calculated the importance of the different cycles for the ozone destruction rate $\frac{d[O_3]}{dt}$ as a function of the NO_x mixing ratio (see Figure 2.4) for given 6 ppt iodine oxide.
Assuming no loss of reactive halogens and including all self and cross reactions leading to O_3 destruction channels, an upper limit of the ozone loss rate as a function of XO concentration can be expressed as:

$$-\frac{d[O_3]}{dt} = 2 \cdot \sum_{i,j} k_{X_iO+Y_jO}[X_iO][Y_jO] + \sum_i k_{X_iO+HO_2}[X_iO][HO_2] \tag{2.14}$$

where the combined effects of the cycles I (including all self and cross reactions) and cycle II are taken into account.
At high NO_x concentrations the exchange reactions with the reservoir species $XONO_2$ can significantly alter the partitioning of reactive halogen species.

$$XO + NO_2 \longrightarrow XONO_2 \tag{2.15a}$$
$$XONO_2 + h\nu \longrightarrow XO + NO_2 \tag{2.15b}$$

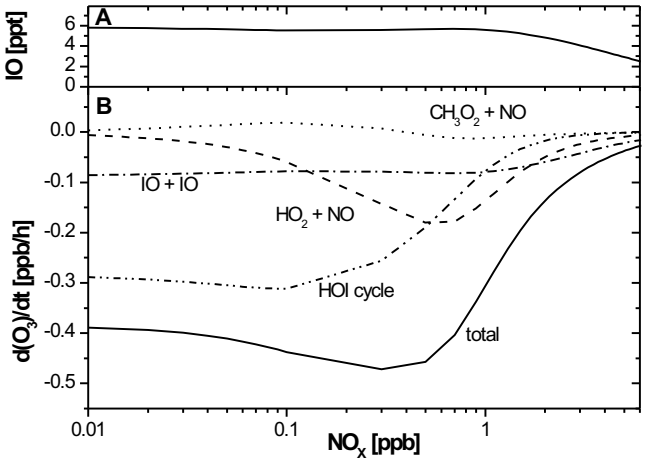

Figure 2.4: *Ozone destruction rates of the different catalytic reaction cycles for the case of iodine, as a function of the NO_x concentration (adapted from Stutz et al. [1999]).*

However, these reactions represent a null cycle with no net chemistry unless the photolysis of $XONO_2$ takes place in the XO + NO_2 channel. If X + NO_3 were formed instead, additional O_3 loss would result.
Apart from its importance for the destruction of ozone the reaction of halogen oxides with hydroperoxy radicals (2.12c) followed by the photolysis of the product from this reaction, the hypohalous acids HOX (2.12d), also have a strong influence on the ratio of OH/HO_2 [*Stutz et al.* 1999; *Hebestreit* 2001]. In analogy to reaction 2.12c, XO can also react with organic peroxy radicals (RO_2, R = organic group), e.g. the methyl peroxy radical, CH_3O_2, instead of HO_2. It has been shown in laboratory experiments that this reaction is very efficient for X = Br [*Aranda et al.* 1997]. HOBr was formed in about 80 % of the reactions.
The efficiency of the catalytic ozone destruction cycles involving halogen radicals strongly depends on the number of cycles that the reactive compounds X and XO can pass before being lost to a reservoir species. Regarding the halogen group from fluorine over chlorine and bromine to iodine, the reactivity of the halogen atoms decreases strongly. To assess the role of a halogen species in ozone destruction the branching ratio for the reaction of X with ozone (2.9a) and the reactions with hydrocarbons RH has to be considered. For bromine and iodine the reactions with HO_x are also important

branching reactions:

$$X + RH \longrightarrow HX + R \tag{2.16a}$$
$$X + HO_2 \longrightarrow HX + O_2 \tag{2.16b}$$
$$XO + HO_2 \longrightarrow HOX + O_2 \tag{2.16c}$$

Fluorine atoms released in the troposphere react very quickly with atmospheric water vapor, which is much more abundant than hydrocarbons (e.g. CH_4). HF is stable against photolysis or reaction with OH. Therefore fluorine will always remain in this passive form and has no effect on ozone chemistry [*Wayne et al.*].
Chlorine atoms react rapidly with CH_4 and other hydrocarbons to form HCl. However, Cl can be in principle be activated by reaction of HCl with OH, and under certain circumstances it is released as a byproduct of autocatalytic bromine release (see section 2.4.1).
Bromine atoms only react with unsaturated hydrocarbons and already oxidized compounds like aldehydes.
Iodine atoms almost exclusively react with ozone or other radicals.

The relative reaction rate $\frac{R_{O_3}}{R_{O_3}+\sum R_{RH}+R_{HO_2}}$ is a measure of the probability of the reaction of a halogen atom with ozone. In Table 2.5 the situation for the four halogens is listed.
Table 2.5 show, that fluorine is of no importance in the atmosphere since conversion to HF is very fast. Therefore, only the reactive halogen species chlorine, bromine and iodine are considered. In the case of chlorine about half of it is consumed by the reaction with hydrocarbons. For bromine, however, the probability for reaction with ozone is 98% and even higher with almost unity for iodine.
Assuming that all XO radicals formed in the reaction of X with O_3 are 100% reconverted to X atoms by self and cross reactions, the fraction of the rates R_{O_3} of reaction 2.9a and the sum of the rates $R_{RH} + R_{HO_2}$ of reactions 2.16a and 2.16b, $\frac{R_{O_3}}{\sum R_{RH}+R_{HO_2}}$ is an approximation of the mean number of catalytic ozone destruction cycles that a halogen atom can pass. From the last column in Table 2.5 one can see that Br and especially I are much more efficient in destroying ozone than Cl.
To describe the partitioning between the main RHS X and XO the ratio of the halogen oxide concentration [XO] and the corresponding halogen atom [X] is determined by the relative rates of the reactions which convert X into XO (the halogen reaction with ozone 2.9a and the reaction with hydrocarbons RH and HO_x (2.16a, 2.16b) and the reactions transforming XO to X

X	RH	k^*_{X+RH} (k_{X+O_3}) $[cm^3 s^{-1}]$	$typ[RH]$ ($typ[O_3]$) $[cm^{-3}]$	$R_{RH} = k_{X+RH}[RH]$ ($R_{O_3} = k_{X+0_3}[O_3]$) $[s^{-1}]$	$\frac{R_{O_3}}{R_{O_3}+\sum R_{RH}+R_{HO_2}}$	$\frac{R_{O_3}}{\sum R_{RH}+R_{HO_2}}$
F	H_2O	$1.4 \cdot 10^{-11}$	$7 \cdot 10^{16}$	$2.8 \cdot 10^6$	$3.5 \cdot 10^{-6}$	$3.5 \cdot 10^{-6}$
	CH_4	$6.4 \cdot 10^{-11}$	$4.0 \cdot 10^{13}$	$2.6 \cdot 10^3$		
				$\sum R_{RH} = 2.8 \cdot 10^6$		
	(O_3	$1.0 \cdot 10^{-11}$	$1.0 \cdot 10^{12}$	10.0)		
Cl	CH_4	$1.0 \cdot 10^{-13}$	$4.0 \cdot 10^{13}$	4.0	0.52	0.92
	C_2H_6	$5.7 \cdot 10^{-11}$	$3.0 \cdot 10^{10}$	1.7		
	C_3H_8	$1.4 \cdot 10^{-10}$	$1.0 \cdot 10^{10}$	1.4		
	CH_2O	$7.3 \cdot 10^{-11}$	$1.0 \cdot 10^{10}$	0.73		
	C_2H_2	$2.1 \cdot 10^{-10}$	$1.0 \cdot 10^{10}$	2.1		
	C_2H_4	$3.1 \cdot 10^{-10}$	$5.0 \cdot 10^9$	1.5		
				$\sum R_{RH} = 11$		
	(O_3	$1.2 \cdot 10^{-11}$	$1.0 \cdot 10^{12}$	12.0)		
Br	CH_2O	$1.1 \cdot 10^{-12}$	$1.0 \cdot 10^{10}$	0.01	0.984	60
	HO_2	$2.0 \cdot 10^{-12}$	$1.0 \cdot 10^{-8}$	$2.0 \cdot 10^{-4}$		
				$\sum R_{RH} = 2.0 \cdot 10^{-2}$		
	(O_3	$1.2 \cdot 10^{-12}$	$1.0 \cdot 10^{12}$	1.2)		
I	HO_2	$3.8 \cdot 10^{-13}$	$1.0 \cdot 10^8$	$3.8 \cdot 10^{-5}$	0.99997	$3.1 \cdot 10^4$
	(O_3	$1.2 \cdot 10^{-12}$	$1.0 \cdot 10^{12}$	1.2)		

$^*rate\ constants\ taken\ from$ [*DeMore et al.* 1997]

Table 2.5: *Comparison of the branching between reaction 2.16a, 2.16b and 2.9a. The 6^{th} column is a measure of the probability of the reaction with ozone, the last column can be seen as a zero order approximation for the number of ozone destruction cycles a halogen atom can pass before being lost to the reservoir.*

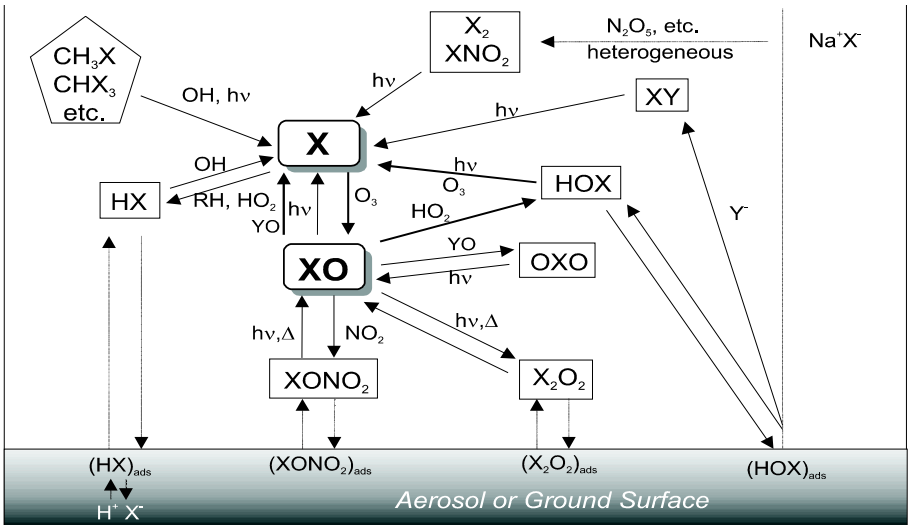

Figure 2.5: *Schematic overview of tropospheric halogen chemistry (X = Cl, Br, I), adapted from Platt and Janssen [1995]. Heavy lines indicate ozone-destruction sequences. Sources of RHS are the release from sea salt and the photolysis of halocarbons.*

(NO reaction, self- or cross-reaction and photolysis (2.13b, 2.9c, 2.13a)):

$$\frac{[XO]}{[X]} = \frac{k_{X+O_3}[O_3] + k_{X+RH}[RH]}{k_{XO+NO}[NO] + 2 \cdot k_{XO+XO}[XO] + k_{XO+YO}[YO] + J(XO)} \tag{2.17}$$

Due to the fast photolysis of the IO radical the IO/I ratio is between 1 and 10 for typical NO_x and O_3 levels (e.g. [*Platt and Janssen* 1995; *Vogt et al.* 1996]). This is significantly lower than that of the other halogens. BrO/Br and ClO/Cl are of the order of 100 and 1000 respectively [*Barrie et al.* 1988].
Figure 2.5 shows a schematic overview of the halogen chemistry in the troposphere (adapted from *Platt and Janssen* [1995]).

2.4 RHS in the Troposphere

Mainly two natural sources are currently known to release halogens into the atmosphere.

1. Release of inorganic halogen compounds from sea-salt

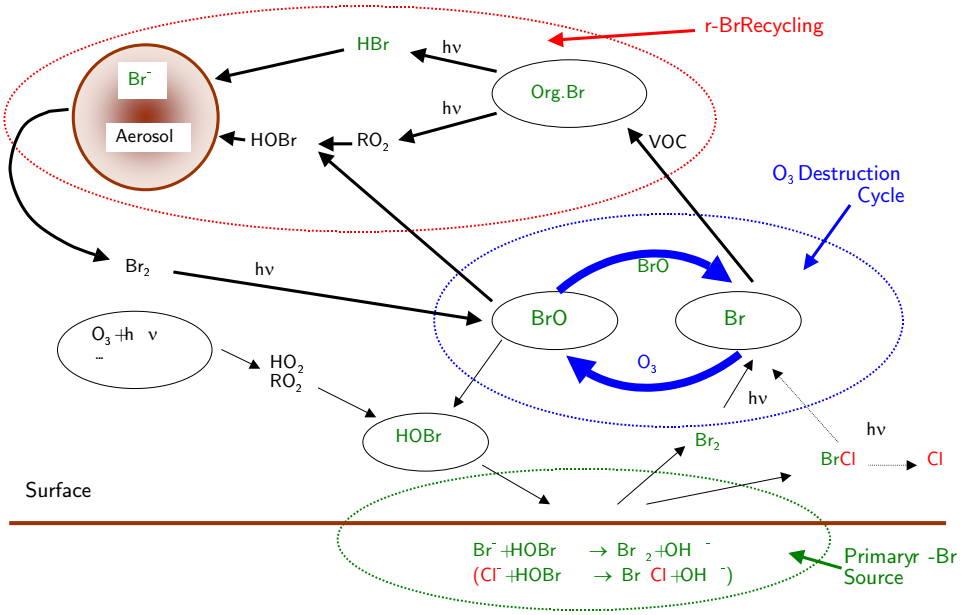

Figure 2.6: *Overview of the tropospheric bromine chemistry including the bromine explosion mechanism.*

2. Photolytic degradation of halogenated organic molecules (organohalogens) from terrestrial and marine sources. Some organohalogens have relatively short photolytic lifetimes in the lower atmosphere, providing a source of reactive halogen atoms in the troposphere. In contrast, long-lived organohalogens can be transported through the tropical tropopause into the stratosphere where they can affect stratospheric ozone.

These two different types of release processes will be the subject of the next section. The inorganic release of halogen compounds mainly important for bromine and chlorine, since the partitioning of sea salt Br^-/I^- is in the order of 10^4, whereas iodine species are mostly emitted by biogenic sources. Therefore, the following sections are focused on the respective halogen.

2.4.1 Reactive Bromine in the Troposphere

The composition of sea salt is dominated by Cl^- with 55.7%, followed by 0.19% Br^- and only $2 \cdot 10^{-5}\% I^-$. Sea salt is deposited on sea ice surfaces, snow and aerosol particles in close contact to the atmosphere. Thus a large

Figure 2.7: *Frostflowers and open lead observed in Kuujjuarapik during 2004 Hudson Bay campaign.*

reservoir of halogens is available at coastal lines and over open oceans.
The role of bromine in the ozone depletion events (ODE) during polar spring is well established. Under presence of sun light tropospheric ozone can be destroyed completely by catalytic reaction cycles involving gaseous reactive bromine, leading to the tropospheric ozone hole. The catalytic ozone destruction cycle is interlinked with autocatalytic bromine release due to heterogenous reactions on highly saline surfaces [*Fan and Jacob* 1992], [*Mozurkewich* 1995], [*Tang and McConnel* 1996]. These surfaces or aerosols that have higher salt concentrations than sea water [*Koop et al.* 2000] can be provided by frost flowers over freshly formed sea ice [*Rankin et al.* 2002], [*Kaleschke et al.* 2004]. Open leads and polynias (linear breaks in the ice) can supply bromide to ice surfaces as well.

Under certain circumstances, including a stable boundary layer, the availability of sunlight and HO_2, these processes can lead to an exponentially increasing release of reactive bromine into the gasphase, being described by the so-called bromine explosion [*Platt and Lehrer* 1996]. Bromine radicals can be formed in presence of sunlight from photolyzable bromine:

$$Br_2 + h\nu \longrightarrow 2Br \qquad \lambda \leq 600nm \tag{2.18a}$$

$$Br + O_3 \longrightarrow BrO + O_2 \tag{2.18b}$$

BrO can be recycled by photolysis, leading to a null cycle, or by its self-reaction:

$$BrO + BrO \longrightarrow 2Br + O_2 \tag{2.19a}$$
$$BrO + h\nu \longrightarrow Br + O \tag{2.19b}$$

The reaction with HO_2 leads to HOBr:

$$BrO + HO_2 \longrightarrow HOBr + O_2 \tag{2.20a}$$

which can undergo heterogenous reactions in the liquid phase or on dry ice surfaces as aerosols, frost flowers or salt surfaces, where reactions with halogen ions take place. According to *Fickert et al.* [1999] the uptake of HOBr on aqueous Cl^-/Br^- solutions with pH $\leq$ 6.5 exceeds 90%, the acidification of sea alt can be provided by acids like HNO_3 or H_2SO_4 or even by self-acidification as proposed by *von Glasow and Sander* [2001]. In the aqueous phase the reaction with halogen ions takes place, leading to the release of Br_2 into the atmosphere.

$$HOBr_{aq} + Br^-_{aq} + H^+_{aq} \longrightarrow Br_{2aq} + H_2O \tag{2.21a}$$
$$Br_{2aq} \longrightarrow Br_2 \tag{2.21b}$$

or the reaction of HOBr with Cl^- ions leads to the formation of BrCl

$$HOBr_{aq} + Cl^-_{aq} + H^+_{aq} \longrightarrow BrCl_{aq} + H_2O \tag{2.22a}$$
$$BrCl_{aq} \longrightarrow BrCl \tag{2.22b}$$

Br_2 and BrCl can be released to the atmosphere, where they quickly photolyze (see Table 2.2). Reaction type 2.21 is enhanced compared to 2.22 (see [*Wang et al.* 1994], [*Foster et al.* 2001]), what leads to a significant increase in reactive gaseous bromine and the bromine explosion can take place leading to the formation of tropospheric ozone holes. The bromine explosion stops if the heterogeneous reservoir ceases to exist due to breaking/melting ice and snow or by loss reactions.

Sinks and Lifetime of BrO

The photolytic lifetime of BrO (Eq. 2.19b) at SZA 70° ranges between 30 to 100 s. The second important reaction channel of BrO besides the photolysis

is the BrO self-reaction

$$BrO + BrO \xrightarrow{85\%} Br + Br + O_2 \quad (2.23)$$

$$\xrightarrow{15\%} Br_2 + O_2 \quad (2.24)$$

The lifetime with respect to the selfreaction is:

$$\tau_{BrO} = \frac{1}{[BrO] \cdot k_{BrO+BrO}} \quad (2.25)$$

At 10 ppt ($2.6{\cdot}10^8$ molec/cm^3) this leads to a lifetime of τ_{BrO} of 1200 s. This lifetime of BrO is inversely proportional to the square of the BrO concentration, therefore at 40 ppt the BrO lifetime would be only 300 s. During daytime, the Br_2 produced with a quantum yield of ∼0.15 is rapidly photolyzed (τ_{Br_2} ∼30 s to 1 min) to yield Br atoms.
Bromine atoms can react with oxidized or unsaturated hydrocarbons (e.g. formaldehyde HCHO, olefines), HO_2 radicals or ozone in the following pathways:

$$Br + RH \xrightarrow{2\%} HBr + R \quad (2.26)$$

$$Br + O_3 \xrightarrow{98\%} BrO + O_2 \quad (2.27)$$

RH denotes the sum of HO_2, HCHO and olefines which react with Br atoms. As long as ozone is not completely depleted ([O_3] > several ppb), almost all Br atoms (>98%) react with ozone leading to no net BrO loss. For the branching ratios see Table 2.5. Depending on RH levels the effective conversion time of BrO to HBr can be up to ∼5000 s. Since the BrO self reaction is significantly faster, it leads to efficient ozone destruction. As it takes about one day to completely destroy e.g. 40 ppb ozone, HBr (Br^-) and HOBr have to be recycled to reactive bromine to explain the ozone losses described at the beginning of this section. In summary, during daytime the BrO lifetime is determined by the reaction of Br atoms with RH to HBr ranging between 1 and 2 hours. During nighttime, the photolysis frequency of BrO is zero. Therefore the BrO self reaction (and possible cross reactions with other halogen oxides) is the only important reaction pathway of BrO radicals. However, at nighttime also the photolysis of Br_2 is not possible, therefore only 85% of the Br atoms can react with O_3 back to BrO. The 15% path to Br_2 therefore leads to an accumulation of Br_2 at night, which acts as a nighttime reservoir species and photolyzes to yield Br atoms during sunrise. This was several times observed during the 2004

Hudson Bay campaign by small dips in the ozone record shortly after sunrise (see Fig. 7.13). In summary the lifetime of BrO radicals during nighttime is determined by the branching ratio of the reaction of Br atoms with RH and O_3 on the one hand and by the branching ratio of the BrO self reaction to yield atomic or molecular bromine on the other hand. At high BrO levels of 40 ppt the lifetime with respect to Br_2 formation is of the order of 2000 s and therefore significantly shorter according to HBr formation (∼15000 s). At lower BrO levels (e.g. 10 ppt) the lifetime with respect to Br_2 formation is in the order of 8000 s. The loss to HBr in this case is negligible with a BrO lifetime of >12 hours. In case of other species present in the boundary layer which can react with BrO, in particular the halogen oxides ClO and IO, and NO_2 but also DMS, Hg^0, etc. the BrO lifetime can be significantly shorter, especially during nighttime, due to formation of reservoir compounds like BrCl, IBr, $BrONO_2$, etc.

Interaction Reactions of Reactive Bromine

Bromine chemistry is of great importance regarding the interaction with DMS. Sulfate aerosols are an important species leading to the formation of CCNs, they also grow through the uptake of SO_2 with a subsequent oxidization of S(IV) to S(VI):

$$SO_2 + OH \stackrel{+O_2}{\longrightarrow} HO_2 + SO_3 \stackrel{+H_2O}{\longrightarrow} H_2SO_4 \tag{2.28}$$

Vogt et al. [1996] showed that 20% of the available SO_2 is destroyed by HOBr via oxidization on pre-existing particles reducing the formation of new CCNs. In the remote MBL DMS is an important precursor for the formation of sulphate aerosols which is oxidized by BrO in a catalytic cycle [*Toumi* 1994].

$$BrO + DMS \longrightarrow Br + DMSO \tag{2.29}$$

followed by the reaction 2.18b. Model calculation by *Boucher et al.* [2003] showed that BrO is responsible for 28.8% global DMS loss, whereas calculations of *von Glasow et al.* [2002b] showed that BrO is responsible for up to 44% of DMS oxidization in the remote MBL. However, the fate of atmospheric DMSO remains unclear. If DMSO is preferentially oxidized to methanesulfonic acid, the formation of CCNs from SO_2 and sulfate aerosols will be reduced. However, these estimations depend sensitively on appearance and distribution of BrO in the marine troposphere, which is recently

well indicated by a variety of measurements ([*Leser et al.* 2003; *Saiz-Lopez et al.* 2004] and [*Sander et al.* 2003] and references herein), but the concentrations found are frequently close to the detectable limits of 1-2 ppt. A recent and good overview on inorganic bromine in the MBL is given by *Sander et al.* [2003] and *von Glasow et al.* [2004].

Of great importance, especially in polar regions is the relation between bromine and mercury chemistry. Mercury (Hg) is present in the atmosphere in its gaseous elemental form (Hg^0, GEM). It has a long atmospheric lifetime of ∼1 year (see *Slemr et al.* [1985]), due to its low solubility in water and low chemical reactivity. It is also easily re-emitted to the atmosphere after deposition on surfaces. As a result, GEM is almost uniformly distributed on global scale. *Pirrone et al.* [1996] estimated the global anthropogenic Hg emissions of 1660 - 2200 t/year to be responsible for one third of the total Hg emissions. The rest is assumed to be from natural emissions and re-emission of previously deposited mercury. GEM shows a distinct behavior in polar regions compared to mid-latitudinal sites, as its boundary layer concentration varies simultaneously with ozone, what indicates the involvement of halogen chemistry [*Schroeder and Barrie* 1998]. GEM depletion events have been observed in many Arctic stations (e.g. *Poissant et al.* [2005]) and are most likely also important in the Antarctic [*Ebinghaus et al.* 2002]. However, it is still unclear whether a reaction with Br [*Ariya et al.* 2002] or BrO [*Boudries and Bottenheim* 2000; *Hönninger* 2002] is responsible for the GEM depletion events. It is understood that Hg^0 is oxidized to form highly toxic and bio-accumulative Hg(II) species during bromine explosion events. Since these species are less volatile and much more water soluble, their deposition is more rapid (*Lu et al.* [2001]) compared to Hg^0 what results in a flushing of toxic Hg(II) in meltwater during summer time and its subsequent bio-accumulation. The significant input of that toxic pollutant in water systems and therefore in the food chain represents a threat to the arctic ecosystem and the local indigenous population.
A comprehensive review of the role of mercury in the atmosphere is given by *Schroeder and Munthe* [1998], who reported the first mercury depletion event, shown in Figure 2.8.

Frostflowers as Possible Sources for Bromine

Frost flowers are discussed as a likely reservoir of bromide ions to sustain the bromine explosion. They have a large surface area and a high salinity (about triple the salinity of sea water). *Kaleschke et al.* [2004] introduced a

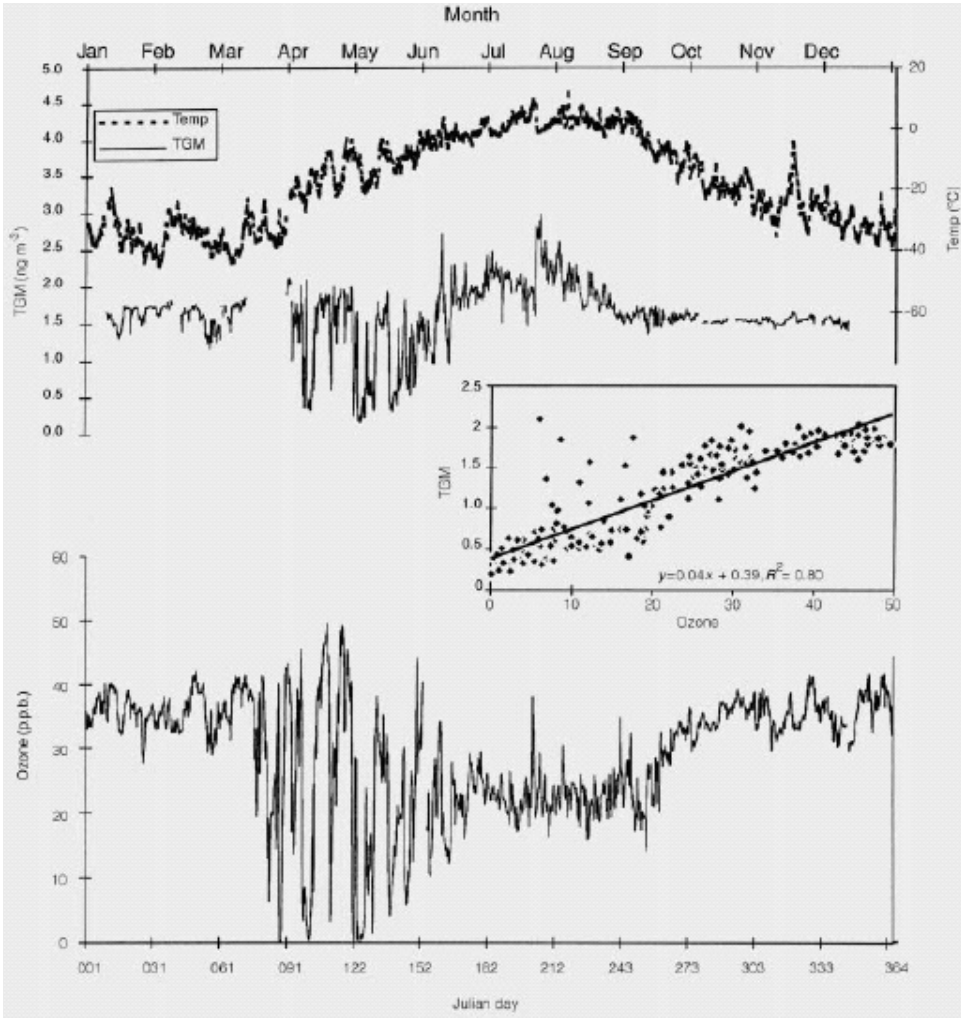

Figure 2.8: *Depletion of TGM during springtime in 1995 was firstly reported by Schroeder and Barrie [1998]. The time series recorded 1995 in Alert, Canada shows a strong correlation of ozone and mercury depletion after polar sunrise.*

model for the computation of the **p**otential **f**rost **f**lower (PFF) areas. The PFF area is basically calculated from the new ice fraction and the surface temperature making use of satellite remote sensing of the sea ice surfaces. The results of the model computation (which serve as a theoretical upper limit of the actual area covered by frost flowers) have been compared to BrO VCDs (vertical column density). It has been shown that more than

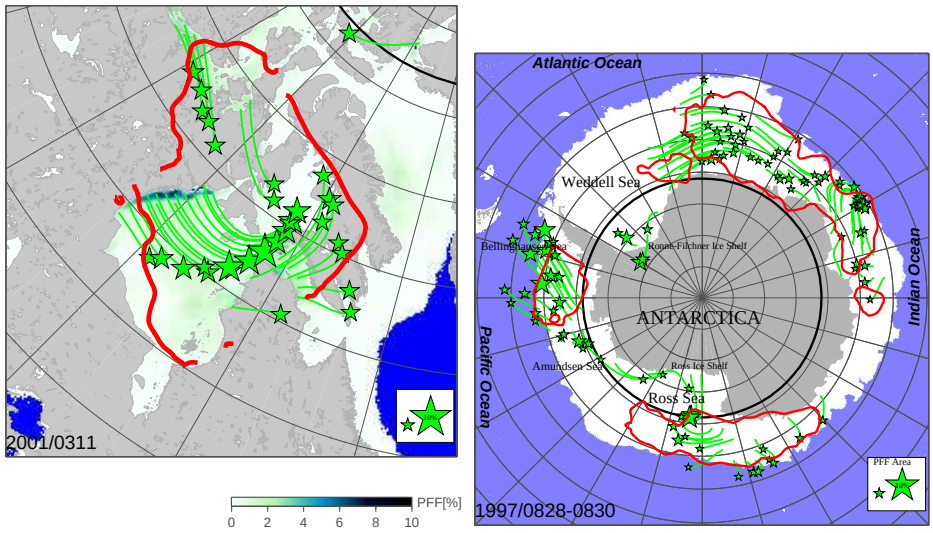

Figure 2.9: *Enhanced BrO (red isolines) and PFF trajectories over the Hudson Bay at March 11, 2001 (left) and the Antarctic ocean (right) where maximum values of two consecutive days are shown: August, 28-29 (PFF) and 29-30 (BrO). Green stars are endpoints of 24h air trajectories starting at a frost flower area coverage of greater than 1% sampled every 62.5 km (left) and 0.4% sampled every 187 km (right). The total PFF coverage is proportional to the size of the stars. PFF coverage for the Hudson Bay is displayed color coded. Images adapted from (Kaleschke et al. [2004])*

2/3 of all trajectories during 1996 to 2002 originating from areas with high PFF reach areas of enhanced BrO in both hemispheres. Almost all cases of enhanced BrO abundances during polar sunrise were associated with a high probability of frost flowers. However, it has been argued that the snowpack is a very important source of bromide ions, because snow is porous, permeable and has a high surface area. Snow is also an important reservoir for OH in the Arctic [*Domine and Shepson* 2002] since the Arctic air is usually very dry and UV-radiation reduced. Probably the oxidation of H_2O_2 in the snowpack is a more important source of OH. Also HCHO is emitted from the snowpack which is probably due to equilibrium processes. Many heterogeneous processes can take place on the quasi liquid layer at the surfaces of ice crystals. During their lifetime the specific surface area (surface area per mass) of ice crystals decreases and the concentration of reactants at the

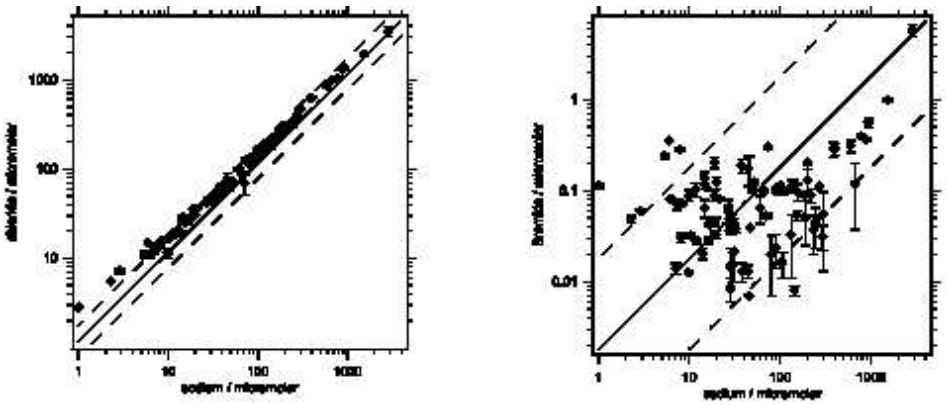

Figure 2.10: *Chloride/sodium (left) and bromide/sodium partitioning (right) from surface snowpack samples taken near Barrow, Alaska. Figure adapted from Simpson et al. [2004].*

surface increases driving out compounds into the gasphase. Measurements near Barrow, Alaska [*Simpson et al.* 2004] have shown that bromine depletions frequently occurs in the snowpack. In general Cl^- is well correlated to Na^+ but Br^- is not as can be seen in Fig. 2.10.
Thus, bromine explosion chemistry re-volatilizes Br^- from snow and distributes it more evenly over a larger region. Some snow is depleted by more than 90%. Bromide is transported farther inland than is sodium and appears to be equalized throughout the region, so Br^- is dominated by the bromine explosion chemistry and that chemistry impacts snow hundreds of kilometers onshore. The likely endproduct of reactive bromine chemistry is HBr which can be deposited over a broad region enhancing bromide concentrations.
Frost flowers on the other hand are not significantly depleted in bromine and alkaline. They could be acidified by e.g. atmospheric SO_2. The depletion of bromide in frost flowers is, even if they are considered the sole source of atmospheric bromine, negligible since the bromide abundance is very large and the brine layer on which frost flowers grow can be regarded as an infinite bromide reservoir.

2.4.2 Reactive Iodine in the Troposphere

The major source for reactive bromine species in the MBL is thought to be the autocatalytic release from sea salt surfaces as described in the previ-

Species	***Lifetime*** τ	***Reference***
CH_3I	2-6d	[*Röhl et al.* 1997]
C_2H_5I	1-5d	[*Rattigan et al.* 1997]
2-C_3H_7I	2-3d	[*Wayne et al.* 2000]
1-C_3H_7I	2-4d	[*Wayne et al.* 2000]
CH_2ClI	10.5-26h	[*Rattigan et al.* 1997]
CH_2BrI	61min	[*Mössinger et al.* 1998]
CH_3Cl	1.3a	[*Yvon-Lewis and Butler* 2002]
CH_2Cl_2	5-6m	[*Yvon-Lewis and Butler* 2002]
$CHBrCl_2$	30d	[*Bilde et al.* 1998]
CH_2I_2	3.6min	[*Mössinger et al.* 1998]
CH_3Br	0.8a	[*Yvon and Butler* 1996]
CH_2Br_2	47d	[*Mössinger et al.* 1998]
CH_2BrCl	0.5a	[*Bilde et al.* 1998]
$CHBr_2Cl$	30d	[*Carpenter et al.* 1999]
$CHBr_3$	2-4w	[*Yvon and Butler* 1996]
CF_3I	1d	[*Rattigan et al.* 1997]

Table 2.6: *Halogenated hydrocarbons and their respective lifetimes.*

ous section. However, the main source for reactive iodine in coastal regions are volatile iodinated hydrocarbons (VHOCs), which are emitted biogenically by macroalgae and phytoplankton species to the atmosphere. These iodocarbons are more or less quickly photolyzed or degraded by OH radicals to release iodine atoms to the lower part of the atmosphere, where they react in the order of seconds with ozone to form the IO radical.

$$RI + h\nu \longrightarrow R + I \tag{2.30a}$$

$$I + O_3 \longrightarrow IO + O_2 \tag{2.30b}$$

An overview on the lifetimes of a variety of VHOCs is given in Table 2.6. The shortest lifetime is in the order of minutes for CH_2I_2, whereas it is in the order of days for the frequently and widespread observed CH_3I (e.g. *Schall et al.* [1994, *Singh et al.* [1983]).
IO could contribute to ozone destruction in a comparable way as BrO, even in very low concentrations, due to the high number of ozone destruction cycles the iodine atom can pass before being lost to the reservoir (see Table

2.5). Additionally, recent studies are indicating a great relevance of reactive iodine in new particle formation processes ([*Jimenez et al.* 2003; *O'Dowd et al.* 2002; *Burkholder et al.* 2004; *Hoffmann et al.* 2001]). Events of particle formation with concentrations of up to 10^6 particles/cm^3 have been observed in marine environments e.g. [*O'Dowd et al.* 2002]. may affecting climate. Therefore, the investigation of sources, appearance and distribution of reactive iodine species in the MBL on a global scale is of high interest and current research activities also within the framework of this thesis.
The current understanding of the particle formation process is so far quite limited. *O'Dowd et al.* propose that particle formation in coastal environments is dominated by polymerization of the OIO radical [*O'Dowd et al.* 2002]. However, field observations of OIO in the marine environment are very limited ([*Allan et al.* 2000]), even if great effort was made for its detection. This, as well as observations presented in this thesis seem to indicate that OIO is present in coastal regions, but in concentrations clearly below 10 ppt.
Although there is evidence for iodine and iodine oxides in marine aerosols [*McFiggans et al.* 2004; *Jimenez et al.* 2003], the mechanism for the particle formation is unclear and the question for the primary source of iodine has more than one possible answer. Diodomethane is biogenically emitted by a variety of macroalgae, e.g. [*Carpenter et al.* 1999; *Schall and Heumann* 1993]. Due to its short photolytic lifetime iodine atoms are released within minutes into the atmosphere. The observed levels of CH_2I_2 are in the order of some ppt, which is sufficient to explain the appearance of IO up to several ppt (see Table 4.1) as observed in several coastal environments [*Carpenter et al.* 2001; *McFiggans et al.* 2000; *McFiggans et al.* 2000]. These findings will also be confirmed by model studies within this thesis performed with the results of the 2003 Brittany campaign.
Recently, the successful detection of molecular iodine (I_2) at Mace Head was reported with highly elevated concentrations in close correlation to minima in tidal height, indicating macroalgae as the source of it [*Saiz-Lopez and Plane* 2004].
However, it is unclear if the appearance of I_2 is a common phenomenon in the marine boundary layer and represents a key question of this work.

Sources of Reactive Iodine

Generally the iodinated hydrocarbons have comparatively short photolytic lifetimes regarding other organohalogens (see Table 2.6). Therefore the photo-dissociation of iodocarbons (Eq. 2.31b) is the dominating source, de-

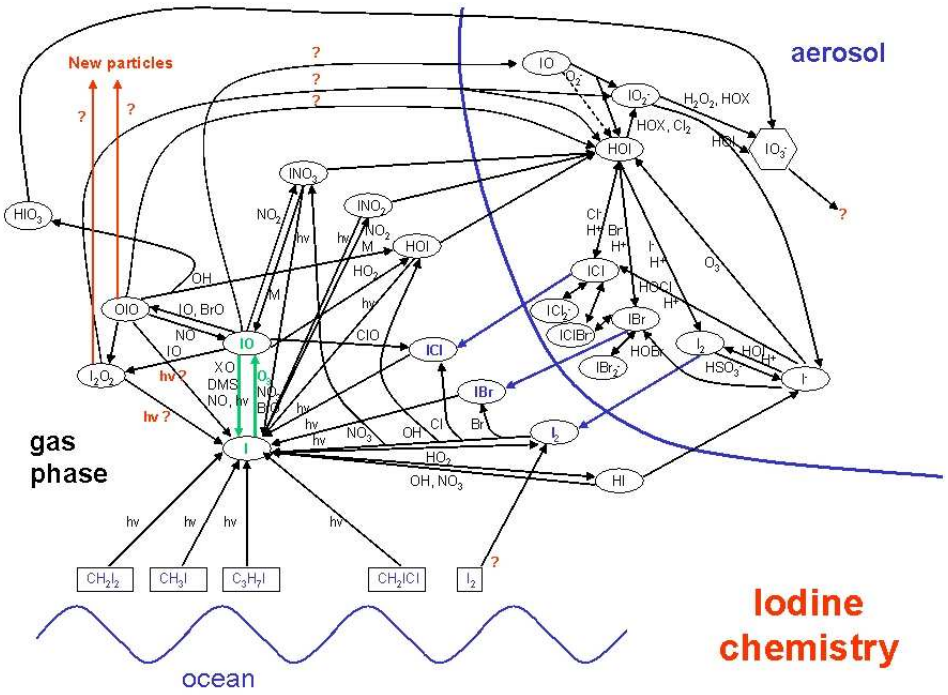

Figure 2.11: *Schematic overview on the atmospheric iodine cycle in the marine boundary layer. Iodine atoms are set free via photolytic destruction of short lived iodinated hydrocarbons or I_2(?) molecules. Iodine reacts quickly with O_3 to form IO. Self and cross reactions with IO, XO leads to autocatalytic destruction of O_3. Formation and fate of OIO, I_2 and I_2O_4 is indicated with a question mark, due to a lack of knowledge.*

livering I atoms to the atmosphere during daytime. The second important reaction (2.31b) is the degradation of VHOCs by OH radicals:

$$RI + h\nu \longrightarrow R + I \tag{2.31a}$$
$$RCH_2I + OH \longrightarrow RCHI + H_2O \tag{2.31b}$$

The release of molecular iodine by macroalgae was already proposed by *Miyake and Tsnogai* [1963]. They found in laboratory studies with macroalgae that volatile iodine species such as I_2 or HOI are released to the atmosphere. Free iodine might escape to the gasphase according to the overall reaction:

$$2I^- + \frac{1}{2}O_2 + H_2O + h\nu \longrightarrow I_2 + 2OH \tag{2.32}$$

The natural release of molecular iodine (I_2) by algae is known as 'iodo-volatilisation' which may lead to enhanced iodine content in the atmosphere in coastal areas [*Dangeard* 1933]. However, the details of that mechanism is up to date unclear and the reader is referred to the work of *Küpper et al.* [1998].

Reaction Cycle of Iodine Species

The most probable pathway of I atoms is the reaction with ozone (Eq. 2.30b), assuming typical ozone concentrations of 40 ppb in the MBL and the rate constant $k_{I+O_3} = 1.2 \cdot 10^{-12} cm^3 molec^{-1} s^{-1}$ as indicated in Table 2.2 the lifetime of I is in the order of 1 second. Under low NO_x conditions the fast photolysis of IO leads to a recycling of the I atom via the reaction with ozone and a net null cycle regarding ozone destruction.
In contrast to other halogens I atoms do not react with hydrocarbons to form HI. However, HI is formed by the reaction:

$$I + HO_2 \longrightarrow HI + O_2 \tag{2.33}$$

The re-activation of I from HI as a reservoir can take place by the reaction:

$$HI + OH \longrightarrow I + H_2O \quad k = 7.1 \cdot 10^{-11} cm^3 molec^{-1} s^{-1} \tag{2.34}$$

due to the short lifetime of HI of 3-4 hours (assuming typical OH concentration of $1{\cdot}10^6 molec/cm^3$). The photolytic lifetime of $IONO_2$ and INO_2 is as well in the order of hours, therefore these species act as well as a temporary reservoir species and not as a sink for reactive iodine.
The IO selfreaction, evaluating the rate coefficient and product yield measurements is subject of a large number of laboratory studies (e.g. [*Harwood et al.* 1997], [*Bloss et al.* 2001]). However, the understanding of reaction products and their yields is still incomplete.

$$IO + IO \longrightarrow OIO + I \tag{2.35a}$$
$$\longrightarrow I_2 + O_2 \tag{2.35b}$$
$$\longrightarrow 2I + O_2 \tag{2.35c}$$
$$IO + IO + M \longrightarrow I_2O_2 + M \tag{2.35d}$$

The overall rate constant is $k_{IO+IO} = 9.1 \cdot 10^{-11} cm^3 molec^{-1} s^{-1}$[*Atkinson et al.*] and branching ratios are indicated in Table 2.5. The yield of I atoms of Eq. 2.35c is assumed to be relatively small. The I atoms will rapidly converted back to IO via Eq. 2.30b. The yield of Eq. 2.35b is assumed to be small as well. Further on I_2 has a short photolytic lifetime in the order of 10 seconds (under daylight conditions), that the iodine is recycled in the same way as in Eq. 2.35c on a short time scale. The chemical properties of I_2O_2 are currently not known, it may be assumed that the iodine dimer is thermally unstable at room temperature in analogy with the chlorine and bromine dimers Cl_2O_2 and Br_2O_2 [*DeMore et al.* 1997].
In contrast to the homologous OClO and OBrO, which are quickly photolyzed during daytime, model and laboratory studies suggest that OIO may be photostable, since the calculated threshold wavelength for its photodissociation via

$$OIO + h\nu \longrightarrow IO + O(^3P) \tag{2.36}$$

is 418 nm [*Misra and Marshall* 1998], while its visible absorption spectrum covers the wavelength region between 480 - 640 nm [*Cox et al.* 1999]. Although OIO photolysis after Eq. 2.36 is assumed to be negligible, laboratory investigations by *Plane et al.* [2001] suggested that the photon induced dissociation reaction

$$OIO + h\nu \longrightarrow I + O_2 \tag{2.37}$$

is of importance for the atmosphere, because it would lead to a photolytic lifetime in the order of few seconds. This is in agreement with their observations of the OIO molecule just after sunset [*Allan et al.* 2001], [*Plane et al.* 2001]. This reaction would also enhance ozone destruction by reactive iodine, due to the destruction of two ozone molecules during each IO self reaction cycle (see Cycle 2.35). However, these observations have not been confirmed so far, and no final agreement on the photolytic stability of the OIO molecule is reported today. Due to the ability of OIO to polymerize, the formation of OIO might be a possible sink for reactive iodine.
The current understanding of iodine chemistry is shown in Figure 2.11. The main reaction pathways are indicated and uncertain reactions, especially reactions involving IO and OIO to stable particulate iodine are marked with an interrogation symbol.

Therefore estimations and modelling studies are up to date limited due to a significant lack of kinetic data and moreover they are as well limited by the insufficient data sets on iodine precursor gas fluxes from the ocean (e.g. [*Davis et al.* 1996]).
Nevertheless the impact of iodine species on ozone is not quantitatively investigated, reactive iodine in the atmosphere has a potentially high impact on the destruction of ozone in the troposphere (e.g. *Jenkin* [1992], *Solomon et al.* [1994], *Davis et al.* [1996]). For example *Davis et al.* [1996] estimated 6% loss of total tropospheric ozone column for the tropical marine environment due to iodine chemistry and stated that in regions of high biological activity this could be increase up to 30%. Despite the fact that iodine chemistry has a significant lack of information, some simple estimations on potential ozone destruction by iodine species are made, within this thesis.
In contrast to the remote atmosphere, the polluted atmosphere provides NO_x species, which react with the iodine species. The dominating reaction is that of IO and NO_2:

$$IO + NO_2 + M \longrightarrow IONO_2 + M \tag{2.38}$$

(2.39)

Photolysis and thermal decomposition are the two possible pathways for $IONO_2$ (besides a possible heterogenous uptake [*Holmes et al.* 2002]):

$$IONO_2 + h\nu \longrightarrow I + NO_3 \tag{2.40a}$$

$$\longrightarrow IO + NO_2 \tag{2.40b}$$

$$IONO_2 + M \longrightarrow I + NO_3 \tag{2.40c}$$

The absorption cross-section of $IONO_2$ was measured by *Moessinger et al.* [2002] over the wavelength range 245-415 nm. The resulting photolysis rate coefficient for $IONO_2$ is j($IONO_2$) = 0.045 s^{-1}, estimated for typical summer daytime conditions in the MBL at 53° N. That results in a photolytic lifetime of less than one minute. Heterogeneous uptake of $IONO_2$ on sea salt aerosol is assumed to take place in the order of hours, as calculated by *Moessinger et al.* [2002]. Thus, during daytime photolysis is expected to be the major loss process for $IONO_2$, what implies that IO is not lost from the gasphase. However, the reaction of $IONO_2$ with sea salt aerosol may become a significant loss process for $IONO_2$ during night time. The uptake of $IONO_2$ is expected to form di-halogens ICl and IBr [*Holmes et al.* 2002], which are released to the gasphase during night. Iodine would therefore not

be lost from the gasphase permanently, due to the photolysis of IBr and ICl at dawn. Thermal decomposition of $IONO_2$ may contribute to the night time loss of $IONO_2$. But this is suggested to be a very slow process at ambient temperatures, according to *Allan and Plane* [2002]. The comparison of removal rates of $IONO_2$ by photolysis and thermal dissociation is shown in Figure 2.12.
$IONO_2$ could contribute to ozone destruction if the photolysis product yields I + NO_3 (Eq. 2.40a) and not the products of IO + NO_2, which would result in no net effect. However, the photolysis products and the ratios of Eq. 2.40 have not been reported yet and no recommendations are given from *Atkinson et al.* []. However, $IONO_2$ is not expected to act as a stable reservoir of atmospheric iodine during daytime.

Potentially of high interest is the reaction of I_2 with NO_3 at dark conditions, since the detection of IO (up to 3 ppt) during night time was reported recently by *Saiz-Lopez and Plane* [2004]. They proposed a reaction mechanism for the building up of IO in absence of sunlight via the NO_3 radical and molecular iodine (which is assumed to be present in coastal regions see Chapter 6):

$$NO_3 + I_2 \longrightarrow I + INO_3 \tag{2.41a}$$
$$I + O_3 \longrightarrow IO + O_2 \tag{2.41b}$$

With a reaction rate of $k_{NO_3+I_2} = 1.5 \cdot 10^{-12} \frac{cm^3}{molec \cdot s}$ for T=285K, [*Atkinson et al.* 1997]. It is to note that no recommendation was found in the actual *Atkinson et al.* issue from March 2005. The appearance of the IO radical during night time was investigated within the field campaigns at the North Sea in 2002 and in Brittany 2003, see Chapter 5.

Homogeneous Nucleation of Iodine Oxides

Within recent field studies particle formation possibly related to iodine chemistry in the marine atmosphere [*O'Dowd et al.* 2002] has been observed. In the 1998 PARFORCE campaign at Mace Head, Ireland nucleation events with particle concentrations up to 10^6 cm^{-3} were observed under certain conditions. The nucleation mechanism is not definitely clear, but correlation with solar flux and low tide and the identification of iodine oxides in the particles led to the proposal that volatile iodocarbons (mainly the short lived CH_2I_2) are precursors for the particle formation. *O'Dowd et al.* [2002],

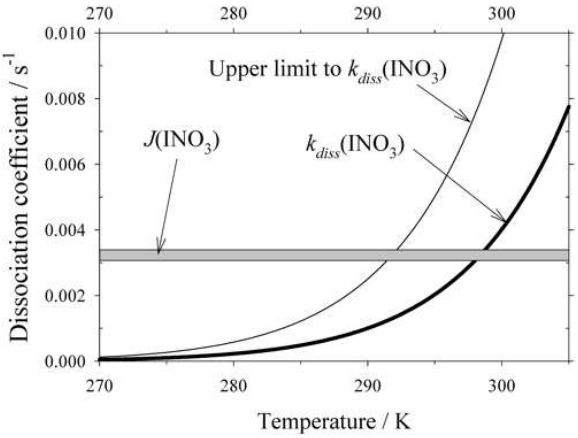

Figure 2.12: *The removal of $IONO_2$ by photolysis and thermal dissociation, as a function of temperature. Estimated for standard conditions of the lower troposphere, adapted from Allan and Plane [2002].*

Hoffmann et al. [2001], *Jimenez et al.* [2003] and *Burkholder et al.* [2004] have studied that hypothesis by a series of laboratory experiments. They photolyzed CH_2I_2/ozone/air mixtures in the near UV and measured the formation of ultra-fine particles. The results led *Hoffmann et al.* [2001] to the suggestion of the reaction mechanism, to explain new particle formation:

$$CH_2I_2 + h\nu \longrightarrow CH_2I + I \tag{2.42a}$$
$$I + O_3 \longrightarrow IO + O_2 \tag{2.42b}$$
$$IO + IO \longrightarrow OIO + I \tag{2.42c}$$
$$OIO + OIO \longrightarrow I_2O_4 \tag{2.42d}$$
$$I_2O_4 + OIO \longrightarrow' particle' \tag{2.42e}$$

Reaction 2.42d stands for multiple OIO addition steps leading to the formation of stable iodine oxide clusters. Within this mechanism, aerosol formation results from single component homogeneous nucleation of OIO. But as the kinetic and photochemical properties of the OIO radical are currently not well understood, this is object of current research. The proposed particle formation mechanism is up to date not verified but [*Hoffmann et al.* 2001] demonstrated that UV photolysis of CH_2I_2 in presence of ozone gas mixtures lead to iodine oxide particle formation. *Jimenez et al.* [2003] extended these laboratory studies by including low atmospherically relevant concentrations of CH_2I_2 down to 15 ppt. *Jimenez et al.* studied as well

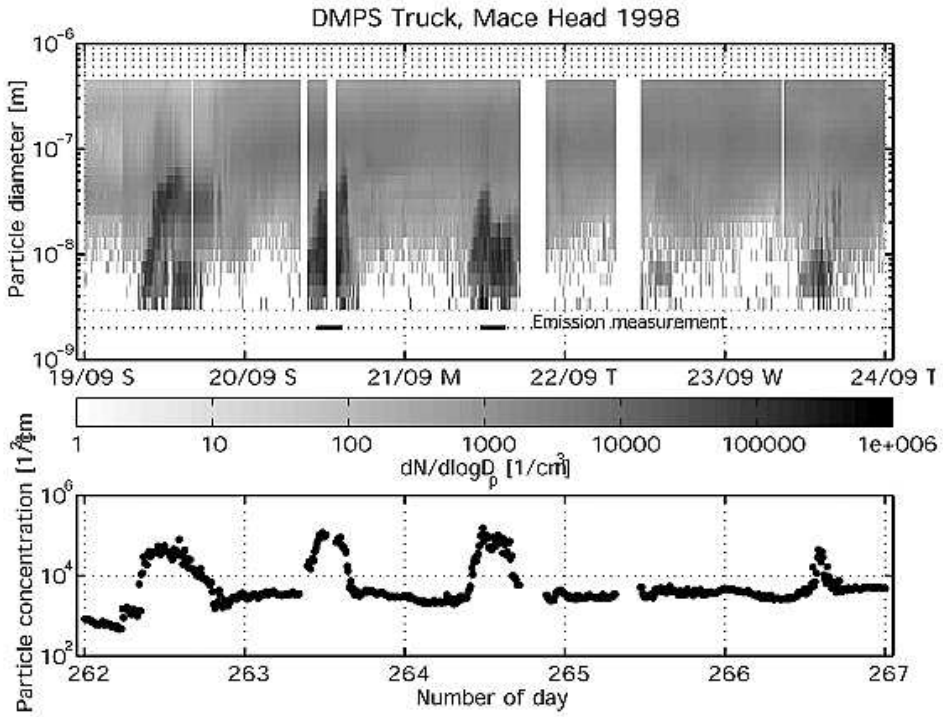

Figure 2.13: *Example for observed particle burst events during a 6 day period of the 1999 PARFORCE 2 campaign at Mace Head. The five TEM (transmission electron microscopy) sampling periods are indicated with horizontal bars below the spectra (adapted from [Mäkelä et al. 2002]).*

the composition and physical properties of the particles and found that the particles mainly consist of iodine oxides, what supports the hypothesis of *Hoffmann et al.*. *Burkholder et al.* [2004] did further laboratory studies on the iodine oxide nucleation system to better evaluate thermonucleation processes. This nucleation model was used to interpret experimental observations and atmospheric model calculations. *Burkholder et al.* found, that reported levels of OIO of up to 3 ppt, as reported in literature [*Allan et al.* 2001] is insufficient to explain the observed particle formation events with particle concentrations of 10^6 $particles/cm^3$, as observed during 1998 PARFORCE campaign.

However, they suggest that it may be possible that high concentrations of OIO ($>$ 10 ppt), are present in localized 'hot spots' along the coast re-

gion, what means that the coastal region would consist of an inhomogeneous source of OIO. Following dilution of the aerosol produced in the 'hot spot', could account for observed particle concentrations.
The role of molecular iodine in particle formation processes is up to date not clear.
The detection of I_2 was reported the first time by *Saiz-Lopez and Plane* [2004] during 2002 NAMBLEX campaign in Mace Head. They found significant amounts of I_2 of up to 25 ppt during daylight in the MBL. These observations and the linkage of emissions of iodine and the appearance of macroalgae lead *McFiggans et al.* [2004] to further investigations and studies with the laminaria macroalgae. *McFiggans et al.* [2004] demonstrated that that ultrafine iodine containing particles are produced by intertidal macroalgae if exposed to ambient levels of ozone. Moreover he stated that the particle composition is similar, both to those formed in the chamber photo-oxidation of diiodomethane and in the oxidation of molecular iodine by ozone and concluded that if atomic iodine is involved in the observed particle bursts, it is of the order of 1000 times more likely to result from molecular iodine- than diioodomethane photolysis.
I_2 is so far only reported from Mace Head and it is unclear if the findings and the strongly enhanced levels of molecular iodine are representative for coastal regions and furthermore of global relevance. Within this thesis, field campaigns in the biological active region of Brittany, at the French Atlantic Coast and the German North Sea Coast were conducted to investigate this.

Chapter 3

DOAS

The measurement technique used in this thesis based on the **D**ifferential **O**ptical **A**bsorption **S**pectroscopy (DOAS) method. The principles of this technique will be introduced in this chapter. A variety of applications for the DOAS method is existing, but for the field campaigns described in this thesis, the active longpath DOAS technique was employed. This technique and main instrumental constituents will be described. Furthermore the principles of the analysis and concepts for numerical retrieval algorithms determining trace gas concentrations from atmospheric spectra, will be described in detail.

3.1 The DOAS technique

The DOAS method was already introduced in 1979 by Platt [*Platt et al.* 1979] to measure atmospheric trace gas concentrations using an artificial light source. Since then, DOAS has been applied to measure trace-gas concentrations in the troposphere and stratosphere [*Platt* 1994; *Solomon et al.* 1987] as well as under simulated atmospheric conditions [*Etzkorn* 1998]. In fact, several important atmospheric trace gases were measured for the first time using DOAS, e.g. OH [*Perner et al.* 1976], HONO [*Perner and Platt* 1979; *Platt and Perner* 1980], NO_3 [*Platt et al.* 1980], BrO [*Hausmann and Platt* 1994] and IO [*Alicke et al.* 1999] in the troposphere, and OClO and BrO [*Sanders et al.* 1988] in the stratosphere. A large number of other molecules absorbing light in the UV and the visible wavelength region, e.g. NO_2, NO, NH_3, ClO, O_3, SO_2, CS_2,OIO, I_2 and HCHO can also be detected [*Platt* 1978; *Platt* 1994].

The DOAS method is a very sensitive measurement technique for these trace gases since they exhibit strong and highly structured absorptions in the UV and visible spectral regions. Because DOAS is capable of measuring ambient air in the open atmosphere it is especially useful in the detection of highly reactive species, such as the free radicals OH, NO_3, halogen oxides (BrO, IO, etc.) or NO_2. The simultaneous determination of the concentration of several trace gases, by analyzing the sum of their absorptions in one wavelength interval, reduces measurement time and allows analysis of the average chemical composition of the observed air mass at high temporal resolution.

3.1.1 Absorption of Light

In Figure 3.1 the components of a simplified DOAS set-up to measure tropospheric trace gases are shown. Light, with an initial intensity $I_0(\lambda, L)$, emitted by a suitable light source passes through the observed air mass and is collected by a telescope. Extinction of light along the lightpath, due to absorption processes by different trace gases and scattering by air molecules and aerosol particles, reduces the initial intensity. After the light has travelled a pathlength L, $I_0(\lambda, L)$ is reduced to $I(\lambda, L)$ as expressed from Equation 3.1 using Lambert-Beer's law:

$$I(\lambda, L) = I_0(\lambda, L) \cdot \exp^{\int_{l=0}^{l=L} -\left(\sum_j \sigma_j(\lambda,p,T)\cdot c_j(l)+\varepsilon_R(\lambda,l)+\varepsilon_M(\lambda,l)\right)dl} + N(\lambda) \quad (3.1)$$

where for each trace gas species j the parameter $\sigma_j(\lambda,p,T)$ is the absorption cross-section which depends on the wavelength λ, the pressure p and the temperature T, $c_j(l)$ the number density at the position l along the light path of total length L. The Rayleigh-extinction and Mie-extinction coefficients are described by ε_R and ε_M. $N(\lambda)$ is the photon noise dependent on $I(\lambda, L)$. In Figure 3.1a the spectrum of $I(\lambda, L)$ that results from light that has passed an atmospheric volume with only one absorber (formaldehyde: HCHO) is shown. In the employed longpath DOAS instrument, the light is focused directly into a quartz fiber transmitting the light to the entrance slit of a grating spectrograph, with a detector system recording the spectrum of the dispersed light. Due to the limited resolution of the spectrograph, the spectral resolution of spectrum $I(\lambda, L)$ is degraded. The mathematical description of this process is a convolution of $I(\lambda, L)$ with the instrument function H of the spectrograph. Figure 3.1b shows the spectrum $I^*(\lambda,L)$ after a convolution with a typical instrument function H as it is projected by the spectrograph on the detector. By the multi channel detector the wavelength range is mapped into n discrete pixels, numbered i, each integrating

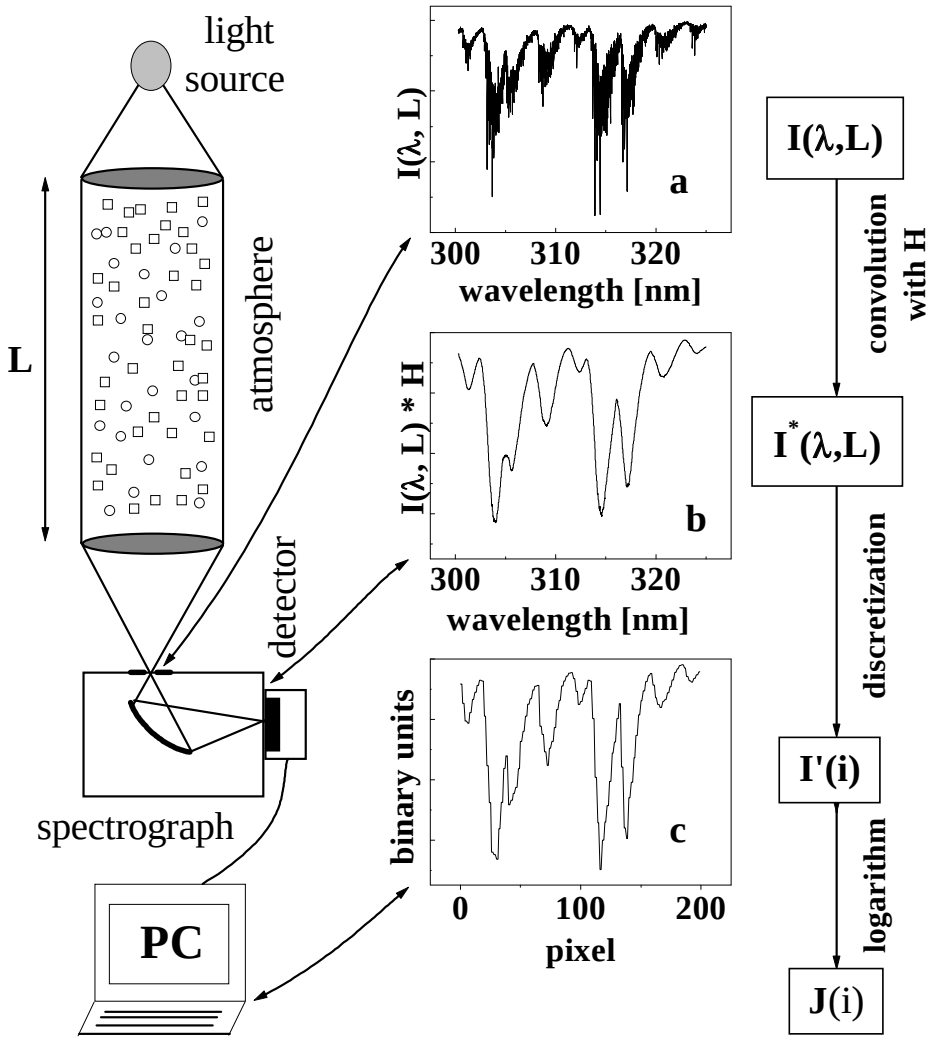

Figure 3.1: *The components of a simplified DOAS set-up. Collimated light undergoes absorption processes on its way through the observed air mass. (a): an example-spectrum of this light entering the spectrograph is shown, assuming only formaldehyde (HCHO) to be present in the observed air mass. This absorption spectrum shows the rotational-vibronic structure of HCHO. (b): the same spectrum convoluted by the spectrographs instrumental function reaches the detector. (c): the spectrum after it was mapped by the detector to discrete pixels as it is actually stored to the hard-disk of a PC and can be analyzed numerically.*

the light in a wavelength interval from λ(i) to λ(i+1). This interval is given by the wavelength-pixel-mapping Γ_I of the instrument. In the case of a linear dispersion (Γ_I: λ(i)=λ(0)+$\gamma\cdot$ i) the spectral width of a pixel ($\Delta\lambda$(i) = λ(i+1) - λ(i) = γ) is constant. The signal I'(i) seen by a pixel i (omitting any instrumental factors, i.e. the response of individual pixels) is given by:

$$\mathrm{I'(i)} = \int_{\lambda(\mathrm{i})}^{\lambda(\mathrm{i+1})} \mathrm{I^*}(\lambda', \mathrm{L})\mathrm{d}\lambda' \tag{3.2}$$

In general the wavelength-pixel-mapping Γ_I of the instrument can be approximated by a polynomial:

$$\Gamma_\mathrm{I} : \lambda(\mathrm{i}) = \sum_{\mathrm{k}=0}^{\mathrm{q}} \gamma_\mathrm{k} \cdot \mathrm{i}^\mathrm{k} \tag{3.3}$$

The parameter vector (γ_k) determines the mapping of pixel i to the wavelength λ(i). A change in parameter γ_0 describes a spectral shift of the spectrum. Changing γ_1 squeezes or stretches the spectrum linearly. Parameters γ_k with higher k describe a distortion of the wavelength scale of higher order. Changes in the parameter vector γ_k can be caused by different measurement conditions of the spectra, as the employed grating spectrographs usually show a temperature drift when not thermally stabilized. It is therefore necessary to correct these effects in the analysis procedure. Figure 3.1c shows the discrete spectrum I'(i) as it is recorded and stored in a computer.

The DOAS technique was especially designed to match the needs of absorption spectroscopy in the atmosphere [*Platt* 1994]. In contrary to absorption spectroscopy in the laboratory, the absolute absorption signal of an observed trace gas in the atmosphere can not be accessed due to the lack of information about the measurement light intensity in the absence of the atmosphere. The basic concept behind DOAS allows to bypass this lack of information separating the cross-section σ_j into two parts:

$$\sigma_\mathrm{j} = \sigma_\mathrm{j}^\mathrm{b} + \sigma_\mathrm{j}' \tag{3.4}$$

where for a given trace gas j σ_j^b represents broadband spectral features and σ_j' the differential cross-section which represents narrowband spectral structures. Considering only σ_j' in the spectra evaluation process avoids interferences from Rayleigh- and Mie-extinction. The separation of the absorption cross-section is illustrated in Figure 3.2 for ozone.

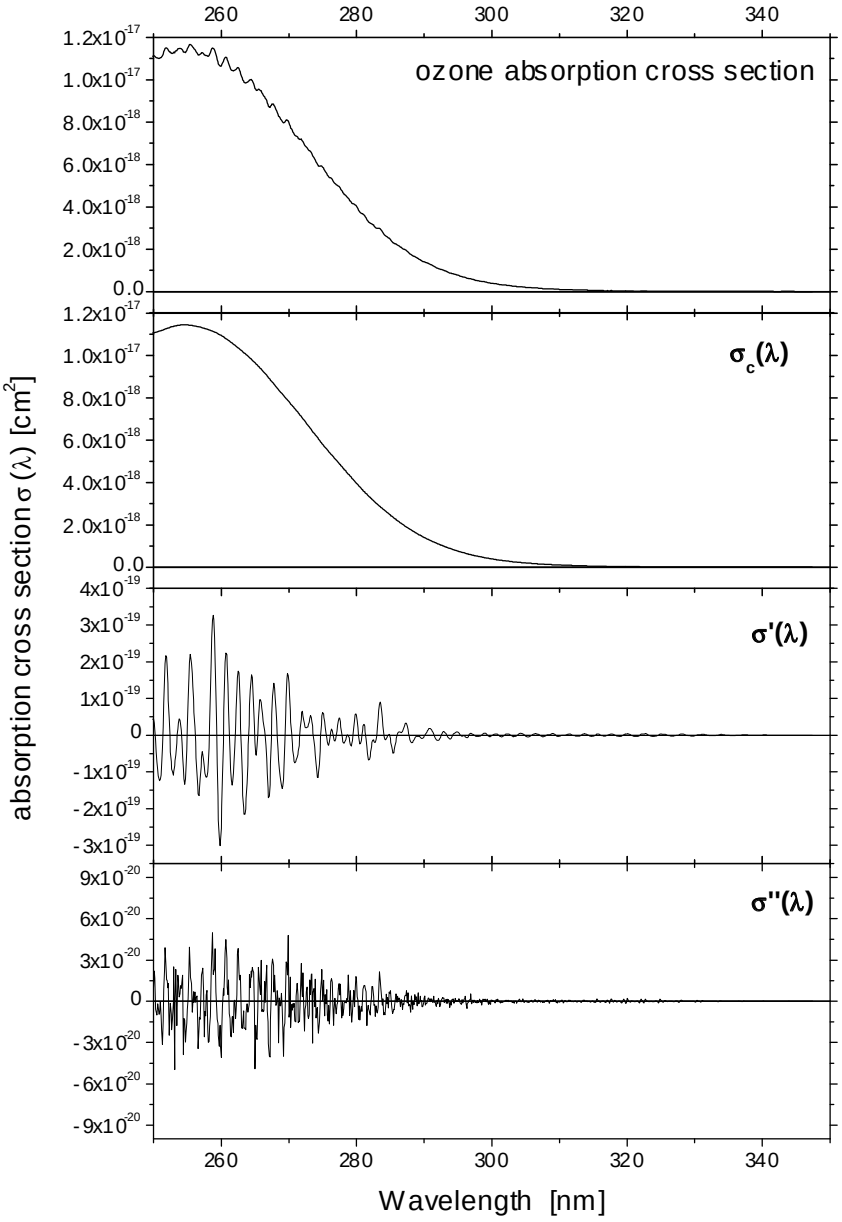

Figure 3.2: *The fundamental DOAS principle is the separation of the absorption cross-section (in this example of ozone, upper part) into 'slowly' varying (broad-band, second from top), 'rapidly' varying (narrow band, third from top), and high frequency parts (bottom graph) by applying a numerical band pass filter in the evaluation procedure.*

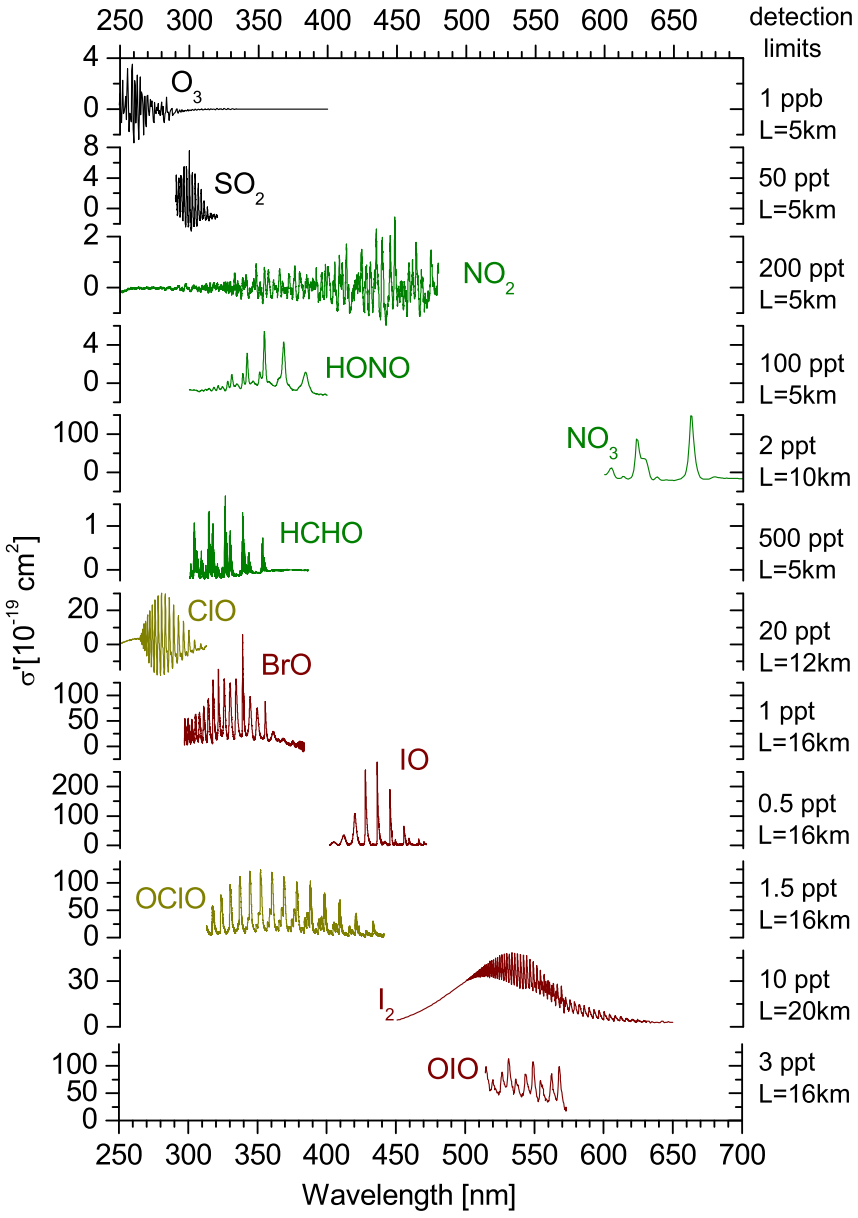

Figure 3.3: *Differential absorption cross-sections $\sigma'(\lambda)$ of selected atmospheric trace gases measurable by the DOAS technique. The indicated detection limit assumes a minimal detectable optical density of 10^{-3} on the indicated lightpath.*

The logarithm of I′(i) (see Figure 3.1c), J(i)= ln(I′(i)), can be described by:

$$J(i) = J_0(i) + \sum_{j=1}^{m} a'_j \cdot S'_j(i) + B'(i) + R'(i) + A'(i) + N'(i) \qquad (3.5)$$

where for each trace gas species j, $S'_j(i)$ denotes the differential absorption structure. Thus ($S'_j(\lambda)$=ln(exp(-$\sigma'_j(\lambda)$)·H) corresponds to the convolution of the differential cross-section of the trace gas j with the same instrument function H. B′(i) represents the broadband absorption, R′(i) the sum of extinction by Mie- and Rayleigh scattering, A′(i) summarizes any variations in the spectral sensitivity of the detector or spectrograph and N′(i) = ln(N(λ)) is caused by the detector noise and photon statistics. The scaling factors $a'_j = \bar{c}_j \cdot L$ are then the product of the average number densities over the pathlength L.

The overlaying absorption structures of several trace gases are represented by the sum in Equation 3.5. In practice the number of absorbers m can be limited to those trace gases with absorption structures sufficiently strong to be detectable with the used DOAS instrument. As the strength of the absorption structures varies with wavelength, the number of trace gases to be included in Equation 3.5 varies with the observed wavelength interval and the trace gas composition of the probed airmass. Typically m = 2-10 trace gas absorptions can be identified in a single atmospheric DOAS spectrum [*Platt* 1994]. The concentrations of these trace gases can therefore be measured simultaneously. To retrieve the concentrations, the superimposed absorption structures have to be separated numerically. The task of the evaluation procedure is: (1) to retrieve the parameters a'_j (Equation 3.5) and thus the concentration of the trace gases taking into account all the atmospheric and instrumental effects. (2) to estimate the error $\Delta a'_j$ of the parameters a'_j and therefore of the measured trace gas concentrations. Both tasks can be solved with linear least-squares methods if no instrumental effects are encountered [*Stutz and Platt* 1996].

3.1.2 Principles of the Analysis Procedure

The evaluation procedure is based on a model that describes the physical behavior of DOAS spectra according to Equation 3.5. The logarithm of the discrete measured intensity, J(i), is modelled by a function F(i):

$$F(i) = P_r(i) + \sum_{j=1}^{m} a'_j \cdot S'_j(i) \qquad (3.6)$$

where the absorption structures of the trace gases S_j, e.g. measured in the laboratory or calculated by convolution of high resolution literature cross-section with the instrument function H are input data to the procedure. The polynomial $P_r(i)$ describes the broadband spectral structures caused by the characteristics of the lamp $I_0(i)$, the scattering processes $R'(i)$ the spectral sensitivity $A'(i)$ and the broadband absorptions by the trace gases $B'(i)$. It can be expressed as:

$$P_r(i) = \sum_{h=0}^{r} c_h \cdot (i - i_c)^h \tag{3.7}$$

where the parameter $i_c = int(n/2)$ represents the center pixel of the spectral region used for the evaluation. The polynomial refers to i_c to maximize the influence of the nonlinear terms. The scaling parameters a_j (Equation 3.6) and the polynomial coefficients c_h (Equation 3.7) are found by linearly fitting F(i) to J(i). The scaling factors a_j are used in the following to calculate the average concentration of the respective trace gases:

$$\overline{c_j} = \frac{a_j}{\sigma'_j \cdot L} \tag{3.8}$$

where σ'_j denotes the differential absorption cross-section of trace gas j and L the absorption pathlength.
In order to match the wavelength-pixel-mapping of all spectra, the analysis procedure aligns the reference spectra $S'_j(i)$ (wavelength-pixel-mapping Γ_j) to the spectrum J(i) (wavelength-pixel-mapping Γ_J). The procedure therefore has to recalculate the reference spectrum $S^*_j(i)$ with the wavelength-pixel-mapping Γ_J. This can be approximated as 'shifting and stretching/squeezing' the reference spectrum in wavelength. Since Γ_j (identical to Γ_I in Equation 3.3) is a strongly monotonous function, its inverse also can be described by a polynomial:

$$\Gamma_j^{-1} : x(\lambda) = \sum_{k=0}^{q} \beta_k \cdot \lambda^k \tag{3.9}$$

where $x(\lambda)$ represents the non integer 'pixel number' that results from this inverse transformation. $S_j(\lambda)$ can now be calculated from the continuous spectrum $S_j(x)$. This spectrum has to be approximated using a (e.g. cubic spline) interpolation on the discrete spectrum $S_j(i)$.

$S^*_j(i)$ with the wavelength-pixel-mapping Γ_J can be calculated by deriving $S_j(\lambda)$ with Γ_j^{-1} from $S_j(x)$, which is approximated by a interpolation on

$S_j(i)$, and then applying Γ_J:

$$S_j(i) \xrightarrow{\text{interpolation}} S_j(x) \xrightarrow{\Gamma_j^{-1}} S_j(\lambda) \xrightarrow{\Gamma_J} S_j^*(i) \tag{3.10}$$

It is possible to refrain from calculating $S_j(\lambda)$ and combine Γ_j^{-1} and Γ_J to a formula, which links i to x using a polynomial with parameters δ_k:

$$x(i) = x(\lambda(i)) = \sum_{k=0}^{q_s \cdot q_l} \delta_k \cdot i^k \tag{3.11}$$

In the analysis procedure a slightly modified equation equivalent to 3.11 is used, which has the advantage that their spectral alignment parameters $d_{j,k}$, determining the transformation, are zero if the wavelength-pixel-mappings of J and S_j are equal:

$$x = i + f_j(i) \qquad \text{with} \qquad f_j(i) = \sum_{k=0}^{p_j} d_{j,k} \cdot (i - i_c)^k \tag{3.12}$$

The spectrum $S_j(d_{j,0},d_{j,1},...)(i) = S_j^*(i)$ has now the wavelength-pixel-mapping Γ_J, which was calculated with the parameters $d_{j,k}$ following Equations 3.10 and 3.12 and a cubic spline interpolation on $S_j(i)$. The parameters $d_{j,k}$ are derived by performing a nonlinear fit of the model F to the spectrum J with fixed parameters a_j and c_h. If $p_j = 0$ the spectrum S_j is shifted by $d_{j,0}$ pixels, if $p_j = 1$ the spectrum is additionally linearly squeezed or stretched according to parameter $d_{j,1}$. Higher values of p_j represent a squeeze or stretch of higher order. To achieve the best physical description of the spectra, it is possible to select the degree of the squeeze process p_j for every reference spectrum S_j. It is advantageous to use one set of parameters $d_{j,k}$ for two or more reference spectra if the wavelength calibration is identical for these spectra in order to reduce the number of degrees of freedom. The analysis procedure is a combination of the well-known nonlinear Levenberg-Marquardt-Method [*Levenberg* 1944; *Marquardt* 1963] determining $d_{j,k}$ and a standard linear least-squares fit [*Albritton et al.* 1976; *Bevington* 1969] to derive the a_j and the c_k. Both methods minimize χ^2 between F and J:

$$\chi^2 = \sum_{i=0}^{n} (J(i) - F(i))^2 \tag{3.13}$$

The procedure begins with the calculation of the linear fit with starting values $d_{j,k}$. The results of this fit, the parameters a_j and c_k, are used as

input data in the following call of the nonlinear Levenberg-Marquardt fit. Only one step of this nonlinear iterative method is then performed. The resulting parameters $d_{j,k}$ are used in the next call of the linear fit. These results are used in the next call of the nonlinear fit. The procedure invokes the two methods alternatingly, always using the result of the last call of one method as values for the other fit method. This procedure is repeated until one of several stopping conditions for the nonlinear fit is fulfilled. Normally the fit is aborted, when the relative changes of χ^2 in the last step is smaller than a given value (usually 10^{-6}) and thus the fit has converged. The fit also stops if a number of repetitions of the iteration determined by the user is exceeded or if the nonlinear method becomes unstable [*Gomer et al.* 1993; *Stutz and Platt* 1996].

3.2 Active Longpath DOAS Instrument

The basic principle of active longpath DOAS (LP-DOAS) is to send a beam of light typically in the visible and or near UV wavelength range generated by an artificial source ('active') on a well-defined lightpath through the atmosphere. The light is then collected by suitable optics and sent to a spectrograph-detector system. Here, the spectrum is analyzed to gain information on the structure and magnitude of absorption by molecules occurring along the absorption path. As each molecule has a characteristic absorption structure, the DOAS technique is suitable to measure the concentrations of different trace gasses at the same time. Of special interest for this thesis are the reactive halogen compounds IO, BrO, OIO and I_2 . In contrast to the active method another well-established application of DOAS is passive DOAS, which uses the sun, the moon or stars as light sources. The measurement geometry of passive DOAS sees either the direct lightpath from the source to the spectrograph as the absorption pathway, mostly with the sun acting as the light source, or straylight coming from one or multiple (MAX-DOAS) distinct zenith and azimuth angles. A recent overview on MAX-DOAS technique and application is given in *Hönninger et al.* [2004].
Within this work three field campaigns were conducted using the active longpath DOAS measurement technique. This is a classical adaption of the DOAS method, and was already successfully operated in a great variety of field studies (e.g. [*Ackermann* 1997; *Geyer* 2000; *Alicke* 1997; *Hebestreit* 2001]).
The main components and characteristics of the operated active LP-DOAS instrument will be described within the next section.

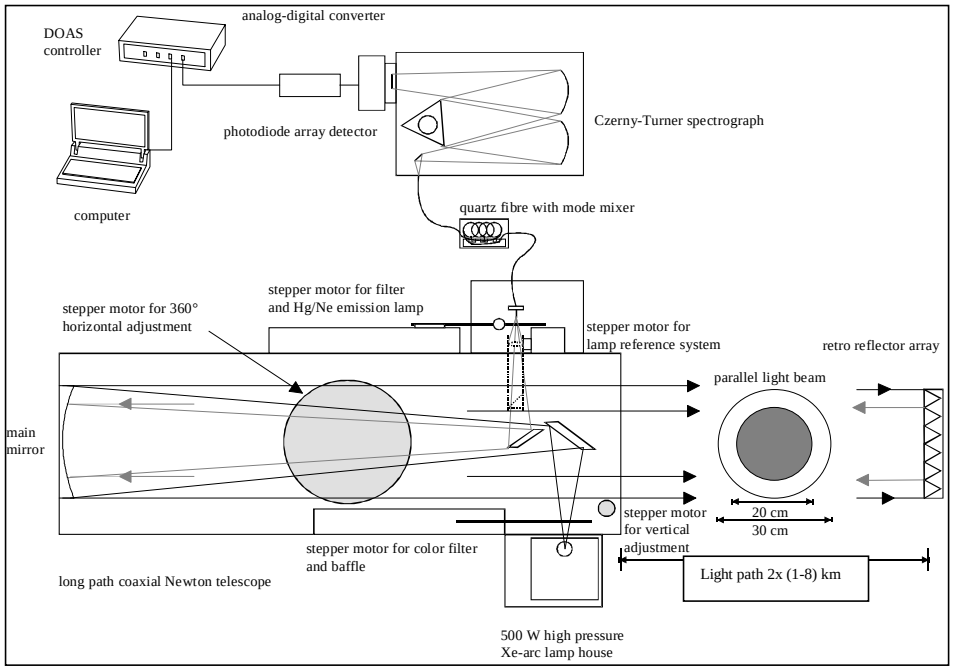

Figure 3.4: *Schematic overview on the set-up of an active longpath DOAS instrument with the main components.*

3.2.1 Telescope System

In this modern version of a longpath telescope, the transmitting and receiving optic are combined in one coaxial Newtonian telescope. As can be seen in Figure 3.4 two elliptical plane mirrors are mounted in the optical axis of the telescope to reflect the outgoing and incoming lightbeams for 90°. The main mirror with a parabolic shape has a diameter of 30 cm and a focal length of 150 cm. To make the outgoing lightbeam parallel, in one focal point of the main mirror the light source is positioned. The light is send through the atmosphere and reflected by a retro-reflector array in several kilometers (up to 15 km) distance. The parallel beam is exactly reflected back into the telescope and focused on a quartz fiber located in the focal plane of the telescope. The fiber transmits the light into the spectrograph, where it is dispersed and imaged on the detector, as the raw spectrum.
However, the light source is not really a point-sized source, the lightbeam diverges along the path through the atmosphere, depending on the size of

the light spot of the lamp and the distance to the reflectors what causes a loss of light. Furthermore the construction of the instrument, the two plane mirrors in the optical axis of the telescope cause a loss of light in the order of 50%, because the light can only send out in the outer ring-shaped area as it is shown in Figure 3.4.
For the automatization of continuous measurements during the field campaigns, several motors are mounted at the telescope. For pointing the lightbeam on the retro-reflector a vertical and horizontal movement of the telescope is provided by two respective motors.
Two additional motors move filterwheels, one in front of the quartz fiber and the other in front of the light source. The filterwheel in front of the lamp housing is equipped with several bandpass filters in order the reduce stray light in the spectrograph. The respective cut-off wavelength is adjusted to the respective wavelength range of the actual measurements. For measurements in the UV range a bandpass filter UG5 of Schott was used or the comparable Hoya U-330. The transmission graph for the Schott UV band pass filters is shown in Figure 3.5. A black baffle was mounted on the filterwheel, to block the light of the lamp for recording background spectra. The filterwheel in front of the quartz fiber was used for moving the calibration lamp. The Ne and Hg line shape spectra were recorded regularly during the measurements to determine resolution and wavelength calibration (see Section 3.3.7).
During the campaign at the North Sea a fifth motor was mounted to move a so-called short-cut system, to focus a part of the outgoing light on the fiber. Lamp spectra recorded with that system are used as lamp reference spectra (see description in Section 3.2.7).

3.2.2 Light Source

The used light source for the LP-DOAS measurements were high-pressure Xe-arc lamps. An image of such a lamp is shown in Figure 3.6.
The light arc is created between the electrodes, which have a distance of less than 1 mm. The high voltage ignition discharge produces a dense plasma in the Xenon gas bulb to produce the light arc. The spectrum of the Xe-arc lamp is therefore a superposition of the thermal emission according to the Planck function and the Xe emission lines. These lines are significantly broadened due to the high pressure of the operating Xe-arc lamp. As the distance between cathode and anode is small, the length of the light arc is small, too. Hence the divergence of the outgoing lightbeam is reduced, by the good approach of a point sized light source. The pressure inside the

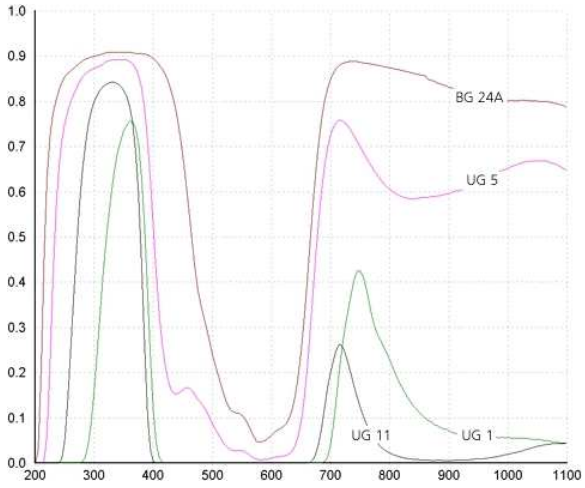

Figure 3.5: *Transmission for UV band pass filters of Schott, the UG 5 filter was applied for measurements in the UV range to reduce straylight.*

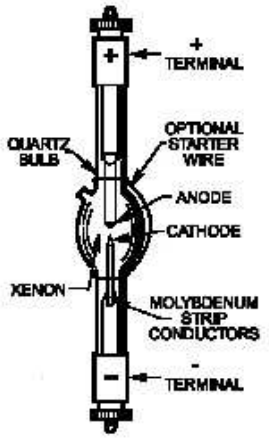

Figure 3.6: *Image of a high-pressure Xe-arc lamp. The electrodes are made of tungsten and the bulb of quartz glass.*

lamp is high, and can reach up to 10^7 Pa during the operation of the lamp, yielding a high density plasma. The color temperature of the Xe lamp used for this work was ∼6000 K, what is comparable to that of the sun, with a maximum of spectral intensity at ∼500 nm. The bulb of the Xe lamp is

Lamp	PLI SX5002 500W	XBO Osram 500W
Power [W]	500	500
Voltage [V]	18	18
Current [A]	29.5	26
Lifetime [h]	200	500
Size of brightest spot [mm·mm]	0.3·0.3	1.0·2.0
Costs [Euro]	500	300

Table 3.1: *Overview on the characteristics of the employed Xenon arc lamps*

made of quartz glass, which is extremely resistant to the high pressure and temperature. The material of the electrodes is tungsten. The cathode has an edged peak to enhance the electron emission, while the anode is made of massive material to absorb the kinetic energy of the incoming electrons. For this work the mainly used lamp was that of PLI HSA-X5002 (Professional Lamp Inc., USA), with an arc size of $0.3 \cdot 0.3\ mm^2$. The lamp was operated at 29.5 A and 18 V and has a mean lifetime of 200 hours. Due to this short lifetime and the relatively high costs a second type of lamp, the Osram XBO 500 W was operated during instrument tests at Heidelberg. An overview on the characteristics of bothe lamp types is given in Tabel 3.1.
Extensive studies on the variability of the emission features of different lamp types caused by flaring lamp plasma were made by *Hermes* [1999]. He found Xe emission lines over broadened parts of the spectrum including the red spectral region. The emission strength and pressure broadening of these Xe lines is variable in time and therefore a limiting factor in the evaluation of the spectra. This will be discussed in more detail in the Section 3.5.

3.2.3 Retro-Reflectors

Quartz prism retro-reflectors reflect light exactly by 180°. One reflector has a diameter of 70 mm and a weight of 430 g. Arrays of these reflectors were used to fold back the emitted light beam of the DOAS telescope. With increasing distance between telescope and reflector the divergence of the lightbeam increases and the reflector arrays have to be adapted in their size. For the lightpaths of ∼10 km, arrays consisting of more than 200 reflector units were constructed and set-up for the field campaigns described in this work.

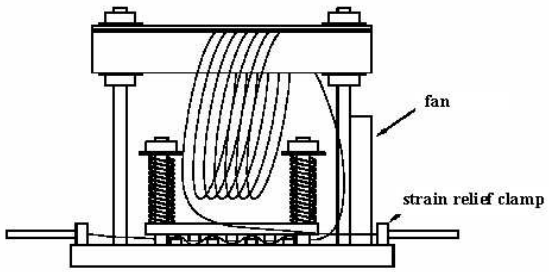

Figure 3.7: *Schematic overview of a quartz fiber mode mixer.*

3.2.4 Quartz Fiber Mode Mixer

To transmit the light from the focal point of the telescope to the entrance slit of the spectrometer, quartz fibers are used. The quartz fibers used during the field campaigns are multi mode step-index fibers with a numerical aperture (N.A.) of 0.12, which fitted best the aperture ratio of the telescope and the spectrometer. However, due to the arrangement of the sending and receiving telescope within one instrument, a ring-shaped parallel light beam is focused on the quartz fiber, which transmits this ring-shaped light cone, as it is into the spectrometer. As a result the grating is not uniformly illuminated. This degrade the performance of the DOAS system, as it can lead to strongly structured residual in the evaluation of spectra. It was found by *Stutz and Platt* [1997] that bending and shaking the quartz fiber in a so-called '*quartz fiber mode mixer*' leads to a more uniform distribution of the different modes and thus to a more homogeneous illumination of the grating and the detector. A schematic overview of a *quartz fiber mode mixer* is shown in Figure 3.7. Diffuser plates would be also suitable, but have a significantly worse light throughput. Mode mixing characteristic varies strongly for the employed quartz fibers and some fibers exhibit very efficient mode mixing without any bending and shaking. However the usage of quartz fiber mode mixers lead in general to a significant improvement of the instrument performance, but it should be noted that the residual noise is generally higher compared to laboratory tests of DOAS systems avoiding the usage of quartz fibers in the instrumental set-up.

3.2.5 Spectrograph

The operated spectrograph was an Acton spectra Pro 500. Basically this device is already developed by Czerny and Turner in 1930 [*Czerny and Turner* 1930]. The quartz fiber transmitting the light from the focal point of the telescope into the spectrograph is adjusted to the focal plane of the convex main mirror of the telescope. The width of the entrance slit in the focal plane is adjusted to the diameter of the quartz fiber, which was 200 μm. The light entering the spectrograph is paralleled by the spherical mirror and reflected onto the plane diffraction grating. The dispersed light is then focused by a second convex spherical mirror onto the detector unit.
The focal length of the spectrograph is 500 mm and the aperture ratio is 6.9. Three different gratings could be mounted on a motorized turntable. For this work a 600 grooves/mm grating was operated, with a dispersion of 3.08 nm/mm, what corresponds to 0.077 nm/channel with the detector array consisting of 1024 diode elements, described in the following section. In order to minimize thermal disadjustments the whole spectrograph unit is thermally isolated and thermostated by a PID control unit. The operation characteristics of the PDA are indicated in Table 3.2.

3.2.6 Detector System

The detector unit is mounted in the focal plane of the spectrograph. The principle item of the unit is a photo diode array (PDA) of Hamamatsu (type S3904-1024) consisting of 1024 Si photo diodes (CMOS) with 25 μm width and 2.5 mm height. The PDA is placed inside an evacuated camera box, filled with 1-2 bar Ar 5.0. A peltier element is used to cool the PDA to reduce the dark current. The capacity of a diode is 10 pF, the full well depth corresponds to $1.286 \cdot 10^8$ photo electrons. A more detailed discussion of the usage of photo diode arrays as DOAS detectors is given by *Stutz* [1991]. Every photo diode represents a n-p junction. During operation an inverse voltage of 2.06 V is applied to the diode inducing a depletion layer which is almost as large as the whole diode area. Incoming light excites a number of electrons proportional to the lights intensity into the conducting layer of the semi conductor. These mobile charge carriers reduce the applied inverse voltage. However, this is also possible by thermally activated transitions of electrons into the conducting layer. This effect is called dark current and must be considered in the evaluations procedure at low light intensities. In order to reduce dark current the PDA was cooled down to temperatures between -40 and -20 °C by a Peltier cascade. Thereby the dark current de-

creases exponentially regarding to the Stefan-Boltzmann law. Dark current depends on the temperature, on the integration time and on the signal operation of the diode array. After the pretended integration time the PDA is read out and signals are amplified electronically. To exclude negative signals under low light conditions (which would reduce the resolution of the digitized values by a factor of two) an offset signal is added to every PDA signal readout. The offset is proportional to the number or readouts per spectrum and must be corrected for during the evaluation process. The signals are digitized by a 16 bit analog-digital converter (full saturation corresponds to $2^{16} = 65{,}536$ counts) and then transmitted to the PC.
Thin surface layers such as a quartz window in front of the PDA can lead to a Fabry-Perot etalon structure in the spectra (see *Stutz* [1991]). This structure is caused by the interference of multi reflected light beams inside this surface layer. Due to the cooling of the detector unit, water vapor would freeze on the PDA and possibly cause an etalon structure. Hence the detector is evacuated and filled with dry argon as inert gas. Another known but not well understood effect of PDAs is the so-called 'memory effect'. That effect describes that structures of a former spectrum remain present in the following spectra. The memory effect is discussed detailed in *Stutz* [1996]. However, the origin is unclear up to date. The memory effect can be reduced by performing dummy scans, multiple scans in absence of light to 'clear' the PDA.
The detailed characterization of the operated PDAs within this work is given in Section 3.3.

3.2.7 Shortcut System

Two different methods to record pure lamp reference spectra to correct structures of the Xe-lamp are used in this work. The shortcut system 1 was used during the 2002 North Sea campaign. A sketch of it is shown in Figure 3.8. It consists of two plane mirrors, the first one is used to reflect a part of the outgoing lightbeam by 90° on a parabolic mirror. The parabolic mirror is used to focus the light coming from the lamp onto the quartz fiber (folded by a second plane mirror). The advantage of that system is, that lamp references could be recorded regularly within the measurement routine, by just moving the plane mirrors into the lightbeam. The parabolic mirror is fixed and does not need to be adjusted by every movement of the motors. The earlier systems used a lens system to focus on the quartz fiber, but as the lenses are dispersive mediums, the imaging of lamp spectra showed principle problems. The applied mirror solved the problem with the disper-

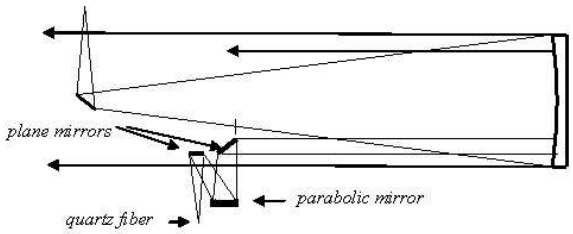

Figure 3.8: *Sketch of the shortcut system used during the 2002 North Sea campaign. A small plane mirror in the outgoing lightbeam reflects light on a parabolic mirror. The mirror has to be adjusted that its focal point matches exactly the entrance of the quartz fiber.*

siveness of the lamplight. But it was found, that the arrangement of the second reflecting mirror caused astigmatic effects, which degrade the imaging quality of the used system. Nevertheless, the system was applied during the North Sea campaign. The lamp reference spectrum was recorded after every atmospheric spectrum. Each atmospheric spectrum was divided by its belonging lamp spectrum in the analysis, to reduce the error caused by inhomogeneities of the used PDA (see Section 3.3.6). Conclusively it turned out, that variations in the lamp spectra on a short time scale cause significantly higher residual structures than the inhomogeneities of the detector.
A second method recording lamp spectra was used for the campaigns in Brittany and Hudson Bay. A rotating retro-reflector array was mounted in front of the telescope to reflect the outgoing beam back to the main mirror and onto the quartz fiber. The advantage of this method is, that the imaging properties are identical to that of the atmospheric spectra, just on a shortened lightpath. The homogeneity of the outgoing beam was always assumed for the previous shortcut systems, when imaging only a small part of the outgoing beam onto the quartz fiber. By the rotating shortcut system, major parts of the outgoing ring of light are reflected back and imaged on the entrance of the fiber. The main disadvantage is, that this system was not automated and lamp spectra had to be recorded manually, each day.

3.2.8 Automated fiber alignment

A special automated fiber alignment was designed for the longpath DOAS measurements on lightpaths longer than 8 km. Air is a dispersive medium and the refraction index depends on temperature and pressure. These atmo-

spheric parameters depend on meteorological conditions, which can change significantly during the period of the measurements. Therefore the light-beam has to be re-adjusted from time to time onto the retro-reflector. This can be done in a first approach by adjusting the horizontal and vertical motors of the telescope, but if the lightpath exceeds 8 km of length it was found that the precision of the stepsize of the motors was insufficient. Therefore the fiber entrance was motorized, with one horizontal and one vertical stepper motor, mounted on a micrometer table. Within the measurement routine re-adjustments of the fiber entrance could be included regularly in an automated way.

3.3 Characterization of the Detector System

For the field campaigns described in this work, two different detectors were used to record spectra for the DOAS analysis. Detector 1 was operated during the 2002 North Sea and detector 2 during the 2003 Brittany and 2004 Hudson Bay campaign. Both detectors are of the same type, manufactured by Hoffmann Messtechnik, Germany and equipped with a Hamamatsu S3904-1024 PDA. Table 3.2 summarizes the characteristics, including the linearity, offset and dark current of the respective PDAs. As the campaigns differ significantly in their meteorological conditions, the characteristic is given for each of the three campaigns.

3.3.1 Offset

The offset was determined by adding 10,000 scans at minimum exposure time (60 ms) at dark conditions. The resulting spectrum provides an averaged electronic readout signal of 10,000 scans and a dark current of 600 s. However, the dark current can be neglected as the ratio of dark current to offset is in the order of 10^{-4}. Offset spectra were taken several times during a field campaign, and it could be verified that the structure and the average counts per scan (readout) were stable.

3.3.2 Dark Current

The dark current was determined by the scanning of one spectrum with long exposure time. The exposure time is usually between 500 and 1000 s. The dark current signal decreases exponentially with decreasing temperature of the PDA, but stable cooling of the Peltier cascade is limited to $\sim$30 K

against ambient temperature. Several detector pixels exhibit peak dark current signals of more than 10 times the average dark current signal, which can be most likely attributed to endowment defects of the diodes material. For both operated detectors the number of 'hot pixels', which are defined by exceeding the average dark current signal by more than 50% was below 8. As the offset spectrum, the dark current was recorded several times during the field campaigns, in particular if the temperature of the PDA was set to another parameter (e.g. Hudson Bay).

3.3.3 Residual Noise

The residual noise can be separated in electronic and photon noise. The electronic noise is caused by the resolution of the digitalization, noise of the analog digital converter (ADC) and other electronic components. The electronic noise was determined by subtraction of two offset spectra, taken in succession. The root mean square (rms) of that spectrum is scaled down to one scan, by the division of a factor 2N, with N being the number of scans added in one offset spectrum.
Another source of noise in a spectrum is the photon noise, which is the square root of the number of photons according to Poisson statistical theory. Considering the well depth of the used diodes (1 count = 1962 photo electrons), the photon noise (1σ) of a spectrum with 10^4 and 10^6 counts are $2.3 \cdot 10^{-4}$ and $2.3 \cdot 10^{-5}$, respectively. The photon noise must be added to the electronic noise in order to get the total residual noise.

Experimentally the residual noise was determined by the division of two spectra, corrected for offset and dark current, taken in succession with the same integration time. The light source was a halogen lamp, directly mounted in front of the quartz fiber of the DOAS telescope. The peak to peak value of the residual structure was determined from the calculated spectrum. Figure 3.10 shows the resulting variation of the residual noise with the number of counts for detector 2, operated during the Brittany and Hudson Bay campaign. As expected, the noise decreases with the square root of the number of counts.

The electronic noise of detector 2 shows a higher electronic noise than that of detector 1 as can be seen in Table 3.2. This was investigated more detailed, and it turned out that the PDA has fixed pattern noise, the noise is separated for the even and odd pixels with a shift of 4 counts. This is to seen in Figure 3.9.

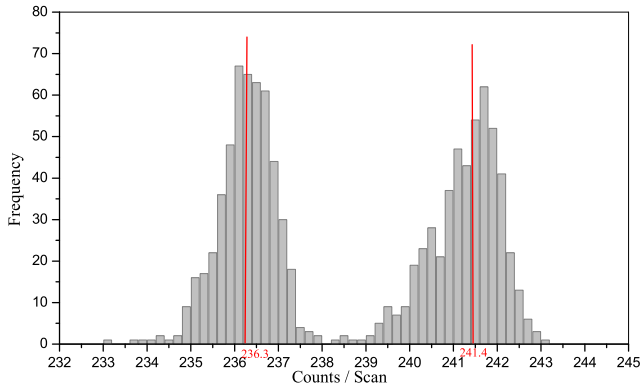

Figure 3.9: *Two offset spectra and their frequency distribution. The two maxima represent the respective mean values for the even and the odd electronic offset signals. The maxima of the distributions are shifted ∼4 counts to each other.*

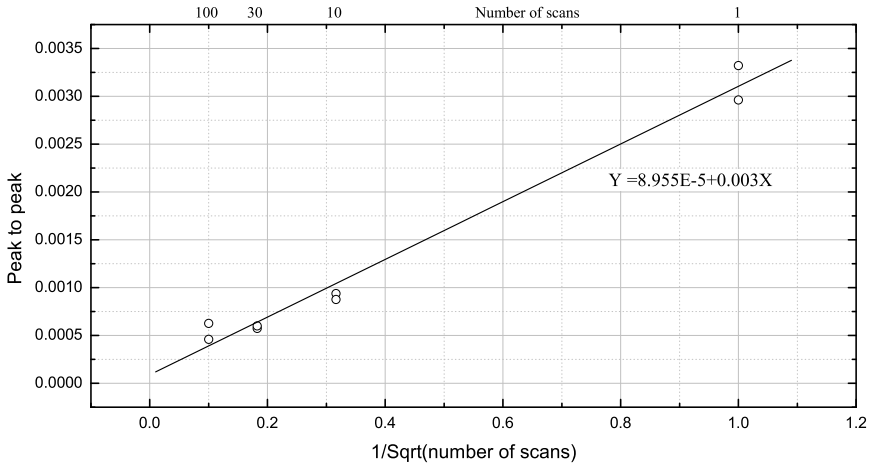

Figure 3.10: *Peak to peak in dependency on the number of scans over the range of 508-588 nm*

	North Sea	Brittany	Hudson Bay
Detector	PDA 1	PDA 2	PDA 2
PDA Temp. [$°C$]	-20	-20	-35/-25
Spec. Temp. [$°C$]	20	20	5/15
Offset [$cts/scan$]	202.4	238.5	248.6
Dark Current [cts/s]	1.4	1.65	0.59
Electronic Noise [cts]	3.1	4.9	4.4
1σ-Res. noise [cts]	$3.8 \cdot 10^{-4}$	$3.0 \cdot 10^{-4}$	$3.3 \cdot 10^{-4}$

Table 3.2: *Characteristics of the PDAs used for the DOAS measurements performed during three field campaigns. The 1σ-residual noise is given for 100 scans in the 380 - 460 nm wavelength range.*

3.3.4 Dispersion, Resolution

The wavelength to pixel-mapping was experimentally achieved by recording a mercury reference spectrum after every movement of the grating. So it could be used to determine the precise wavelength pixel mapping of each atmospheric spectrum. With a linear fit, the shift of every reference spectrum to a well known mercury reference was defined. The resulting shift was applied to the atmospheric spectra to achieve the identical dispersion. The error made by this shift procedure could be estimated to be smaller than one pixel and could therefore be neglected. Additionally to remark is, that for the following evaluation procedures shift and squeeze were principally allowed, a feature which can adjust slight inconsistencies in the wavelength-pixel mapping.

3.3.5 Memory Effect

Illuminating the PDA with light of high intensity or strong gradients in the intensity (e.g. mercury reference spectrum) can cause the so-called memory effect. The signature of recorded spectra can be observed in the following spectra, although the detector is darkened. This phenomenon was already studied by *Stutz* [1996].

The characterization of the memory effect is rather difficult since its origin is not clear. *Geyer* [2000] made more detailed studies on the phenomenon and developed strategies in order to reduce the disturbing effect in the spectra. Conclusively he found out, that the memory effect decreases with time and the best strategy to reduce the memory effect is to wait several seconds after each record of spectra with high light intensity. Therefore so-called *dummy scans* were included in the automated measurement routine after the record of mercury or neon spectra. Experimentally realized are *dummy scans*, by a high number of read-outs (typically 50 - 100) with short integration time at dark conditions.

3.3.6 Diode Sensitivity Structure

A serious problem occurring when using diode arrays as DOAS detectors is the variability of the diode sensitivity from pixel to pixel. The pixel sensitivity depends on the wavelength of the incoming light and can vary up to some percent between the pixels of one PDA [*Stutz* 1996]. Since DOAS is intended to observe optical densities down to less than 10^{-3} it is necessary to remove the diode sensitivity structures from a spectrum. The most simple idea would be the division of each spectrum by a lamp reference spectrum scanned just before or after each spectrum. This was tested with the shortcut system 1 during the campaign at the North Sea. However, it was found that this procedure leads to additional lamp structures in the spectrum since the Xe emission lines show temporal variations, which exceed the diode sensitivity structure.

MCT Technique

Another common method to eliminate the diode sensitivity structures in longpath DOAS spectra is the '*multi channel technique*' (MCT) introduced by *Knoll et al.* [1990] and detailed described for the application on DOAS measurements by *Stutz* [1996], *Brauers et al.* [1995]. The basic idea of the MCT is the combination of multi channel detection system (PDA) with the scanning technique generally used to cover a larger spectral region with a single channel detection system. Every spectrum is separated in several (e.g. 9) single spectra with slightly different wavelength calibration. These single spectra are recorded subsequently one after another. The spectral shift is performed automatically by the spectrograph system. Adding up all single spectra to a *sumspectrum*, the diode resident sensitivity structure remains

at each channel, but the spectral information changes depending on the step width of the MCT. The *sumspectrum* can be compared to the application of a low pass filter to the original spectrum as spectral structures are broadened by the shift. It is therefore important that the step width has to be smaller than any spectral structure like absorption bands, otherwise these structures not only remain in the *sumspectra* but would also be duplicated near itself. Then every single spectrum is divided through the *sumspectrum*, that diode resident structures are removed from the single spectra. In the following the single spectra are re-shifted to the correct wavelength calibration and summed up. It was found, that the MCT technique decreases the errors of evaluated trace gases, if the spectral regions of their characteristic absorption is not dominated by water vapor absorptions [*Geyer* 2000]. Water vapor consists of a strongly line shaped spectrum, which is not compliant to the realizable step width of the MCT technique. Hence the MCT technique was successfully applied for absorbers with characteristic absorptions below 440 nm. Above that limit the MCT technique was clearly found to increase the error of the evaluated trace gases. The MCT technique was applied for all measurements during the North Sea campaign, but only for spectra in the range of $390 - 470$ nm (IO) during the Brittany campaign. The MCT technique was not applied for spectra recorded in the $300 - 380$ nm range for two reasons. The homogeneity of the new detector 2 was already better than 1%. The light intensities over a lightpath of $\sim$10 km show significant attenuation by scattering processes in the atmosphere. Though generally long exposure times for spectra in the UV are needed. Additionally the MCT technique requires to record each spectrum several times (typically 9). For the composition of the final spectrum the record of a calibration reference, a mercury spectrum is needed after the application of each step of shifts. All over this technique is very time consuming, so that the measurement strategy was changed for the campaign in Brittany.

3.3.7 Measurement Routines

The measurements during the field campaigns were fully automated and controlled by the software *DOASIS*, developed at the Institute for Environmental Physics, Uni Heidelberg [*Kraus* 2003] (see Section 3.4.1). For the three campaigns just slightly different measurement routines were programmed in the *j-script* language. A variety of restrictions on the measurement routine were made, to prevent greater loss of measurement time. The estimated exposure time of a test spectrum was used to define the number of scans. Depending on the atmospheric visibility 10 - 100 scans per spectrum were

made, with a limit of 30 minutes accumulation time for one spectrum. In the case of MCT measurements the number of scans was restricted to a maximum of 30 scans, nevertheless adding 9 times 30 scans, one MCT spectrum consists of up to 270 scans. Additionally the single spectra consisting of 30 scans could be evaluated separately, leading to time series with very high time resolution. A schematic flow diagram is shown in Figure 3.11. Measurements at 335 nm were denied by the routine if an accumulation of 10 scans in 30 minutes was not possible. During the Brittany campaign MCT measurements were made at 430 nm only during day. At night the grating was set additionally to 640 nm for measurements of NO_3. After the positioning of the grating, the exposure time is optimized in a first step, this includes also an optimization of the light point position on the fibre with the help of the automated fiber alignment. In the second step the atmospheric spectrum was taken, followed by the background spectrum. For the determination of the the wavelength to pixel mapping a spectrum of a reference lamp (Hg or Ne) was recorded after each re-positioning of the grating of the spectrograph.

3.4 Spectra Analysis and Evaluation Algorithms

For this work extended data sets were recorded during three field campaigns. During each campaign several wavelength ranges were measured to detect a variety of reactive halogen species (RHS). In this section, the general analysis procedure is introduced, followed by a detailed description of evaluation yielding the concentrations of the absorbers BrO, IO, OIO and I_2 besides the non halogen species.

3.4.1 Software

DOASIS is a software package, developed at the Institute for Environmental Physics by *Kraus* [2003]. However, the software is a so-called all-round tool that should provide all features from data acquisition, spectra processing and analysis, it is still in working progress and test state, that not all features provided by this software could be applied in this work. *DOASIS* was used for the full control of the automated measurements and for most preprocessing steps yielding the spectra for the final analysis. The analysis of the spectra was performed with the software *WinDOAS* [**?**]. *WinDOAS* is a software developed at *IASB/BIRA* (Belgian Institute for Space Aeronomy), for the analysis of UV-VIS spectra by the DOAS method.

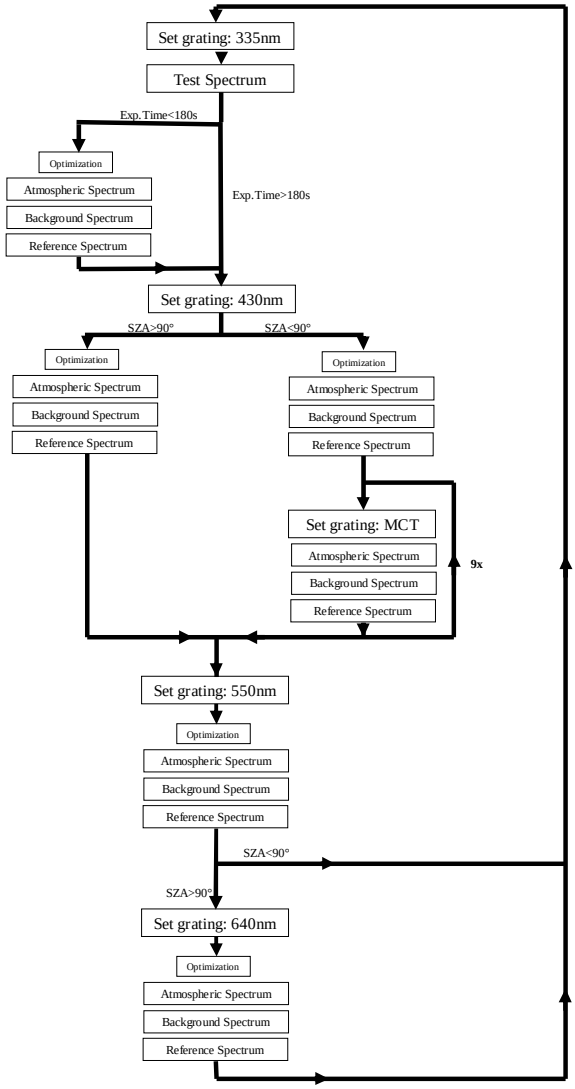

Figure 3.11: *A schematic overview on the measurement routine programmed for the automated measurements during the field campaigns. Reference spectra were taken with mercury or neon lamps to determine the wavelength to pixel mapping.*

3.4.2 Spectra Preprocessing

Each recorded spectrum is offset corrected in respect to the number of scans. The atmospheric spectra are background corrected, with the corresponding background spectra, which was recorded immediately after the atmospheric spectrum according to the respective exposure time of the atmospheric spectrum. The correction of the the dark current is included herein. By using the mercury reference spectrum, the shift for each spectrum to the correct wavelength dispersion was determined and applied to the spectra.
In case of the MCT spectra the procedure changed slightly. The 9 MCT spectra were summed up before the shift was applied, the resulting *sumspectrum* served later on as a highpass filter. The respective shift is then applied on the 9 spectra, which again are summed up after a division by the *sumspectrum*. This division by the broadened *sumspectra* is equivalent to a highpass filter and removes the channel fixed structures/inhomogenities. (see description of MCT spectra processing in Section 3.3.6). Spectra, which have not been recorded by the MCT technique are highpass filtered, that broadband absorption structures caused by atmospheric Rayleigh- and Mie-scattering was greatly reduced.

3.4.3 Differential Absorption Cross-Sections

In Table 3.3 all utilized absorption cross-sections with their respective resolution and references for this work are given. It should be noted, that the quality of the analysis regarding the retrieval of concentration for the trace gases is highly sensitive for the chosen cross-section. To compare results of different evaluations, the different cross-sections have eventually scaled to each other.

IO

For the evaluation of IO, the cross-section of Hönninger [*Hönninger* 1999] with $\sigma_{diff}(427.2\ nm) = 2.6 \cdot 10^{-17} cm^2$ was used. But it should be noted that within the ReHaTrop project new measurements of the IO cross-section yielded a higher maximum of the 4-0 transition band of $\sigma(427.2\ nm) = 3.55 \cdot 10^{-17} cm^2$ [*Crowley* 2004]. The cross-section of *Hönninger* [1999] was recorded at very high resolution of 0.09 nm, but scaled to the cross-section of *Bloss et al.* [1998], which was recorded with a the low resolution of 1.13 nm FWHM, what explains the differences. These recent results have to be applied on the results presented in this work (and previous works) by a re-scaling the cross-section of IO of *Hönninger* to the current $\sigma(427.2\ nm)$

Species	Resolution	Reference
HCHO	0.025 nm	*Meller and Moortgat* [2000]
O_4	2 cm^{-1}	*Greenblatt et al.* [1990]
O_3	5 cm^{-1}	*Voigt et al.* [2001]
NO_2	0.5-1 cm^{-1}	*Voigt et al.* [2002]
NO_3	1 nm	*Sander* [1986]
H_2O	0.001 nm	*Coheur et al.* [2002]
BrO	0.4 nm	*Wilmouth et al.* [1999]
OBrO	0.7 nm	*Rattigan et al.* [1995]
OClO	1 cm^{-1}	*Kromminga et al.* [1999]
IO	0.09 nm	*Hönninger* [1999]
OIO	1.13 nm	*Bloss et al.* [2001]
I_2	0.1 nm	*Saiz-Lopez et al.* [2004]

Table 3.3: *The differential absorption cross-sections used for the data analysis in this work.*

value. That results in 26.7% less absolute concentration of the IO radical in the atmosphere than assumed in this work and in previous publications.
To compare different cross-sections, the resolution of the spectra should always be taken into account (see also *Hönninger* [1999]).

O_4

The Greenblatt spectrum [*Greenblatt et al.* 1990] is the only reference available for O_4. It was therefore used for this analysis, even if the resolution of the spectrum is just 0.3 nm and worse.

H_2O

Water vapor absorptions are difficult to handle, since the spectrum consists of a nearly uncountable number of dense and sharp lines. Data sets providing the water absorption spectrum are available from Hitran [*Rothman et al.* 1998] and for 380 - 770 nm of *Coheur et al.* [2002]. The provided data bases were scaled to the respective temperature and pressure profiles by a software written by C. Frankenberg [*Frankenberg* 2004]. Especially in the 500-600 nm

range, the Coheur spectrum contains a couple of additional lines, compared to Hitran. Hence using the spectrum of Coheur was favored and delivered significant better results and lower residuals for the analysis of OIO and I_2.

NO_2

The favored cross-section for NO_2 was that of Bremen [*Voigt et al.* 2002] at 280 K or alternatively a cell reference. A cell reference was recorded several times during the campaign, by using the shortcut system of the DOAS instrument and a quartz cuvette containing 1.5% NO_2 . Convolution of the cross-section was done with a mercury or neon line. This projection on a small part of the PDA is called the apparatus function assuming a homogeneous PDA. To record the reference spectrum with the same instrument as the atmospheric spectrum has therefore the advantage of the same PDA sensitivity structure. However to retrieve the absolute cross-section the cell reference has to be scaled to a known spectrum.
For the campaign in Brittany the differences between the cell and the Bremen reference were minor due to a well homogenous PDA, and the Bremen reference was utilized.

OIO

The uncertainties regarding the OIO literature cross-sections are very high. In literature the absorption cross-section for OIO at 548.6 nm and a spectral resolution of ∼1 nm is given to be between $(1.09 - 2.7) \cdot 10^{-17} cm^2/molec$, as reported by *Himmelmann et al.* [1996], *Ingham et al.* [2000], *Cox et al.* [1999]. In this work, the cross-section of *Bloss et al.* [1998] as indicated in Table 3.3 was used, which is in good agreement to recent measurements by *Spietz and Gomez* [2004], of the university of Bremen .

3.4.4 Convolution

Resolution and wavelength pixel mapping of the reference spectra has to be adjusted to that of the atmospheric spectra. This was already introduced in Section 3.1.2. To simulate that, the high resolution literature cross-sections have to be convoluted with the respective instrumental function. The instrumental function is approached by a mercury or neon reference spectrum. The convolution process was done with the software *WinDOAS* and for tests as well with *DOASIS*. The results of the convoluted spectra with the different software tools do not show significant differences. For OIO, I_2 and O_4

the differences are smaller than 1%. For NO_2 the distinctions raise up to 1.5% maximum in the peaks of the spectra and for H_2O up to 2%.

3.4.5 Systematic Errors

The errors of DOAS measurements is a composition of instrumental and statistical errors. The instrumental error describes all errors made by the recording of the spectra, whereas the statistical error is made by the analysis. The following systematic errors have to be encountered:

- Uncertainties and errors of the literature cross-sections. Usually the differential absorption cross-sections have errors below 15%. More problematic are especially cross-sections of the iodine oxides, OIO and IO since their absolute cross-sections for the main band reported in literature vary significantly.

- Convolution process and insufficient accuracy in wavelength-pixel mapping can cause errors up to 1-3%

- The systematic error of the DOAS spectrograph was determined by *Stutz* [1996] to be smaller than 3%

- Errors made by determining the length of the lightpath can be neglected, as besides modern and precise global positioning systems (GPS) a laser distance instrument was used. The error of the laser distance instrument is given to be in the order of centimeters, whereas the length of the lightpath is in the order of kilometers.

3.4.6 Effects of Residual Structures

A common problem in the evaluation of DOAS spectra is due to the occurrence of structures others than noise in the residuum of the fit. These structures may indicate unknown absorbers or caused by the instrument itself and occur randomly in most of the cases. Stable residual structures cause systematic errors in the analysis which cannot be described by statistical methods. First the question arises how these residuals can be described. In a pure noise spectrum the width of any structure is usually only one pixel, thus indicating the independence of the pixel intensities. In residuals, groups of neighboring pixel intensities appear to change simultaneously in a random way. Therefore it can be suspected that the errors of these pixel intensities are not independent from each other. A way of simulating this would be

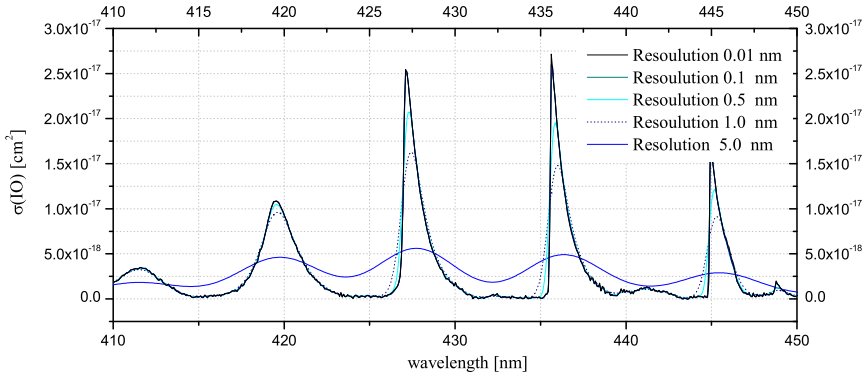

Figure 3.12: *The cross-section of Hönninger [1999] convoluted with gauss functions of different FWHM. Increasing the resolution of the recorded spectra results in an increase of the absolute value of the cross-section.*

smoothing, e.g. by a running mean, a pure noise spectrum. In a running mean every pixel intensity is replaced by the average of its neighboring pixel intensities. Therefore the errors of the individual pixel intensities are no longer independent from each other. Smoothed noise spectra look similar to residuals normally found in the analysis of atmospheric spectra. Therefore the assumption of independence of the errors appears to be invalid. This is also the case if measured spectra are smoothed in some way prior to the fitting procedure, as it is common to reduce noise. However, the statistical error for the derived concentrations can be determined from the random structures of the residual according to *Stutz and Platt* [1996] and *Stutz* [1996]. Within the fitting process a statistical error is determined for every reference spectrum adapted and stated as a 1σ-error. This error takes into account the number of absorption bands, the intensity of the analyzed spectrum and more related quantities as uncertainties in the wavelength-pixel mapping. This resulting 1σ-error underestimates the realistic error and must be corrected by multiplication with a factor. The factor was considered to be 3 for all absorbers evaluated in the 500 - 600 nm wavelength range, as large structures, caused by insufficient correction of water absorption structures and variable lamp features remain in the residual. To estimate a realistic error for absorbers in the wavelength range of 400 to 500 nm the factor was

considered to be 2. This simple approximation given above simplifies the problem, but for exact computation of the detection limit for DOAS a more detailed study comprising the shape of the absorption structure and specifics of the instrument has to be done. Apart from the algorithm used by *Stutz and Platt* [1996], *Hausmann et al.* [1999] supposed a Monte-Carlo algorithm to compute the detection limits with respect to the fitting algorithm and the residuals. However, systematic errors due to unknown absorbers, so-called X-absorbers or stable residuals can be partially corrected for by fitting a typical residual or the mean residual of a series of spectra to the single spectra. If this technique is applied with care, it partially corrects the systematic errors and instrumental effects and therefore decreases the detection limits. A more in-depth analysis of the residuals can be done by a principle components analysis algorithm applied to the DOAS retrieval as suggested by *Ferlemann* [1998]. As the more sophisticated algorithms both require lots of computation time, they seem unsuitable for the huge amounts of data that accumulate during several extensive field campaigns. Therefore, the method of *Stutz and Platt* [1996] has been applied.

3.4.7 Detection Limit

The detection limit is dependent on the statistical error. Commonly the detection limit is given as the 2σ-error, but as described above that leads not to a realistic error or detection limit. Therefore the detection limit for all absorbers evaluated in this work, is given as the 1σ-error multiplied with the respective factor, resulting from the estimations with the analyzed residual structures in the different wavelength ranges. The statistical error is clearly varying with every single spectrum and is therefore not constant in time. Furthermore different lightpaths are used depending on visibility and weather conditions. The concentrations of the trace gases, as well as the statistical errors, are calculated by dividing the fitcoefficients by the length of the lightpath. This leads to a negative correlation of the detection limit with the lightpath. Additionally the signal-to-noise ratio is higher at high atmospheric visibility, leading to short integration times. That reflects that the statistical errors for measurements on the short lightpaths are generally higher.

3.5 Fitting Procedure and Retrieval of Trace Gas Concentrations

The non-linear least squares fit is performed by the software *WinDOAS*, to achieve the trace gas concentration along the lightpath. The mathematical description of the fit is explained in Section 3.1.2 and within this Section the chosen parameters for the different fitscenarios are described, which were used to retrieve the final concentrations for the RHS. Prior to evaluation, all spectra were corrected for the offset by subtracting an offset spectrum, weightened by the numbers of scans. The dark current and background was corrected weightened by the respective integration time of the spectra. A high-pass filter was applied on the spectra to remove the broad-band structures due to scattering processes and broad-band absorption. This was not needed for the MCT spectra, as they are already divided by broadbanded *sumspectra* (see Section 3.4.2).

3.5.1 Analysis Procedure BrO

The evaluation range was set to 323-352.5 nm, including 6 vibrational transitions of the A $^2\Pi_{3/2} \leftarrow X^2\Pi_{3/2}$ of BrO transitions to provide a clear spectral identification. Besides the lamp spectrum, a 5th order polynomial and cross-sections of O_4, O_3, NO_2 and HCHO (see references in Tab. 3.3) were applied. Shift and stretch was allowed in the fitscenario for ozone, as it is the strongest absorber. The resulting shift and stretch was then applied to the weak absorbers HCHO, NO_2 and BrO. Consistency tests of the results were performed with ozone and NO_2 (see Chapter 5.2.2). The resulting ozone concentration showed excellent agreement to that of the additionally operated in-situ monitor, the result of this comparison is shown in Figure 5.13 during the 2003 Brittany campaign. The sampling time of the in-situ instrument was set to 5 minutes, which is also the time scale of the DOAS measurements. Consistent results were also achieved for NO_2 analyzed in the UV region with that of the visible wavelength range (418-440 nm) of the IO analysis.

A sample evaluation is given in Figure 3.13. The absorption structure of BrO is comparable to the residual an unambiguous detection of BrO was therefore not possible.

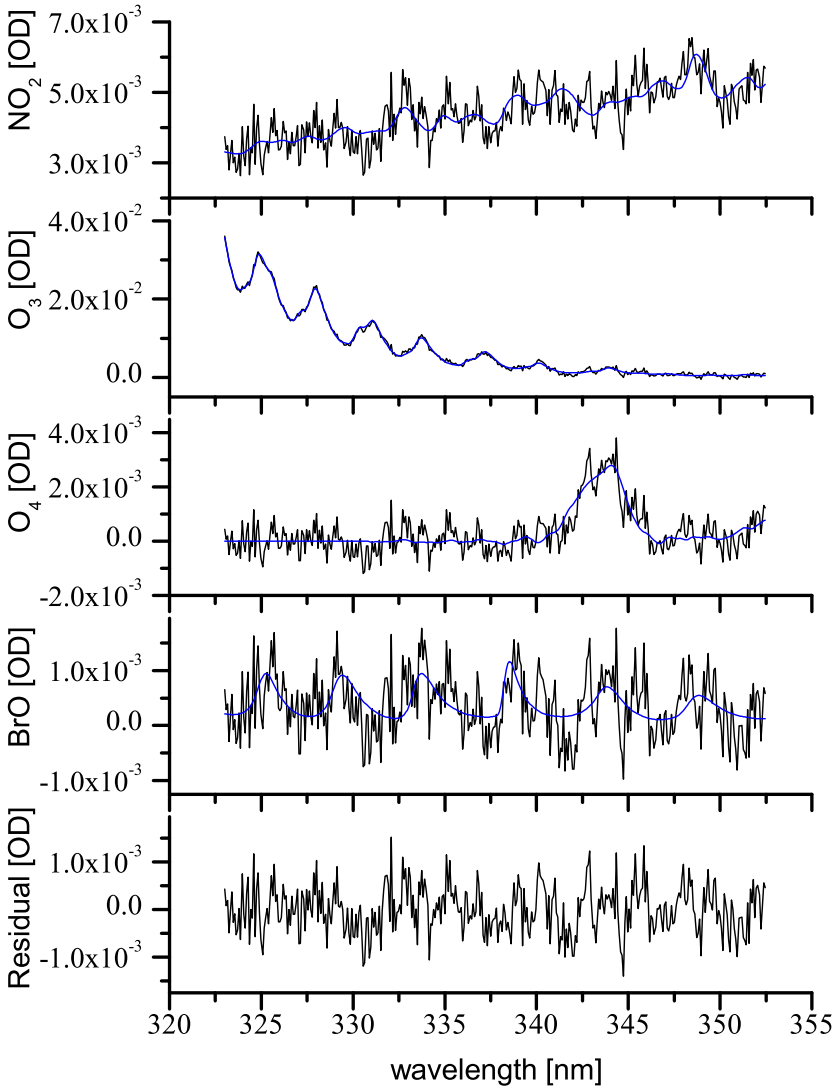

Figure 3.13: *Sample evaluation of the BrO evaluation, the spectrum was taken on 2nd June 2003 09:46 GMT, during Brittany campaign . The absorption structures of BrO were not clearly identified above the residual, even if there is some evidence for it in this example. The corresponding BrO concentration for the lightpath of 18.94 km is 1.45±0.88 ppt.*

3.5.2 Analysis Procedure IO

IO was analyzed between 418 and 440 nm, where three of the strongest absorption bands (3-0, 4-0, 5-0) of the electronic transition $A^2\Pi_{3/2} \leftarrow X^2\Pi_{3/2}$ are found. The strong 2-0 band was excluded to avoid conflicts with overlapping water vapor absorptions and broadened lamp structures in the range of 440-450 nm. The cross-section of *Hönninger* [1999] recorded with a resolution of 0.09 nm and $\sigma_{diff}(427.2nm) = 2.6 \cdot 10^{-17} cm^2$ of the 4-0 transition band was applied, besides NO_2 (see Table 3.3). For the removal of spectral lamp features a daily recorded lamp spectrum was fitted as well.
The software *WinDOAS* [*Fayt and van Rozendael* 2001] was used to perform a non-linear least squares fit, by adjusting simultaneously the IO, NO_2 and lamp reference in addition to a 5th order polynomial to the atmospheric spectra.
In Figure 3.14 a sample evaluation of June 5th 2003 in the afternoon gives an overview on the spectral identification of IO. The presented spectrum corresponds to a concentration for IO of 2.99±0.2 ppt, which demonstrates the clear identification of three IO absorption bands already at moderate levels.

3.5.3 Analysis Procedure I_2, OIO

I_2 and OIO were evaluated in the range of 530 to 568 nm to provide good spectral identification but to avoid greater conflicts with highly varying structures caused by the used light source. O_4, NO_2 , OIO and I_2 cross-sections (references in Table 3.3) were applied to the fit scenario. The shift and squeeze is allowed for all fitted species but linked together for all atmospheric absorbers, except O_4. The lamp reference was treated individually, with no restrictions on shift and squeeze. A sample evaluation of October 5th 22:07 GMT is illustrated in Figure 3.15. 16 absorption bands of I_2 could be clearly identified.
Water absorption structures are present over major parts of that wavelength range. Due to uncertainties in the available data bases, the removal of water absorptions in the spectra is partly insufficient and causes high residual structures (see Section 3.4.3). Additionally temporarily varying structures caused by the operated high pressure lamp of the type PLI have to stated. Since these structures vary temporarily, the remaining structures in the residual are not stable or in a simple way to interpret as an instrumental effect. For these cases the method described by *Stutz* [1996] yields a factor of ∼3 to estimate the realistic error from the fit error.

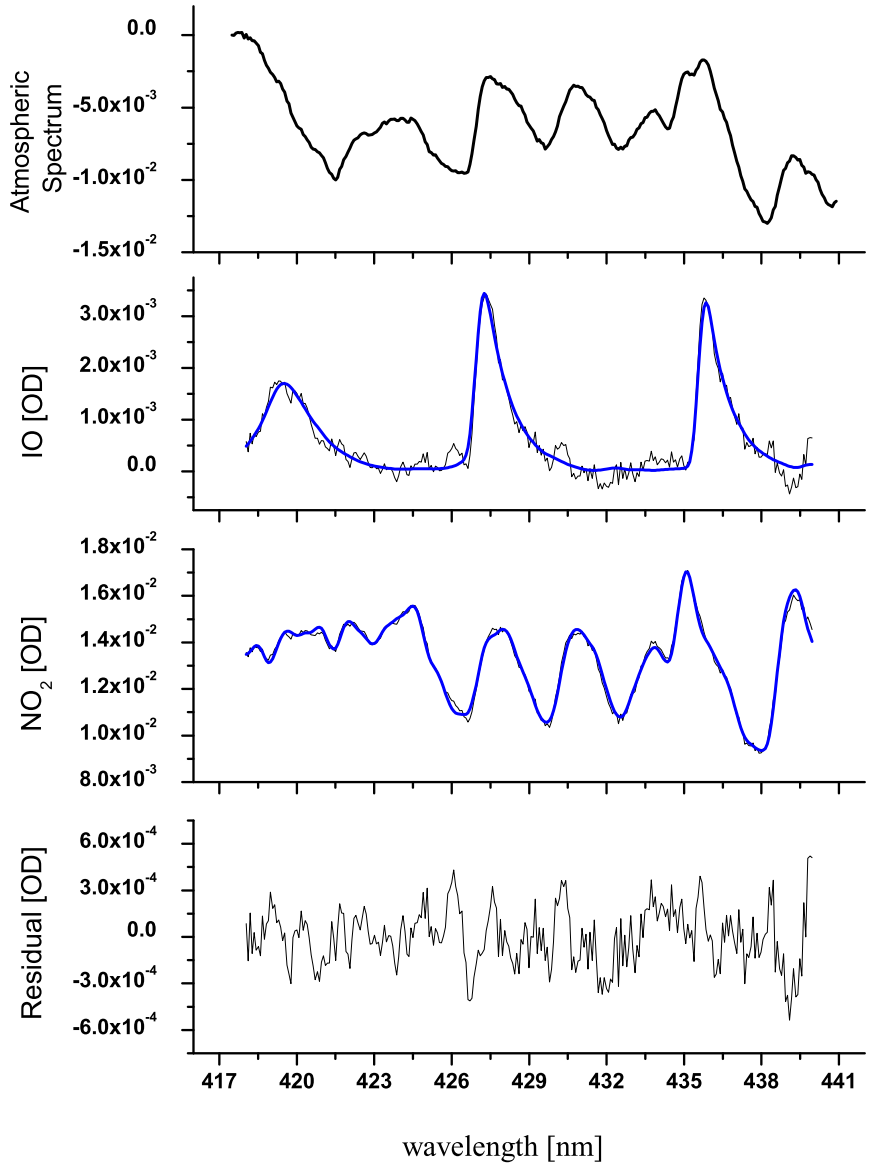

Figure 3.14: *Sample evaluation of IO. The spectrum was taken on June 5th 2003 at 16:00 GMT. IO is clearly identified and the concentration corresponds to 2.99±0.2 ppt assuming a lightpath of nearly 19 km. The residual has a peak to peak noise of* $1.06 \cdot 10^{-3}$ *and does not show any regularly structures.*

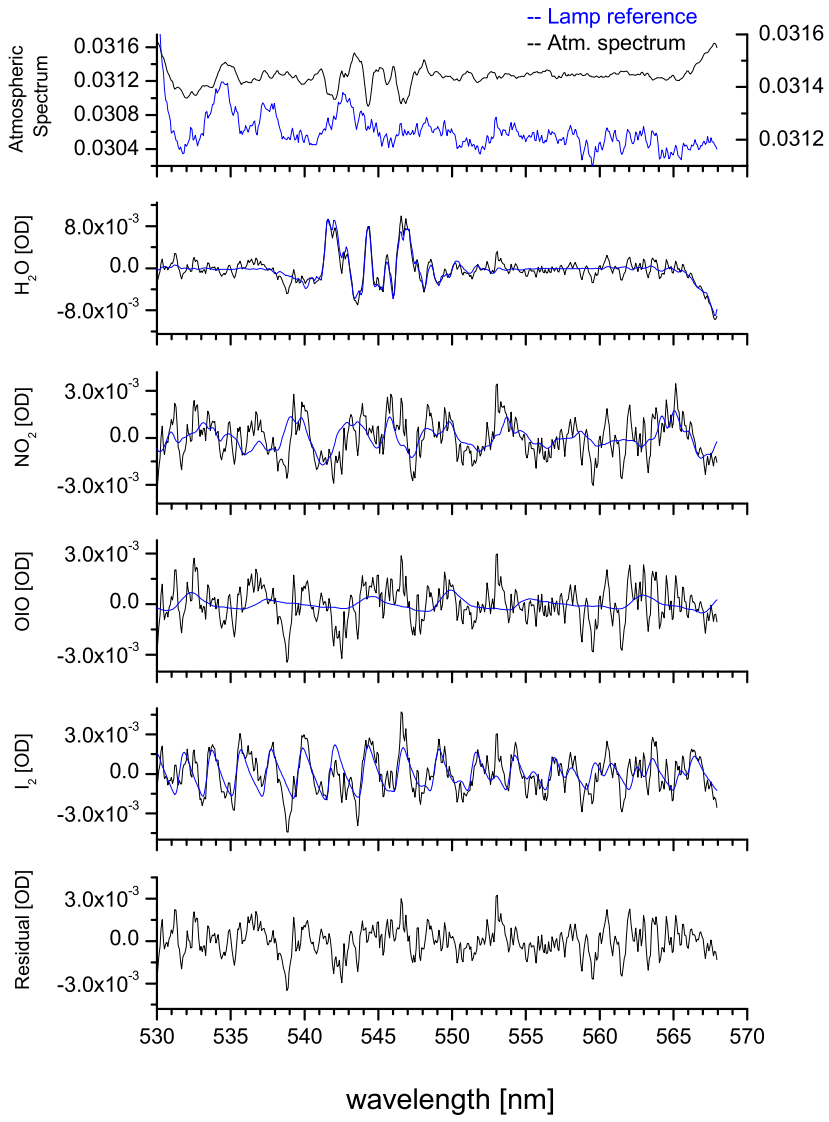

Figure 3.15: *Example for the spectral identification of I_2. The spectrum was taken on October 5th 1998 22:07 GMT during the PARFORCE campaign in Mace Head. The corresponding concentration of I_2 is 61.29±9.36 ppt, and for OIO 5.70±3.19 ppt.*

3.6 Measurements of Organohalogens with GC/ECD-ICP-MS

During the field campaigns described in this work, organohalogens as potential precursor species for RHS in the atmosphere were measured by the GC/ECD-ICP-MS technique. These measurements were performed by the group of Heumann et al. of the university of Mainz. A very brief overview on this technique is given here.

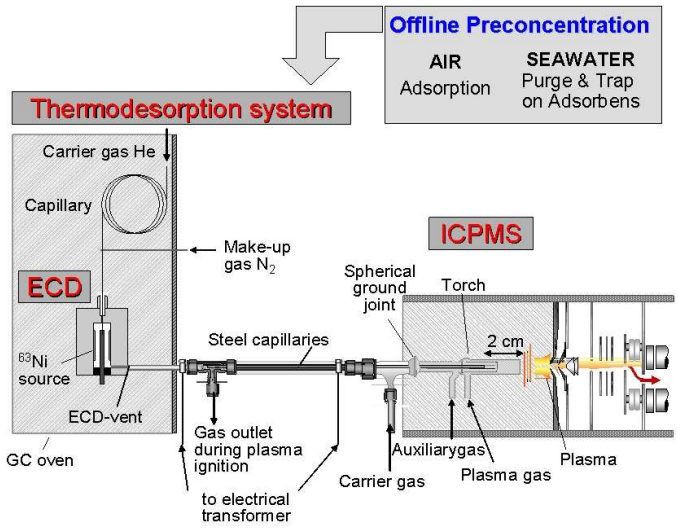

Figure 3.16: *Schematic overview on the GC/ECD-ICP-MS, which is a highly sensitive detection method for halogenated hydrocarbons.*

The detection of organohalogens was realized by an GC/ECD-ICP-MS (Electron capture detector on-line coupled to an inductively coupled plasma mass spectrometer). Since the detection system is not mobile, air and water samples were taken at the campaign site and analyzed at a later date in the laboratory in Mainz. The air sampling was carried out by adsorption on carbosieve SIII or carboxen in the field and subsequent thermal desorption of the analytes into a cold trap in the laboratory. After the cryo-focusing procedure the VHOCs were separated in a capillary column and determined by an electron capture detector (ECD) on-line coupled to an inductively coupled plasma mass spectrometer (ICP-MS). For the analysis of chlorinated and brominated compounds ECD is a highly sensitive method, but for io-

dinated compounds the ICP-MS has the advantage of element specific detection, which is especially important for the identification of unknown and coeluating chromatographic peaks. A schematic overview on the GC/ECD-ICP-MS system is given in Figure 3.16. The system is described in full detail in the Ph.D. thesis of *Schwarz* [2003].

Chapter 4

Dagebüll, German North Sea Coast

Within the ReHaTrop project, which is part of the German AFO2000 (Atmospheric Research Program) program, all in all three field campaigns were conducted to investigate the appearance and distribution of RHS in mid-latitudinal regions. Two of the three campaigns were conducted in the marine environment, the first one in 2002 at the German North Sea Coast and the second one in 2003 at the French Atlantic Coast. These two coastal measurement sites differ significantly in their biological activity, but show similarities in the NO_x pollution in the respective atmospheres.
During both field campaigns organohalogen measurements by GC/ECD-ICP-MS were made by the collaborating group of Heumann et al. of the University of Mainz. Organohalogens are presumed as an important precursor species for reactive halogen species in the atmosphere and the correlation of organohalogens, especially the short lived species with RHS was an important scientific question within the ReHaTrop project.
In the following a detailed description of the measurement site in Dagebüll, German North Sea Coast and a short overview on the acquired results is given. The discussion of yielded results is linked to the results of the second campaign in Brittany 2003, which is foremost detailed described in Chapter 5.

4.1 Description of the Measurement Site

The campaign was conducted between April 18th and May 17th in 2002 in Dagebüll (54.73 N, 8.69 E) at the German North Sea Coast at the Wadden

Sea. The campaign site is indicated in Fig. 4.1. The nature reserve Wadden Sea is the largest national park in central Europe, comprising a stretch of land affected by tides, flooded by sea water during high tide and remaining dry during low tide. The campaign took place in early spring and the generally stormy and rainy weather conditions were not supportively for the DOAS measurements, which requires good atmospheric visibility conditions. As well affected by the poor weather conditions was the nature, growing of plants, especially macroalgae started late in that year. Smaller populations of young macroalgae were only found in protected areas, as the water pool in 500 m distance (see location 2 in Fig. 4.1) described in Section 4.1.2. Hence, the biological activity observed during the campaign was relatively low, what is well demonstrated by the results of organohalogen measurements (see Table 4.1).

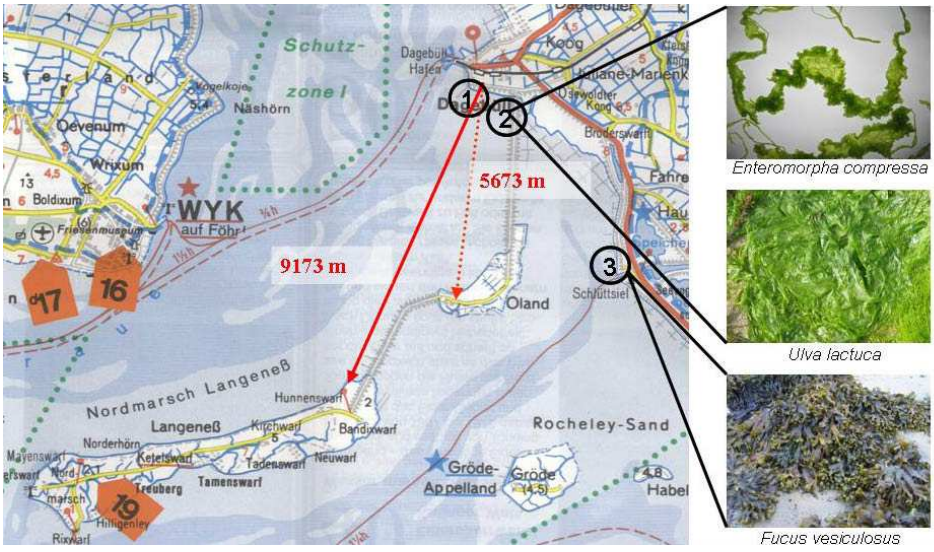

Figure 4.1: *The campaign site at Dagebüll, German North Sea Coast. The red arrows indicate the two lightpaths through the intertidal zone, which is represented by light blue color. The locations 1 to 3 indicate the sites, where organohalogen measurements were conducted.*

4.1.1 Supplementary Measurements and Meteorology

Besides the DOAS instrument, which was set-up in a mobile container, supplementary in-situ measurements of O_3 with the Horiba ozone moni-

tor (APOA-360, HORIBA Europe GmbH) and NO measurements with the ECO-Physics NO monitor (CLD 770 ppt) were conducted. Both monitors were installed inside the container and sampled air 30 cm above the the container roof (∼3 m height). To obtain information on number and size distribution of the aerosols an optical particle counter, (*PALAS*) was installed. Additionally to that equipment, a spectro radiometer was operated for retrieving further information on photolysis frequencies.
Meteorological conditions were measured with the Hoffmann Messtechnik weather station (HMT), to derive temperature, pressure, humidity, wind direction, wind speed and solar radiation.

The HMT weather station was set up in the direct neighborhood of the container, on the top of the dyke. An overview on the meteorological conditions is given in Figure 4.2. For the purpose of comparison a data set of the meteorologic service of Wittdün was provided. Wittdün is located on the island Amrum in ∼6 km distance to the measurement site. The weather record of the meteorologic station of Wittdün shows reasonable agreement to the data taken with the HMT weather station.

4.1.2 Organohalogens

To determine the impact of the appearance of macroalgae on VHOCs, air samples for the GC/ECD-ICP-MS analysis (see Section 3.6) were taken at mainly three different locations, as illustrated in Figure 4.1. Several air samples were taken close to the DOAS instrument (30 m) at location 1, within the intertidal zone during low tide above sandy ground but with no macroalgae in the vicinity. The majority of air samples were taken at a small water pool in 500 m distance (location 2) to the DOAS instrument. This pool was not influenced by the tide, what means it was not regularly flooded in times of high tide, but during springtide and stormy conditions. Due to this a small population of green algae (see photos on right side of Fig. 4.1) could grow in this protected area. A small population of the common macroalgae fucus vesiculosus inhabited a part of the coast line 3 km away of the DOAS measurement site in Schüttsiel (see location 3 in Fig. 4.1). Few air samples were taken there. The resulting concentrations by the GC/ECD-ICP-MS analysis of air samples is shown in Table 4.1.

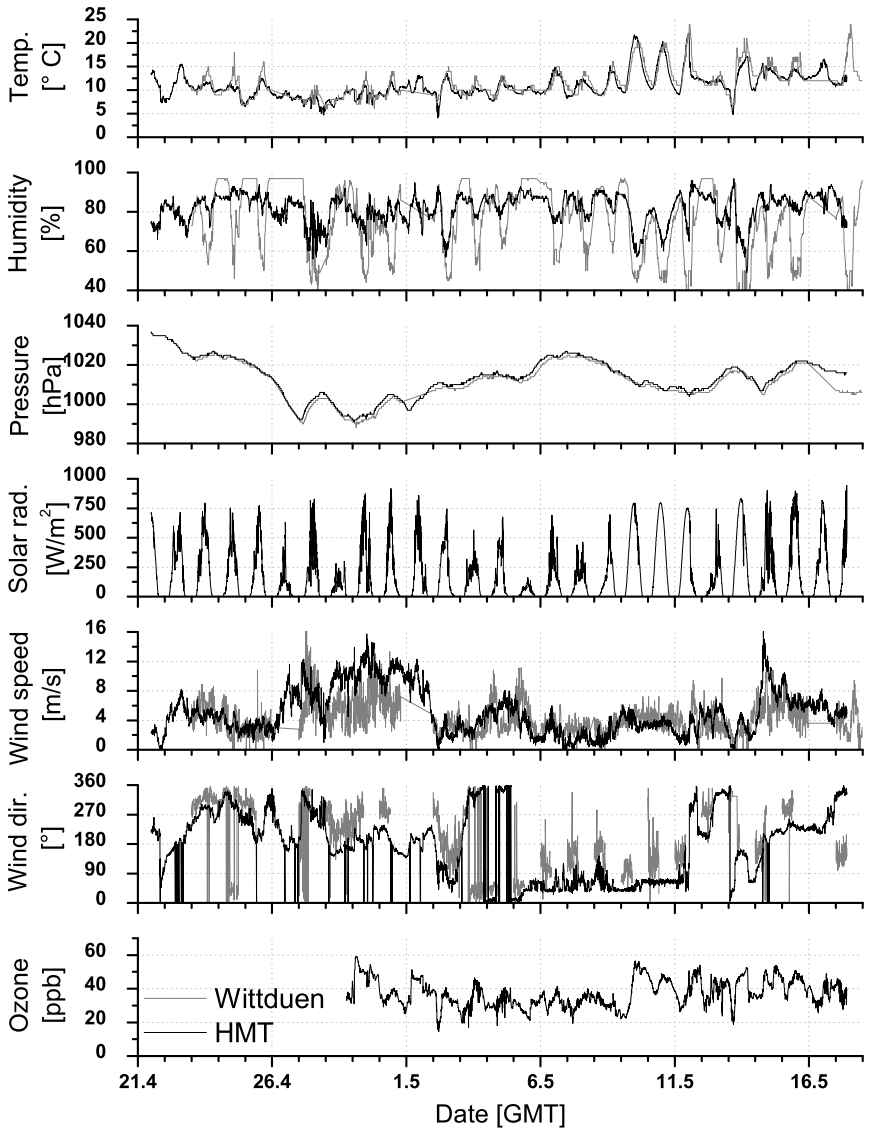

Figure 4.2: *The meteorologic conditions during the 2002 North Sea campaign. Black lines indicate measurements with the HMT weather station operated directly at the DOAS measurement site. Indicated in grey is data provided by the meteorological service of Wittdün on the island Amrum in ∼6 km distance.*

Species Air samples [*pptv*]	**Lilia** Brittany *this work* 2003	**Brest** Brittany *Pruvost* 2000	**Mace Head** Ireland *Carpenter et al.* 1999	**Dagebüll** North Sea *this work* 2002	**Gran Can.** Can. Isl. *Ekdahl et al.* 1998
CH_3I	7.6 - 1830	5.7 - 386	0.1 - 1.5	4.7 - 23.5	24 - 84
C_2H_5I	2.22 - 96.9		0.02 - 1.2	0.3 - 0.7	
2-C_3H_7I	0.2 - 9.1			0.1 - 0.3	
1-C_3H_7I	0.35 - 34.8			0.01 - 1	
CH_2ClI	0.35 - 12.4		nd - 0.02	0.1 - 3	nd - 19
CH_2BrI	0.55 - 9.9			0.04 - 0.2	
1-C_4H_9I	0.84 - 321			0.2 - 1.1	10 - 89
2-C_4H_9I	0.12 - 12.3		0.02 - 0.3	0.02 - 0.1	
i-C_4H_9I	0.2 - 14.4			0.04 - 0.2	
CH_2I_2	0.11 - 19.8		0.02 - 0.4	0.3 - 3.1	
CH_3Br	12.2 - 875		9 - 26	3.1 - 23.2	
C_2H_5Br	11.3 - 865		0.1 - 0.5	0.3 - 1.8	
CH_2Br_2	2.36 - 262	1 - 12.1		0.4 - 2	37 - 340
$CHBrCl_2$	12.5 - 246	0.3 - 1.8		0.1 - 1.2	6 - 290
$CHBr_2Cl$	3.5 - 128.2	0.3 - 1.9	0.3 - 1.8	0.2 - 1.2	19 - 130
$CHBr_3$	10.5 - 393	3.8 - 58	2 - 16	1.1 - 11.2	500 - 2500

Table 4.1: *The concentration range of all continuously detected iodinated and brominated hydrocarbons is indicated for the 2002 North Sea and 2003 Brittany campaign. If comparable data was available the range of published data is given respectively. 'nd' means below the detection limit.*

Fingerprints and Impact of Macroalgae on Appearance of Organohalogens

Within incubation experiments performed with several macroalgae during the 2002 North Sea campaign, characteristic production patterns for different algae species were found. However, the general production pattern seems to be unique for different algae species, it is to note that the absolute

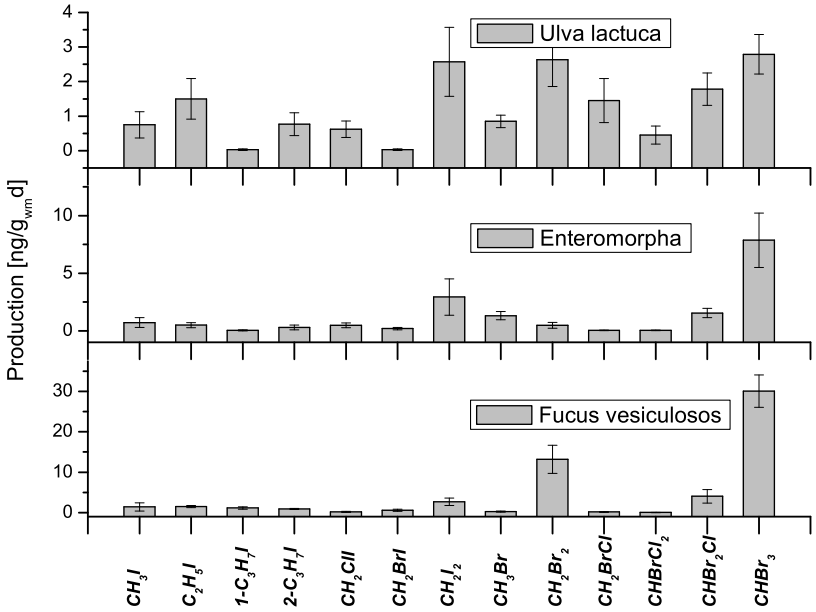

Figure 4.3: *Fingerprints of three different algae found at the German North Sea Coast. The data is averaged on several incubation experiments during 2001 and 2002 at the German North Sea Coast (adapted from Schwarz [2003]).*

production rate differed partly significantly between single incubation experiments, what may be explained by the observed impact of stress factors, as well as the biological state and age of the plant. In Figure 4.3 the resulting fingerprints of three different algae species, populating the German North Sea coast is shown.
These resulting fingerprints show remarkable agreement to organohalogen measurements taken at the three in Fig. 4.1 indicated locations, which were dominated by the respective type of macroalgae as can be seen in Figure 4.4. The comparison to the fingerprints resulting from incubation experiments shows the clear impact of macroalgae on the detected levels of organohalogens and indicates that the production pattern is characteristic for the individual algae species in their respective natural habitat.
During the campaign in 2002 a phytoplankton bloom was detected, and the emission rates of the organohalogens CH_3I and C_2H_5I increased closely

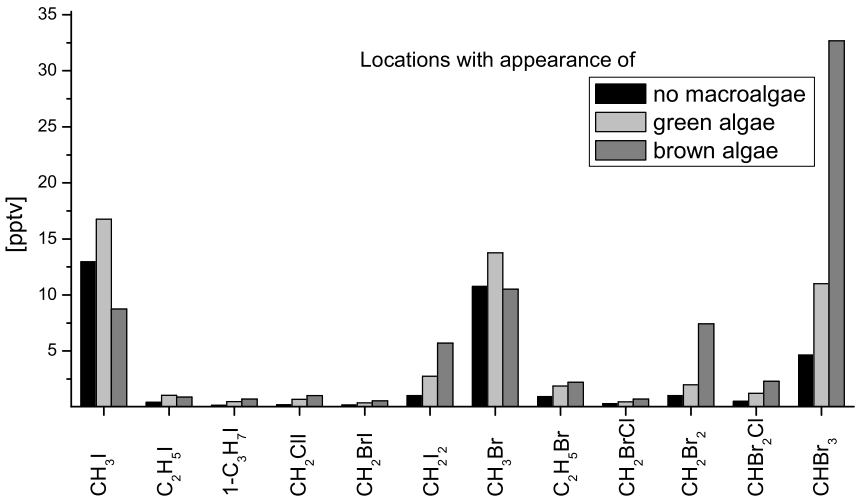

Figure 4.4: *Average concentrations of organohalogens in air samples taken at three different locations during the North Sea campaign (Dagebüll) in spring 2002. The shading of the bars indicates the type of algae found at the sampling site. Except for CH_3I and CH_3Br the concentrations are significantly lower if no macroalgae are present in the vicinity at the sampling site. (adapted from Schwarz [2003]).*

correlated to that. These elevated levels of CH_3I during a phytoplankton bloom was already reported before by *Oram and Penkett* [1994].

In Figure 4.4, CH_3I and CH_3Br show comparable concentrations at all of the locations, which can be easily understood by the long photolytic lifetimes of both species.

Open ocean source and the impact of microplankton on appearance of VHOCs was already indicated by estimations of *Carpenter* [2003], who found that seaweed production calculated from measured emission rates in conjunction with biomass estimates could not support the levels of CH_3I and CH_2ICl measured in surface coastal waters off the coast of Mace Head. That leads to their suggestion of additional marine sources for these compounds.

Species	*Av.D.L.*	*Min/Max D.L.*	*Av.conc.*	*Max conc.*
NO_2	0.02 ppb	0.01/0.05 ppb	1.9 ppb	8.10±0.02 ppb
O_3	2.8 ppb	1.8/23 ppb	37.25 ppb	59.3±2.6 ppb
IO	0.28 ppt	0.18/0.65 ppt	0.35 ppt	1.90±0.65 ppt
OIO	2.75 ppt	1.18/12.19 ppt	4.27 ppt	15.26±6.65 ppt
BrO	1.47 ppt	0.6/4.08 ppt	0.2 ppt	2.98±1.36 ppt

Table 4.2: *Overview on the resulting concentrations and detection limits of the 2002 North Sea campaign.*

4.1.3 Active Longpath DOAS Measurements

The active longpath DOAS telescope was the main instrument, operated to measure a variety of RHS and related species like ozone and NO_2. Therefore spectra were taken in the respective relevant wavelength regions: BrO (O_3, O_4, HCHO, NO_2) in the 335±40 nm (UV), IO (NO_2, H_2O) in the 430±40 nm and OIO (I_2, NO_2, H_2O) in the 550±40 nm (green) region. The schematic program flow diagram for the automated measurement is shown in Figure 3.11 in a slightly different way, since the MCT technique (see Section 3.3.6) was applied on all wavelength ranges not only for the 430±40 nm range as shown in Fig. 3.11, since only one halogen oxide could be identified.

Lightpath

The DOAS telescope was set up inside a mobile container positioned on the top of a dyke at few meters distance to the waterfront in times of high tide. The lightpaths were set up in a way that they pass completely over unflooded areas in times of low tide. In Figure 4.1 a map of the measurement site is shown, where the intertidal zone is indicated as the light shaded area and both lightpaths are indicated with red lines. One lightpath (drawn line) crossed the intertidal zone in just 3-7 m height to the small island Langeneß in 9170 m distance (total length 18.34 km) and the second one in the same height above the ground to the small island Oland in 5170 m (total length 11340 m) distance. The low height of the lightbeam above the ground turned out to be a source of significant lightloss. In times of low water a thick layer

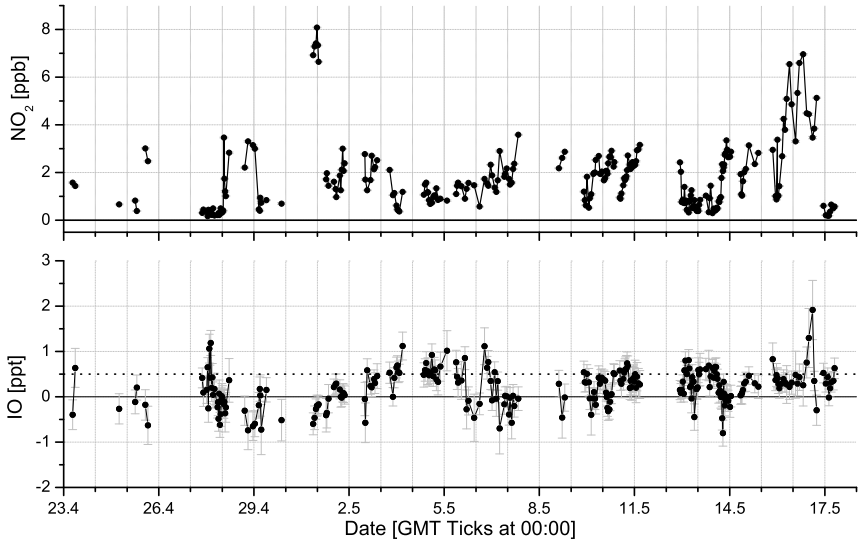

Figure 4.5: *The time series for IO and NO_2 for the 2002 North Sea campaign. The mean detection limit for IO was about 0.5 ppt (dashed line)*

of aerosols was observed closely above the intertidal zone attenuating the light throughput along the absorption path, the more detailed evaluation procedure for these species will be described in the next chapter, as it was identical to the Brittany evaluation.

4.1.4 Results of DOAS Measurements

The results of the RHS measurements during the 2002 North Sea campaign will be presented within the next subsections and will be included in the discussion of the results of the Brittany campaign.

Results of IO Measurements

The evaluation procedure for IO was introduced in Section 3.5.2. IO was the only identified halogen oxide during the North Sea campaign. The concentration exceeded rarely the mean detection limit of about 0.5 ppt. The maximal value during the campaign was found on 16th of May 2002 at midday,

but no correlation with the tidal height or any elevated levels of organohalogens was found. The generally low concentration of IO is in agreement with the results of measurements of the short-lived organoiodides since they are assumed to be the source for reactive iodine in the atmosphere. The complete time series for IO and NO_2 is shown in Figure 4.5.

Results of BrO, OIO and I_2 Measurements

Due to the low atmospheric visibility conditions during the campaign, only very few spectra in the UV range were accumulated and measurements of a connected time series were not possible. Furthermore BrO remained throughout the campaign below the detection limit of 1.47 ppt and could not be identified in the spectra.
An unambiguous identification of OIO and I_2 was not successful either. The respective detection limits are indicated in Table 4.2.

Chapter 5

Brittany, French Atlantic Coast

In this chapter a detailed description of the measurement site and the results of the Brittany campaign will be given. Prior to this a short overview for motivation choosing the Atlantic Coast in Brittany as an interesting measurement site is given.

Short-lived volatile halogenated organic compounds (VHOCs) like CH_2I_2 (photolytic lifetime in the order of minutes) are very likely precursors for reactive halogen oxides like IO, via the reaction

$$\begin{aligned} \mathrm{RI} &\xrightarrow{h\nu} \mathrm{R} + \mathrm{I} \\ \mathrm{I} + \mathrm{O_3} &\longrightarrow IO + O_2 \end{aligned}$$

The VHOCs are emitted by macroalgae and phytoplankton species in biologically active coastal sites, what could be demonstrated by the organohalogen measurements of the 2002 North Sea campaign.
The high bio-activity in Brittany is known and was impressively demonstrated by measurements of *Pruvost* [2001], who had measured a variety of organohalogens in the region of Brest, Brittany. The resulting concentrations of CH_3I, CH_3Br and other brominated and iodinated species were highly elevated and exceeded results of similar measurements in coastal regions (e.g. Mace Head, Ireland) up to several orders of magnitude (see Table 4.1).
Recent publications reported the detection of IO up to several ppt at bioactive coastal sites, e.g. *Alicke et al.* [1999], *Allan et al.* [2000], *Carpenter et al.* [2001]). These findings support that short-lived iodocarbons emitted

by algae are an important source for reactive iodine in the marine boundary layer.

Already 15 years ago Brauers and Platt [*Brauers* 1990] aimed the detection of IO in south of Brittany within two campaigns in July 1988 and June 1989. However, the spectral identification of IO was not successful at that time and *Brauers* estimated an upper limit for IO of $1 \cdot 10^7$ $molec/cm^3$ ($\sim$0.4 ppt). The apparent discrepancy of the observed bio-activity and the failure for the detection of the IO radical is still an open question, but will be shortly discussed in Section 5.2.1. To enlighten this matter a further campaign in the region of Brittany was of high interest and realized in 2003 within the ReHaTrop project.
The 2003 Brittany campaign and the results will be described in the following sections.

5.1 Description of the Measurement Site

The field campaign took place in Lilia at the French Atlantic Coast of Brittany from May 6th to June 13th 2003 to study the appearance of halogen oxides (BrO, IO, OIO), additionally I_2 and other related species like O_3 and NO_2. The LP-DOAS-instrument was set up at the port of Lilia (48.62 N, 4.55 W), 50 km north of Brest.
The Northwest of the French Atlantic Coast is characterized by a craggy coast line, influenced by cold water flows, a preferred habitat for macroalgae. Extended fields of a great variety of macroalgae were present all along the coast of Brittany (see Picture on right side of Figure 5.1).
The diversity of algae species ranged from green brown to red algae, e.g. *Laminaris, Fucus Vesicolosus, Ascophyllum Nodosum.* The agriculture of the algae has become an important part of the industry in Brittany and the region represents today one of the biggest exporters of algae products worldwide, with a crop of 75.000 - 80.000 t per year [*Ecomusée Plouguerneau* 2003].

5.1.1 Lightpaths for DOAS Measurements

The DOAS-telescope (detailed description in Chapter 3.2) was set up inside of a mobile container, which was positioned on a parking lot, just few meters to the waterfront in times of high tide. Two different lightpaths (see red arrows in Fig. 5.1) were set up in a way that the lightbeams passed in 10-14 m

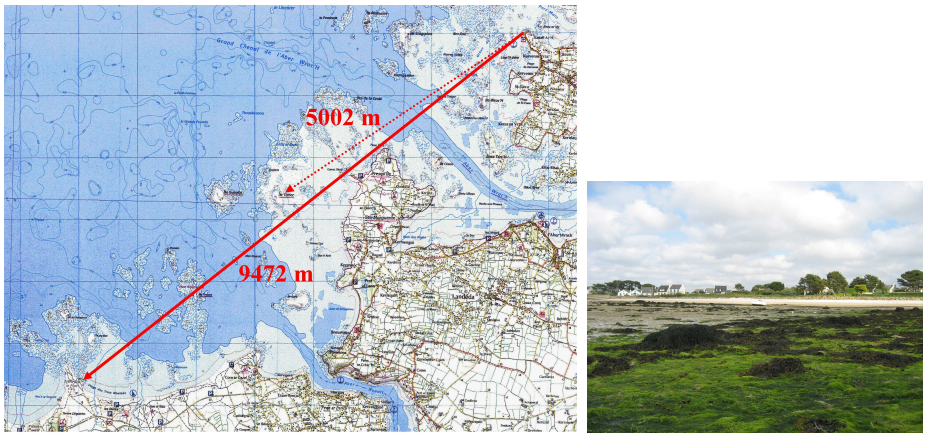

Figure 5.1: *The campaign site at Lilia (48.62 N, 4.55 W), French Atlantic Coast. The red arrows indicate the two light-paths along the coast. The intertidal zone is marked with white shaded areas. In these areas extended fields of macroalgae (right side) are exposed to ambient air at times of low tide.*

height above the intertidal zone. The mainly used lightpath was realized by setting up a retro-reflector-array consisting of 180 single reflectors in a distance of 9472 m, which results in a total length for the absorption path of 18944 m. For times of low atmospheric visibility a smaller array consisting of 50 reflectors was set up on a small island (Île Tariec) in 5002 m distance (total length 10004 m). In Figure 5.1 the white shaded areas indicate the intertidal zone, where the water is completely removed in times of low tide. About 60% of the long lightpath of 9472 m crossed the intertidal region, over macroalgae fields in times of low tide and 40% crossed over sea water. For the short lightpath (dashed line Fig. 5.1) the partitioning of intertidal zone to sea water was about 7:3.
The tide in Brittany is very pronounced , the water level reaches differences up to 14 m, what represents the highest tidal range in Europe. During the field campaign in 2003 the tidal range was about 7.5 m in maximum at the measurement site of Lilia.

5.1.2 Meteorological Conditions and Supplementary Measurements

Measurements of meteorological conditions were made with the Hoffmann Messtechnik weather station (HMT), to derive temperature, pressure, humidity, wind direction, wind speed and solar radiation. Additionally a Sonic Anemometer, Metek USA-1 was installed to retrieve detailed information on the wind profile. Both stations were positioned in the direct neighborhood of the container, which was equipped with the DOAS telescope.
Furthermore in-situ measurements of ozone were performed with the HORIBA ozone monitor (APOA-360, HORIBA Europe GmbH) and NO measurements with the ECO-Physics NO monitor (CLD 770 ppt). Both monitors were installed inside the container and sampled air 30 cm above the the container roof ($\sim$3 m height). To obtain information on number and size distribution of the aerosols an optical particle counter (PALAS) was installed.

The measurement site was situated in the north-west of Brittany, directly at the Atlantic Coast. The air masses reaching the site came mainly by south-westerly flows from the open Atlantic. A representative 120 hours backward trajectory is shown in Figure 5.3. Just one week (May 27th - June 1st) of the campaign was strongly influenced by easterly flows, when highly polluted air masses were transported over land to the site. Within this timeframe the measurements were strongly disturbed by low visibility and hazy conditions, that even on the short light path the signal of the returning light was too weak for receiving a sufficient signal to noise ratio of the DOAS measurements. However, clean air was most of the time transported by westerly flows to the site, a not negligible pollution by NO_x species has to be accounted for (see Fig. 5.12). A mean NO_2 concentration of 0.98 ppb with peaks of up to 7.5 ppb have been detected.
An overview on the general weather conditions is given in Fig. 5.2. The temperature remained very stable during the whole campaign, with only few peaks and drops as can be seen in the first panel of Fig. 5.2. The temperature averages in 13.5$\pm$2°C with a minimum of 7.7°C and a maximum of 21.5°C. As it is usually the case for coastal sites the wind speed was relatively high with an average of 3.2 m/s, with some stormy periods, when the wind speed rose up to 13.9 m/s. The frequency distribution of the wind direction is illustrated in Figure 5.3. The campaign took place close to the summer solstice, with an average of sunlight hours (SZA$<$ 90°) of 15.5hours.

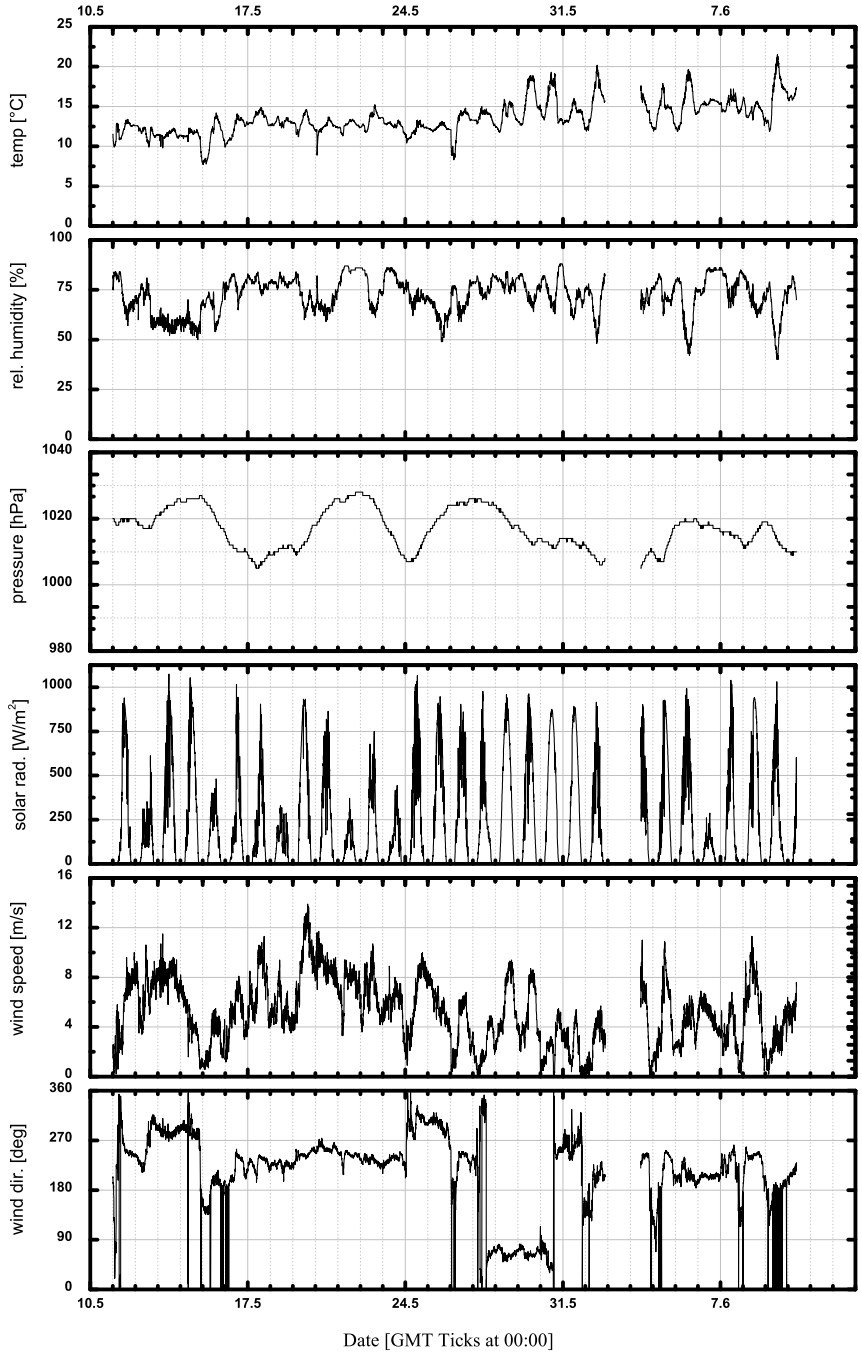

Figure 5.2: *Overview on the meteorological conditions during the campaign. The data were retrieved by a Hoffmann Messtechnik weather station operated next to the DOAS measurement site.*

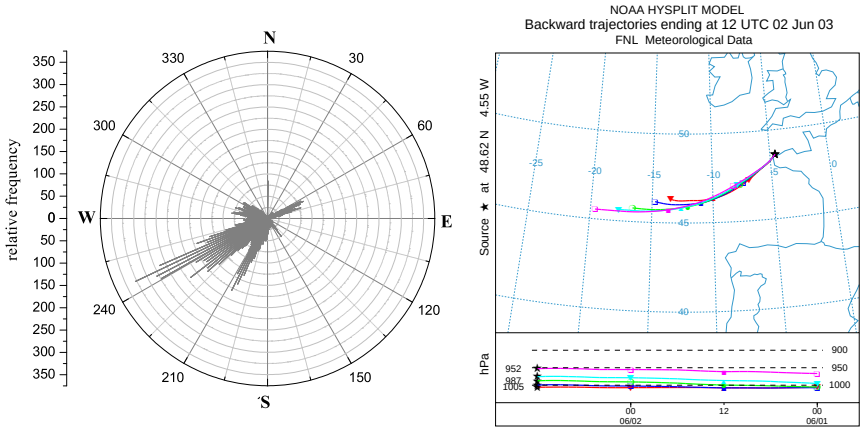

Figure 5.3: *Left: Relative frequency distribution of the wind direction during the Brittany campaign in intervals of 1°.*
Right: A representative 120 h backwards trajectory for the 2003 Brittany campaign of June 2nd.

5.1.3 Measurements of Organohalogens

Within the framework of the project this campaign (as well as 2002, North Sea Coast) was supported by a organohalogen measurements by the group of Heumann et al. of the Institute of Inorganic and Analytical Chemistry of the University of Mainz, see Section 3.6. Since the impact of macroalgae could be demonstrated by the data taken during the 2002 North Sea campaign, the location for taking air samples was fixed to one single position. That means that the measurements of RHS and VHOCs were co-located and all air samples were taken next to the DOAS instrument to achieve a better correlation of the appearance of organohalogens with the RHS measurements. The detected concentration ranges of the organohalogens are summarized in Table 4.1, besides the data for the German North Sea Coast. Data from two other coastal regions (Brest and Gran Canaria) is indicated whenever reported measurements were available.
The detected species show significantly elevated levels for the measurement site in Lilia (Brittany) what can be seen in Figure 5.4, where the average and maximal detected concentration of iodocarbons at three measurement sites (North Sea, Brittany and Mace Head) are compared. In several cases (e.g. CH_3I, CH_3Br) the observed levels exceed that of other coastal regions of up to two orders of magnitude, demonstrating the outstanding biological activity of Brittany.

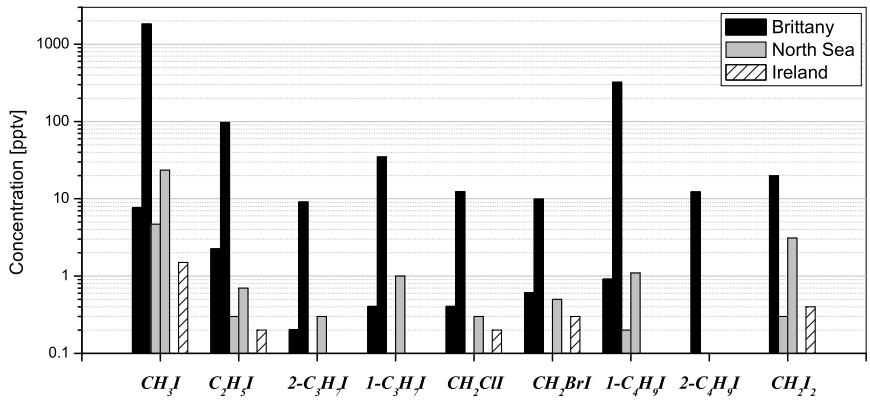

Figure 5.4: *Diagram for different iodinated VHOCs at three different coastal sites. For each location the average and maximal detected concentrations is indicated. Note the logarithmic scale.*

5.2 Active LP-DOAS Measurements

The main measurements were performed with an active longpath DOAS telescope. The detailed instrumental setup is explained in Chapter 3.2. The spectra were recorded alternating in the near UV (335±40) nm, Blue (430±40) nm and Green (550±40) nm wavelength range. The program flow diagram in Figure 3.11 gives a schematic overview on the automated measurement routine.
In dependence on weather conditions and visibility the measurement routine was regularly optimized. Especially measurements in the near UV are not generally possible over a light path of ∼10 km, because of the low light intensities. Therefore measurements in this wavelength range were skipped in favor of good time resolution for the IO, OIO and I_2 spectra (center wavelength 430 nm and 550 nm), during times of low atmospheric visibility. The MCT technique (detailed description in 3.3.6) was applied to the measurements in the 430±40 nm range during daylight conditions as indicated in Fig. 3.11.

An overview on the appearance and the maximal detected concentrations during the 2003 Brittany campaign is shown in Table 5.1.

The Brittany campaign in 2003 was focused on the detection of IO and BrO in the MBL, but as explained above the main part of the campaign time was scheduled for measurements of IO, combining the MCT technique and the conventional method.
The DOAS measurements were continuously conducted during day and night and the time series for all evaluated species of the 2003 Brittany campaign is given in Figure 5.5.

5.2.1 Results of the IO Analysis

The particular description of the IO analysis and an example for the spectral identification of IO is already described in Section 3.5.2.

Species	*Av.D.L.* [ppt]	*Min/Max D.L.* [ppt]	*Av.conc.* [ppt]	*Max conc.* [ppt]
NO_2	30	10/130	$0.98 \cdot 10^3$	$(7.48 \pm 0.04) \cdot 10^3$
O_3	1230	717/4653	$42.67 \cdot 10^3$	$(88.89 \pm 5.01) \cdot 10^3$
IO	0.23	0.13/0.96	0.73	7.7 ± 0.5
BrO	1.35	0.72/4.71	0.75	3.99 ± 1.30
OIO	2.46	0.69/5.80	-0.24	13.3 ± 3.3
I_2	10.15	2.84/23.95	-0.76	23.29 ± 10.6

Table 5.1: *Overview on the resulting concentrations and detection limits of the 2003 Brittany campaign. The average, the minimal and maximal value of the detection limit (D.L.) and the concentration (conc.) for each evaluated species is given.*

During the 2003 Brittany campaign the highest concentration of IO of about 7.7 ± 0.5 ppt was detected. The maximum of about 8 ppt was reported as well by measurements of previous campaigns in Mace Head (*Alicke et al.* [1999], *Carpenter et al.* [2001]). Hitherto the appearance of IO was reported mainly from coastal sites (see Table 2.1), where biogenic sources for reactive iodine in the gasphase can be assumed.

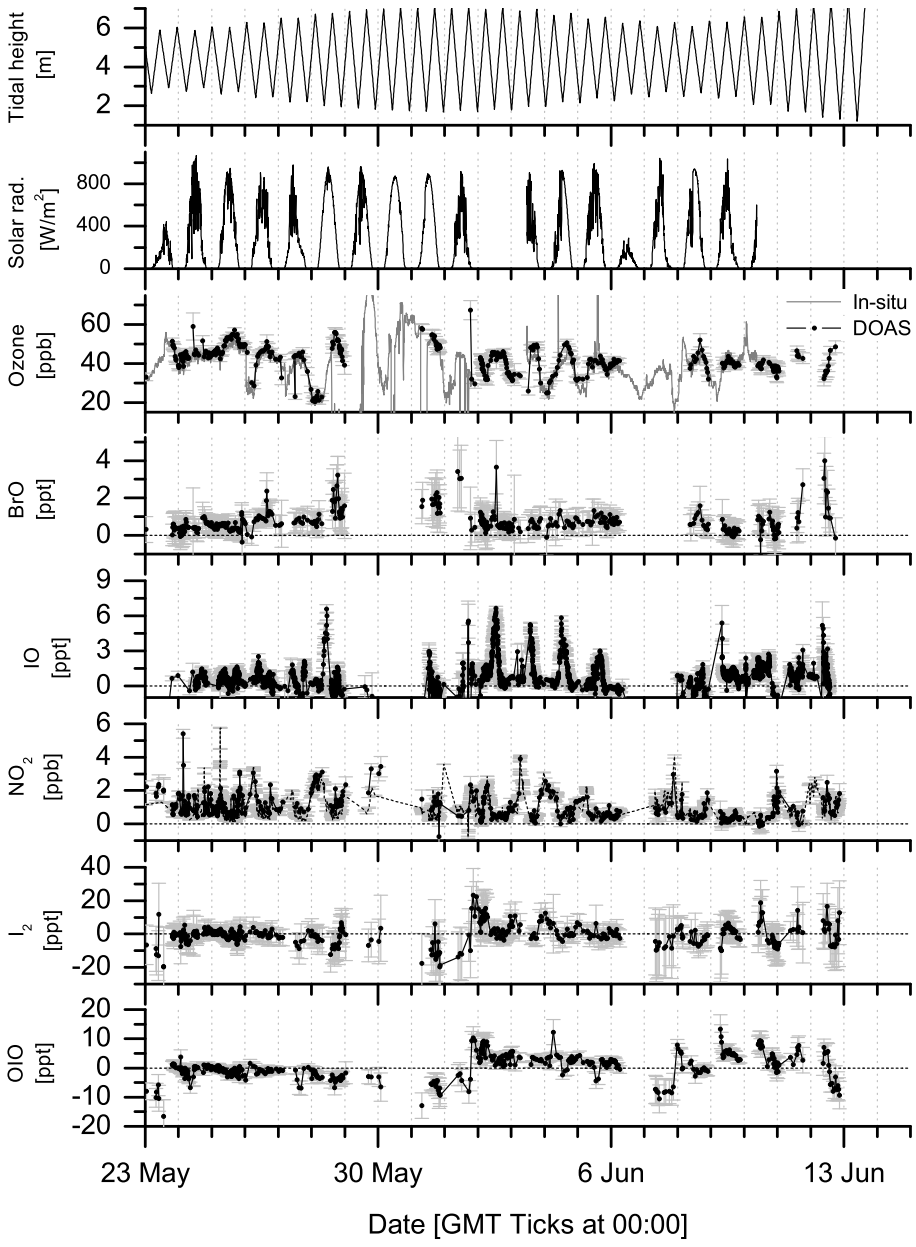

Figure 5.5: *The time series for the RHS compounds, NO_2 and O_3 of the campaign in Lilia, Brittany during May and June in 2003. Both I_2 and OIO could not be identified above their respective detection limits.*

Small amounts of the IO radical of up to 1.0 ppt have been found during times of high tide, but since the water level in Brittany is very distinct and the coastal line very craggy, a complete coverage of the algae was never assured. Hence, a possible open ocean source for reactive iodine can not necessarily be inferred from these results. However, the data set demonstrates clearly that macroalgae, exposed to the atmosphere are the main contributors for reactive iodine in the lower atmosphere.
That is comprehensible to see by a closer look at a sequence of the time series recorded in May between 24th - 28th, which is shown in Figure 5.6 in the upper panel. High tide occurred at the hours of midday. The IO peaked two times a day and showed a minimum on midday. The peaks coincided with low tide, when the area of uncovered algae increased and the productivity of most VHOCs was significantly elevated (compare Fig. 5.7). In the lower panel of Figure 5.6 low water was found on midday, and a nicely pronounced IO daytime cycle on four consecutive days could be observed, with peak IO concentrations apparently more elevated than during the May period (see different y-axis scale in Figure 5.6), when low tide occurred in the morning and afternoon hours. Qualitatively these results can be confirmed by modelling studies with the marine boundary layer model *MISTRA*, which will be discussed in Section 5.2.5.

Organohalogens as Precursor Species

The impact of tidal effects on the appearance of organohalogens could be analyzed in detail during the 2003 Brittany campaign. For most organohalogens a strong increase of the concentrations during low tide periods was observed. This is detailed described and discussed within the diploma thesis of *Winterlik* [2003]. Exemplarily this is demonstrated in Figure 5.7 for the short-lived iodocarbons CH_2I_2 and CH_2IBr. As could be expected by the short photolytic lifetime (see Table 2.6), the concentrations of these species is significantly lower during daytime as can be seen from Figure 5.7. However, a clear anti-correlation to tidal height could be observed for the nighttime data, which is shown in the upper panel of Figure 5.7. Two points for CH_2I_2 exceed 10 pptv during high tide, in both cases very shortly after sunset, what may indicate a late accumulation of this specie.

Nighttime Activation of IO

Recently reported is detection of significant IO levels during night. *Saiz-Lopez and Plane* [2004] reported observations of IO up to 3 ppt on two

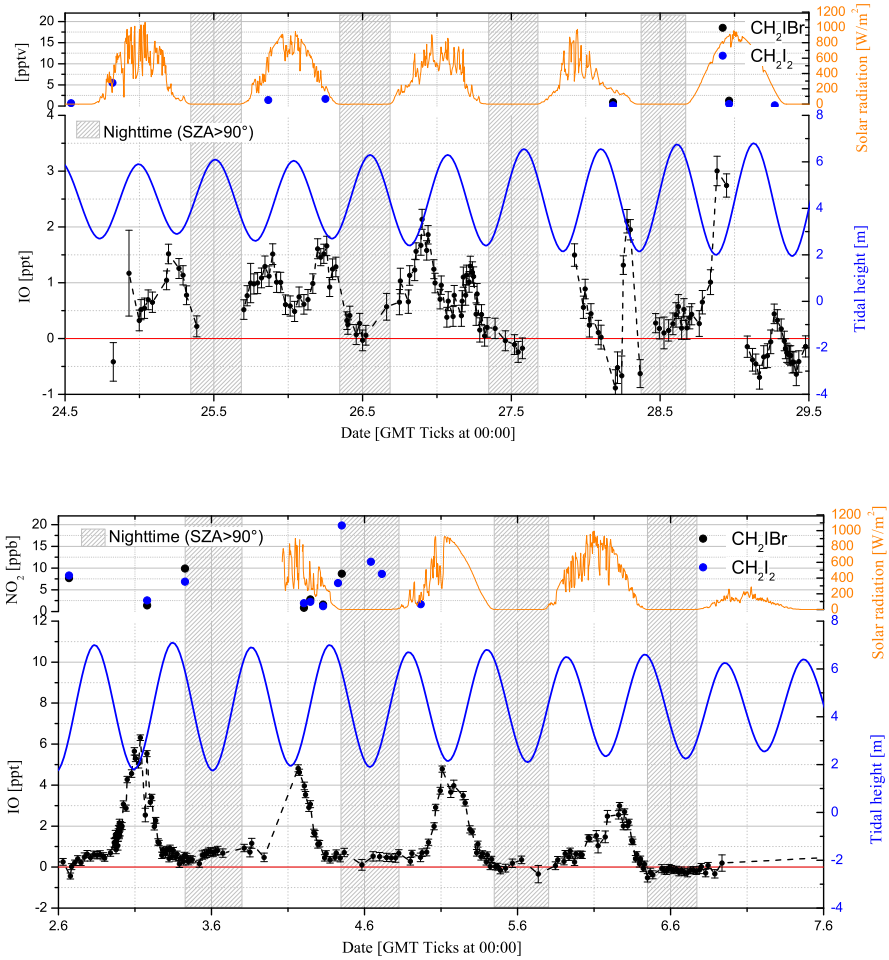

Figure 5.6: *Sequences of the recorded time series for IO of the 2003 Brittany campaign. The blue line indicates the tidal height and grey shaded areas indicate dark conditions (SZA* $\geq 90°$*).*
Upper panel: High tide occurred at midday and the IO peaks are observed in the morning and in the evening well correlated to the minima of the water level.
Lower panel: The minimum in tidal height coincides with maxima of solar flux and we observed the strongest peak of the IO concentration on four consecutive days.

nights during the 2002 NAMBLEX campaign at Mace Head and suggested a reaction mechanism for molecular iodine with the NO_3 radical in absence of sunlight.

$$\begin{aligned} NO_3 + I_2 &\longrightarrow I + INO_3 \\ I + O_3 &\longrightarrow IO + O_2 \end{aligned} \tag{5.1}$$

$k_{NO_3+I_2} = 1.5 \cdot 10^{-12} \frac{cm^3}{molec \cdot s}$ *for T=285K* [*Atkinson et al.* 1997]

The wavelength range of the IO was routinely covered by the DOAS instrument at night during the whole campaign time as described before. For spectra with SZA $\geq 90°$ no unambiguous identification of the IO absorption bands was possible. A statistical analysis for the whole dataset is shown in Figure 5.8. For SZA $> 90°$ only few points exceeded 2 ppt and a detailed analysis of these data points showed that all of them have comparably high residual structures, presumably caused by insufficiently removed lamp structures.

The statistical result of the IO nighttime concentration delivered a mean concentration of -0.15±0.9 ppt with a mean detection limit of about 0.3 ppt. That represents more or less the upper limit for a the nighttime activation

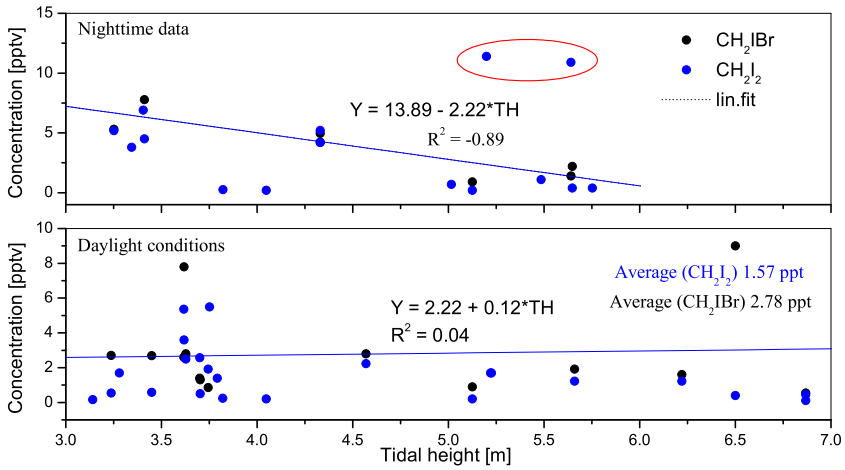

Figure 5.7: *Concentration of the short-lived iodocarbons CH_2IBr and CH_2I_2 in absence (upper panel) and in presence (lower panel) of sunlight during the 2003 Brittany campaign. At night the observed concentration of the iodocarbons significantly decreasing with increasing water level.*

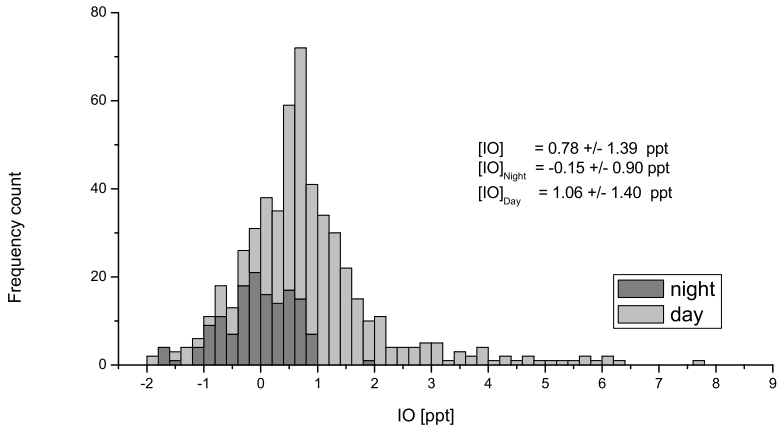

Figure 5.8: *Frequency distribution of IO concentration separated for daytime (SZA* $< 90°$*) and nighttime data.*

of IO in Brittany.

Regarding the frequency diagram 5.8 the IO daytime concentrations show a clear shift towards higher values, whereas the nighttime concentrations scatter between -1 and +1 ppt. This is as well to see in the correlation plot of tidal height and IO concentration shown in Figure 5.10, where the data is again separated for daytime ($SZA < 90°$) and nighttime concentrations. A clear anti-correlation of the daytime values of IO with tidal height is observed, whereas no correlation could be found for the nighttime data. This is in agreement with the results of *Hebestreit* [2001], who found during 1998 PARFORCE campaign in Mace Head a strong correlation of IO with tidal height with daytime data, but none for the nighttime by a statistical analysis of data from a 5 week measurement campaign (see also Chapter 6).

The generally low concentration of the IO dataset of the 2002 North Sea campaign did not show any correlation of observed concentrations with tidal height in agreement with the observations of the iodinated organohalogens and was therefore not taken into account for further investigation of the nighttime activation.

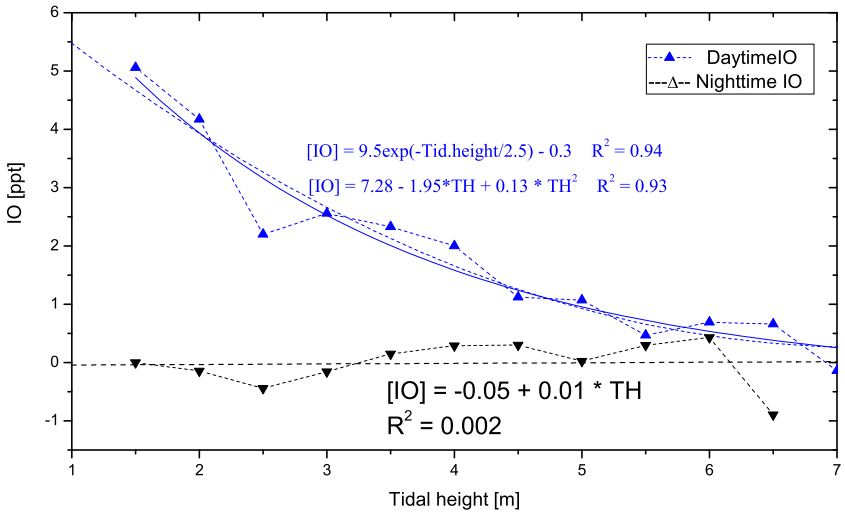

Figure 5.9: *Correlation plot for IO with tidal height. The IO concentrations are averaged on units of 0.5 m tidal height. A clear anti-correlation was found for the daytime data and none for the nighttime data.*

Comparison with IO Measurements of 1988/1989 Brittany Campaign

In 1988 and 1989 the detection of IO at the coast of Brittany was not successful. *Brauers et al.* operated an active DOAS system using a slotted disk machine as detector unit and gave a detection limit for IO of about 0.4 ppt on a lightpath of 6 km.
Since the slotted disk machine is known for its excellent signal to noise ratio (although long integration times are needed to account for the low light throughput), the reason for the discrepancy in the observation of IO is unlikely an insufficient sensitivity of the instrument. In the last decade great improvement on light sources and more precise measurements of the IO absorption cross section have been made and may explain some of the discrepancies. However, the main difference seems to be a change in the bio-activity in the past decade at the coast of Brittany. The former measurement site Point de Penmarch' was not far away, ∼100 km in the south and very similar to Lilia in 2003 regarding the appearance of algae. The measurements in the 80ies were conducted about one month later in the

year (June/July) than the current measurements in 2003. That the generally lower bio-activity was responsible for the observations in 1988/89 is also indicated by the measurements of CH_3I (which can be likely assumed as an indicator of the general bio-activity) performed by *Tsetsi et al.* [1989], who found concentrations of methyliodine in the order of just 1 ppt, compared to up to 1800 ppt (average concentration 260 ppt) of CH_3I found in late spring 2003.

5.2.2 Results of BrO Analysis

Due to the long exposure times necessary for the UV range the MCT technique wasn't supplied and measurements were restricted to times with excellent atmospheric visibility conditions. The acquisition of one spectra took in average 5-15 minutes. The analysis procedure, the evaluation range and the applied absorption cross sections are described in Section 3.5.1. A sample evaluation of one spectrum of the 2003 Brittany campaign is shown in Fig. 3.13.
Allover 405 spectra were analyzed, however, an unambiguous identification of BrO absorption in these spectra was not possible. The results of the statistical analysis are illustrated in Fig. 5.11, where the BrO concentrations show a slight shift in positive direction. However, in the day and nighttime plot, the daytime data scatter as the nighttime data around 0.6 to 0.7 ppt, what may indicate a systematic error in the analysis of the BrO evaluation and no real BrO absorption.
The average detection limit for BrO of the 2003 Brittany campaign was about 1.35 ppt, as indicated in Table 5.1. The full time series is shown in Fig. 5.5.

Reactive Bromine from Biogenic Sources

The results confirm upper limits for BrO in the MBL of 1.5-2 ppt as reported before from several coastal sites (see recent overview of *Sander et al.* [2003] or *von Glasow et al.* [2004] and references herein). BrO concentrations below the detection limit are as well expected by the respective model studies for the Brittany campaign (see Section 5.2.5).
The measurements in Brittany can also be understood as an upper limit for BrO from organic sources, since CH_2IBr is a potential source for reactive bromine in the gasphase. CH_2IBr was observed in exceptionally high concentrations (up to 10 ppt), which have not been reported before. Brominated organohalogens have lifetimes in the order of days and weeks, except

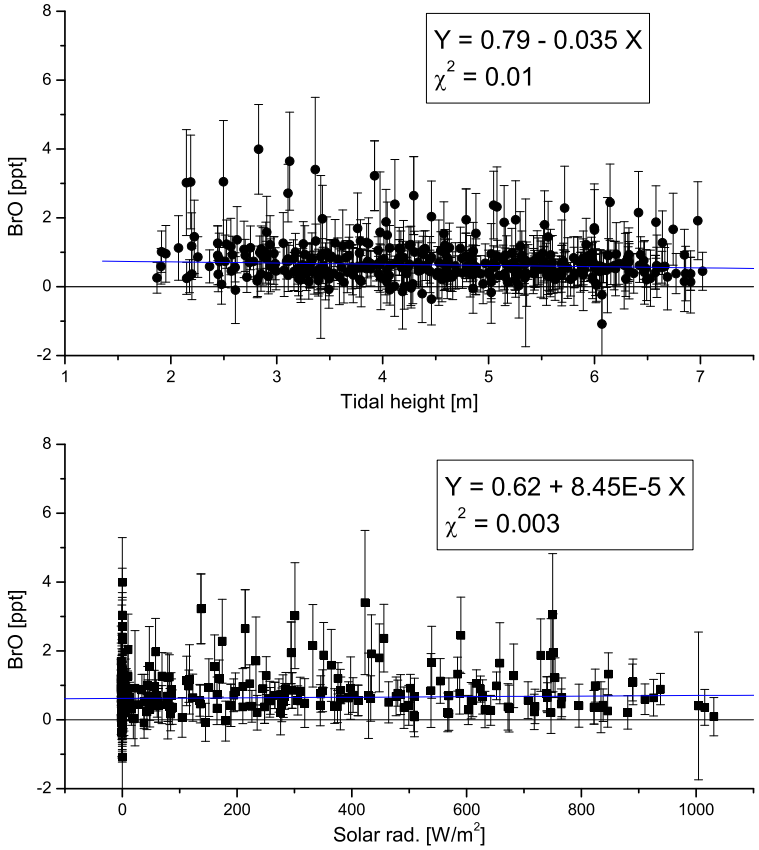

Figure 5.10: *Correlation of BrO from 2003 Brittany campaign with solar radiation and tidal height. For both parameters no dependence was found.*

CH_2IBr, which has a photolytic lifetime of just 61 min [*Mössinger et al.* 1998]. A statistical analysis of all BrO data taken during the Brittany campaign gives no indication that organic species are precursors for BrO since there is no dependency of the BrO signal to tidal height, solar radiation or the appearance of brominated hydrocarbons. The respective correlation plots for BrO are shown in Figure 5.10.

However, due to the insufficient sensitivity of the instrument no further conclusions can be drawn from that, but these findings are in reasonable agreement to modelling results of the Brittany campaign, (see Section 5.2.5), where BrO is expected to remain below 1 ppt, even assuming biogenic

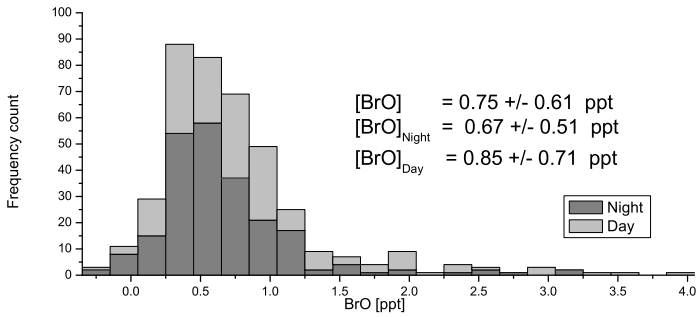

Figure 5.11: *The frequency distribution of the resulting BrO concentrations of the 2003 Brittany campaign, separated for day (SZA* $< 90°$*) and nighttime data.*

sources (CH_2IBr) of the maximal detected level of 10 ppt. Nevertheless, the highly elevated level of 10 ppt of CH_2IBr affects the BrO concentration in a considerable way, although below the detection limit of the DOAS instrument of 1.5 ppt.

Comparison with Ozone and NO_2

Within the evaluated spectral range of BrO, ozone and NO_2 were analyzed as well and the resulting concentrations for ozone could be compared to the results of the ozone in-situ monitor, representing a good quality and consistency check for the evaluation procedure. The sampling time of the in-situ instrument was set to 5 minutes, which is as well the time scale of the DOAS measurements. Since the DOAS results represent the mean concentration over a 10 km lightpath along the coast, the good agreement to the in-situ results indicates that no strong gradients exist for ozone in the boundary layer. The timeseries of the ozone in-situ measurements together with the results of the DOAS analysis is shown in Figure 5.12 in the upper panel. The comparison shows a generally good agreement (correlation coefficient of 0.83, see Fig. 5.13) between the two measurement methods, except the record of May 29th, where the ozone dropped down to 0 ppb, but this was caused by instrumental problems of the in-situ monitor. During the campaign ozone was present at typical continental levels of 30-50 ppb.
In the lower panel of Fig. 5.12 the results of the NO_x measurements are shown. NO_x is an indicator for anthropogenic pollution and a significant pollution of up to 300 ppt NO during the campaign had to be accounted

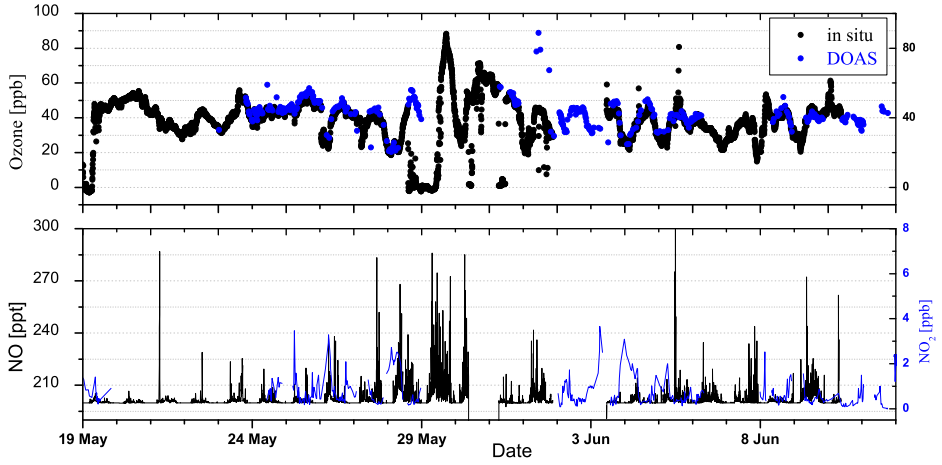

Figure 5.12: *The ozone level had typical northern hemispheric levels of 30-50 ppb. The NO_2 reached an average concentration of 0.9 ppb, which represents a moderate pollution. Data marked in blue are retrieved from DOAS measurements*

for.

5.2.3 Analysis of I_2 and OIO

For the detection of OIO, measurements in the 510-590 nm region were routinely performed during the whole campaign (see program flow diagram in Fig. 3.11). In the same wavelength region as the OIO absorption structures appear, that of I_2 are to find as well (see Figure 5.14).
I_2 was observed for the first time in Mace Head during the 2002 NAMBLEX campaign by *Saiz-Lopez and Plane* [2004]. They reported I_2 concentrations of up to 93 ppt at night (and 25 ppt during daytime) by using active long-path DOAS technique. The peak concentrations appeared closely correlated to low tide indicating macroalgae as the primary source.
Due to the generally strong appearance of macroalgae at the coast of Brittany an intensive analysis of the spectra was done. The evaluation procedure was already briefly introduced in Section 3.5.3 but will be carried out in more detail within this section.

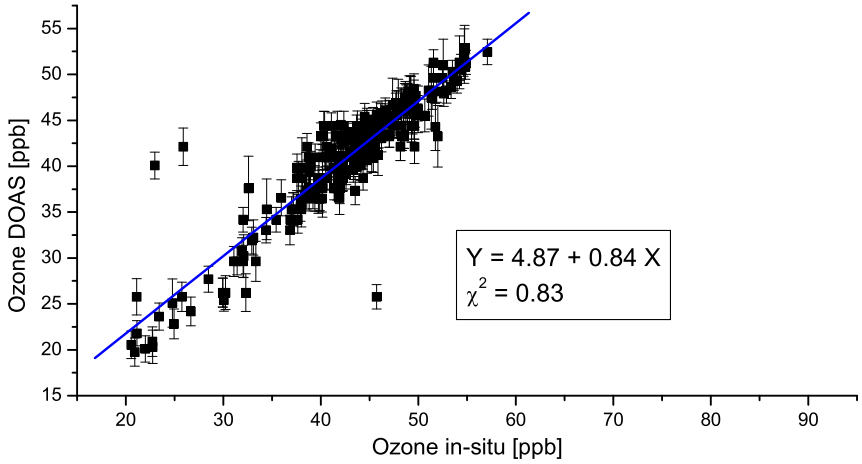

Figure 5.13: *The correlation coefficient is 0.83 for the ozone measurements with the in-situ monitor and the DOAS analysis in the UV wavelength range.*

Absorption Cross Section and Lamp Reference Spectra

The main known absorbers in the 508-588 nm range are H_2O, NO_2, O_4, OIO, and I_2. For the evaluation procedure the strong and temporarily varying lamp features have to be accounted for as well.

The last published cross section of I_2 is that from Tellinghuisen 1973 with the low resolution of 2.6 nm. A more actual cross section with a resolution of 0.1 nm (at 500 nm) was provided by *Saiz-Lopez et al.* [2004]. The available differential absorption cross sections for the I_2 evaluation range are shown in the overview of Figure 5.14.

The spectral features of the Xe-arc lamp had to be removed, what is the critical point of the analysis. Lamp reference spectra were taken daily by using the shortcut system 2 (see Section 3.2.7). However, these lamp spectra showed significant variations in their structures partly caused by a loss of pressure during their lifetime of ∼2 weeks, but as well on a shorter timescale. The lamp was exchanged on 23rd of May and on 7th of June. It turned out, that the lamp structures were generally much more stable in the beginning than at the end of their lifetime. Lower residual structures and less variations of the fit coefficient resulting from the evaluation procedure could be

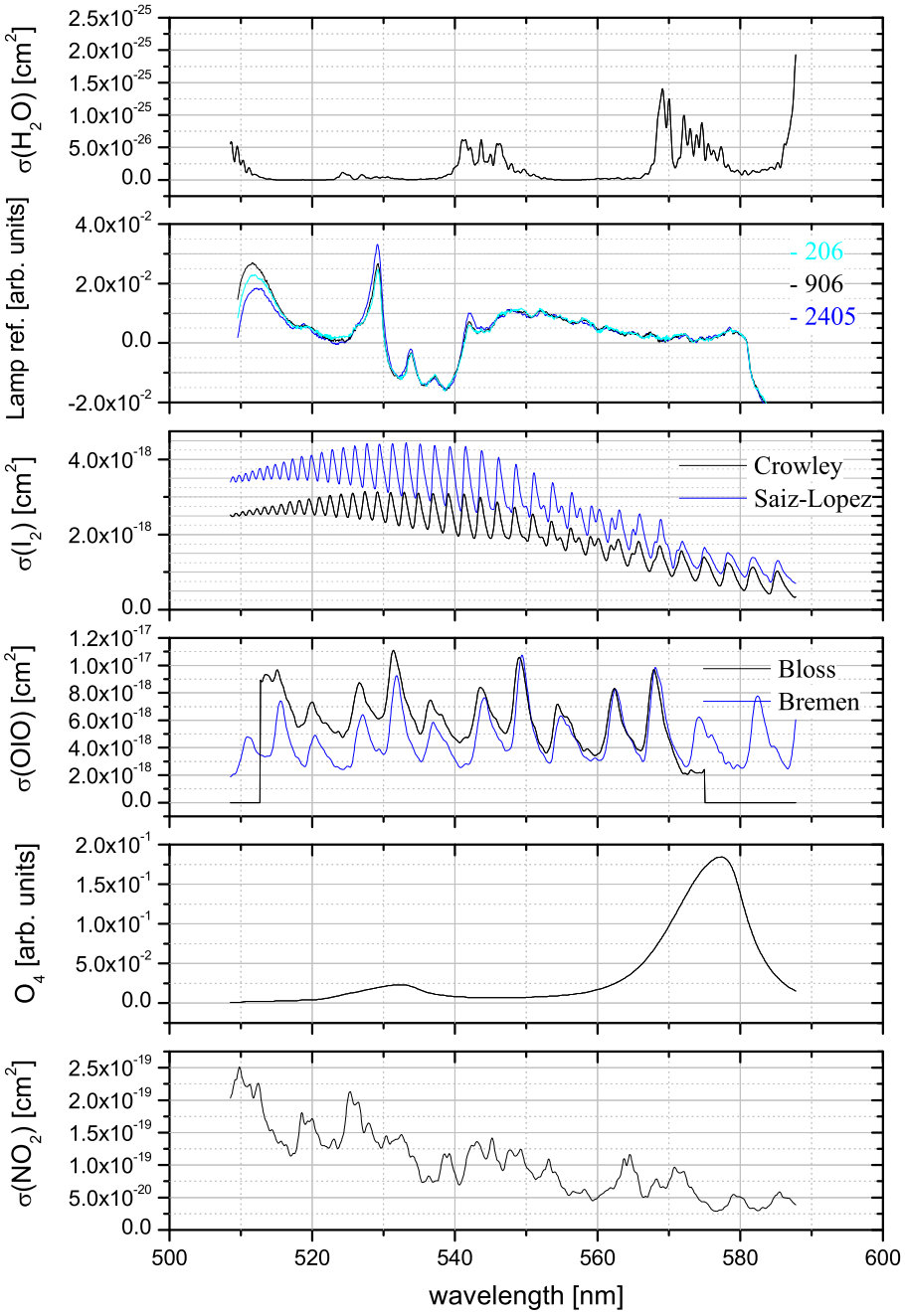

Figure 5.14: *Overview on absorption cross sections for the OIO and I_2 evaluation. Lamp spectra are shown in the second panel for three different days.*

observed for the data of May, when a new lamp was operated. According to this, the evaluation was split up in several parts, where lamp references of different days and 'burning state' were used.
It should be noted, that the strongly varying lamp structures in the 500-600 nm range seem to be a problem caused by the operated PLI lamp itself. It is less likely that the electronic supply of the Hoffmann Messtechnik lamp housing is responsible for the observed variations, resulting from a comparison with lamp spectra taken at the PARFORCE campaign in 1998 with a different lamp housing of the Müller company.
Lamp spectra of different high pressure Xe-arc lamp manufacturers were investigated by *Hermes* [1999] within a diploma thesis. The quotient spectra of different lamp types of lamps are shown in Figure 5.15. Due to the very high pressure (up to 10^7 Pa under operating conditions) of the operated PLI lamp, its spectrum may fit best with the test lamp of the manufacturer Narva. The comparison of *Hermes* [1999] showed as a result, that the spectrum of the XBO lamp of Osram, which is frequently used for active longpath DOAS measurements had a significantly flatter and more unstructured spectrum in the 500-600 nm range than the one of the Narva.

Evaluation Range

Highly varying spectral features in the lamp spectrum are to find at 526.5 - 543.4 nm as can be seen in Figure 5.16, where lamp spectra recorded on different days were compared. These high temporal variations in parts of the spectra restrict the evaluation range.
A quantitative comparison of representative lamps taken on different days was made by fitting one lamp to another and checking for the remaining structures and the parameters of the residual values $\Delta = Max - Min$ and RMS. The residual structures are clearly dominated by the strong features in the 526.5 nm and 548 nm range. The $\Delta = Max - Min$ of the residual in this range reaches 0.008 peak to peak, while it drops to 0.004 in the higher wavelength range. The fit improves much, if two different lamps are fitted simultaneously. Δ remains only slightly dominated by the structures at 529.5 nm, but drops for the full range down to less than 0.004 peak to peak and to 0.001 - 0.002 within the flatter wavelength range (above 550 nm).
Due to these difficulties in removing the lamp structures it is preferable to evaluate in the higher wavelength range. But since the analysis is focused on the detection of the weak absorber I_2, a good spectral identification over a broad evaluation range should be considered as well.

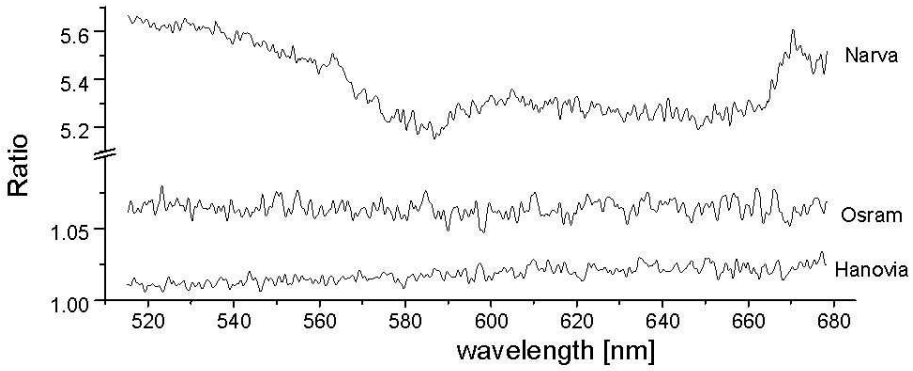

Figure 5.15: *The ratio of two spectra for the different types is shown. The Narva shows significantly higher structures in the quotient spectra compared to the Osram lamp (adapted from Hermes [1999])*

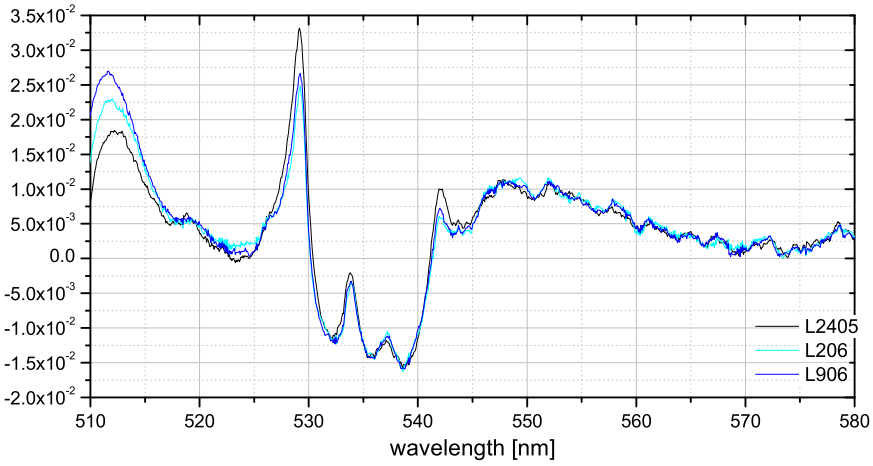

Figure 5.16: *Lamp spectra highpass filtered (binomial, 5000), of three different days. The main variations are to find in the strongly structured range of 525-545 nm.*

References	χ^2	*RMS*	*Shift* [nm]	*Squeeze*
NO_2, OIO, O_4, H_2O, I_2	$8.74{\cdot}10^{-7}$	$8.69{\cdot}10^{-4}$	-0.114	$-9.8{\cdot}10^{-4}$
Lamp	$8.74{\cdot}10^{-7}$	$8.69{\cdot}10^{-4}$	$-8.6{\cdot}10^{-3}$	$-9.45{\cdot}10^{-4}$

Table 5.2: *The table shows the averaged results for the shift and squeeze parameters, resulting from the final evaluation.*

The strongest absorption bands of I_2 are to find within 530-545 nm unfortunately overlapping with the highly variable lamp features in the 526.5 - 543.4 nm region. In the higher wavelength range conflicts with strong water absorption have to be accounted for. Water vapor absorption structures could not perfectly removed, due to the incompleteness of the available data bases (see Section 3.4.3).

However, the best compromise for the evaluation range was ascertained to be 530-568 nm. A rough estimation of the detection limit for I_2 for the chosen evaluation range can be (in a very conservative way) estimated by the assumption of a $2 \cdot 10^{-3}$ peak to peak residual structure (resulting from the lamp to lamp fit in the respective evaluation range), a lightpath of $\sim$19 km and the assumption that a spectral identification is possible if the absorption structures of I_2 are in the same order as the residual structure.

$$c_{det_{limit}} = \frac{2 \cdot 10^{-3}}{2 \cdot 10^{-18} cm^2 \cdot 1.9 \cdot 10^6 cm} = 20.2\ ppt \tag{5.2}$$

Evaluation and Example for OIO and I_2 Analysis

As described in Section 3.1.2 the software *WinDoas* was used for the evaluation procedure. Besides the atmospheric absorbers a 5th order polynomial was added according to the extended evaluation range of 530-568 nm. Shift and squeeze parameters in the non-linear least squares fit were allowed for all species, but linked together for all atmospheric absorbers, since it can be assumed that the wavelength mapping of the references spectra from literature is sufficiently precise and no shifts among each other exist. The lamp reference spectra were treated individually but as well with no restrictions on shift and squeeze parameters. In Table 5.2 an overview on the resulting shifts and squeeze parameters is given. The resulting shift for the lamp reference remained below 0.08 nm.

To illustrate the insufficient identification of the I_2 and OIO absorption structures, a sample evaluation of June 4th 2003, 22:37 GMT is illustrated in Figure 5.17.

Alternative Evaluation Approach and Mean Residual

Further evaluation approaches with more free parameters and restrictions for shift and stretch parameters for the I_2 reference spectrum were made, since the cross section and the quality of its wavelength calibration is not ensured. No noteworthy differences in the results were observed, and a spectral identification of the absorption structure remained without success.
Instead of using a lamp reference, a second approach to identify any structures of I_2 was made by applying an atmospheric spectrum taken at midday. This was done to see if the fit coefficient shows any systematic differences for day and night spectra. In the atmospheric spectrum absorptions of NO_2 and water are already contained that the small expected amplitude of I_2 is better emphasized. The result of that alternative evaluation is compatible to that described before. However, the unambiguous identification of I_2 in the spectra above the average detection limit of ∼20 ppt remained without success.

Comparison with NO_2

The results of the NO_2 concentration of the 430 nm range was compared to that of the 335 nm evalutation range with very good agreement. This comparison was also done for the NO_2 results from the OIO, I_2 evaluation. The resulting comparison is shown in Figure 5.18. Generally the comparison shows good agreement and differences could be explained by the recording of the spectra. The spectra were taken in succession, resulting in a time shift among them. Furthermore it must be considered that the spectra differ in their exposure times and in different number of scans.
The advantage of the IO analysis range is, that the evaluation is of higher quality, due to the higher differential absorption cross section of NO_2 in this region. This could also explain the strongest discrepancies in case of low concentration of NO_2.

5.2.4 Results of OIO and I_2 at Brittany

The resulting time series of NO_2, OIO and I_2 for the whole campaign time is shown in Figure 5.5. During the measurement period in the end of May,

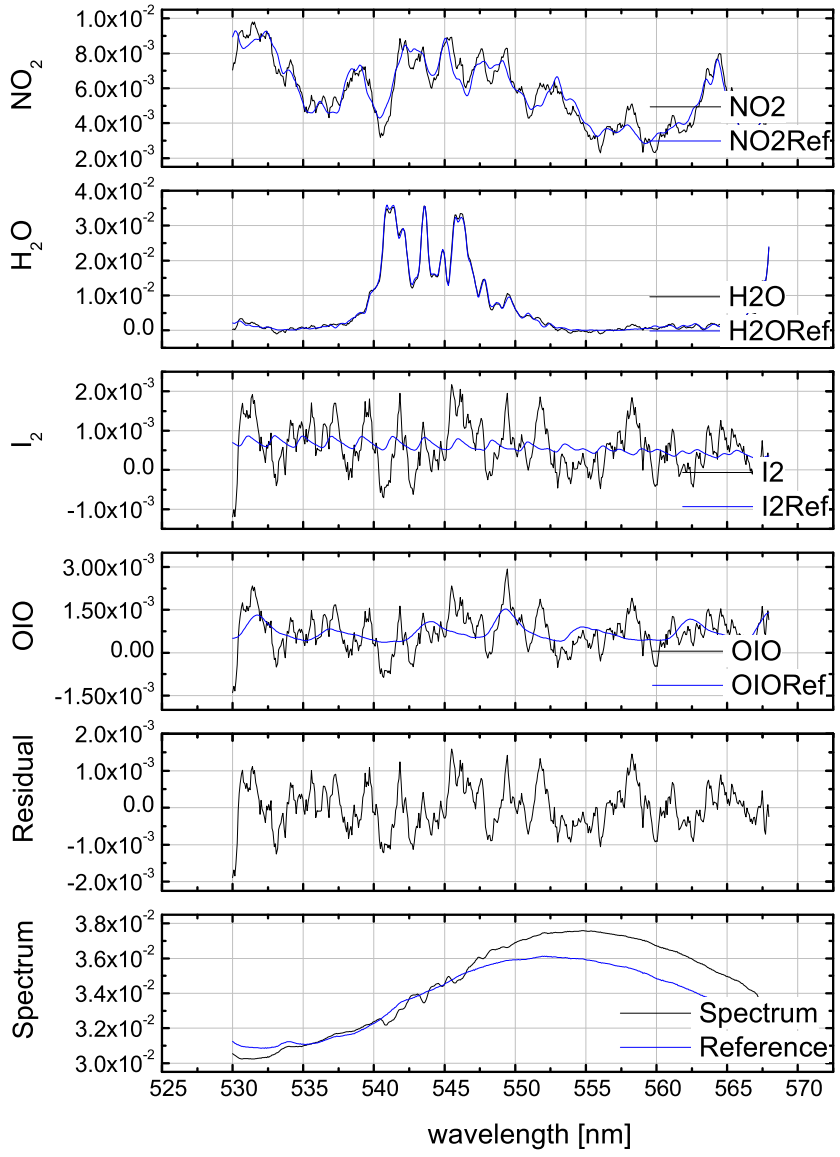

Figure 5.17: *A sample evaluation of June 4th 2003, 22:37 GMT. In the lowest panel the atmospheric spectrum and the fit result for the lamp reference is shown. In the upper panels the residual structure and the results of the evaluation of the atmospheric absorbers are illustrated. Above the residual neither OIO nor I_2 are to identify.*

the I_2 concentration remained very close to zero, whereas the resulting concentration scatter between -10 to 20 ppt in the sequence of June. However, these results are within their respective error bars in agreement with zero. As pointed out before, no clear spectral identification of I_2 or OIO absorption structures were possible. Just few data points exceed the detection limit, but in these cases, the error bars are already indicating that the residual structures are higher than in average.
All in all 524 data points are taken into account in this analysis and some statistical estimations could be done. The frequency distribution for the resulting OIO and I_2 is shown in Figure 5.19. In average both I_2 and OIO show slightly negative concentrations.

Correlation of I_2 and OIO with Solar Radiation and Tidal Height

Under sunlight conditions I_2 photolyzes quickly in the order of 10 s [*Saiz-Lopez and Plane* 2004]. Therefore the dependence on I_2 concentration on solar zenith angle was taken into account. The correlation for both OIO and I_2 with SZA is shown in Figure 5.20. But no dependence on solar radiation on the appearance of both species was found. Since the photostability for OIO molecule is still unclear the non existent correlation of OIO, shown in

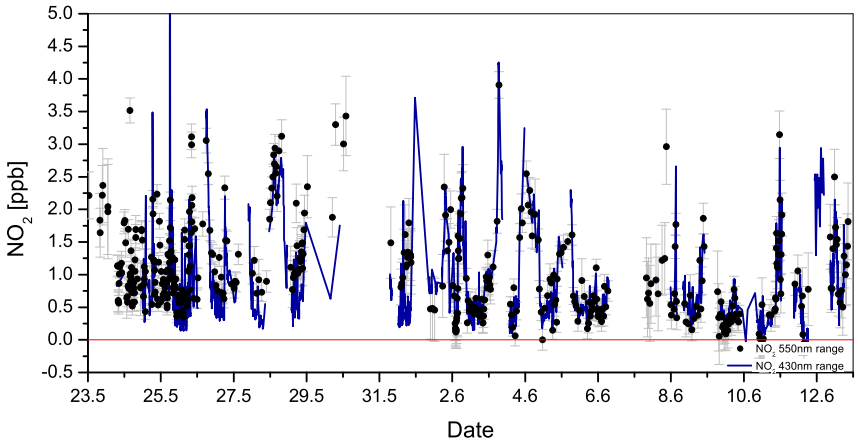

Figure 5.18: *The time series for NO_2 resulting from two different evaluations. The blue line indicates the results of the NO_2 analysis resulting from the 430 nm range and the black points indicate results from the OIO, I_2 evaluation.*

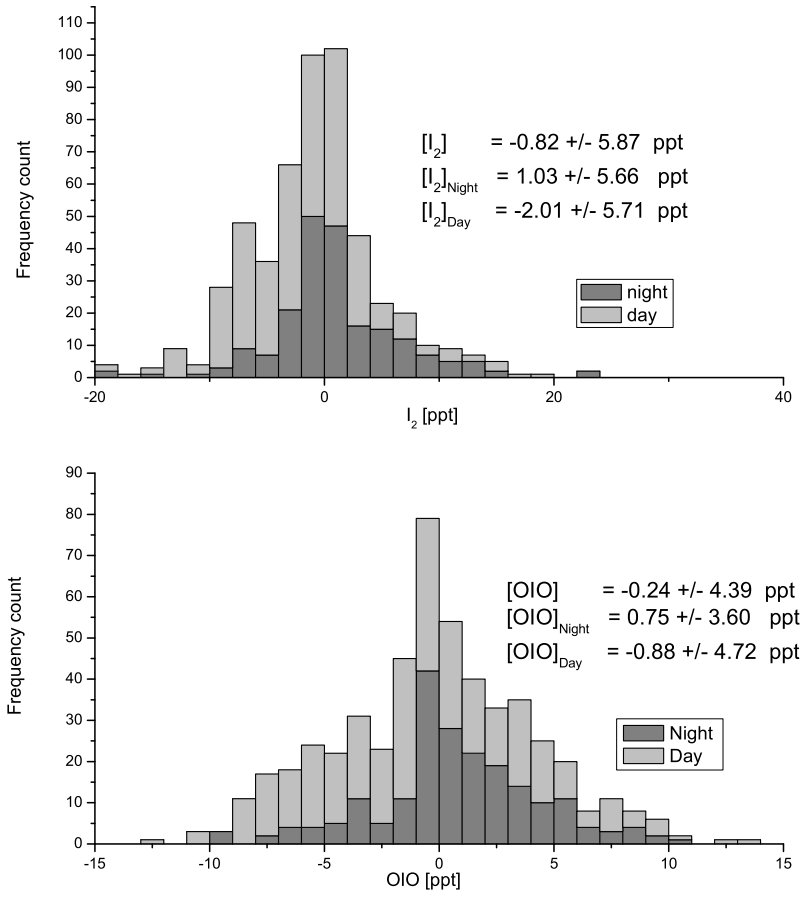

Figure 5.19: *Frequency distribution for resulting I_2 (upper panel) and OIO (lower panel) concentrations from 2003 Brittany campaign. Data is separated in daytime ($SZA < 90°$) and nighttime values.*

Figure 5.20 in the lower panel gives no indication for further conclusions. If exposed macroalgae are the source of I_2 as suggested by *Saiz-Lopez and Plane* [2004] from their observations in Mace Head in 2002 there should be any difference in the concentrations of I_2, OIO observable in dependence on tidal height. In Figure 5.21 the correlation plot for I_2 and OIO with tidal height is shown, but conclusively it is to state that there was practically no dependence found.

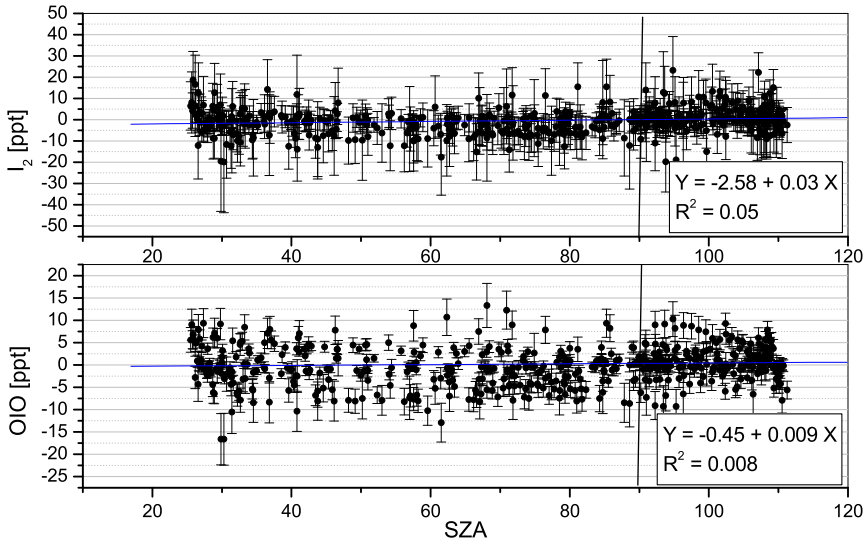

Figure 5.20: *The correlation of the solar zenith angle with the concentrations of I_2 and OIO are shown.*

5.2.5 Comparison to Model Studies

In order to check some of the conclusions gained from the measurements for consistency with the present understanding of atmospheric chemistry, the results were studied by respective model calculations with the marine boundary model *MISTRA*.

Model Description

The 1D column model *MISTRA* was used, which includes detailed particle microphysics as well as chemical reactions in the gas and aerosol phase, focusing on reaction cycles of halogen compounds. *MISTRA* has already been used to address different aspects of halogen chemistry in the marine boundary layer ([*von Glasow and Sander* 2001], [*von Glasow et al.* 2002a; *von Glasow et al.* 2002b]). The model configuration used for the Brittany data-set mostly resembles the base run described in detail in *von Glasow et al.* [2002a], representing conditions for a clean marine mid-latitude summer atmosphere. The chemical reaction scheme (especially regarding iodine chemistry) has been updated according to present knowledge. The meteorological conditions assumed represent a cloud-free day in Brittany in the

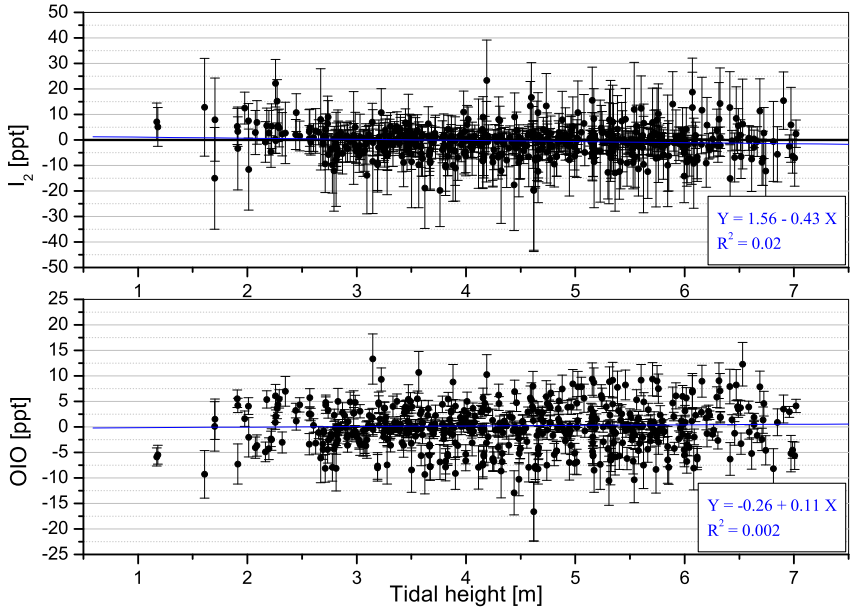

Figure 5.21: *The correlation of tidal height with the appearance of I_2 and OIO during 2003 Brittany campaign is shown.*

	CH_3I	C_2H_5I	C_3H_7I	CH_2ClI	CH_2BrI	CH_2I_2
daytime mean	249	31.9	2.3	0.9	1.5	1.8
daytime max.	1830	96.9	34.8	2.9	7.8	11.4
midday max.	542	9.1	23.5	2.9	7.8	5.4

Table 5.3: Mixing ratios of organoiodides (ppt) as measured in Brittany and prescribed in the model runs. Here, "daytime"stands for 5 a.m. - 7 p.m., "midday"stands for 9 a.m. - 3 p.m..

beginning of June (latitude 48.62 N, sun declination 22°). Furthermore, higher NO_2 mixing ratios compared to *von Glasow et al.* [2002a] of about 1 ppb (as measured in Brittany) have been assumed.
After spin-up of meteorology and chemistry assuming open-ocean conditions, different scenarios are computed, each extending over 6 model hours. During three model hours (hours 2 to 4), constant mixing ratios of organoiodides are prescribed in the lowest 15 m of the model, relying on values measured in

Brittany (see 5.3). This can be understood as a most simple representation of enhanced concentrations of alkyl iodides during low tide periods. Each scenario is computed for morning (4 - 10 a.m. local time, assuming low tide from 5 - 8 a.m.) and midday hours (10 a.m. - 4 p.m., assuming low tide from 11 a.m. - 2 p.m.). Additional sensitivity studies are performed assuming constant fluxes instead of constant mixing ratios of organoiodides in order to check more realistically for qualitative differences between the morning and midday scenarios. Also, the effect of a hypothetical I_2 flux on atmospheric chemistry is investigated.

Model Results

Figure 5.22 shows the effect of prescribed organoiodide concentrations as measured in Brittany (see Table 5.3) on IO, BrO and ozone for scenarios assuming low tide during midday. After 3 hours of prescribed organoiodide concentrations, IO mixing ratios reach about 1.5 ppt, 11 ppt, and 5 ppt for the different organoiodide concentrations described above (Table 5.3), which is in reasonable quantitative agreement with the DOAS measurements. For equivalent alkyl iodide concentrations in the morning hours, the modelled IO mixing ratios are about a factor of 4 lower. In all cases, the comparatively short-lived CH_2I_2 contributes by far the largest part to the modelled IO mixing ratios. For example, omitting the huge amount of CH_3I (1830 ppt) in the 'daytime max.' scenario decreases IO only by 7% after 3 hours. It should be noted that compared to clean marine air with only some ppt NO_2, a NO_2 mixing ratio of about 1 ppb (as used here) decreases the IO mixing ratios produced by a given amount of CH_2I_2 considerably. Recycling of reactive iodine by aerosol processing is responsible for roughly 10% of the modelled IO.

The model-predicted BrO never exceeds 1 ppt and thus ranges generally below the DOAS detection limit, supported by the measurement results. These lower BrO values compared to *von Glasow et al.* [2002a] are mainly due to the higher NO_2 concentrations in the model configuration. In these simulations, BrO significantly increases with increasing emissions of organoiodides. This increase is to a large part directly related to the release of Br from the photolysis of CH_2BrI, which could be shown by a comparison of otherwise identical simulations with and without 7.8 ppt CH_2BrI.

A further effect of organoiodide emissions is the destruction of ozone via photochemically produced I radicals. For the 'daytime max.' scenario, roughly 1 ppb ozone is destroyed after 5 hours (which could not be detected in the field, but is still quite significant).

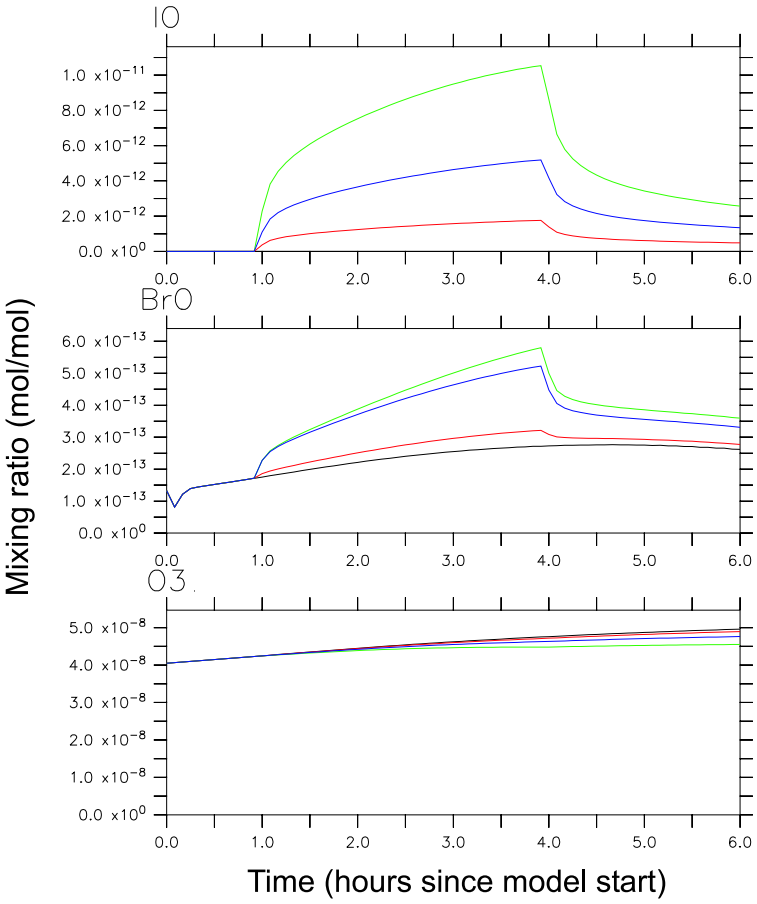

Figure 5.22: *Comparison of scenarios for midday hours assuming different prescribed concentrations of organoiodides: black - no organoiodide emissions; red - organoiode emissions according to daytime mean (see Table 5.3); green - organoiode emissions according to daytime max. (see Table 5.3); blue - organoiode emissions according to midday max. (see Table 5.3). The model run starts at 10 a.m., organoiodides are present from 11 a.m. - 2. p.m.*

Figure 5.23 shows a comparison of scenarios assuming low tide during morning hours or during midday, respectively. In contrast to the simulations above, where constant concentrations of alkyl iodides were prescribed, a constant flux of iodine-precursors is assumed. Whereas the first assumption is suitable for a quantitative comparison with measurement results, the latter should be a more realistic specification for a qualitative comparison of different times of the day. A constant flux of $4{\cdot}10^9$ molec/cm^{2}s of CH_2I_2 leads to about 4 ppt CH_2I_2 at midday, whereas in the morning hours CH_2I_2 mixing ratios reach up to 15 ppt due to lower photolysis rates at higher zenith angles. For the same reason, I radical concentrations and thus IO mixing ratios are higher for the midday than for the morning scenario. After 3 hours of emission, the ratio between midday and morning IO is about 2.3, which qualitatively affirms the measurement results which are shown in Figure 5.6.
Apart from scenarios assuming organoiodide emissions, Figure 5.23 also shows otherwise identical scenarios prescribing a constant flux of molecular iodine (10^{10}molec/(cm^{2}s)) instead of organoiodides. This leads to mixing ratios of I_2 in the model of well below 0.5 ppt, the mixing ratios in the early morning being highest for the reason discussed above. Despite of these low I_2 mixing ratios, the effect on IO is considerable: After 3 hours of emission, modelled IO mixing ratios rise up to 8 ppt in the morning, and 16 ppt in the midday scenario. This finding can be explained by the short photolytic lifetime of about 10 seconds for I_2 compared to some minutes in case of CH_2I_2. Hence, the model results suggest that even very low mixing ratios of I_2 (which are far below the DOAS detection limit) could have a large impact on iodine chemistry. However, the model simulations discussed above seem to indicate that the presence of molecular iodine is not necessary to explain the observed IO mixing ratios in Brittany.
It should be noted that these simulations contain some simplifications that have to be kept in mind when interpreting the results: For instance, it is assumed that all emission occur into the same air mass, only accounting for vertical, but not for horizontal mixing. Furthermore, a possible nucleation of iodine oxides was not accounted for, which could potentially be an important sink for IO. Therefore, these model results have to be regarded rather as an overestimation than an underestimation of IO. Hence, in spite of the agreement between observations and modelling without including molecular iodine, it cannot be excluded that I_2 may be an important precursor for IO. This conclusion is also supported by the fact that DOAS measurements are representative for mean concentrations along the light path and thus cannot resolve possible hot spots, while the model results are more representative

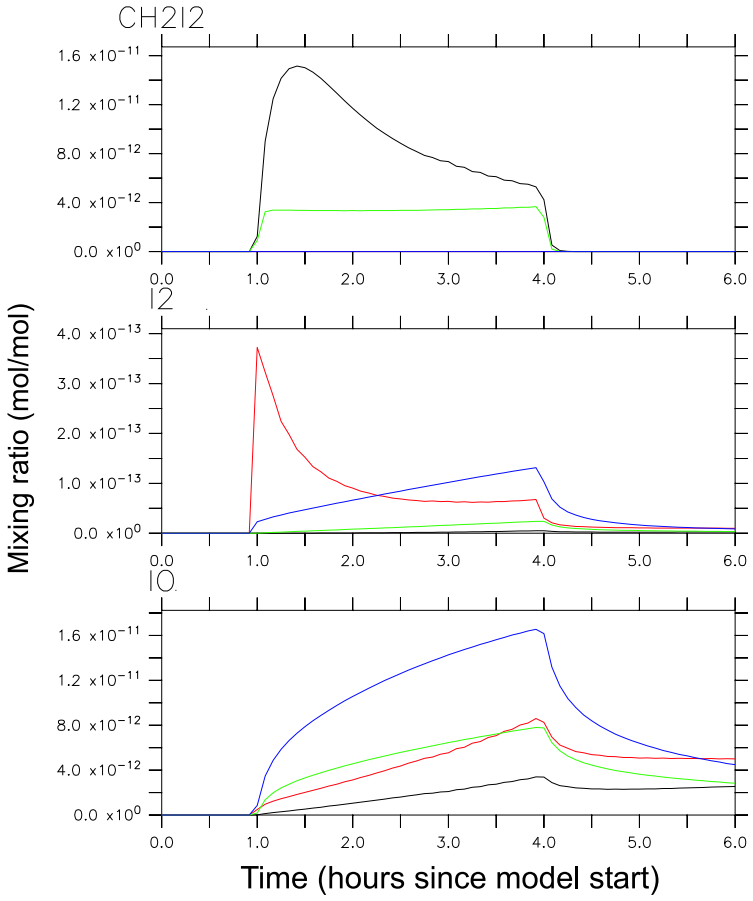

Figure 5.23: *Comparison of two morning and two midday hours scenarios assuming constant fluxes of organoiodides or I_2, respectively: black - organoiodide emissions only, morning; green - organoiodide emissions only, midday; red - I_2 emissions only, morning; blue - I_2 emissions only, midday. The 'morning' runs start at 4 a.m., emissions extend from 5 - 8 a.m., the 'midday' runs start at 10 a.m., emissions extend from 11 a.m. - 2 p.m..*

for smaller-scale conditions.

Chapter 6

Appearance of OIO and I_2 in the MBL

The appearance and the magnitude of OIO and I_2 in the MBL is of great interest due to the possible impact on new particle formation processes. However, the OIO molecule was not found above the detection limit of about 3 ppt, neither in the Brittany nor in the North Sea data set. Furthermore it has to be considered that longpath DOAS measurements along the absorption-paths of ∼20 km were not suitable to detect inhomogeneous sources for OIO as proposed by *Burkholder et al.* [2004] (see Section 2.4.2), due to averaging over extended airmasses in time and space.

Since macroalgae under oxidative stress are considered to be a further source for reactive iodine in the marine boundary layer as suggested by *Saiz-Lopez and Plane* [2004], the unsuccessful detection of I_2 during the 2003 Brittany campaign need further explanations and investigations, due to the potential high impact of molecular iodine in the gasphase even in low concentrations (see results of model studies in Section 5.2.5).
The detection of I_2 was up to date only reported by the recent measurements in Mace Head in 2002 [*Saiz-Lopez and Plane* 2004]. Already in 1998 an extensive field campaign was conducted there within the PARFORCE project. Within that field campaign extended data with an active longpath DOAS telescope were taken for the detection of BrO, IO and OIO but I_2 was not accounted for within the previous analysis. To verify the result of the appearance of I_2 of the 2002 Mace Head campaign, a re-analysis of the 1998 spectra was done and the results will be presented and discussed, especially regarding the comparison to the 2003 Brittany results within this chapter.

Figure 6.1: *The measurement site at Mace Head. Intertidal areas are shaded in darker color. Tidally influenced areas with fields of macroalgae are located in easterly direction, Bertraghboy Bay, Ard Bay of the indicated lightpaths (red lines), which mainly crossed over sea.*

6.1 Mace Head 1998

In September/October of 1998 the group of *U. Platt* of the Institute for Environmental Physics in Heidelberg conducted active longpath DOAS measurements during the field campaign in Mace Head, Ireland (53.33 N, 9.90 W) in the framework of the PARFORCE (New Particle Formation and Fate in the Coastal Environment) project. Spectra were taken for the detection of BrO, IO and OIO. The results are already published for BrO ([*Hönninger* 1999], [*Sander et al.* 2003]) as well as for IO [*Carpenter et al.* 2001; *Hebestreit* 2001].
Since I_2 was not accounted for in the original analysis, all spectra in the 500-600 nm range were re-analyzed. Due to a variety of intensive field studies at Mace Head within the recent years, a detailed description of the measurement site can be found elsewhere (e.g. *Hebestreit* [2001]). The site is in some points very similar to that of Brittany. The coast line is significantly influenced by tidal effects and the combination of a rocky coast and cold

water resulted in a strong appearance of macroalgae.
The DOAS telescope was set-up close to the water front. The lightpath was 7.27 km (total length 14.54 km) long pointing to the opposite side of the bay, where a retro-reflector was positioned. The short indicated lightpath of 2.6 km in Figure 6.1 is about a factor 3 shorter, resulting in a detection limit of ∼60 ppt for I_2. Therefore all spectra of the short lightpath were excluded from the evaluation. The lightbeam crossed mainly over sea water with only small areas at the border that were affected by the tides. However, in easterly direction of the lightpath extended fields of macroalgae are exposed to the atmosphere during times of low tide (Bertraghboy Bay, Ard Bay, see Fig. 6.1).

Species	*Av.D.L.* [ppt]	*Min/Max D.L.* [ppt]	*Av.conc.* [ppt]	*Max conc.* [ppt]
NO_2	70	20/600	610	$(6.54\pm0.07)\cdot10^3$
O_3	$4.3\cdot10^3$	$1.4/15.5\cdot10^3$	$32.35\cdot10^3$	$44\pm3.9\cdot10^3$
IO	0.91	0.3/6	0.48	7.2±0.3
BrO	2.45	0.88/9.45	-1.28	4.1±4.2
OIO	3.1	1.4/9.3	1.75	6.7±0.5
I_2	9.99	7.6/27.6	6.6	61.29±12.09

Table 6.1: *Overview on the resulting concentrations and detection limits of the evaluated species from 1998 Mace Head campaign. The results of NO_2, O_3, IO, BrO and OIO for Mace Head are adapted from the original analysis by Hebestreit ([Hebestreit 2001]) and Hönninger ([Hönninger 1999]). The average, the minimal and maximal value of the detection limit (D.L.) and the concentration (conc.) for each species is given.*

6.1.1 Results of I_2 Analysis

For the analysis for the Mace Head spectra, the identical evaluation procedure as described in Section 3.5.3 for the dataset of the 2002 North Sea and 2003 Brittany campaign was applied. The estimated detection limit

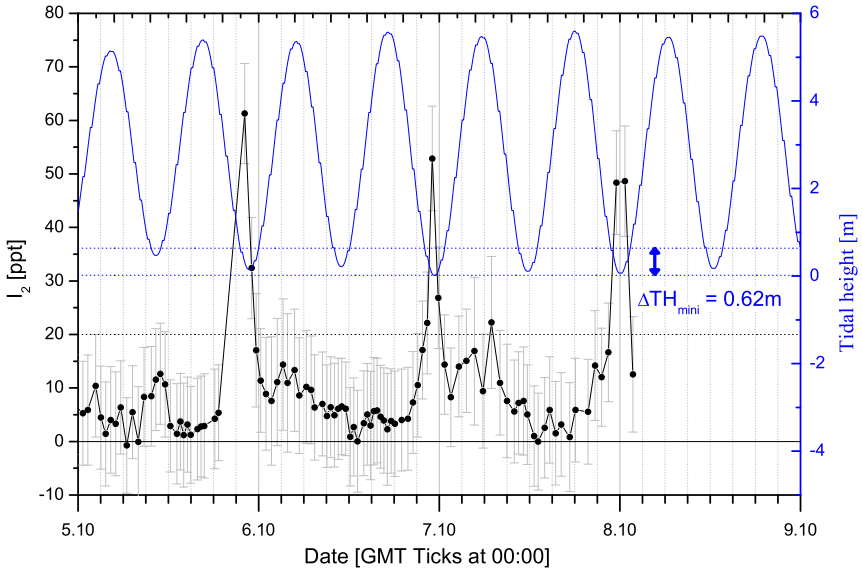

Figure 6.2: *October 5th, 6th and 7th of 1998 PARFORCE campaign in Mace Head, where the highest concentrations up to 60 ppt of I_2 were detected.*

resulting from the mean residual peak to peak value of the analysis is in the same order ($\sim$ 20 ppt) as that of Brittany, whereas the indicated detection limit resulting from the fit-error is about 10 ppt, corresponding to 2σ (see Section 3.4.7).
I_2 absorption was clearly identified above that detection limit with peak concentrations of up to 60 ppt during nighttime. A sample evaluation for the unambiguous detection of I_2 absorption is given in Figure 3.15.
An overview on the results, the detection limits and maximal values is given in Table 6.1.

The highest concentration of I_2 was detected at the end of the 1998 campaign on three consecutive nights. Within a short time frame the I_2 increased fast from below the detection limit to peak values of more than 60 ppt (see Figure 6.2). The abrupt rise of the I_2 concentration is closely correlated to the minima in tidal height. With rising water level I_2 disappeared as fast as it appeared.

The complete I_2 time series with corresponding tidal height is given in Figure 6.3.

Comparison of I_2 Appearance at Different Measurement Sites

I_2 was observed for the first time in Mace Head during the 2002 NAMBLEX campaign by *Saiz-Lopez and Plane* [2004]. They reported I_2 concentrations of up to 93 ppt at night (and 25 ppt during daytime) by using active long-path DOAS technique. The peak concentrations appeared closely correlated to low tide.
Although a generally strong appearance of macroalgae was found at the coast of Brittany no evidence for the appearance of I_2 above the detection limit of $\sim$20 ppt was found.

However I_2 was found up to 60 ppt during the 1998 Mace Head campaign, representing the second observation of I_2 in Mace Head, the question about the differences to other coastal regions arises.
These differing observations are not to explain by the analysis method, as they were identical (see Section 3.5.3) for the data sets of all campaign sites (2002 North Sea and 2003 Brittany).
Mace Head and the coast of Brittany have in common the strong appearance of similar and identical macroalgae species, like the laminaria, which is known for its high content of iodine. The *Laminaria Digitata* (see photo on right side of Figure 6.1) is commonly found in the lower intertidal and sublittoral fringe down to a maximum depth of 20 m in clear waters, where sunlight is still sufficiently available. Hence, the laminaria is not frequently exposed to ambient air, except for times of spring tide, when the water reaches exceptionally low levels. Assuming laminaria species exposed to the atmosphere as the source of molecular iodine in the gas phase, the observations of I_2 on October 5th, 6th and 7th in Mace Head, where a fast increase of I_2 was detected with concentrations of more than 50 ppt on three consecutive nights, closely correlated to exceptionally low water during spring tide would be well explained.
During the time of springtide the sea level is about 0.6 m lower than at normal low tide periods. As can be seen in the close up look in Figure 6.2 where the concentration exceeds very fast the 30 ppt mark if the water level decreased below the normal low tide minimum of 0.64 m. These extraordinarily strong I_2 levels were observed uniquely at the end of the campaign, although this could be as well expected for the beginning of September, due

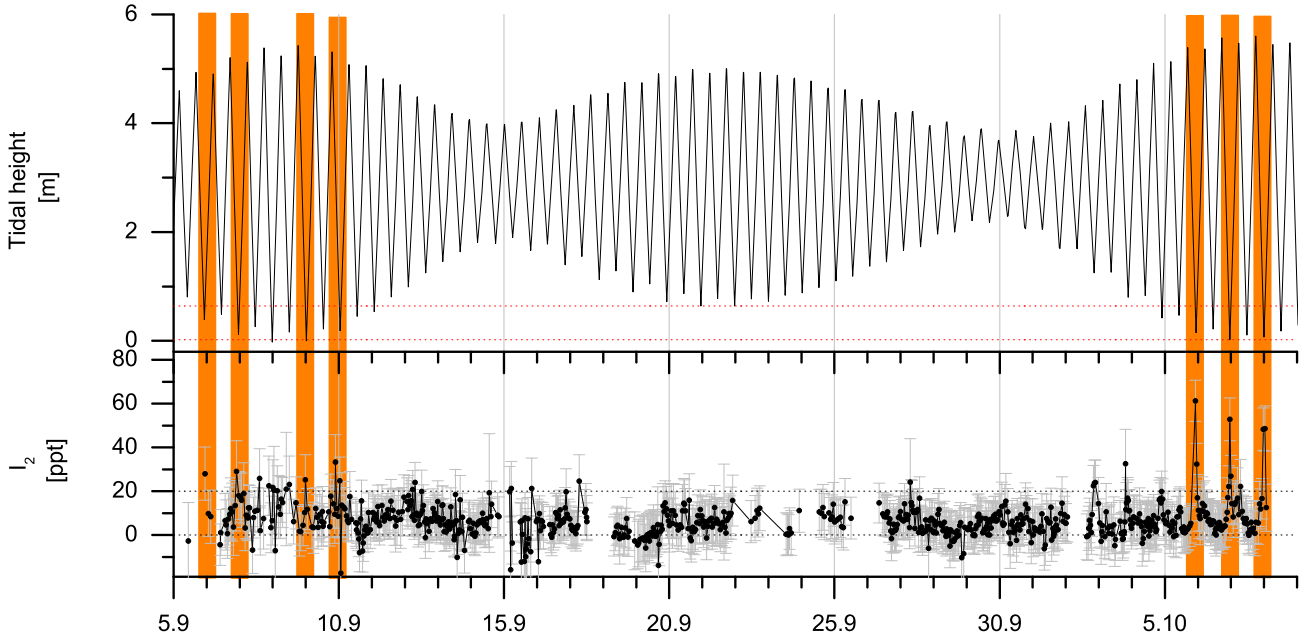

Figure 6.3: *I_2 time series of the Mace Head campaign in 1998. The dotted line indicates the mean detection limit of 20 ppt.*

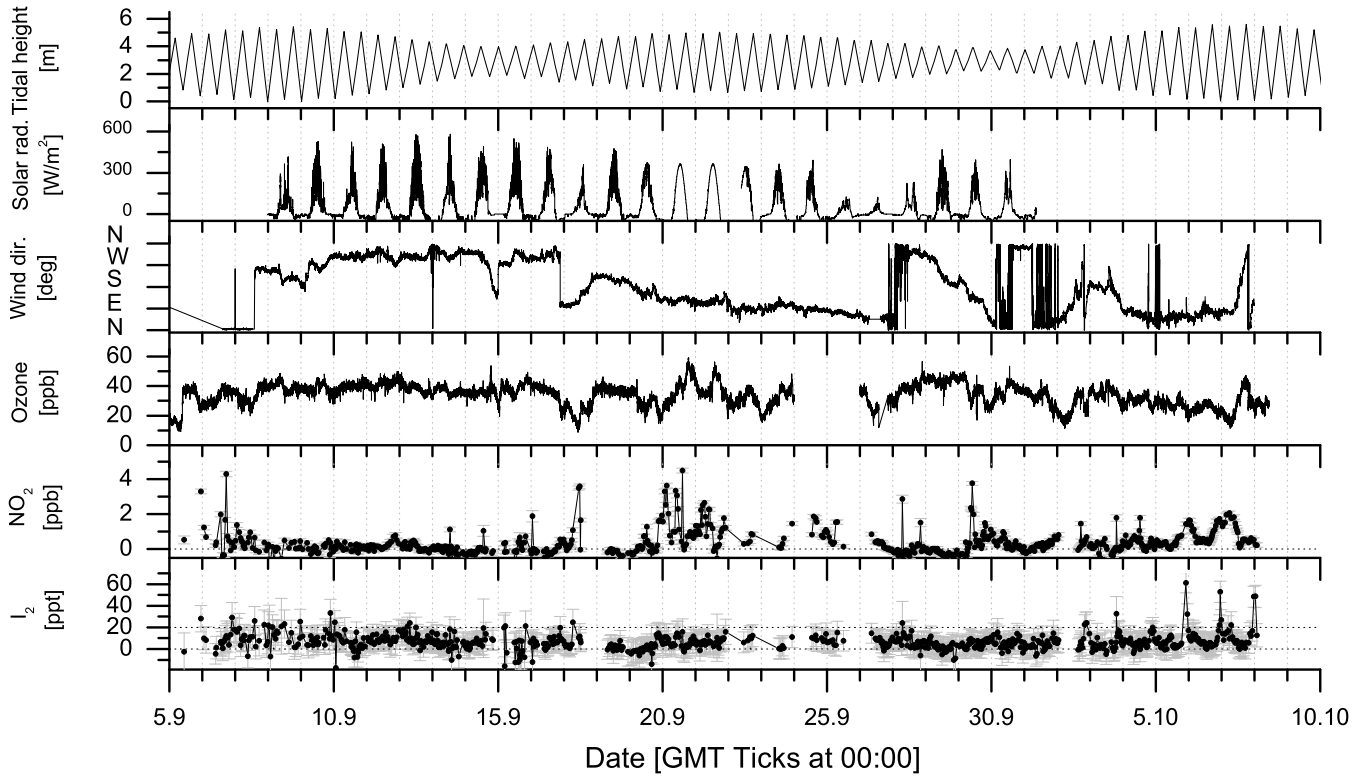

Figure 6.4: *The time series for the 1998 PARFORCE campaign in Mace Head. Tidal height, meteorological parameters besides NO_2, I_2 and O_3 are shown.*

to the spring tide conditions.

Impact of Wind Direction

On 5th to 7th of October the wind came from easterly directions (see Fig. 6.4), where extended algae fields were found (see Figure 6.1). The correlation to the wind direction from the east was missing in the beginning of September, where elevated levels of iodine were observed as well, but where the peak concentrations were not as pronounced as on 5th to 6th an 7th of October. During the normal low tide period in the middle of the campaign, no clearly elevated levels were found, despite the eastern wind direction. If macroalgae inhabiting the lowest part of the intertidal zone are assumed as the source for observed I_2, the fast rise and disappearance of I_2 would be well explained. This indicates as well, that these algae would have huge production rates, in times they are exposed to ambient air due to the limited area that is affected in times of springtide, with just 0.6 m difference in water level.
That picture fits also to the observations in Brittany.

Comparison of I_2 Appearance in Brittany

In Brittany a great variety of different algae was found, regularly exposed to the atmosphere over extended areas during tidal minima, but no evidence for elevated I_2 emissions. Since the laminaria species preferably inhabit areas unaffected by the tide, the plants are located far off the coast due to the high tidal range of up to 14 m, which represents the highest range in Europe. However the laminaria species were present in Brittany but they were not observed to be exposed to the atmosphere during the campaign.

Although these results suggest that only some exclusive algae species are able to emit I_2 in some way to the gas phase, a potential impact of the biological state and age of the plant on the I_2 emissions cannot be excluded. Both campaigns in 1998 and 2002 in Mace Head, where I_2 was found to be present were conducted in late summer and autumn, whereas the campaign in Brittany was conducted in spring.

Furthermore, it has to be mentioned that it cannot be excluded that I_2 is maybe present below the detection limit of about 20 ppt, which would have a considerable impact for atmospheric chemistry as pointed out before (see Section 5.2.5).

Chapter 7

Kuujjuarapik, Hudson Bay

Atmospheric research in the Arctic became more and more important over the last 2 decades for a variety of different reasons. Climate variability and change, seen most notably in reduced sea ice extent and thickness as well as an increase in UV radiation and accumulation of anthropogenically emitted persistent organic pollutants (POPs, e.g. PCBs) already have strong and measureable impact on the arctic environment and ecosystem. Frequently the Arctic is referred to as an early global warning system for climate change since the changes are particularly intensely manifested by recent observations. The average temperature in the Arctic has risen almost twice the rate as in the rest of the world during the past decades. Widespread melting of glaciers and sea ice and rising permafrost temperatures present evidence of strong arctic warming [*ACIA 2004* 2004].
The drastic impact of halogens/halogen oxides on atmospheric chemistry, especially the impact on ozone is well established for the stratosphere. The occurrence of BrO in the troposphere also strongly affects the lower atmosphere's chemistry which has been observed most drastically in the polar regions during periods of complete boundary layer ozone depletion [*Hausmann and Platt* 1994; *McElroy et al.* 1999].
The interaction of reactive bromine species with mercury is most likely responsible for the enrichment of mercury in arctic mammals and especially people who rely on subsistence hunting and fishing in many arctic communities. This represents a strong impact on the arctic ecosystem in general and has no foreseeable consequences. Already today over 50% of people living in the Canadian Arctic have mercury levels above WHO limits [*AMAP* 1997].
Trend studies of BrO in the troposphere and stratosphere by *Hollwedel* [2005] based on satellite data for the period of 1996 - 2001 show that areas in the

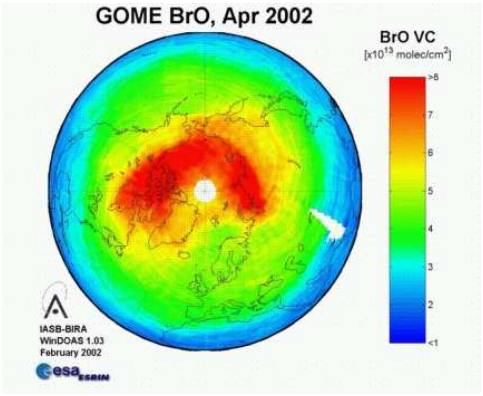

Figure 7.1: *Satellite map of the northern hemisphere, showing an extended BrO cloud over the Hudson Bay area. Map is taken from BIRA-IASB*

troposphere covered by BrO clouds increase in the northern hemisphere about 10% per year. An outline on the current knowledge of halogen chemistry, focused on bromine species is already given in Chapter 2, the reader is also referred to the comprehensive and recent review of *Lehrer et al.* [2004]. However, the impact of bromine chemistry on Arctic and Antarctic atmosphere is subject of a number of recent studies and many open questions remain. It is still unclear what triggers a bromine explosion event, how other halogens (Cl and I species) are involved and what the sources are (see short discussion on the possible role of frost flowers in Section 2.4.1). Seasonality of BrO events and the impact of meteorological conditions like the stability of the boundary layer have still to be explained.

Within this context, an extensive field campaign was conducted in the lower Arctic at the Hudson Bay. The latitude of Kuujjuarapik is 55°N, which is not further north than locations at the German North Sea Coast. However, Kuujjuarapik is clearly influenced by arctic conditions.
On satellite maps the appearance of extended tropospheric BrO clouds has been observed regularly in the Hudson Bay area, including the southern part of it, down to the James Bay (see Figure 7.1).

As can be seen on maps from satellite data in Figure 7.2 the conditions to observe BrO events, which are usually correlated to ozone depletion are excellent in the month of March. The monthly averaged VCDs of BrO in the region of the Hudson Bay is illustrated for the years 1996-1999 [*Hollwedel*

2001]. Highly elevated BrO over extended areas in the northern hemisphere is observed during the months March and April, whereas in May no significantly elevated levels of the radical could be seen.

In the framework of the 2004 Kuujjuarapik campaign at the Hudson Bay, measurements of the biological activity in form of measurements of VHOCs were conducted at this location the first time ever. Additionally one MAX-DOAS and two Mini-Max-DOAS instruments were installed to achieve information on vertical distribution and the appearance of other halogen oxides (e.g. IO, ClO), besides information on spatial distribution by installing the MAX-DOAS instruments at different locations. To be able to study the interaction of RHS with mercury, TGM measurements were performed by the group of Poissant et al. of Meteorological Service of Canada, Montreal.

For the reason described above, the campaign was conducted from March 1st to beginning of April 2004. Kuujjuarapik (55°N) represents the nearly southernmost location where BrO events have been observed in the troposphere (see Figure 7.1 and 7.2). On the satellite maps elevated concentrations seem to be limited to the northern part of the Bay, whereas the southernmost part, the James Bay is normally unaffected by stronger events.

7.1 Description of the Measurement Site

From March 1st to April 3rd 2004 a field campaign in the lower Arctic of Canada was conducted. The research station of the CEN (Centre d'Etudes Nordiques) in the small community Kuujjuarapik-Whapmagoostui, Quebec, at the south-east coast of the Hudson Bay provided logistical and technical support for the campaign. Geographically the site is located in a mid-latitudinal region on 55.29 N, 77.75 W, note the comparable latitude to one of the previous measurement sites in Dagebüll, Germany in 2002. A map with the measurement site is indicated in Figure 7.3.
The distance of Kuujjuarapik to the next big city Montreal is about 1500 km. Due to the great distances, the small village with only 1200 inhabitants is not connected by a road system, hence it is only accessible by aircraft, except a short time during summer, when the ship traffic on the Hudson Bay is feasible.
For the DOAS measurements a small cottage 3 km outside the village was rented, to provide measurements with viewing direction over the frozen Hudson Bay. The cottage was not connected to the electric network, so electric-

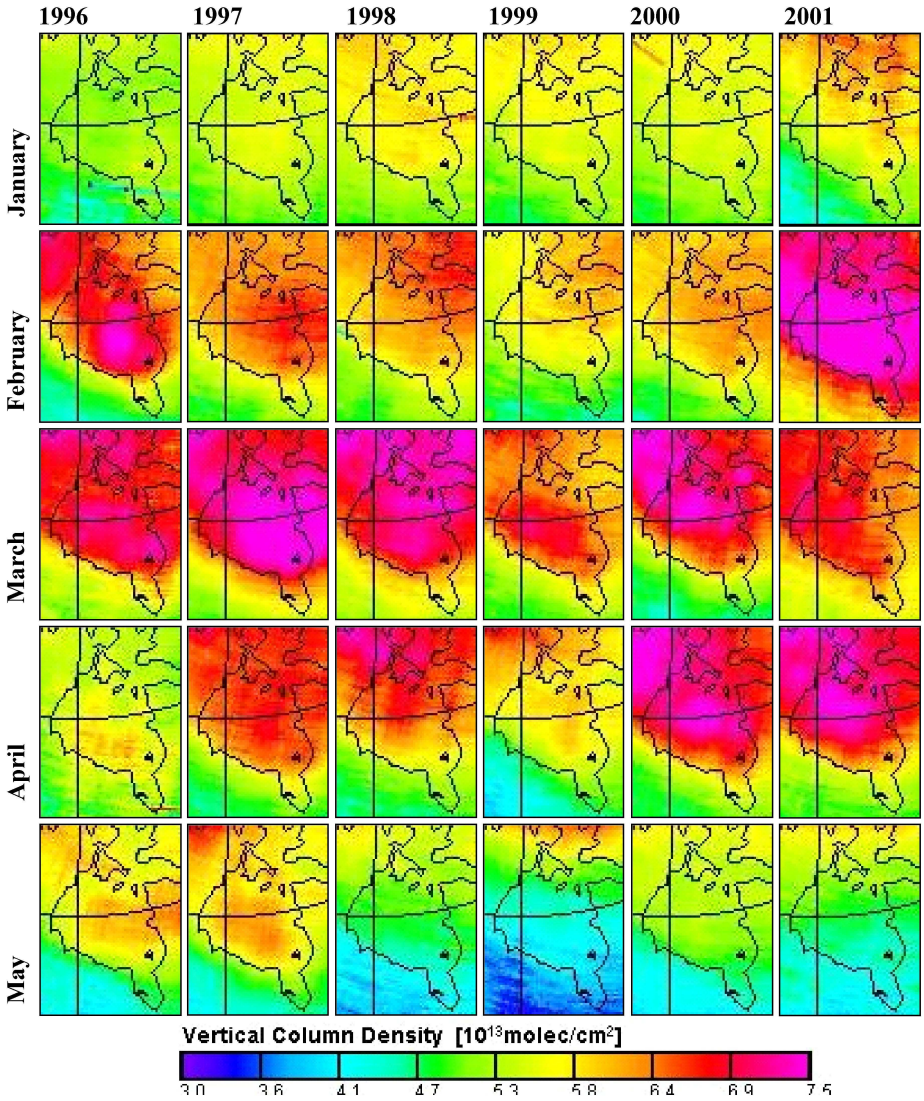

Figure 7.2: *Monthly averaged tropospheric BrO VCDs by satellite observations for the years 1996 - 2001, [Hollwedel 2001].*

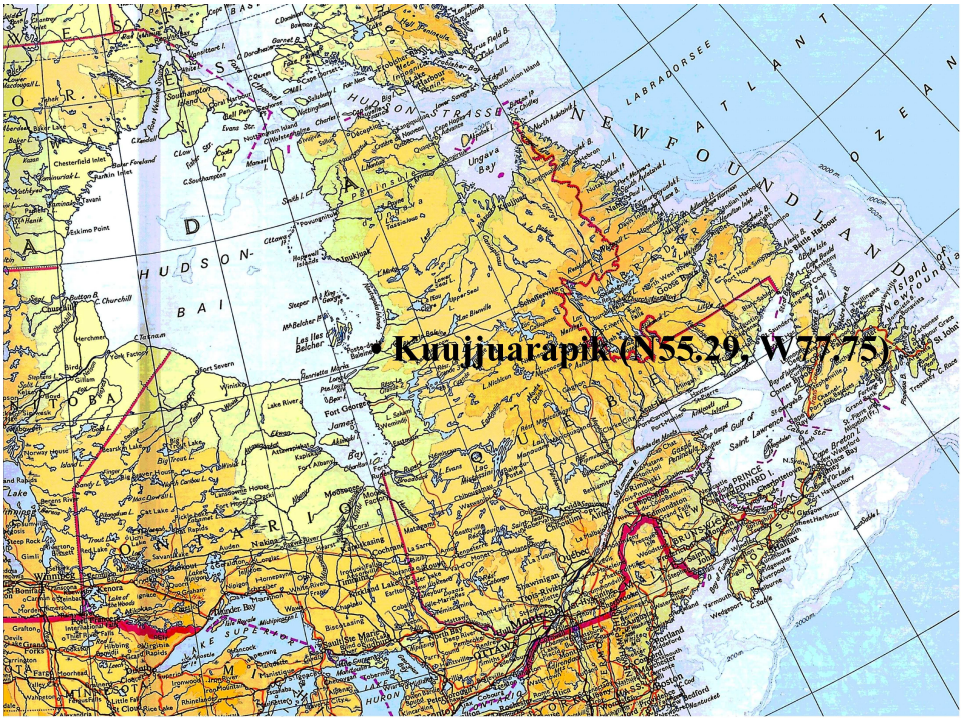

Figure 7.3: *Overview map on the region of the Hudson Bay. Kuujjuarapik (55.29 N, 77.75 W) is located in the south-east of the Bay, 1500 km north of Montreal.*

ity had to be provided by locally available generators. Due to difficulties in realizing a stable power supply, measurements with the longpath DOAS instrument were reduced to the second half of the campaign time.
A map of Kuujjuarapik with indicated position of the DOAS instrument, the research station and the set ups of the lightpaths is shown in Figure 7.4.

7.2 Measurements in Kuujjuarapik

In the following section the operated instruments and the meteorological conditions during the campaign are explained. The results of the main instrument the longpath DOAS telescope as well as a summary of the results of the collaborating groups is given.

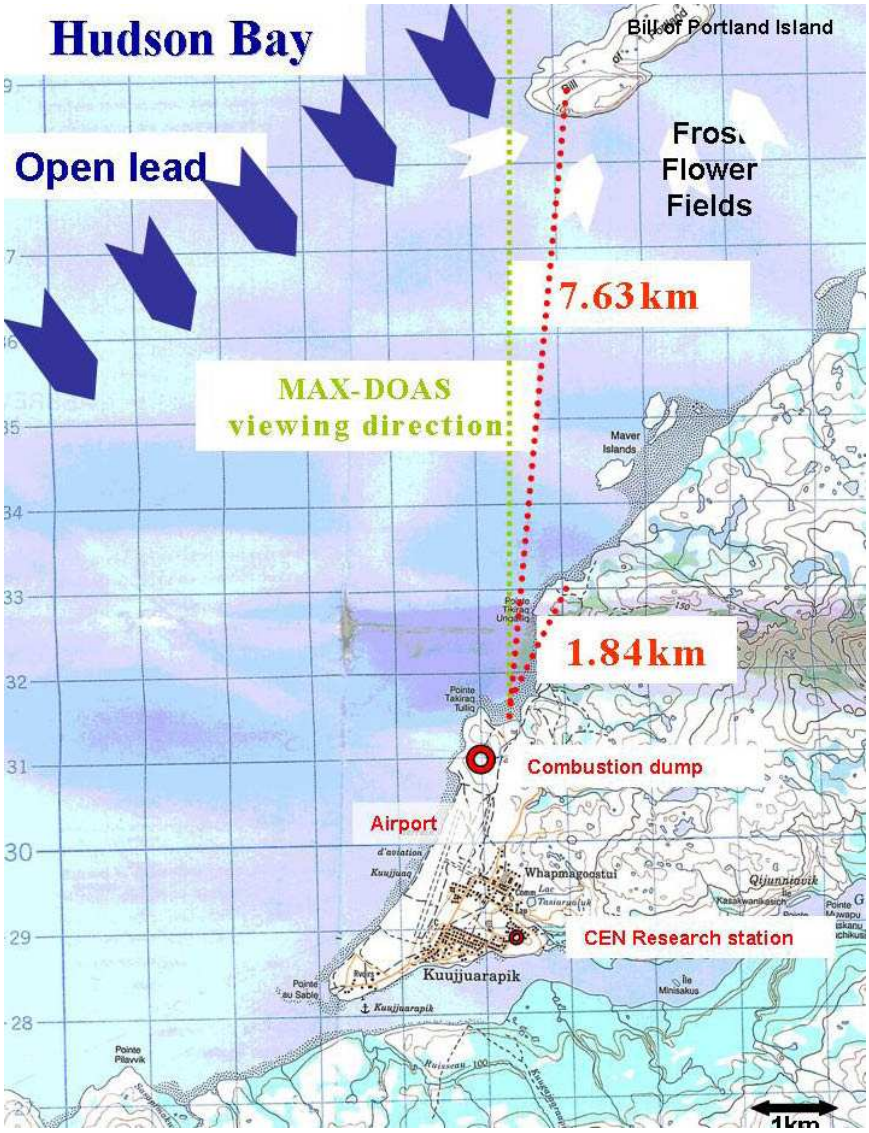

Figure 7.4: *Map of Kuujjuarapik. The measurement site was located ∼3km outside of Kuujjuarapik. Both, MAX-DOAS (viewing direction along the green line) and longpath DOAS instruments (viewing directions of two lightpaths: red lines) were installed with similar viewing directions to the Bill of Portland islands over the frozen Hudson Bay. Airport area and location of the dump are indicated on the map. The research station is located within the small village at the Great-Whale river. At the station two Mini-DOAS systems were installed by G. Hönninger with south-westerly viewing directions.*

7.2.1 Instrumental

At the research station a weather station of the CEN is installed and the extended data is provided. Since the DOAS telescope and the additional instruments were installed several kilometers outside of the village, a meteorological station of HMT Hoffmann Messtechnik was set up next to the cabin of the DOAS instrument. Measurements of solar radiation, wind speed and direction, pressure and temperature were performed. With minor exceptions (partly explained by the different locations), these data agree well with that of the weather station of the CEN in the village.
An in-situ ozone monitor of Horiba was operated for additional and continuous ozone measurements with a sampling time of 5min. A comparison of both, the in-situ O_3 monitor operated at the CEN station and the Horiba monitor outside at the Hudson Bay was done as can be seen in Figure 7.13.
Additionally to the longpath DOAS measurements a Multi-Axis (MAX)-DOAS instrument was installed with viewing direction nearly parallel to one of the lightpaths of the active DOAS instrument(Fig. 7.4). The MAX-DOAS measurements were performed and evaluated by F.Filsinger in the framework of a diploma thesis [*Filsinger* 2004] at the Institute for Environmental Physics, Heidelberg.

With the active long path DOAS instrument mainly measurements in the wavelength range of BrO absorption were performed (at a center wavelength of 335 nm and a 80 nm window). In this range also O_3, NO_2, SO_2 and HCHO show narrow banded absorption structures and were evaluated, too.
During the blizzard on March 21st ice and snow entered the cottage through the uncovered window. Ice in the mechanic of one filterwheel caused irreparable damage, so that regular measurements of mercury references had to be cancelled and no MCT measurements could be performed from that time on.

7.2.2 Meteorological Conditions

An overview on the weather conditions, taken with the HMT station at the cottage during the campaign is given in Figure 7.6. The temperature was strongly varying from -35.6°C up to +10.1°C, while the normal mean temperature for March is -17.8°C. Untypical for this part of the year is the frequent transport of warm air masses from the South/East to the campaign site as can be seen in the wind frequency distribution diagram of Figure 7.5. Due to these warm periods the Hudson Bay ice broke up over an extended

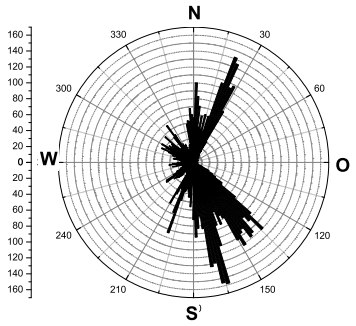

Figure 7.5: *Frequency distribution of the wind direction during the campaign.*

area just few kilometers away from the coast line. The approximated position of the lead is indicated in Figure 7.4 and a picture of the open lead is shown in Figure 2.7.
Solar radiation remained over the whole campaign time below 750 W/m^2 and reached on several days only 250 W/m^2. Regarding the wind speed panel, two periods with wind speed rising up to more than 12 m/s can be seen. The strong wind was accompanied by heavy snow (blizzard), so that DOAS measurements during these periods were strongly disturbed.

Local Pollution

The region of Nunavik is twice as big as Germany but nearly uninhabited. Only 10,000 people live in 14 small communities along the coast of the Hudson Bay, Hudson Strait and Ungava Bay. The environment is therefore nearly unaffected by the local human activities. Local traffic by trucks, the more common ski-doos and the local power plant could not be seen as elevated NO_x levels in the DOAS measurements. The airport is located close to the site and since the village is only accessible by plane during winter months, on average two planes arrived there per day. A clearly detectable influence on the NO_2 abundance was seen, when the waste of the local garbage dump was combusted. Since this was only the case in times of southerly wind flows, the effect of NO_2 and SO_2 levels detected by the DOAS measurements did not affect the interesting BrO events, which were generally associated with north-westerly airflows from arctic regions, which are representative for clean background conditions.

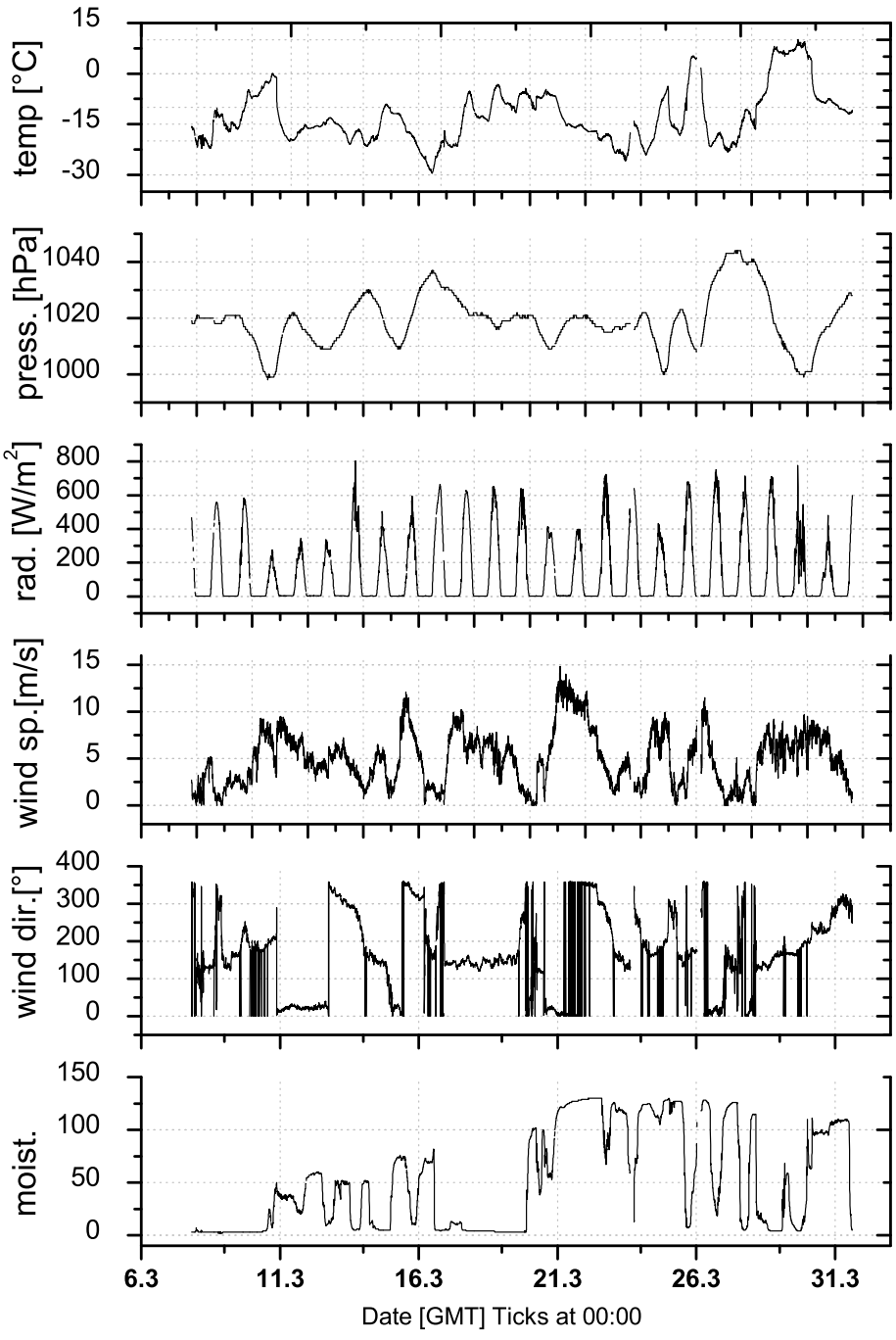

Figure 7.6: *Weather conditions during the campaign in Kuujjuarapik starting from March 6th. The temperature ranged from less than -30° C up to more than +10° C. The blizzard conditions are indicated by the stormy periods on March 21st and March 15th.*

7.2.3 Lead and Frostflowers

Frostflowers are ice crystals which grow typically on refrozen leads or in the vicinity of polynyas (openings between drift ice). Due to the significantly enhanced salinity, frostflowers are thought to be a potential halogen source for the bromine explosion (see 2.4.1).
Since the beginning of the campaign an extended lead in the ice of the Hudson Bay could be observed not far away from the coast line. The approximate extension and position of the lead in the sea ice cover is indicated by the blue arrows in Figure 7.4. Responsible for the open lead are high wind speeds, blowing the ice away from the coast in combination with the transport of warm air masses from the south. The observed lead opened up for a duration of hours or days. The lead either closed when onshore winds pushed the ice pack back or it refroze when cold (polar) air masses reached the site and the temperature decreased. In the area of the Bill of Portland island several fields of frostflowers could be observed at tidal cracks in the sea ice. The assumption that extended fields of these frostflowers could be growing in the vicinity of the lead could not be verified, but is very likely. Generally the extension of open water areas was increasing during the campaign, which could be well verified by maps of sea ice coverage, provided by the Uni Bremen [*Kaleschke et al.* 2001]. In Figure 7.7 the area of the Hudson Bay and the thickness of the sea ice is indicated day by day for the whole campaign time. The spatial resolution of these maps is too poor for detailed analysis of the smaller lead at Kuujjuarapik. However a general trend of increasing areas with thin ice or broken up areas can be observed for the whole area of the Hudson Bay.

7.2.4 Longpath DOAS Measurements

Lightpath

The possibilities to measure across the Hudson Bay were constrained by the topography. The long lightpath was set up towards the Bill of Portland island over a distance of 7627 m, with a retro-reflector array mounted at a height of ∼30 m on a rock. The short lightpath with a length of 1840 m was set up towards a small peninsula, with a retro-reflector array in a height of just 12 m above the ice surface of the Bay.
The decision to operate on the long or short lightpath was not only dependent on the actual weather and visibility conditions, but also on snow drift and wind direction. Frequently the reflectors had to be cleaned from snow cover. Therefore the majority of the measurements were performed on the

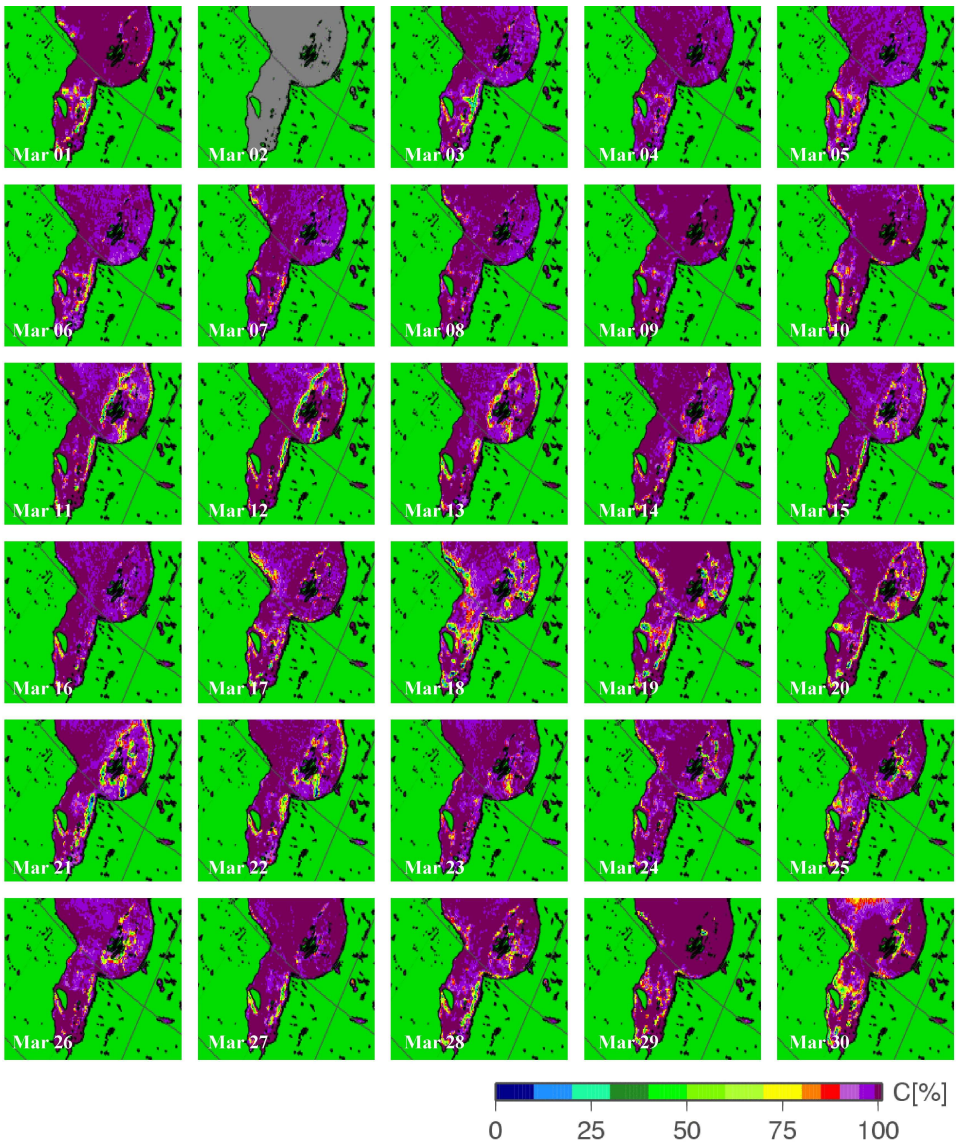

Figure 7.7: *Day to day map of ice coverage in the area of the Hudson Bay. These maps are provided on the web by the University of Bremen [Kaleschke et al. 2001]. A clear increase of areas with broken surfaces from beginning to end of March can be observed.*

short lightpath, because the reflector of the short lightpath was accessible by a walking while the Bill of Portland island had to be accessed by ski-doos,

which were not available all the time.

Measurements of BrO

Active longpath measurements were performed between 19th March and 1st April 2004. The longpath DOAS instrument is described in detail in Section 3.2.1. Spectra were recorded mainly in the near UV (335 ± 40 nm) and in the blue spectral range (430±40 nm) for the measurement of the halogen oxides BrO and IO. Due to the problematic weather conditions described above, mainly the short lightpath was used for the measurements. The length of the absorption path was therefore a factor ∼4 shorter than that of the long lightpath. Hence, measurement errors and average detection limits are in general 4 times higher.
BrO and ozone were analyzed in the 310-330 nm range, where 5 strong absorption bands of the BrO molecule are found. An example for the evaluation is given in Figure 7.8.
An overview of the results and the detection limits is given in Table 7.1. Non halogen species like HCHO and SO_2 remained below the detection limit for the entire measurement period. Very rapid ozone depletion, within less than 30 min was detected on March 23rd shortly before sunset. Coincidentally the BrO concentration rose to more than 35 ppt. Within the following 24 hours the ozone recovered to the typical values of 40-50 ppb. The second ozone depletion event was detected between 26th and 28th of March. The ozone decreased slowly over one day down to 10 ppb. However BrO increased during that period up to 20 ppt. Both events are detected in times of north westerly airflows, when the air reaching the site travelled straight across the frozen Hudson Bay. Whereas the events ended always closely correlated to a change in the meteorologic conditions (wind direction and wind speed) at the campaign site.
The time series of BrO and ozone measurements is shown in Figure 7.9.

Measurements of IO and ClO

IO was evaluated between 418-440 nm comprising 3 strong absorption bands (3-0, 4-0, 5-0) of the electronic transition $A^2\Pi_{3/2} \leftarrow X^2\Pi_{3/2}$. Besides IO, references of NO_2, H_2O and O_4 and a daily recorded lamp reference spectrum was included in the DOAS fit. Slight variations ($< 10^{-3}$) of lamp features in the references were the limiting factor of the IO analysis. However, due to the short lightpath, the detection limit is on average 2.1 ppt as can be seen in Table 7.1 and no identification of the IO absorption structure

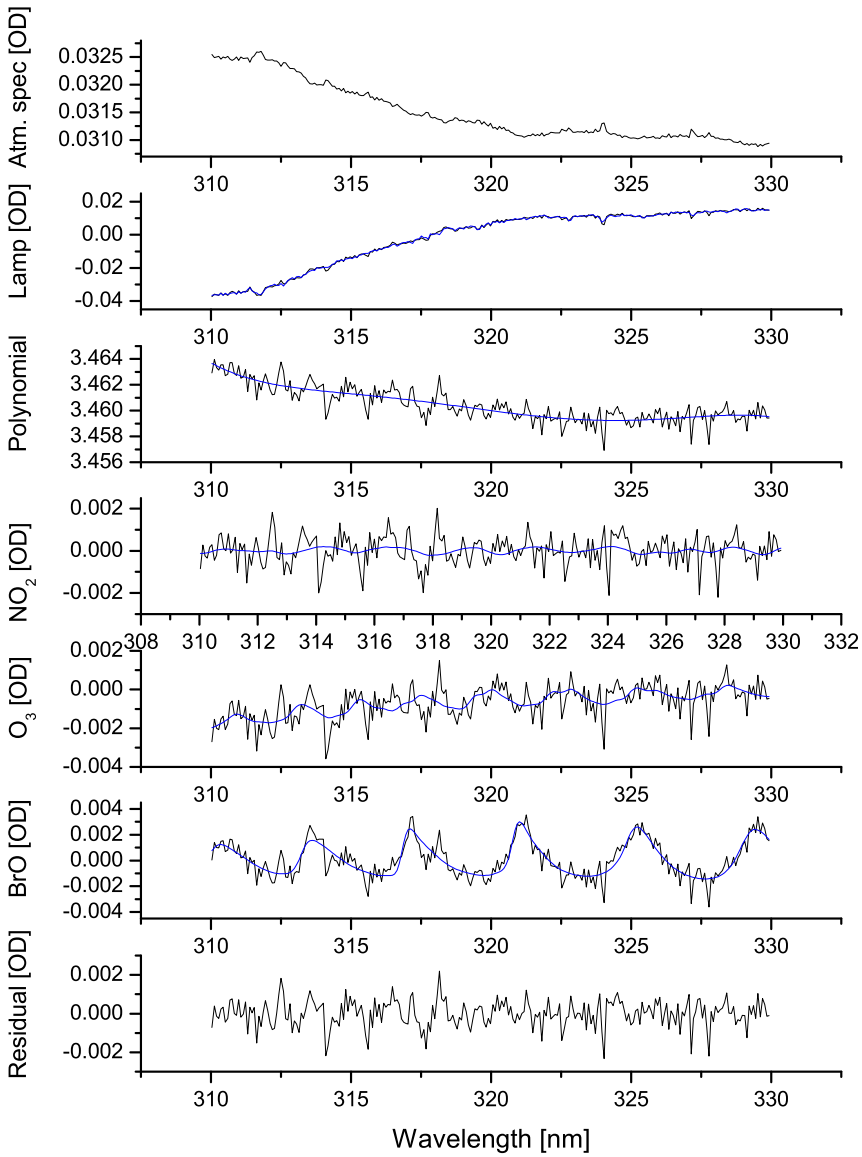

Figure 7.8: *Sample evaluation for BrO, taken on 23rd March, GMT 22:38 during 2004 Hudson Bay campaign. The concentration of BrO corresponds to 34.3 ± 4.8 ppt.*

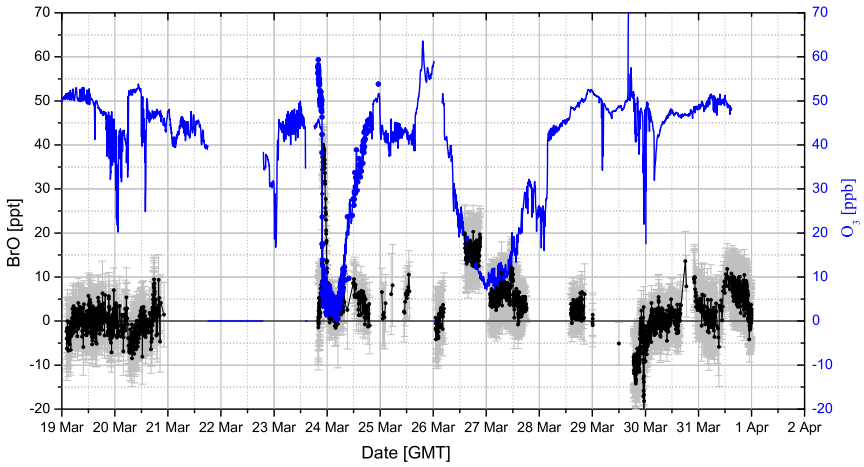

Figure 7.9: *Time series of BrO and ozone taken during 2004 Hudson Bay campaign.*

Species	*Av.D.L.*	*Av.conc.*	*Max conc.*
BrO	5.5 ppt	2.9 ppt	35.8 ± 4.6 ppt
O_3	4.9 ppb	44.8 ppb	64.8 ± 5.4 ppb
NO_2	0.2 ppb	0.1 ppb	0.4 ± 0.2 ppb
SO_2	0.4 ppb	0 ppb	< D.L.
HCHO	0.6 ppb	0.2 ppb	< D.L.
IO	2.1 ppt	0.3 ppt	< D.L.

Table 7.1: *Overview over the resulting concentrations and detection limits for the evaluated species during the 2004 Hudson Bay campaign. The relatively high detection limits are due to the short lightpath, which was frequently used.*

above the residual could be reported.
During one afternoon, measurements in the 300±40 nm range were performed to optimize the signal to noise ratio in the 300 nm range for the detection of ClO. However, the light intensities in this wavelength range are very low and long exposure times were necessary to obtain spectra for the

evaluation. The remaining residual remained above $2 \cdot 10^{-3}$ peak to peak, which corresponds to a detection limit of 37 ppt, assuming the length of the absorption path of 15.2 km. The detection limit of more than 30 ppt was too high to detect potentially realistic concentrations of few ppt.

7.2.5 MAX-DOAS Measurements

MAX-DOAS measurements were conducted during the Hudson Bay campaign simultaneously and parallel to the longpath DOAS measurements (viewing direction of the instrument is indicated in Figure 7.4 with a green line). These measurements were performed and evaluated in the framework of a diploma thesis at the Institute for Environmental Physics [*Filsinger* 2004]. Therefore only a short summary of the results is presented in this work. The time series of the MAX-DOAS measurements for BrO is shown in Figure 7.10. During the measurement period from March 19th to April 2nd 2004, tropospheric BrO above the detection limit was found on March 23rd, 26th, 30th, and 31st. The detection limit was assumed to be the 2σ fit error.

As it was shown in several studies [*Leser et al.* 2003], [*Hönninger et al.* 2004], the MAX-DOAS technique represents a highly sensitive detection method for trace gases located in the boundary layer. On the basic idea of MAX-DOAS so-called Mini-MAX-DOAS systems [*Bobrowski* 2002] were developed, which are small and light weight. Besides the MAX-DOAS measurements parallel to the longpath measurements, 2 Mini-MAX-DOAS instruments were operated at the research station in the village with southwesterly viewing directions. One of the instruments was equipped with a spectrometer set to the wavelength range 330-470 nm, providing measurements of IO and NO_2. The second instrument was equipped with a spectrometer set to the wavelength range 300-430 nm, which covers the strongest absorption bands of the BrO molecule. The time series for the resulting BrO and O_4 $\Delta SCDs$ from the Mini-Max-DOAS system is shown in Figure 7.11.

7.2.6 Measurements of VHOCs

For a more comprehensive understanding of atmospheric processes and chemistry during polar ozone depletion events measurements of our own group were supported by additional participating groups. Within the project the group of Heumann et al. of the University of Mainz conducted measurements on VHOCs as for the field studies at the North Sea and Brittany before. The biological activity in this arctic region during the campaign was

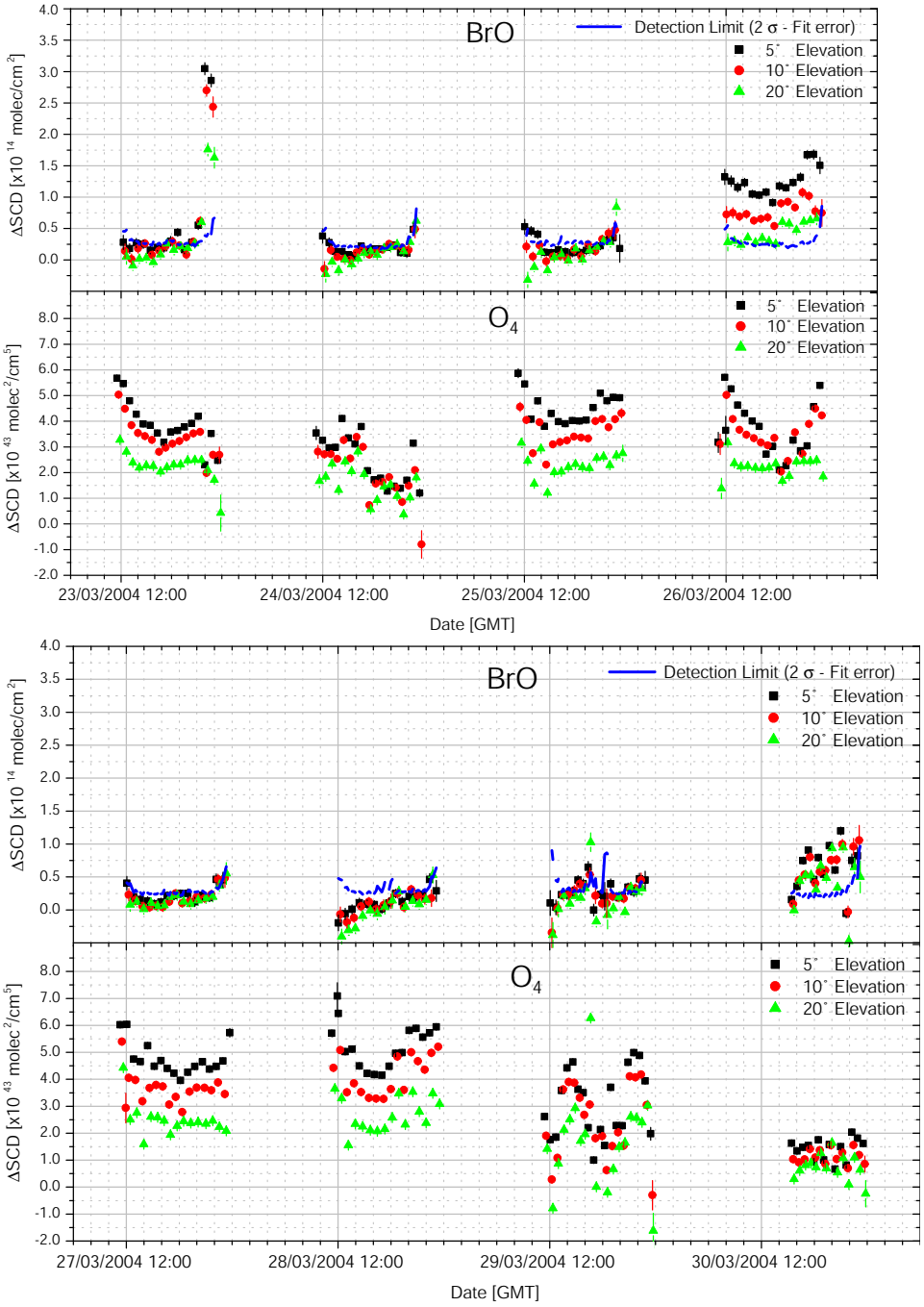

Figure 7.10: *Results of MAX-DOAS measurements during 2004 Hudson Bay campaign. The instrument was set up with nearly parallel viewing direction to the active LP-DOAS instrument. Adapted from Filsinger [2004]*

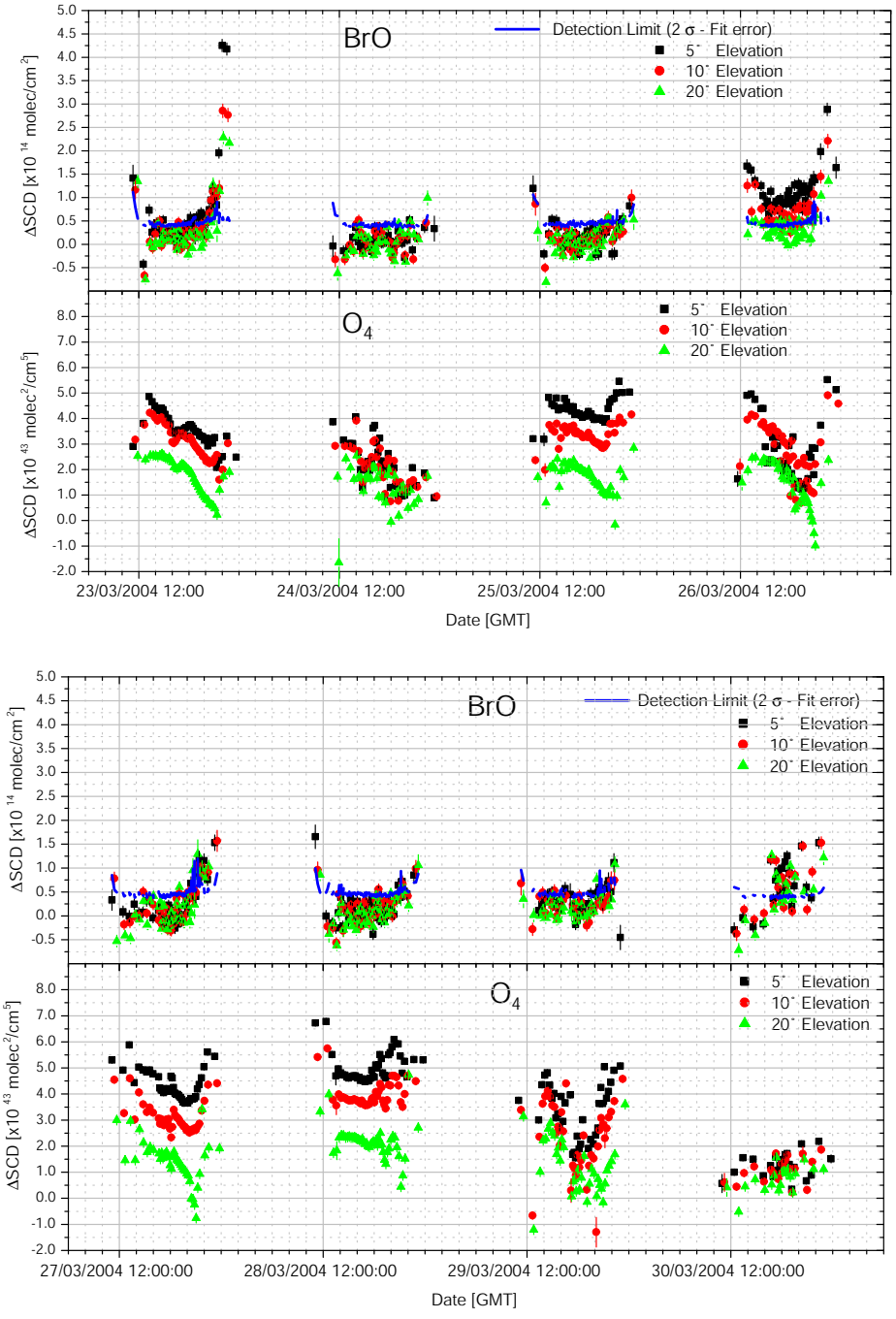

Figure 7.11: *Results of UV-Mini-MAX-DOAS measurements. The instrument was operated at the CEN research station with south-westerly viewing direction. Adapted from Filsinger [2004].*

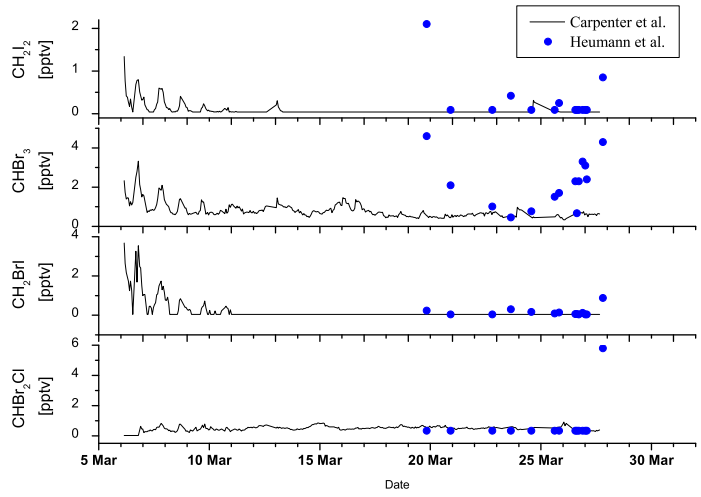

Figure 7.12: *Comparison of some organohalogen measurements taken during 2004 Hudson Bay campaign by Carpenter et al. and Heumann et al..*

assumed to be low and air sample tubes could not be easily exchanged as in previous campaigns. The number of air samples was therefore limited to 25, but they were all taken if coinciding DOAS measurements were performed, that means that air samples were taken in the second half of the campaign, including a profile (∼2 hours steps) of one day.
VHOCs were also measured by the group of Carpenter et al, University of York, UK. The group operated an automated GC-MS with a time resolution of 30 min. The instrument was installed in laboratories provided by the research station. The comparison of these two data sets is shown for the organohalogens CH_3Br, CH_2BrCl and the photolytically short-lived compounds CH_2I_2 and CH_2IBr in Figure 7.12. Carpenter et al. found elevated levels of most organohalogens in the beginning of the campaign from 5th to 10th of March. After that date no significant concentrations of organohalogens were found. Measurements of organohalogens of Heumann et al. were sampled from the 19th of March, when additional DOAS measurements were performed.

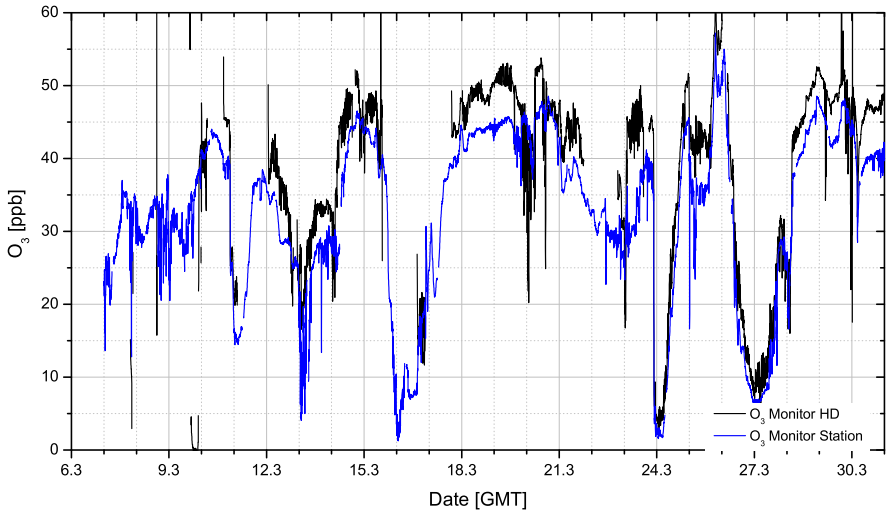

Figure 7.13: *Comparison of two in-situ ozone monitors. The Horiba monitor (black line) was installed next to the DOAS telescope at the Hudson Bay, the second monitor of Poissant et al. (blue line) was installed at the CEN research station ∼2 km away. Both monitors had a sampling time of 5 minutes. With respect to the different measurement sites, smaller differences could be explained. However the systematic difference for ozone concentrations above 40 ppb is probably due to calibration errors.*

7.2.7 Comparison of Ozone in-situ Monitors

The Horiba ozone monitor was operated in the cottage, next to the DOAS telescope. For comparison the data of the ozone monitor installed by Poissant et al. at the CEN research station was kindly provided. The comparison shows some disagreements in the range of concentrations above 40 ppb, see Figure 7.13

To compare the in situ data with the results of the active longpath data one has to keep in mind that the cross section for O_3 is strongly temperature dependant in the UV range. Cross sections for ozone are available for 246 K and 280 K. Since the temperature was varying significantly, the fitting procedure was partly difficult and obviously structures belonging to ozone remained.

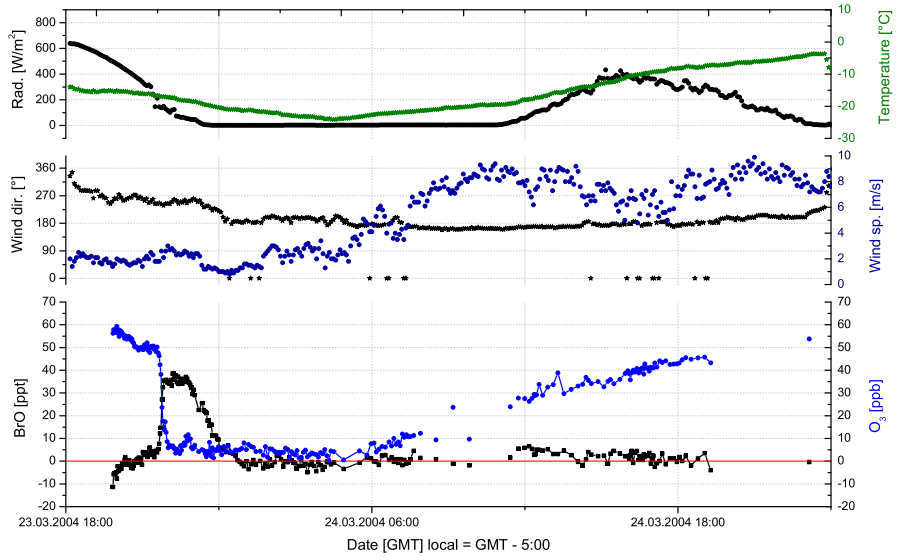

Figure 7.14: *The BrO event of March 23rd. At 17:00 local time, the BrO mixing ratio increased within 30 minutes to more than 35 ppt, while the ozone was nearly completely destroyed.*

7.3 Discussion of Results from Hudson Bay Campaign

In the following the two observed ODE (ozone depletion events) of March 23rd and March 26th, with coinciding elevated BrO levels will be discussed.

7.3.1 BrO Event of March 23rd

The major event of the whole campaign happened on March 23rd late in the afternoon. Within 30 minutes the BrO mixing ratio increased from below the detection limit (∼5 ppt) to more than 35 ppt. Correspondingly the ozone level decreased from the typical background value of 50 ppb to below the detection limit. BrO, ozone and corresponding meteorology data for March 23rd is shown in Figure 7.14.
This event happened very late in the afternoon, just before sunset. In Figure 7.14 solar radiation is indicated in the upper panel. At GMT 23:30 it was completely dark, and the BrO concentration decreased rapidly to

values below the detection limit (5 ppt) within the following ∼30 minutes. The measurements provide excellent time resolution of about 3 minutes per spectrum, and the rapid decrease is shown in the lower panel of Figure 7.15. The ozone level remained below 5 ppb for nearly 8 hours and recovered then continuously over 12 hours to the typical concentration of 50 ppb. This recovering process of ozone started slowly at GMT 6:00, in absence of sunlight. The ozone enriched air mass was clearly transported to the measurement site. The origin of these air masses is located in the north west, in direction of the Beaufort Sea as can be seen from the trajectory plots in Figure 7.16.
It should be noted that these air masses do not cross the Hudson Bay anymore, but travel over land surrounding the sea ice surfaces of the Hudson Bay in westerly direction. Closely correlated to the recovering process is the increase in the windspeed from below 2 m/s to more than 10 m/s, indicating already the instabilities of the boundary layer.
The very close correlation of meteorologic parameters, especially to the wind direction and the very rapid decrease of ozone in less than 30 min from nearly 40 ppb indicates that the recorded BrO event cannot be explained by local chemistry. With the current knowledge (see Section 2.4.1) of the bromine explosion, the catalytic ozone destruction by 25 ppt BrO leads to an ozone destruction rate of ∼0.5 ppb/hour. The fast drop in ozone therefore indicates that either the current understanding of the chemistry is not complete or that is is caused by transport processes. Air masses enriched in reactive bromine most likely have destroyed the ozone catalytically over several days, before reaching Kuujjuarapik measurement site. To reconstruct where the air parcels enriched in bromine came from and which way they travelled, backward trajectories with HYSPLIT [*HYSPLIT* 1997] were calculated for March 23rd and shown in Figure 7.17.
In the left Figure a 120 hour backward trajectory of March 23rd, GMT 19:00 is shown. The air masses origin from the northern area of the Nunavut territory and travelled across the Hudson Bay, which represents an extended sea ice surface. The ice fraction observations of [*Kaleschke et al.* 2001] indicate as well, that the Hudson Bay broke up over extended areas during the campaign time with fresh sea water providing brine for frozen surfaces in the vicinity, which could be an efficient bromine supply.

Comparison of Longpath and MAX-DOAS Data

The highest ΔSCD values of BrO with the MAX-DOAS system during the whole campaign were recorded in the late afternoon on March 23rd 2004 in

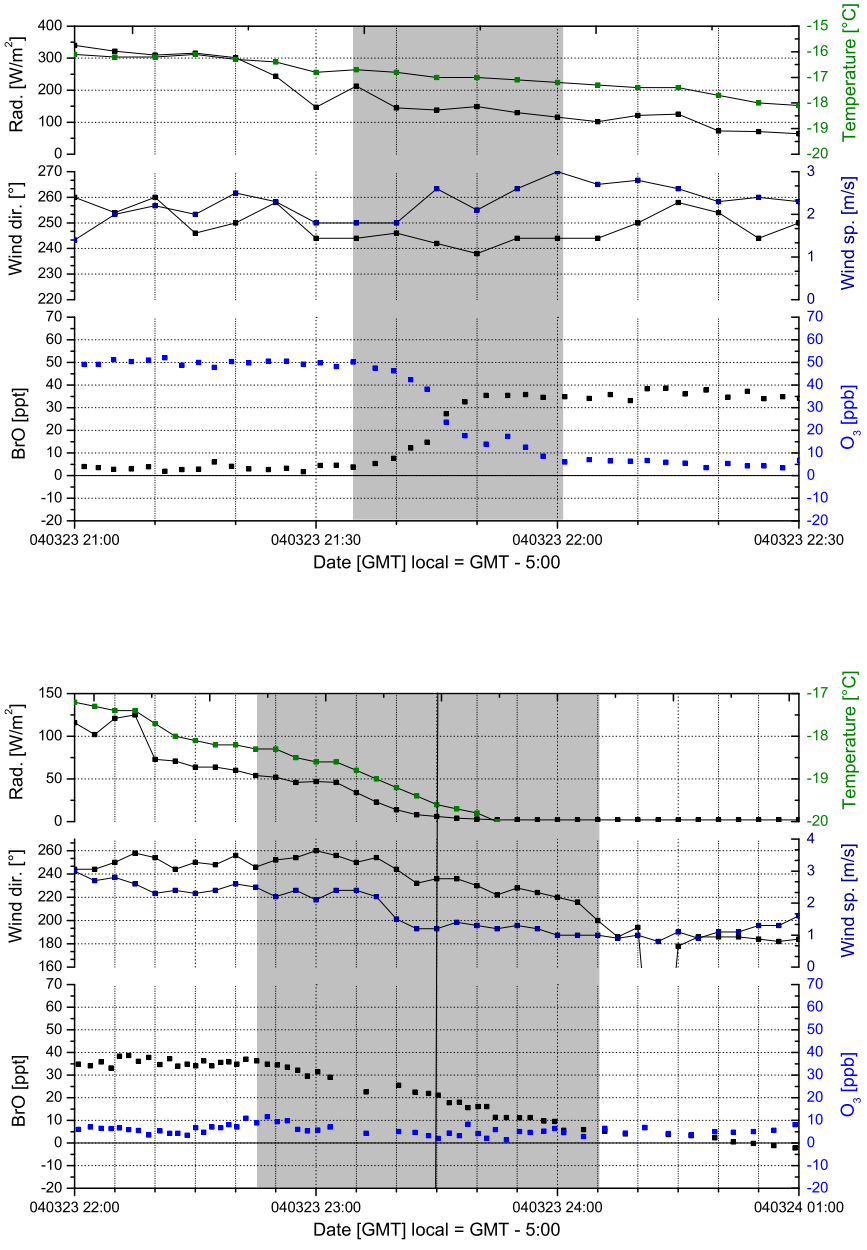

Figure 7.15: *The BrO event of the 23rd 2004 at high time resolution. In the upper panel the fast increase of BrO within 30 min is shown. In the lower panel the rapid decrease of BrO in absence of solar radiation is shown.*

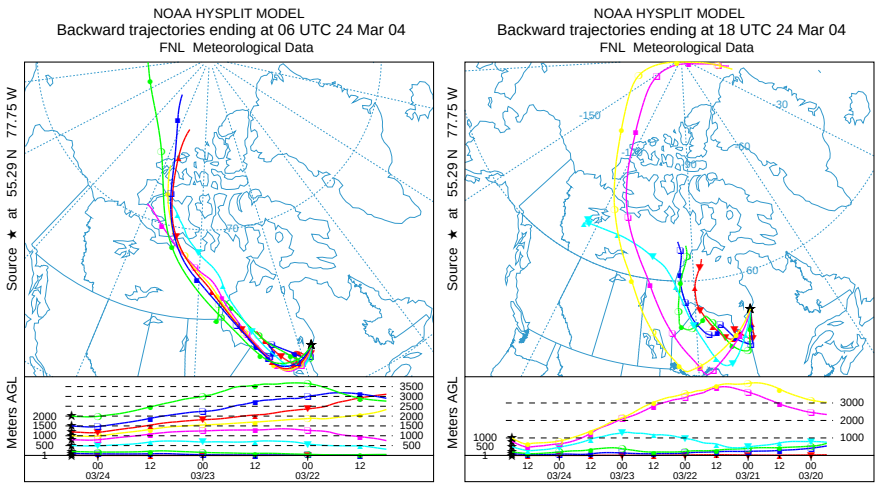

Figure 7.16: *Backward trajectories of March 24th at GMT 06:00 (left) and 18:00 (right). From 6:00 a clock on, the direction of the origin of air masses transported to the site drift continuously westwards, surrounding the Hudson Bay.*

agreement with the longpath DOAS data. These measurements are shown in Figure 7.18 with coinciding ozone levels, recorded with the HORIBA ozone in-situ monitor.

At GMT 22:00 BrO ΔSCDs rose from values close to the detection limit to maximum levels of $3 \cdot 10^{14}$ $molec/cm^2$ for the lowest telescope elevation of 5°. The lower telescope elevations show higher ΔSCDs indicating that BrO is present in the lowest part of the troposphere. Simultaneously, the O_3 mixing ratio recorded by the ozone monitor at the research station dropped very rapidly from 40 ppb to below 10 ppb. A good approximation for the BrO mixing ratio in the boundary layer can be estimated by assuming a typical well mixed boundary layer height of 1 km. By simple geometric calculation, the absorption path within the BL for the 5° telescope elevation angle is 10 km:

$$c(BrO) \leq \frac{3 \cdot 10^{14} molec/cm^2}{1 \cdot 10^6 cm \cdot 2.7 \cdot 10^{19} molec/cm^3} = 11 \ ppt \qquad (7.1)$$

The MAX-DOAS technique relies on sunlight for the lightsource. Since the observed event occurred very shortly before sunset just two measurement points were recorded with low time resolution. A comparison of absolute concentrations of the two different measurement techniques, the active long-

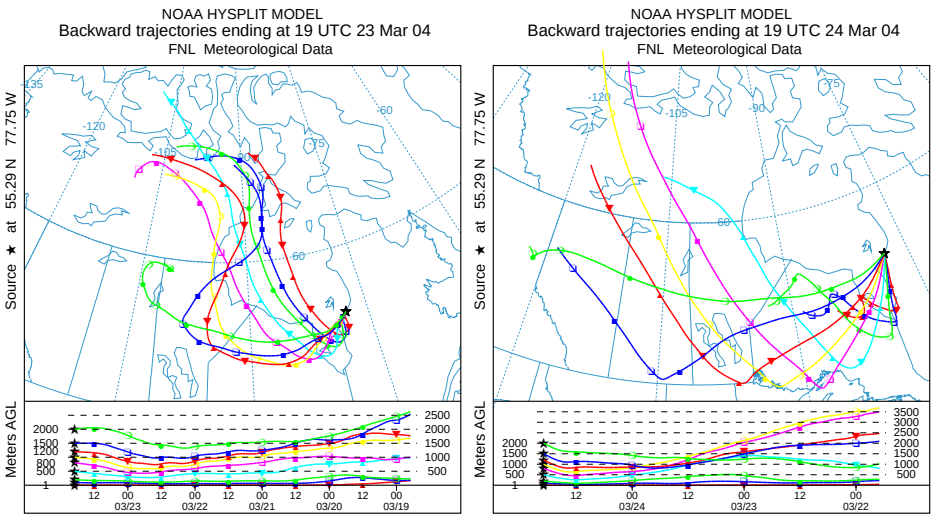

Figure 7.17: *Left: 120 hours backward trajectories for March 23rd GMT 19:00. The trajectories are calculated from 1 to 2000m in ten steps. The surface near layer is transported very straight from the North to the site, while with increasing height of the layers the origin of the air masses drift clearly westwards over land masses. Right: 72 hours backward trajectories for March 24th GMT 19:00. The trajectories are calculated from 1 to 2000m in ten steps. Airmasses transported to the site come from westerly directions, without crossing the frozen surfaces of the Hudson Bay. On this day, neither the longpath DOAS nor the MAX-DOAS system could observe elevated levels of BrO.*

path and the MAX-DOAS technique is problematic:
An intercomparison of the resulting concentration is only valid if BrO is homogeneously distributed in the boundary layer, since the absorption paths analyzed by the respective technique are obviously different. The MAX-DOAS method is sensitive for the lowest part of the atmosphere, but vertical profiles have to be calculated or modeled by a radiative transfer model (e.g. TRACY [*von Friedeburg* 2003]) However modelling is up to date only feasible for clear sky conditions and since the meteorological conditions during the discussed BrO event on March 23rd were guided by a thick and low cloud layer (as often found during ODEs), indicating a strong inversion layer, a quantitative comparison of the two data sets seems not appropriate.
However, the qualitative comparison, regarding the time scale of the event shows good agreement for both techniques. With both techniques the max-

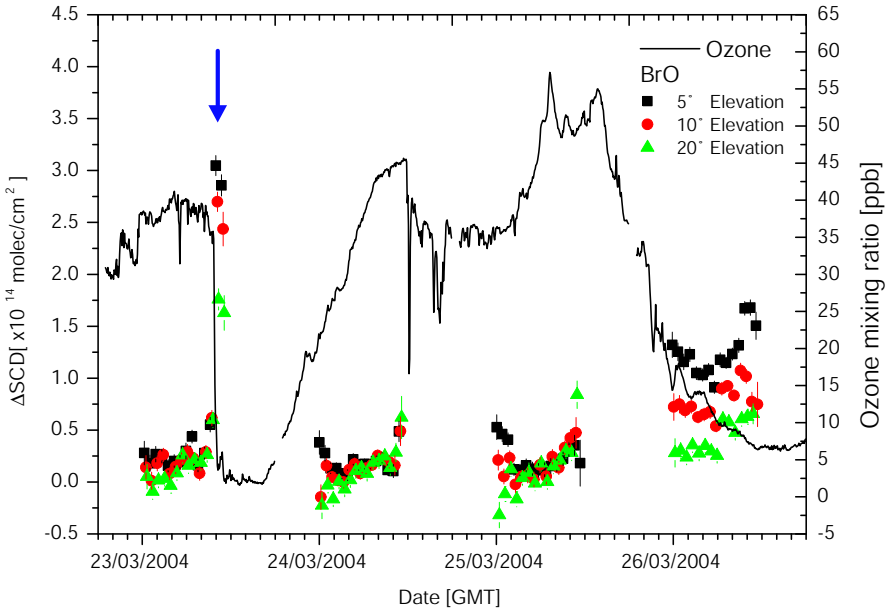

Figure 7.18: *The BrO ΔSCDs with simultaneously measured ozone for March 23rd 2004.*

imal detected concentrations have been observed on March 23rd compared to the remaining measurement time.

A strong vertical gradient of the BrO concentration may also account for the different results. The trajectories of March 23rd show the origin of the air masses in the north reaching the measurement site by travelling across the Hudson Bay and provoking the strong event. In Figure 7.17 the backward trajectories with a vertical extent from 1 - 2000 m are illustrated. Air masses close to the surface (up to 500 m) travelled from northern directions crossing the Hudson Bay to the measurement site. With increasing height, the origin of the air masses travel from the north to the west, before reaching the site. Note that only the lower airmasses travelled over the frozen Hudson Bay, while the upper layers surround the Hudson Bay, and travelled mainly over land. The BrO mixing ratios measured by the longpath DOAS system, showed very elevated levels close to the ground. In contrast, the MAX-DOAS measurements seem to show a significant decrease in the mixing ratio. However the technique of MAX-DOAS is sensitive for the lowest kilometers of the atmosphere. If the BrO radical is enriched in the lowest part of the

boundary layer the MAX-DOAS setup will nevertheless be sensitive and therefore integrate over the vertical profile with decreasing concentration upwards.
On the following day March 24th GMT 19:00 the airmasses of all vertical layers travel over westerly landmasses not crossing the Hudson Bay. That way is comparable to the way of airmasses on 23rd, above 500 m height.
Differences were observed as well in the measured BrO SCDs for the Mini-MAX-DOAS instrument and the MAX-DOAS instrument as can be seen in Figure 7.10 and 7.11. That may supports the presumption of inhomogeneous distribution of the BrO within the boundary layer.
However instrumental differences besides the different viewing geometry has to be considered. The observed differences between Mini-MAX-DOAS and MAX-DOAS systems is described in full detail in *Filsinger* [2004].

Besides the BrO measurements, IO was measured by the second Mini-MAX-DOAS system. The detection of IO was not successful, and an upper limit for tropospheric difference slant column density was estimated to be Δ SCD $\leq 6.4 \cdot 10^{13} molec/cm^2$ what would represent a mixing ratio of 2.4 ppt, if homogeneous mixing of a 1 km BL is assumed.

7.3.2 BrO Event of March 26th

The second observed BrO event related to a severe ozone depletion occurred on March 26th. The ozone depletion event and the recorded meteorologic conditions for the complete episode is shown in Figure 7.19.
The ozone depletion started during the night of March 26th, when very high windspeed of up to 12 m/s were recorded. Regarding the wind direction, the decrease of ozone is nearly parallel to the change in the wind direction from north-west to west. Coinciding to the drift of the wind direction the temperature decreased rapidly from 0°C to -20°C. As these meteorologic observation clearly indicate, arctic air masses were again transported to the measurement site, enriched with bromine.
Unfortunately no BrO data during sunrise were recorded, due to the coverage of the retro-reflectors with snow caused by the blizzard at night. BrO data in the late morning show a BrO level of 10 - 15 ppt. This level remained during the day until the end of the longpath records in the late afternoon. These observation agrees in principle with the MAX-DOAS observations, which detected a constant elevated level of BrO of approximately 5.2 ppt (+4.4 ppt, -1.5 ppt). However, the quantitative comparison of the BrO concentrations (as already discussed for the comparison of the data of 23rd

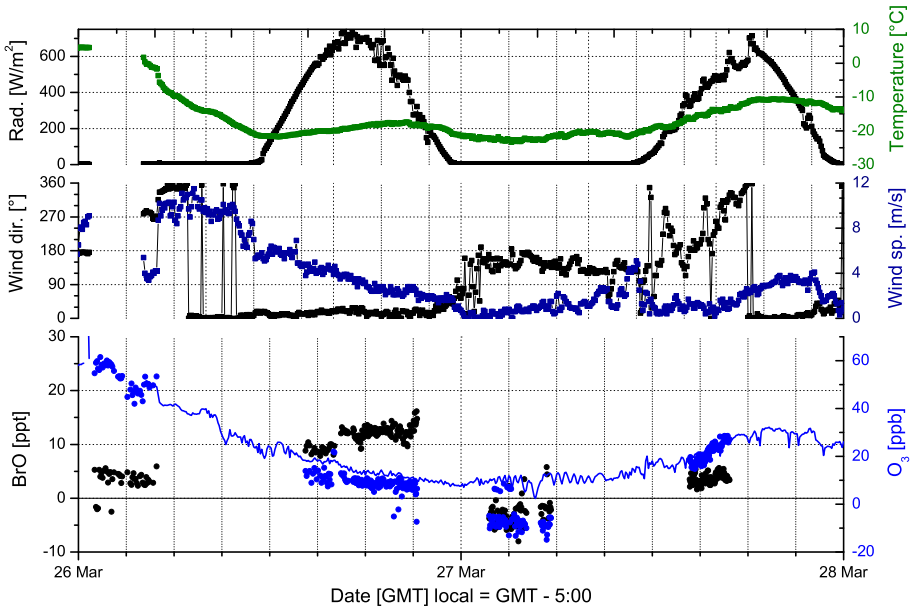

Figure 7.19: *Ozone depletion event starting on March 26th and coinciding BrO measurements of the longpath DOAS instrument. Meteorologic parameters are shown in the upper panels.*

March) of these two instruments is somehow problematic. However, the constant level of BrO is well observed with both instruments. Interestingly the meteorological conditions during the morning, where ozone was depleted down to 10 ppt, the sky was cloudfree in contrast to the thick layer observed on March 23rd. Clouds came up during the afternoon of the 26th. On March 27th, GMT 12:00 the ozone started to recover - again correlated to a clear change in the wind direction to southerly directions (see also the increase in temperature).

7.3.3 VHOCs as Precursor Species for Halogen Oxides

Organohalogens were measured the first time during polar spring within this campaign. In March the region of the Hudson Bay including Kuujjuarapik is clearly influenced by arctic conditions. A thick layer of snow covered main parts of the earth's surface. Only some trees (firs) are visible proofs for biological existence. Therefore the biological activity was assumed to be low.

Interestingly during the coldest period at the beginning of the campaign from March 5th to 10th, the automated mass spectrometer of the group of Carpenter et al. found significantly elevated levels of several organohalogens (see Figure 7.12) showing a strong diurnal behavior, what indicates photolytically induced chemistry and release of organohalogens in a complete different way to the well observed biogenic emissions from macro and microalgae. Nevertheless possible sources for the observed organohalogen concentrations could have a biological source. The observed extended lead in the Hudson Bay connected the sea and the atmosphere, that potentially ice algae could be involved in the emissions of some observed VHOCs. The high bio-activity of icealgae was already reported before by e.g. *Schall and Heumann* [1993]. However, the observations of increasing potential of bioactivity by increasing temperature and extension of the open lead seem not to agree with the observation of Carpenter et al., who found detectable levels of VHOCs only in the beginning of the campaign and nearly no significant concentrations or even an increasing trend until end of March. Of high interest are the elevated levels of short-lived organo-iodides CH_2I_2 and CH_2IBr, which have been observed in concentrations of several ppt under sunlight conditions. These observations represent a possibly significant source for reactive iodine in the arctic boundary layer. Unfortunately the DOAS systems did not record any spectra during these 'organo-active' period, that the impact of diiodomethane on the IO levels could not be studied (CH_2I_2 is accounted for the dominant precursor species of observed IO in the MBL). Biogenic sources for IO was also suggested by *Frieß et al.* [2001], who explained the observed seasonal variations of IO in the Antarctic MBL, with higher amounts during summer than during winter, by the smaller distance to the open sea, where the iodocarbons are most likely emitted.
Air samples for the analysis with the GC/ECD-ICP-MS of the group of Heumann et al. were taken only during the second half of March, due to the limited number of available air sampling tubes. The results are shown as well in Figure 7.12 indicated as blue dots. The differences are partly significant. This can be potentially explained by the different sampling locations. All air samples for Heumann et al. were taken at the longpath DOAS measurement site directly at the Hudson Bay, whereas the samples of Carpenter et al. were taken at the CEN research station in Kuujjuarapik, 2 km in land. If biogenic emissions are assumed, elevated levels closer to the source (open lead) may be explained.
Less likely is that the air samples could be contaminated by the storage and/or transport. The samples were covered by aluminium after the adsorption and stored in the refrigerator. For the transport a styrodurbox

with coolpads provided a cool and dark environment during the travel. The procedure of storage in cool and dark environment was tested before several times and caused in general an error for the analysis of the air samples smaller than 10% [*Schwarz* 2003].

7.3.4 Comparison to Campaign of 2001

In April and May 2001 the first field campaign at Kuujjuarapik was conducted, see *Hönninger* [2002], *Sebastián* [2004] and *Hönninger et al.* [2004]. The results of the previous campaign are in good agreement to the current. The observed ODEs were closely correlated to transported air masses from the North as in the previous campaign indicating that not much local chemistry can be observed on 55°N as the source regions are further in the North where extended areas of frozen sea salt surfaces are located. The observation of bromine induced air chemistry depends in these mid-latitudes strongly on wind direction - as soon as air masses from the south reaching the site the BrO events are rapidly stopped. A likely source region for reactive bromine is the north-west area of Hudson Bay, which is also suggested by *Kaleschke et al.* [2004] since there frequently breaks in the ice are observed and high BrO levels were observed from satellite.
The comparison of LP-DOAS with MAX-DOAS, also in quantitative comparison was significantly better in 2001 than in 2004. This could be partly explained by the usage of the short lightpath of just 2 km for the majority of the measurements, which is not very representative for the airmasses if they are not very well mixed, but therefore very sensitive for inhomogeneities and gradients. These gradients are also indicated by the quantitative comparison of MAX-DOAS and MINI-MAX-DOAS instruments, which were operated with different viewing directions.

7.3.5 Satellite Observations

Results and maps from satellite (Sciamachy) observations for the northern hemisphere of BrO vertical columns are available on the web [*BIRA-IASB*]. The maps for the days March 16th to 31st are shown in Figure 7.20. As can be seen from these actual data, the BrO events even from space extend not significantly further south than the Kuujjuarapik measurement site.

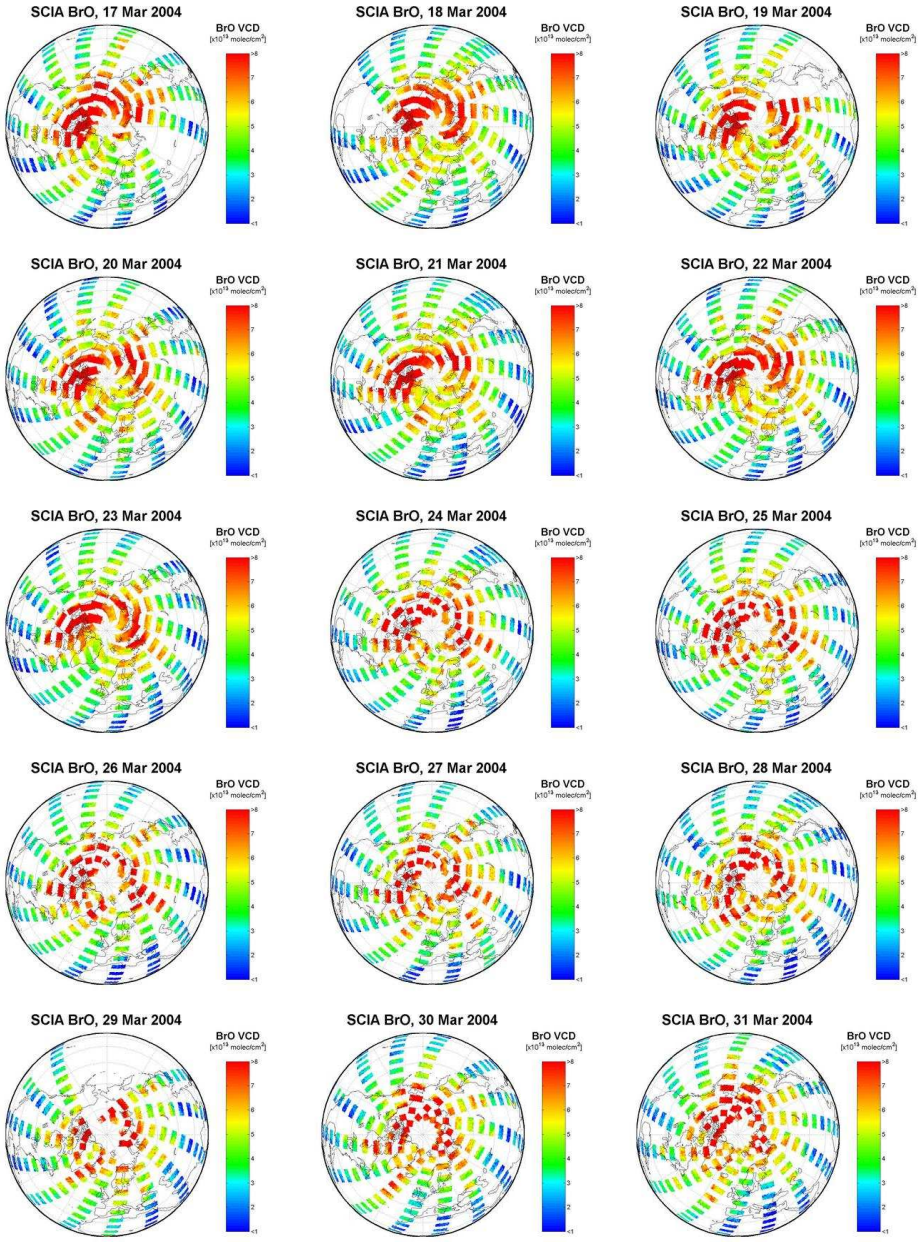

Figure 7.20: *BrO distribution on the northern hemisphere from space.*

Chapter 8

Conclusions and Outlook

In this work, extensive measurements of reactive halogen species at several mid-latitudinal regions were conducted with the well established active long-path DOAS method to investigate appearance and distribution of RHS in the boundary layer. Three field campaigns were conducted in the framework of the ReHaTrop project, which is part of the *AFO2000 program*, the first in 2002 at the German North Sea Coast, 2003 at the French Atlantic Coast in Brittany and in spring 2004 in the lower Arctic at the Hudson Bay.

The ground based measurements in the lower Arctic at the Hudson Bay yielded high levels of the BrO radical of more than 35 ppt in the boundary layer, coinciding with nearly complete surface near ozone depletion. The observations are in qualitative agreement with MAX-DOAS measurements, which were conducted parallel to the active measurements.

These observations are in reasonable agreement with previous measurements using active and passive DOAS technique during the ground based field campaign in spring 2001 in Kuujjuarapik.

The rapid increase of BrO and the coinciding decrease of ozone could be explained by transport processes of airmasses from northern regions, where extended sea ice areas are located.
No elevated levels of BrO have been found, if the air masses did not come from these 'source' regions. and no direct evidence for the impact of locally observed frostflowers and the open lead was found.

Changes in the airmasses leading to instabilities of the boundary layer al-

ways led to the end of the observed BrO events, which explains the close correlation of ozone recovery and increasing wind speed.

The detection of IO and ClO was not possible above the detection limit of about 2.1 ppt and 37 ppt, respectively.

In the framework of the project unexpected high levels of VHOCs were found, which are indicating interesting snow pack chemistry. However, the impact of these elevated organohalogen concentrations on RHS could not be investigated, since the measurements were not performed at the same time.

Two of the field campaigns were conducted in coastal environments, which differed significantly in the presence of macroalgae and therefore in their respective bioactivity. To compare coastal sites, characterized by similar bioactivity a re-analysis of data taken during 1998 PARFORCE campaign was taken into account. It was found that significant differences exist.

The observations of the Brittany campaign were modelled with the marine boundary layer model MISTRA to test wether the current understanding of halogen chemistry as represented in the model is consistent with the data.

The three coastal environments were compared and the results are summarized in the following:

IO was found, as the only halogen oxide in all three coastal environments. The maximum level of IO corresponded always to the detected level of organoiodides found at the respective sites.

BrO was identified in none of the locations and the upper limit of its appearance in the MBL of 1.5-2 ppt was found to be in agreement to model calculations, even assuming contributions of observed biological sources as CH_2IBr of up to 8 ppt. In this area the development of new measurement techniques is suggested, to provide detectable levels of BrO in the sub-ppt range, which would deliver valuable data for estimations of the relevance of BrO chemistry in the troposphere for global modelling.

The agreement of model calculations for the conditions of Brittany with the measurements is quite satisfactory: The IO mixing ratios observed by DOAS can be explained by the photolysis of observed levels of organoiodides alone, the presence of molecular iodine is not necessary.

Clearly demonstrated was the impact of appearance of macroalgae on organohalogens and moreover different types of macroalgae show individual emission patterns, so-called fingerprints.

The upper limit of OIO at the North Sea and in Brittany is about 3 ppt in average but no conclusions about the so-called 'hot spot' theory, which is suggested to explain particle burst events as observed in Mace Head, was possible, due to the long lightpath of ∼10 km used for the DOAS measurements. The combination of spatially resolved OIO and IO measurements and particle bursts is addressed to future field campaigns.
The question about the representativity of I_2 levels in coastal regions is obvious:
I_2 was found within the re-analysis of 1998 Mace Head data with peak concentrations of up to 60 ppt at night. These highly elevated levels were found closely correlated to exceptionally low water levels (spring-tide conditions), indicating macroalgae inhabiting the lowest part of the intertidal zone as the source. Since these observations of significantly elevated levels of I_2 were not found at the more or less comparable coastal site of Brittany further investigations and observations of the differences of these environments has to be done, to be able to estimate the global relevance of reactive iodine species in the atmosphere.

Furthermore the biological state, as the age of the plant should be investigated, which could be realized by longterm observations

However, the current measurement technique has a relatively high detection limit and regarding the model studies it could be assumed that even very low concentrations of I_2 under daylight conditions affect the marine atmosphere strongly. Therefore new measurement techniques or a simple improvement of the light source (e.g. LED) used for the active DOAS measurements would provide important information.

List of Figures

List of Tables

References

ACIA 2004 (2004). ACIA, Impact of a warming Arctic: Arctic Climate Impact Assesment. http://wwww.acia.uaf.edu.

Ackermann, R. (1997). *Messung von Iodoxid und Quecksilber in der Atmosphäre.* Diploma thesis, Institut für Umweltphysik, Universität Heidelberg.

Albritton, D. L., A. L. Schmeltekopf, and R. N. Zare (1976). An Introduction to the Least-Squares Fitting of Spectroscopic Data. In R. K. Narahari and M. W. Weldon (Eds.), *Molecular Spectroscopy: Modern Research.* Orlando, Florida, USA: Academic Press.

Alicke, B. (1997). *Messung von troposphärischen Halogenoxidradikalen in mittleren Breiten.* Diploma thesis, Institut für Umweltphysik, Universität Heidelberg.

Alicke, B., K. Hebestreit, J. Stutz, and U. Platt (1999). Iodine oxide in the marine boundary layer. *Nature,* Vol. 397, 572–573.

Allan, B. and J. Plane (2002). A study of the recombination of IO with NO_2 and the stability of INO_3: Implications for the atmospheric chemistry of iodine. *Journal of Physical Chemistry,* Vol. 106, 8634–8641.

Allan, B. J., G. McFiggans, and J. M. C. Plane (2000). Observation of iodine monoxide in the remote marine boundary layer. *J. Geophys. Res.,* Vol. 105, 14363–14369.

Allan, B. J., J. M. C. Plane, and G. McFiggans (2001). Observations of OIO in the remote marine boundary layer. *Geophys. Res. Lett.,* Vol. 28, 1945–1948.

AMAP (1997). Arctic Monitoring and Assessment Programm. Arctic Pollution Issues: A State of the Arctic Enironment Report. Oslo.

Aranda, A., G. LeBras, G. Verdet, and G. Poulet (1997). The $BrO+CH_3O_2$ reaction: Kinetics and the role in the atmospheric budget. *Geophys. Res. Lett.,* Vol. 24, No. 22, 2745–2748.

Ariya, P. A., A. Khalizov, and A. R. Gidas (2002). Reactions of gaseous mercury with atomic and molecular halogens: Kinetics, product studies, and atmospheric implications. *Journal of Phys. Chem. A,* Vol. 106, 7310–7320.

Atkinson, R., D. Baulch, R. Cox, R. Hampson Jr., J. Kerr, M. Rossi, and J. Troe (1997). Evaluated kinetic, photochemical and heterogeneous data for atmospheric chemistry. *J. Phys. Chem. Ref. Data,* , No. 26, 521–1011.

Atkinson, R., D. L. Baulch, R. A. Cox, J. Crowley, R. F. Hampson, Jr., R. Hynes, M. Jenkin, J. A. Kerr, M. J. Rossi, and J. Troe. Summary of Evaluated Kinetic and Photochemical Data for Atmospheric Chemistry: Web Version July 2004. J. Phys. Chem. Ref. Data.

Barrie, L., J. Bottenheim, R. Schnell, P. Crutzen, and R. Rasmussen (1988). Ozone destruction and photochemical reactions at polar sunrise in the lower Arctic atmosphere. *Nature,* Vol. 334, 138–141.

Bates, D. R. and M. Nicolet (1950). Atmospheric hydrogen. *Publ. Astron. Soc. Pac.,* Vol. 62, 106–110.

Bedjanian, Y., G. LeBras, and G. Poulet (1997). Kinetics and Mechanism of the $IO + ClO$ Reaction. *J. Phys. Chem. A,* Vol. 101, 4088–4096.

Bevington, P. (1969). *Data Reduction and Error Analysis for the Physical Sciences*. New York: McGraw-Hill.

Bilde, M., T. J. Wallington, C. Ferronato, J. J. Orlando, G. S. Tyndall, E. Estupinan, and S. Haberkorn (1998). Atmospheric chemistry of CH_2BrCl, $CHBrCl_2$, $CHBr_2Cl$, $CF_3CHClBr$ and CBr_2Cl_2. *J. Phys. Chem.,* Vol. 102, 1976–1986.

BIRA-IASB. http://www.oma.be/BIRA-IASB.

Bloss, W., D. Rowley, R. Cox, and R. Jones (1998). Kinetic and photochemical studies of iodine oxide chemistry. *Ann. Geophys. Suppl. II,* Vol. 12, C717.

Bloss, W. J., D. M. Rowley, R. A. Cox, and R. L. Jones (2001). Kinetics and Products of the IO Self-Reaction. *J. of Phys. Chem. A,* Vol. 105, 7840–7854.

Bobrowski, N. (2002). *Volcanic gas studies by multi axis differential optical absorption spectroscopy*. Diploma thesis, Institut für Umweltphysik, Universität Heidelberg.

Bobrowski, N. (2005). Measurements of ClO in a volcanic plume, Pers. comm.

Bobrowski, N., G. Hönninger, B. Galle, and U. Platt (2003). Detection of bromine monoxide in a volcanic plume. *Nature,* Vol. 423, No. 6937, 273–276.

Boucher, O., C. Moulin, S. Belviso, O. Aumont, L. Bopp, E. Cosme, R. von Kuhlmann, M. G. Lawrence, M. Pham, M. S. Reddy, J. Sciare, and C. Venkataraman (2003). DMS atmospheric concentrations and sulphate aerosol indirect radiative forcing: a sensitivity study to the DMS source representation and oxidation. *Atm. Chem. and Phys.,* Vol. 3, 49–65.

Boudries, H. and J. W. Bottenheim (2000). Cl and Br atom concentrations during a surface boudary layer ozone depletion event in the Canadian High Arctic. *Geophys. Res. Lett.,* Vol. 27, No. 1, 517–520.

Brauers, T. (1990). *Messsungen freier Radikale in der maritimen Atmosphäre.* Ph.D. thesis, Institut für Umweltphysik, Universität Heidelberg.

Brauers, T., M. Hausmann, U. Brandenburger, and H.-P. Dorn (1995). Improvement of Differential Optical Absorption Spectroscopy using Multi-Channel-Scanning-Techniques. *Appl. Opt.,* Vol. 34, No. 21, 4472–4479.

Burkholder, J. B., J. Curtius, A. R. Ravishankara, and E. R. Lovejoy (2004). Laboratory studies of the homogeneous nucleation of iodine oxides. *Atm. Chem. and Phys.,* Vol. 4, 4943–4988.

Carpenter, L., K. Hebestreit, W. Sturges, S. Penkett, P. Liss, B. Alicke, and U. Platt (1999). Observation of short-lived alkyl iodides and bromides at Mace Head, Ireland: links to biogenic sources and halogen oxide production. *J. Geophys. Res.,* Vol. 104, 1679–1689.

Carpenter, L., P. Liss, U. Platt, and K. Hebestreit (2001). Coastal zone production of IO precursors: a 2-dimensional study. *Atm. Chem. and Phys.,* Vol. 1, 9–17.

Carpenter, L. J. (2003). Iodine in the marine boundary layer. *Chem. Rev.,* Vol. 103, 4953–4962.

Chapman, S. (1930). On ozone and atomic oxygen in the upper atmosphere. *Philos. Mag.,* Vol. 10, 369–383.

Coheur, P.-F., S. Fally, M. Carleer, C. Clerbaux, R. Colin, A. Jenouvrier, M.-F. Mérienne, C. Hermans, and A. C. Vandaele (2002). New water vapor line parameters in the 26000-13000 cm^{-1} region. *Journal of Quantitative Spectroscopy and Radiative Transfer,* Vol. 74, No. 4, 493–510.

Cox, R. A., W. J. Bloss, and R. L. Jones (1999). OIO and the atmospheric cycle of iodine. *Geophys. Res. Lett.,* Vol. 26, 1857–1860.

Crowley, J. (2004). Annual Report ReHaTrop, http://www.afo-2000.de/001/afo2000.htm.

Crutzen, P. J. (1970). The influence of nitrogen oxide on the atmospheric ozone content. *Q.J.R. Meteorol. Soc.,* Vol. 96, 320–327.

Crutzen, P. J. (1973). A discussion of the chemistry of some minor constituents in the stratosphere and troposphere. *Pure Appl. Geophys.,* Vol. 106-108, 1385–1399.

Czerny, M. and A. Turner (1930). *Z.Phys.,* Vol. 61, 792.

Dangeard, P. (1933). Mechanism of iodine volatilization and the role of the iodogenic cells of Laminaria. *Comptes Rendus des Seances de la Societe de Biologie et de Ses Filiales,* Vol. 113, 1203–1205.

Davis, D., J. Crawford, S. Liu, S. McKeen, A. Bandy, D. Thornton, F. Rowland, and D. Blake (1996). Potential Impact of iodine on tropospheric levels of ozone and other critical oxidants. *J. Geophys. Res.,* Vol. 101, 2135–2147.

DeMore, W. B., S. P. Sander, C. J. Howard, A. R. Ravishankara, D. M. Golden, C. E. Kolb, R. F. Hampson, M. J. Kurylo, and M. J. Molina (1997). Chemical Kinetics and Photochemical Data for Use in Stratospheric Modeling No. 12. Jet Propulsion Laboratory, Pasadena, Publication 97-4.

Dickerson, R. R., K. P. Rhoads, T. P. Carsey, S. J. Oltmans, J. P. Burrows, and P. J. Crutzen (1999). Ozone in the remote marine boundary layer: A possible role for halogens. *J. Geophys. Res.,* Vol. 104, 21385–21395.

Domine, F. and P. B. Shepson (2002). Air-snow interactions and atmospheric chemistry. *Science,* Vol. 297, 1506–1510.

Ebinghaus, R., H. H. Kock, C. Temme, J. W. Einax, A. G. Lowe, A. Richter, J. P. Burrows, and W. H. Schroeder (2002). Antarctic springtime depletion of atmospheric mercury. *Env. Sci. and Technol.,* Vol. 36, 1238–1244.

Ecomusée Plouguerneau (2003). Ecomusée des géomoiniers de Plouguerneau - Sur la route des algues. *Patrimoine maritime de Bretagne,*.

Ekdahl, A., M. Pedersen, and K. Abrahamsson (1998). A study of the diurnal variation of biogenic volatile halocarbons. *Mar. Chem.,* Vol. 63, 1–8.

Etzkorn, T. (1998). *Untersuchungen atmosphärisch relevanter Reaktionssysteme mittels Differentieller Optischer Absorptionsspektroskopie*. Ph.D. thesis, Institut für Umweltphysik, Universität Heidelberg.

Fan, S. and D. Jacob (1992). Surface ozone depletion in Arctic spring sustained by bromine reactions on aerosols. *Nature,* Vol. 359, 522–524.

Farman, J. C., B. G. Gardiner, and J. D. Shanklin (1985). Large losses of total ozone in Antarctica reveal seasonal ClO_x/NO_x interaction. *Nature,* Vol. 315, 207–210.

Fayt, C. and M. van Rozendael (2001). WinDOAS. ISAB/BIRA Belgium, http://www.oma.be/BIRA-IASB.

Ferlemann, F. (1998). *Ballongestützte Messung atmosphärischer Spurengase mit DOAS*. Ph.D. thesis, Universität Heidelberg.

Fickert, S., J. W. Adams, and J. N. Crowley (1999). Activation of Br_2 and BrCl via uptake of HOBr onto aqueous salt solutions. *J. Geophys. Res.,* Vol. 104, 23719–23727.

Filsinger, F. (2004). *MAX-DOAS Measurements of Tropospheric BrO at the Hudson Bay*. Diploma thesis, Institut für Umweltphysik, Universität Heidelberg.

Fishman, J. and P. Crutzen (1978). The origin of ozone in the troposphere. *Nature,* Vol. 274, 855–858.

Foster, K. L., R. A. Plastridge, J. W. Bottenheim, P. B. Shepson, B. J. Finlayson-Pitts, and C. W. Spicer (2001). The Role of Br_2 and BrCl in Surface Ozone Destruction at Polar Sunrise. *Science,* Vol. 291, 471–474.

Frankenberg, C. (2004). Hitranvoigt. Software.

Frieß, U. (2001). *Spectroscopic Measurements of Atmospheric Trace Gases at Neumayer-Station, Antarctica*. Ph.D.thesis, Institut für Umweltphysik, Universität Heidelberg.

Frieß, U., T. Wagner, I. Pundt, K. Pfeilsticker, and U. Platt (2001). Spectroscopic Measurements of Tropospheric Iodine Oxide at Neumeyer Station, Antarctica. *Geophys. Res. Lett.,* Vol. 28, 1941–1944.

Geyer, A. (2000). *The Role of the Nitrate Radical in the Boundary Layer*. Ph.D. thesis, Institut für Umweltphysik, Universität Heidelberg.

Gomer, T., T. Brauers, F. Heintz, J. Stutz, and U. Platt (1993). *MFC User Manual, Vers. 1.98*. Institut für Umweltphysik, Universität Heidelberg.

Greenblatt, G. D., J. J. Orlando, J. B. Burkholder, and A. R. Ravishankara (1990). Absorption Measurements of Oxygen between 330 and 1140 nm. *J. Geophys. Res.,* Vol. 95, 18577–18582.

Gros, V., N. Poisson, D. Martin, M. Kanakidou, and B. Bonsang (1998). Observations and modeling of the seasonal variation of ozone at Amsterdam Island: 1994-1996. *J. Geophys. Res.,* Vol. 103, 28103–28109.

Harwood, M., J. Burkholder, M. Hunter, R. Fox, and A. Ravishankara (1997). Absorption Cross Sections and Self-Reaction Kinetics of the IO Radical. *J. Phys. Chem. A,* Vol. 101, 853–863.

Hausmann, M., U. Brandenburger, T. Brauers, and H.-P. Dorn (1999). Simple Monte Carlo methods to estimate the spectra evaluation error in differential-optical-absorption spectroscopy. *Appl. Opt.,* Vol. 38, No. 3, 462–475.

Hausmann, M. and U. Platt (1994). Spectroscopic measurement of bromine oxide and ozone in the high Arctic during Polar Sunrise Experiments 1992. *J. Geophys. Res.,* Vol. 99, 25399–25413.

Hebestreit, K. (2001). *Halogen Oxides in the Mid-Latitudinal Planetary Boundary Layer*. Ph.D. thesis, Institut für Umweltphysik, Universität Heidelberg.

Hebestreit, K., J. Stutz, D. Rosen, V. Matveiv, M. Peleg, M. Luria, and U. Platt (1999). DOAS Measurements of Tropospheric Bromine Oxide in Mid-Latitudes. *Science,* Vol. 283, 55–57.

Hegels, E., P. J. Crutzen, T. Klüpfel, D. Perner, and P. J. Burrows (1998). Global distribution of atmospheric bromine monoxide from GOME on earth-observing satellite ERS 2. *Geophys. Res. Lett.,* Vol. 25, 3127–3130.

Hermes, T. (1999). *Lichtquellen und Optik für die Differentielle Optische Absorptionsspektroskopie*. Diploma thesis, Institut für Umweltphysik, Universität Heidelberg.

Himmelmann, S., J. Orphal, H. Bovensmann, A. Richter, A. Ladstätter-Weissenmayer, and J. Burrows (1996). First Observation of the OIO Molecule by Time-Resolved Flash-Photolysis Absorption-Spectroscopy. *Chem. Phys. Lett.,* Vol. 251, 330–334.

Hoffmann, T., C. D. O'Dowd, and J. H. Seinfeld (2001). IO homogeneous nucleation: An explanation for coastal new particle formation. *Geophys. Res. Lett.,* Vol. 28, No. 10, 1949–1952.

Hollwedel, J. (2001). Analysis of GOME data for Alert2000 and the Hudson Bay for spring 2001. Pers. comm.

Hollwedel, J. (2005). *Observations of Tropospheric and Stratospheric Bromine Monoxide from Satellite*. Ph.D. thesis, Universität Heidelberg.

Holmes, N. S., J. W. Adams, and J. N. Crowley (2002). Uptake and reaction of HOBr on frozen and dry NaCl/NaBr surfaces between 253 and 233 K. *Atm. Chem. and Phys.,* Vol. 2, 79–91.

Hönninger, G. (1999). *Referenzspektren reaktiver Halogenverbindungen für DOAS-Messungen*. Diploma thesis, University of Heidelberg.

Hönninger, G. (2002). *Halogen Oxide Studies in the Boundary Layer by Multi Axis Differential Optical Absorption Spectroscopy and Active Longpath-DOAS*. Ph.D. thesis, Institut für Umweltphysik, Universität Heidelberg.

Hönninger, G., N. Bobrowski, E. Palenque, R. Torrez, and U. Platt (2004). Reactive bromine and sulfur emissions at Salar de Uyuni, Bolivia. *Geophys. Res. Lett.,* Vol. 31, No. 4.

Hönninger, G., H. Leser, O. Sebastián, and U. Platt (2004). Ground-based measurements of halogen oxides at the Hudson Bay by active longpath DOAS and passive MAX-DOAS. *Geophys. Res. Lett.,* Vol. 31, No. 4.

Hönninger, G., C. von Friedeburg, and U. Platt (2004). Multi axis differential optical absorption spectroscopy (MAX-DOAS). *Atm. Chem. and Phys.,* Vol. 4, 231–254.

HYSPLIT (1997). Hybrid Single-Particle Lagrangian Integrated Trajectory. http://www.arl.noaa.gov/ready/hysplit4.htm.

Ingham, T., M. Cameron, and J. N. Crowley (2000). Photodissociation of IO (355 nm) and OIO (532 nm): Quantum Yields for $O(^3P)$ and $I(^2P_J)$ Production. *J. of Phys. Chem. A,* Vol. 104, 8001–8010.

Jenkin, M. (1992). The Photochemistry of iodine-containing compounds in the marine boundary layer. *Report Harwell,*, 817–842.

Jimenez, J. L., R. Bahreini, D. R. Cocker, H. Zhuang, V. Varutbangkul, R. C. Flagan, J. H. Seinfeld, C. D. O'Dowd, and T. Hoffmann (2003). New particle formation from photooxidation of diiodomethane CH_2I_2. *J. Geophys. Res.,* Vol. 108, No. 23.

Johnston, H. S. (1971). Reduction of stratospheric ozone by nitrogen oxide catalysts from supersonic transport exhaust. *Science,* Vol. 173, 517–522.

Junge, C. E. (1963). *Air chemistry and radioactivity*, Volume 4 of *Internat. Geophys. Ser.* New York, London: Academic Press.

Kaleschke, L., C. Lüpkes, T. Vihma, J. Haarpaintner, A. Bochert, J. Hartmann, and G. Heygster (2001). SSM/I Sea Ice Remote Sensing for Mesoscale Ocean-Atmosphere Interaction Analysis. *Canadian Journal of Remote Sensing,* Vol. 27, No. 5, 526–537.

Kaleschke, L., A. Richter, J. Burrows, O. Afe, G. Heygster, J. Notholt, A. M. Rankin, H. K. Roscoe, J. Hollwedel, T. Wagner, and H. W. Jacobi (2004). Frost flowers on sea ice as a source of sea salt and their influence on tropospheric halogen chemistry. *Geophys. Res. Lett.,* Vol. 31, No. 16.

Knoll, P., R. Singerand, and W. Kiefer (1990). Improving spectroscopic techniques by a scanning multi channel technique. *Appl. Spectr.,* Vol. 44, 776–782.

Koop, T., A. Kapilashrami, L. Molina, and M. Molina (2000). Phase transitions of sea-salt/water mixtures at low temperatures: Implications for ozone chemistry in the polar boundary layer. *J. Geophys. Res.,* Vol. 105, 26393–26402.

Kraus, S. (2003). A new Doasis release. DOAS Workshop.

Kreher, K., P. V. Johnston, S. W. Wood, and U. Platt (1997). Ground-based measurements of tropospheric and stratospheric BrO at Arrival Heights (78°S), Antarctica. *Geophys. Res. Lett.,* Vol. 24, 3021–3024.

Kromminga, H., S. Voigt, J. Orphal, and J. P. Burrows (1999). UV-visible FT spectra of OClO at atmospheric temperatures. In *Proceedings of the 1st European Symposium on Atmospheric Measurements from Space.* ESA Special Publication.

Küpper, F. C., N. Schweigert, E. Ar Gall, J. M. Legendre, H. Vilter, and B. Kloareg (1998). Iodine uptake in Laminariales involves extracellular, haloperoxidase-mediated oxidation of iodide. *Centre Etudes Oceanologiques Biologie Marine, UPR, Roscoff, Fr.,* Vol. 207, No. 2, 163–171.

Landgraf, J. and P. J. Crutzen (1998). An efficient method for online calculations of photolysis and heating rates. *J. Atmos. Sci.,* Vol. 55, 863–878.

LeBras, G. and U. Platt (1995). A possible mechanism for combined chlorine and bromine catalyzed destruction of tropospheric ozone in the Arctic. *Geophys. Res. Lett.,* Vol. 22, 599–602.

Lehrer, E., G. Hönninger, and U. Platt (2004). A one dimensional model study of the mechanism of halogen liberation and vertical transport in the polar troposphere. *Atm. Chem. and Phys.,* Vol. 4, 2427–2440.

Leser, H., G. Hönninger, and U. Platt (2003). MAX-DOAS measurements of BrO and NO_2 in the marine boundary layer. *Geophys. Res. Lett.,* Vol. 30, No. 10.

Levenberg, K. (1944). A Method for the Solution of Certain Non-Linear problems in Least Squares. *Quart. Appl. Math.,* Vol. 2, 164–168.

Lu, J. Y., W. H. Schroeder, L. A. Barrie, A. Steffen, H. E. Welch, K. Martin, L. Lockhart, R. V. Hunt, G. Boila, and A. Richter (2001). Magnification of atmospheric mercury deposition to polar regions in springtime: the link to tropospheric ozone depletion chemistry. *Geophys. Res. Lett.,* Vol. 28, No. 17, 3219–3222.

Mäkelä, J. M., T. Hoffmann, C. Holzke, M. Väkevä, T. Suni, T. Mattila, P. P. Aalto, U. Tapper, E. I. Kauppinen, and C. D. O'Dowd (2002). Biogenic iodine emissions and identification of end-products in coastal ultrafine particles during nucleation bursts. *J. Geophys. Res.,* Vol. 107, No. 19.

Marquardt, D. W. (1963). An Algorithm for Least Squares Estimation of Non-Linear Parameters. *Soc. Indust. Appl. Math,* Vol. 11, 431–441.

Martinez, M., T. Arnold, and D. Perner (1999). The role of bromine and chlorine chemistry for Arctic ozone depletion events in Ny Ålesund and comparison with model calculations. *Ann. Geophys.,* Vol. 17, 941–956.

Matveev, V., M. Peleg, D. Rosen, D. S. Tov-Alper, K. Hebestreit, J. Stutz, U. Platt, D. Blake, and M. Luria (2001). Bromine oxide - ozone interaction over the Dead Sea. *J. Geophys. Res.,* Vol. 106, 10375–10387.

McElroy, C., C. McLinden, and J. McConnell (1999). Evidence for bromine monoxide in the free troposphere during the Arctic polar sunrise. *Nature,* Vol. 397, 338–341.

McFiggans, G., H. Coe, R. Burgess, B. J. Allan, M. Cubison, M. Rami Alfarra, R. Saunders, A. Saiz-Lopez, J. M. C. Plane, D. Wevill, L. Carpenter, A. R. Rickard, and P. S. Monks (2004). Direct evidence for coastal iodine particles from Laminaria macroalgae - linkage to emissions of molecular iodine. *Atm. Chem. and Phys.,* Vol. 4, 701–713.

McFiggans, G., J. M. C. Plane, B. J. Allan, and L. J. Carpenter (2000). A modeling study of iodine chemistry in the marine boundary layer. *J. Geophys. Res.,* Vol. 105, 14371–14385.

Meller, R. and G. K. Moortgat (2000). Temperature dependance of the absorption cross sections of HCHO between 223 and 323K in the wavelength range 225 - 375 nm. *J. Geophys. Res.,* Vol. 105, 7089–7102.

Misra, A. and P. Marshall (1998). Computational investigations of iodine oxides. *J. Phys. Chem.,* Vol. 102, 9056–9060.

Miyake, Y. and S. Tsnogai (1963). Evaporation of Iodine from the ocean. *J. Geophys. Res.,* Vol. 68, 3989–3993.

Moessinger, J. C., D. M. Rowley, and R. A. Cox (2002). The UV-visible absorption cross-sections of $IONO_2$. *Atm. Chem. and Phys.,* Vol. 2, 227–234.

Molina, L. and F. Rowland (1974). Stratospheric sink for chlorofluromethanes: chlorine atom catalyzed destruction of ozone. *Nature,* Vol. 249, 820–822.

Mössinger, J., D. Shallcross, and R. Cox (1998). UV-VIS absorption cross-section and atmospheric lifetimes of CH_2Br_2, CH_2I_2 and CH_2BrI. *J. Chem. Soc. Faraday Trans.,* Vol. 94 (10), 1391–1396.

Mozurkewich, M. (1995). Mechanisms for the release of halogen atom sea-salt particles by free radical reactions. *J. Geophys. Res.,* Vol. 100, 14199–14207.

Nagao, I., K. Matsumoto, and H. Tanaka (1999). Sunrise ozone destruction found in the sub-tropical marine boundary layer. *Geophys. Res. Lett.,* Vol. 26, No. 22, 3377–3380.

O'Dowd, C., J. Jimenez, R. Bahreini, Roya, Flagan, C. Richard, J. Seinfeld, K. Haemeri, L. Pirjola, M. Kulmala, S. Jennings, and T. Hoffmann (2002). Marine aerosol formation from biogenic iodine emissions. *Nature,* Vol. 417, No. 6889, 632–636.

Oram, D. E. and S. A. Penkett (1994). Observations in eastern England of elevated methyl iodide concentrations in air of Atlantic origin. *Atmospheric Environment,* Vol. 28, No. 6, 1159–74.

Perner, D., D. H. Ehhalt, H. W. Paetz, U. Platt, E. P. Roeth, and A. Volz (1976). OH Radicals in the lower Troposphere. *Geophys. Res. Lett.,* Vol. 3, 466–468.

Perner, D. and U. Platt (1979). Detection of Nitrous Acid in the Atmosphere by Differential Optical Absorption. *Geophys. Res. Lett.,* Vol. 6, 917–920.

Pirrone, N., G. Keeler, and J. Nriagu (1996). Regional differences in world-wide emissions of mercury to the atmosphere. *Atm. Env.,* Vol. 30.

Plane, J. M. C., B. J. Allan, and S. H. Ashworth (2001). On the Chemistry of Iodine Oxides in the Marine Boundary Layer. *Geophys. Res. Abs.,* Vol. 3.

Platt, U. (1978). Dry Deposition of SO_2. *Atmos. Env.,* Vol. 12, 363–367.

Platt, U. (1994). Differential Optical Absorption Spectroscopy (DOAS). In M. W. Sigrist (Ed.), *Monitoring by Spectroscopic Techniques*. New York: John Wiley & Sons, Inc.

Platt, U. and G. Hönninger (2003). The role of halogen species in the troposphere. *Chemosphere,* Vol. 52, 325–338.

Platt, U. and C. Janssen (1995). Observation and role of the free radicals NO_3, ClO, BrO and IO in the troposphere. *Faraday Discuss.,* Vol. 100, 175–198.

Platt, U. and E. Lehrer (1996). *Arctic Tropospheric Ozone Chemistry, ARCTOC, Final Report of the EU-Project No. EV5V-CT93-0318, Heidelberg.*

Platt, U. and D. Perner (1980). Direct Measurements of Atmospheric CH_2O, HNO_2, O_3, NO_2 and SO_2 by Differential Optical Absorption in the Near UV. *J. Geophys. Res.,* Vol. 85, 7453–7458.

Platt, U., D. Perner, G. W. Harris, A. M. Winer, and J. N. Pitts, Jr. (1980). Detection of NO_3 in the Polluted Troposphere by Differential Optical Absorption. *Geophys. Res. Lett.,* Vol. 7, 89–92.

Platt, U., D. Perner, and H. W. Pätz (1979). Simultaneous Measurement of Atmospheric CH_2O, O_3 and NO_2 by Differential Optical Absorption. *J. Geophys. Res.,* Vol. 84, 6329–6335.

Poissant, L., M. Pilote, C. Beauvais, P. Constant, and H. H. Zhang (2005). A year of continuous measurements of three atmospheric mercury species (GEM, RGM and Hgp) in southern Quebec, Canada. *Atmospheric Environment,* Vol. 39, No. 7, 1275–1287.

Pruvost, J. (2001). *Étude des composés organiques halogénés volatils en milieu marin. Origines biologiques et anthropiques, échanges avec l'atmosphère - Utilisation comme traceurs transitoires de la circulation dans l'Atlantique de Nord-Est.* Ph.D. thesis, DEA Chimie fine, Chimie Analytique, Chimie de l'Environnement Marin de l'Université de Bretagne Occidentale.

Rankin, A. M., E. W. Wolff, and S. Martin (2002). Frost flowers: Implications for tropospheric chemistry and ice core interpretation. *J. Geophys. Res.,* Vol. 107, 4683.

Rattigan, O., E. Dudley, R. Shallcross, and R. Cox (1997). UV absorption cross-sections and atmospheric photolysis rates of CF_3I, CH_3I, C_2H_5I and CH_2ICl. *J. Chem. Soc. Faraday Trans.,*, 2839–2846.

Rattigan, O., R. Jones, and R. Cox (1995). The visible spectrum of gaseous OBrO. *Chem. Phys. Lett.,* Vol. 230, 121–126.

Richter, A., F. Wittrock, M. Eisinger, and J. Burrows (1998). GOME Observations of Tropospheric BrO in Northern Hemispheric Spring and Summer 1997. *Geophys. Res. Lett.,* Vol. 25, 2683–2686.

Röhl, C. M., J. B. Burkholder, G. K. Moortgat, A. R. Ravishankara, and P. J. Crutzen (1997). Temperature dependence of UV absorption cross sections and atmospheric implications of several alkyl iodides. *J. Geophys. Res.,* Vol. 102, 12819–12830.

Röth, E.-P. (1994). *Ozonloch – Ozonsmog: Grundlagen der Ozonchemie.* Mannheim: Bibliographisches Institut.

Rothman, L., C. P. Rinsland, A. Goldman, S. Massie, D. P. Edwards, J.-M. Flaud, A. Perrin, C. Camy-Peyret, V. Dana, J.-Y. Mandin, J. Schroeder, A. McCann, R. R. Gamache, R. B. Wattson, K. Yoshino, K. Chance, K. Jucks, L. Brown, V. Nemtchinov, and P. Varanasi (1998). The HITRAN Molecular Spectroscopic Database and HAWKS (HITRAN Atmospheric Workstation): 1996 Edition. *J. Quant. Spectroscopy and Rad. Transfer,* Vol. 60, 665–710.

Rowley, D. M., W. J. Bloss, R. A. Cox, and R. L. Jones (2001). Kinetics and Products of the IO+BrO Reaction. *J. of Phys. Chem. A,* Vol. 105, 7855–7864.

Saiz-Lopez, A. and J. Plane (2004). Novel iodine chemistry in the marine boundary layer. *Geophys. Res. Lett.,* Vol. 31, No. 4.

Saiz-Lopez, A., J. M. C. Plane, and J. A. Shillito (2004). Bromine oxide in the mid-latitude marine boundary layer. *Geophys. Res. Lett.,* Vol. 31, No. 3.

Saiz-Lopez, A., R. W. Saunders, D. M. Joseph, S. H. Ashworth, and J. M. C. Plane (2004). Absolute absorption cross-section and photolysis rate of I_2. *Atm. Chem. and Phys.,* Vol. 4, 1443–1450.

Sander, R., W. C. Keene, A. A. P. Pszenny, R. Arimoto, G. P. Ayers, E. Baboukas, J. M. Cainey, P. J. Crutzen, R. A. Duce, G. Hönninger, B. J. Huebert, W. Maenhaut, N. Mihalopoulos, V. C. Turekian, and R. Van Dingenen (2003). Inorganic bromine in the marine boundary layer: a critical review. *Atm. Chem. and Phys.,* Vol. 3, 1301–1336.

Sander, S. P. (1986). Temperature dependence of the NO_3 absorption spectrum. *J. Phys. Chem.,* Vol. 90, 4135–4142.

Sanders, R. W., S. Solomon, M. A. Carroll, and A. L. Schmeltekopf (1988). Ground based Measurements of O_3, NO_2, OClO and BrO during the Antarctic Ozone Depletion Event. In R. D. Bjokov and P. Fabian (Eds.), *Ozone in the Atmosphere, Quadrennial Ozone Symposium 1988*, pp. 65–70. Hampton, Va.: Deepak Publishing.

Schall, C. and K. G. Heumann (1993). GC determination of volatile organoiodine and organobromine compounds in Arctic seawater and air samples. *Fresenius' Journal of Analytical Chemistry,* Vol. 346, No. 6-9, 717–22.

Schall, C., F. Laturnus, and K. G. Heumann (1994). Biogenic volatile organoiodine and organobromine compounds released from polar macroalgae. *Chemosphere,* Vol. 28, No. 7, 1315–24.

Schroeder, W. H. and L. A. Barrie (1998). Is mercury input to polar ecosystems enhanced by springtime ozone depletion chemistry? *IGAC Newsletter,* Vol. 14, 7–8.

Schroeder, W. H. and J. Munthe (1998). Atmospheric Mercury - An Overview. *Atm. Env.,* Vol. 32, No. 5, 809–822.

Schwarz, A. (2003). *Entwicklung einer online Kopplungsmethode von GC mit ECD- und ICPMS-Detektion zur Bestimmung biogener leichtlüchtiger bromierter und iodierter Kohlenwasserstoffe in Meerwasser und der Atmosphäre*. Ph.D. thesis, Institut für Anorganische und Analytische Chemie, Universität Mainz.

Sebastián, O. (2004). *The relative contribution of free radicals to the oxidation chain of Dimethylsulphide in the marine boundary layer*. Ph.D. thesis, Institut für Umweltphysik, Universität Heidelberg.

Simpson, W. R., L. Alvarez-Aviles, T. A. Douglas, M. Sturm, and F. Domine (2004). Halogens in the coastal snow pack near Barrow, Alaska: Evidence for active bromine air-snow chemistry during springtime. submitted to Geophys. Res. Lett.

Singh, H. B., L. Salas, and R. Stiles (1983). Methyl halides in and over the eastern Pacific. *J. Geophys. Res.,* Vol. 88, 3684–3690.

Slemr, F., G. Schuster, and W. Seiler (1985). Distribution, speciation, and budget of atmospheric mercury. *J. Atmos. Chem.,* Vol. 3, No. 4, 407–434.

Solomon, S., R. R. Garcia, and A. R. Ravishankara (1994). On the role of iodine in ozone depletion. *J. Geophys. Res.,* Vol. 99, 20491–20499.

Solomon, S., A. L. Schmeltekopf, and R. W. Sanders (1987). On the interpretation of zenith sky absorption measurements. *J. Geophys. Res.,* Vol. 92, 8311–8319.

Spietz, P. and J. Gomez (2004). New measurements of OIO absorption cross section. Pers. comm.

Stutz, J. (1991). *Charakterisierung von Photodiodenzeilen zur Messung stratosphärischer Spurenstoffe*. Diploma thesis, Institut für Umweltphysik, Universität Heidelberg.

Stutz, J. (1996). *Messung der Konzentration troposhärischer Spurenstoffe mittels Differentieller Optischer Absorptions Spektroskopie: Eine neue Generation von Geräten und Algorithmen*. Ph. D. thesis, Institut für Umweltphysik, Universität Heidelberg.

Stutz, J., R. Ackermann, J. D. Fast, and L. Barrie (2002). Atmospheric reactive chlorine and bromine at the Great Salt Lake, Utah. *Geophys. Res. Lett.,* Vol. 29, No. 10.

Stutz, J., K. Hebestreit, B. Alicke, and U. Platt (1999). Chemistry of halogen oxides in the troposphere: comparison of model calculations with recent field data. *J. Atmos. Chem.,* Vol. 34, 65–68.

Stutz, J. and U. Platt (1996). Numerical Analysis and Estimation of the Statistical Error of Differential Optical Absorption Spectroscopy Measurements with Least-Squares methods. *Appl. Opt.,* Vol. 35, No. 30, 6041–6053.

Stutz, J. and U. Platt (1997). Improving longpath differential optical absorption spectroscopy with a quartz-fiber mode mixer. *Applied Optics,* Vol. 36, No. 6, 1105–1115.

Tang, T. and J. C. McConnel (1996). Autocatalytic release of bromine from Arctic snow pack during polar sunrise. *Geophys. Res. Lett.,* Vol. 23, 2633–2636.

Toumi, R. (1994). *BrO* as a sink for dimethylsulfide in the marine atmosphere. *Geophys. Res. Lett.,* Vol. 21, 117–120.

Tsetsi, M., F. Petitet, P. Carlier, and G. Mouvier (1989). A method for methyl iodide measurements in the troposphere. Physico Chemical Behaviour of Atmospheric Pollutants, Proceedings of the 5th European Symposium.

Tuckermann, M., R. Ackermann, C. Gölz, H. Lorenzen-Schmidt, T. Senne, J. Stutz, B. Trost, W. Unold, and U. Platt (1997). DOAS-observation of

halogen radical- catalysed Arctic boundary layer ozone destruction during the ARCTOC campaign 1995 and 1996 in Ny-Alesund, Spitsbergen. *Tellus,* Vol. 49b, 533–555.

van Roozendael, M., D. W. Arlander, J. Burrows, M. Chipperfield, C. Fayt, F. Hendrick, C. Hermans, P. Johnston, R. Jones, K. Kreher, J.-C. Lambert, N. Tahrin, D. Newnham, K. Pfeilsticker, U. Platt, J.-P. Pommereau, I. Pundt, A. Richter, B. Sinnhuber, A. South, K. Tørnkvist, and T. Wagner (2000). Lessons learned from 2 years of coordinated multi-platform UV-visible observations of atmospheric bromine monoxide. *Proceedings of the Quadrennial Ozone Symposium, Hokkaido University, Sapporo, Japan,*, 157–158.

Vogt, R., P. J. Crutzen, and R. Sander (1996). A mechanism for halogen release from sea-salt aerosol in the remote marine boundary layer. *Nature,* Vol. 383, 327–330.

Voigt, S., J. Orphal, and J. P. Burrows (2001). The temperature dependence (203-293 K) of the absorption cross sections of O_3 in the 230-850 nm region measured by Fourier-transform spectroscopy. *Journal of Photochemistry and Photobiology,* Vol. 143, 1–9.

Voigt, S., J. Orphal, and J. P. Burrows (2002). The temperature and pressure dependence of the absorption cross-sections of NO_2 in the 250-800 nm region measured by Fourier-transform spectroscopy. *Journal of Photochemistry and Photobiology,* Vol. 149, 1–7.

von Friedeburg, C. (2003). *Derivation of Trace Gas Information combining Differential Optical Absorption Spectroscopy with Radiative Transfer Modelling.* Ph.D. thesis, Combined Faculties for the Natural Sciences and for Mathematics, Universität Heidelberg.

von Glasow, R. and R. Sander (2001). Variation of sea salt aerosol pH with relative humidity. *Geophys. Res. Lett.,* Vol. 28, 247–250.

von Glasow, R., R. Sander, A. Bott, and P. J. Crutzen (2002a). Modeling halogen chemistry in the marine boundary layer 1. Cloud-free MBL. *J. Geophys. Res.,* Vol. 107, No. 17.

von Glasow, R., R. Sander, A. Bott, and P. J. Crutzen (2002b). Modeling halogen chemistry in the marine boundary layer 2. Interactions with sulfur and the cloud-covered MBL. *J. Geophys. Res.,* Vol. 107, No. 17.

von Glasow, R., R. von Kuhlmann, M. G. Lawrence, U. Platt, and P. J. Crutzen (2004). Impact of reactive bromine chemistry in the troposphere. *Atm. Chem. and Phys.,* Vol. 4, 2481–2497.

Wagner, T., C. Leue, M. Wenig, K. Pfeilsticker, and U. Platt (2001). Spatial and temporal distribution of enhanced boundary layer BrO concentrations measured by the GOME instrument aboard ERS-2. *J. Geophys. Res.,* Vol. 106, 24225–24235.

Wagner, T. and U. Platt (1998). Satellite mapping of enhanced *BrO* concentrations in the troposphere. *Nature,* Vol. 395, 486–490.

Wang, T. X., M. D. Kelley, J. N. Cooper, R. C. Beckwith, and D. W. Margerum (1994). Equilibrium, kinetic, and UV-spectral characteristics of aqueous bromine chloride, bromine, and chlorine species. *Inorg. Chem.,* Vol. 33, 5872–5878.

Wayne, R., C. Canosa-Mas, and E. Cotter (2000). Laboratory sudies of the reactions of OH radicals with alkyl iodides. Contribution to subproject CMD-GPP, CMC Annual Report.

Wayne, R., G. Poulet, P. Biggs, J. Burrows, R. Cox, P. Crutzen, G. Haymann, M. Jenkin, G. L. Bras, G. Moortgat, U. Platt, and R. Schindler. Halogen oxides: radicals, sources and reservoirs in the laboratory and in the atmosphere. *Atmos. Environ., Special Issue,* Vol. 29, 2675–2884.

Wilmouth, D. M., T. F. Hanisco, N. M. Donahue, and J. G. Anderson (1999). Fourier Transform Ultraviolet Spectroscopy of the A 2P3/2 X 2P3/2 Transition of BrO. *Journal of Physical Chemistry A,* Vol. 103, No. 45, 8935–8945.

Winterlik, J. (2003). *Bestimmung leichtflüchtiger Halogenkohlenwasserstoffe (LHKW) in Küstengewässern der Bretagne und ihrer marinen Atmosphäre mit GC/ECD-ICPMS sowie Entwicklung einer massenspektrometrischen Isotopenverdünnungsanalyse zur Bestimmung bromierter LHKW.* Diploma thesis, Institut für Anorganische und Analytische Chemie, Universität Mainz.

Wittrock, F., R. Müller, A. Richter, H. Bovensmann, and J. P. Burrows (2000). Measurements of iodine monoxide (IO) above Spitsbergen. *Geophys. Res. Lett.,* Vol. 27, 1471–1474.

Yvon, S. and H. Butler (1996). An improved estimate of the oceanic lifetime of atmospheric CH_3Br. *Geophys. Res. Lett.,* Vol. 23, 53–56.

Yvon-Lewis, S. and J. H. Butler (2002). Effect of oceanic uptake on atmospheric lifetimes of selected trace gases. *J. Geophys. Res.,* Vol. 107.

Zingler, J. and U. Platt (2005). Iodine oxide in the Dead Sea valley: Evidence for inorganic sources of boundary layer IO. *J. Geophys. Res.,* Vol. 110, No. D07307.

Dankeschön & Merci & Nakurmik & Thank you

Zu guter Letzt sei noch all denen gedankt, die diese Arbeit überhaupt ermöglicht und zu ihrem Gelingen beigetragen haben.
Für diesen finalen Teil der Arbeit haben sich im Laufe der letzten drei Jahre eine ganze Reihe von Menschen qualifiziert und das aus den unterschiedlichsten Gründen, die sowohl fachlicher, praktischer und natürlich auch sozialer Natur sind. Alle Daten die dieser Arbeit zugrunde liegen, wurden aus Feldkampagnen, die in den verschiedensten Teilen der Erde durchgeführt wurden, gewonnen. Das bedeutete für die gesamte Zeit meiner Promotion ein sehr vielfältiges und äußerst abwechslungsreiches Arbeiten. Im Vordergrund stand nicht immer nur die Wissenschaft, denn drei Kampagnen größeren Umfangs in drei Jahren erfolgreich durchzuführen erforderte auch viel Organisationsarbeit. In Sachen Improvisation, Löten, um Kosten schachern, mit Zoll und Fluggesellschaften feilschen und auch im Koffer und Kisten packen kann ich mich mittlerweile als Profi bezeichnen auch wenn es hierzu durch eine manchesmal harte Schule ging.
Bei den vielen Kontakten während der Kampagnen war ich immer wieder erstaunt und auch erfreut darüber wieviel Interesse das Thema meiner Arbeit hervorruft und wieviel Hilfsbereitschaft und Unterstützung jeglicher Art von zum Teil völlig fremden Menschen mir entgegengebracht wurde. Hierfür möchte ich einmal ein ganz allgemeines Dankeschön aussprechen!

Ganz speziell, sehr herzlich und natürlich an allererster Stelle möchte ich mich bei Herrn Prof. Dr. Ulrich Platt bedanken, der mir die Möglichkeit geboten hat diese Arbeit durchzuführen un mir hierfür das gesamte ReHaTrop Projekt anvertraut hat und die wissenschaftliche Seite dieser Arbeit betreut hat.
Mein Dank gilt auch Herrn Prof. Dr. Frank Arnold für die freundliche Übernahme des Gutachtens dieser Arbeit.

Herzlich bedanken möchte ich mich bei Gerd, auch wenn er diese Zeilen nicht mehr wird lesen können. Er hat mir während meiner gesamten Promotionszeit immer mit Rat und Tat zur Seite gestanden und mich in Sachen Langpfad DOAS und Halogene angelernt. Ohne ihn würde es diese Arbeit überhaupt nicht geben.

In dieser vordersten Riege möchte ich mich auch bei Andreas Lotter bedanken, er hat an allen Kampagnen als tatkräftiger Mitstreiter teilgenommen, und bestimmt das ein oder andere Mal durch seine grenzenlose Gelassenheit das Überleben nicht wunsch- und ordnungsgemäss funktionierender Messgeräte gesichert.
Ein ganz dickes Dankeschön geht an die Gemeinde Dagebüll und das dort zuständige Amt für ländliche Räume. Die Zusammenarbeit war geradezu grandios unkompliziert trotz der vielen besonderen Anforderungen, die vom Starkstromanschluß auf der Deichkrone bis zum Baggertransport eines überdimensionierten Retros reichten. Ein ebensogroßes Dankeschön geht auch an die Halligbewohner von Oland und Langeneß, die uns den Retroaufbau nicht nur erlaubt, sondern auch tatkräftig unterstützt haben! Ganz speziell sei hier Angelika gedankt, die sich rührend um den Retro in ihrem Vorgarten gekümmert hat.
Ein weiteres Dankeschön geht hier schon an Anastasia Schwarz der Uni Mainz, für die sehr unkomplizierte und fruchtbare Zusammenarbeit während der zwei Kampagnen an der Nordsee und auch der Bretagne.

Womit ich mit dem Verteilen der Dankeschöns bei der zweiten Kampagne angelangt wäre, die in der wundervollen Bretagne stattfand.
Je me remercie chaleureusement à la commune de Plougerneau pour l'aide quelle nous a apporté durant et avant notre campagne de recherche au bord d'Atlantique. Merci beaucoup spécialement à Monsieur Sirodot pour son aide et l'organisation d'un branchement électrique au port de Lilia. Aussi je me remercie beaucoup au département de Phare et Balise à Brest pour la permission de faire la recherche par la côte de Lilia avec le DOAS. Spécialement je voudrais dire merci à Madame Sabatier pour sa gentillesse et patience entendre tous mes explications scientifique sur le technique de DOAS pour décider le risque pour les trafic de bateaux par la côte de Lilia à cause de notre mesure envoyer un rayon de lumiére comme un phare.
Merci beaucoup auch an die super Kampagnenhelfer: Roman, der mit beeindruckender Energie etliche Erdnägel im bretonischen Felsplateau versenkt hat, die noch heute vor Ort zu bewundern sind. Lauki: dein Motto lieber eine als zwei linke Hände unterschreibe ich mit rechts! Nicole, auch wenn das Wetter lausig war: Schön dass du da warst.

The third campaign took place in the nearly uninhabited North of Canada, in Kuujjuarapik/Whapmagoostui. My special thank goes to Claude Tremblay, without his support and help in all of the organizational issues, this campaign would never have happened - Nakurmik!
A big thank you is also for Caroline the cook - it was really amazing to meet you!

Merci beaucoup à Laurier Poissant et Martin Pilote pour les dicussions intéresantes au sujet de mercury dans l'environnement d'Arctic.
Ein ganz herzliches Dankeschön natürlich auch an die Kampagnenteilnehmer Andreas, Frank, Gerd und Anita - die mit ihrem Einsatz dafür gesorgt haben, dass mir trotz der Kälte und der ziemlich wiedrigen Umstände die gute Laune nicht vollkommen verging!
Auch wenn ich viel meiner Zeit auf Kampagnen verbracht habe, gibt es natürlich auch jede Menge Dankeschöns in Heidelberg zu verteilen.
Ein ganz lieber Dank geht an Nicole, nicht nur für eine wirklich gute Zusammenarbeit in allen Lebens und Arbeitslagen, sondern auch dafür dass du manchmal nur da warst, um eine Tasse Tee zu trinken und den Kopf wieder frei zu bekommen.
Ein dickes Dankeschön geht natürlich an die gesamte Arbeitsgruppe Luftchem und das IUP für ein gutes Arbeitsklima und eine freundliche Atmosphäre. Ganz speziell sei Oli, Peter, Lotti, Roland, Susanne, Jens, Jutta, Strick, Christoph, Frank, Julia und natürlich den Ballonören, Klausi, Frank, Marcel, Andre, Scholli und auch Hartmut herzlichst gedankt ....sogar den Tomos sei gedankt, auch wenn ich die Zusammenarbeit nicht immer konstruktiv fand, interessant war es dennoch!

Danke natürlich auch an die Werkstatt des IUP - Herr Fletterer, Herr Mantsch ohne ihre Unterstützung und den häufigen Noteinsatz vor Kampagnen hätte so manches Drama seinen Lauf genommen! Besten Dank auch an die Verwaltung, Inge Clos, Frau Weyrich und Caroline Thomas für die viele Geduld und die unkomplizierte Handhabung einiger bis heute nichtdurchschaubarer Bürokratiehürden. Ein ganz herzliches Dankeschön geht auch an die IUP Hiwis Christian und Manon - für die fantastische Sozialbetreuung! Nicht unerwähnt bleiben, sollten auch meine aktuellen und ehemaligen Zimmerkollegen Margarita, Falko, Bärbel und Andreas, letzterem sei hiermit auch verziehen am Rauswurf des Sofas schuldig zu sein.
Ganz herzlich gedankt sei auch meiner Omi und meinem Opi, Herrn Bücher und all meinen Freunden für die großartige Unterstützung und auch einfach dafür daß es euch gibt!